UNIVERSITAT ROVIRA I VIRGILI
DEVELOPMENT OF OPTICAL CHARACTERIZATION METHODS FOR MICRO- AND NANO-SCALE PLANAR PHOTONIC BAND GAP STRUCTURES
Zdenek Kral
DL: T-1537-2009/ISBN:978-84-692-4556-9

DOCTORAL THESIS

Zdeněk Král

Development of optical characterization methods for micro- and nano-scale planar photonic band gap structures

Universitat Rovira i Virgili
Department of Electronic, Electric
and Automatic Control Engineering

UNIVERSITAT ROVIRA I VIRGILI
DEVELOPMENT OF OPTICAL CHARACTERIZATION METHODS FOR MICRO- AND NANO-SCALE PLANAR PHOTONIC BAND GAP STRUCTURES
Zdenek Kral
DL: T-1537-2009/ISBN:978-84-692-4556-9

UNIVERSITAT ROVIRA I VIRGILI
DEVELOPMENT OF OPTICAL CHARACTERIZATION METHODS FOR MICRO- AND NANO-SCALE PLANAR PHOTONIC BAND GAP STRUCTURES
Zdenek Kral
DL: T-1537-2009/ISBN:978-84-692-4556-9

UNIVERSITAT ROVIRA I VIRGILI
DEVELOPMENT OF OPTICAL CHARACTERIZATION METHODS FOR MICRO- AND NANO-SCALE PLANAR PHOTONIC BAND GAP STRUCTURES
Zdenek Kral
DL: T-1537-2009/ISBN:978-84-692-4556-9

UNIVERSITAT ROVIRA I VIRGILI
DEVELOPMENT OF OPTICAL CHARACTERIZATION METHODS FOR MICRO- AND NANO-SCALE PLANAR PHOTONIC BAND GAP STRUCTURES
Zdenek Kral
DL: T-1537-2009/ISBN:978-84-692-4556-9

Zdeněk Král

Development of optical characterization methods for micro- and nano-scale planar photonic band gap structures

DOCTORAL THESIS

Supervised by Dr. Josep Ferré-Borrull

Department of Electronic, Electric
and Automatic Control Engineering

UNIVERSITAT ROVIRA I VIRGILI

Tarragona
2009

UNIVERSITAT ROVIRA I VIRGILI
DEVELOPMENT OF OPTICAL CHARACTERIZATION METHODS FOR MICRO- AND NANO-SCALE PLANAR PHOTONIC BAND GAP STRUCTURES
Zdenek Kral
DL: T-1537-2009/ISBN:978-84-692-4556-9

UNIVERSITAT ROVIRA I VIRGILI
DEVELOPMENT OF OPTICAL CHARACTERIZATION METHODS FOR MICRO- AND NANO-SCALE PLANAR PHOTONIC BAND GAP STRUCTURES
Zdenek Kral
DL: T-1537-2009/ISBN:978-84-692-4556-9

UNIVERSITAT ROVIRA I VIRGILI

Department of Electronic, Electric and Automatic Control Engineering

Avinguda dels Països Catalans, 26
43007 Tarragona
Tel. 977 55 86 53
Fax 977 55 96 05

I, Josep Ferré-Borrull, aggregate professor of the Department of Electronic, Electric and Automatic Control Engineering of the Rovira i Virgili University,

CERTIFY:

That the present study, entitled "Development of optical characterization methods for micro- and nano-scale planar photonic band gap structures", presented by Zdeněk Král for the award of the degree of Doctor, has been carried out under my supervision at the Department of Electronic, Electric and Automatic Control Engineering of this university, and that it fulfils all the requirements to be eligible for the European Doctorate Label.

Tarragona, 20 February 2009

UNIVERSITAT ROVIRA I VIRGILI
DEVELOPMENT OF OPTICAL CHARACTERIZATION METHODS FOR MICRO- AND NANO-SCALE PLANAR PHOTONIC BAND GAP STRUCTURES
Zdenek Kral
DL: T-1537-2009/ISBN:978-84-692-4556-9

DL: T-1537-2009/ISBN:978-84-692-4556-9

Contents

UNIVERSITAT ROVIRA I VIRGILI
DEVELOPMENT OF OPTICAL CHARACTERIZATION METHODS FOR MICRO- AND NANO-SCALE PLANAR PHOTONIC BAND GAP STRUCTURES
Zdenek Kral
DL: T-1537-2009/ISBN:978-84-692-4556-9

UNIVERSITAT ROVIRA I VIRGILI
DEVELOPMENT OF OPTICAL CHARACTERIZATION METHODS FOR MICRO- AND NANO-SCALE PLANAR PHOTONIC BAND GAP STRUCTURES
Zdenek Kral
DL: T-1537-2009/ISBN:978-84-692-4556-9

UNIVERSITAT ROVIRA I VIRGILI
DEVELOPMENT OF OPTICAL CHARACTERIZATION METHODS FOR MICRO- AND NANO-SCALE PLANAR PHOTONIC BAND GAP STRUCTURES
Zdenek Kral
DL: T-1537-2009/ISBN:978-84-692-4556-9

Acknowledgements

In the past four years, many people contributed, either directly or indirectly, to the work resulting in this thesis. Hereby, I would like to thank all of them.

First of all I wish to thank my supervisor Dr. Josep Ferré-Borrull providing me a position to work in the NePhoS group at the University Rovira i Virgili. Josep is real expert and good person, always ready to help and to give valuable advice when it is necessary. I learned from him how to be organized in the work I am doing and how to solve a problem in an efficient way. He helped me, not only in my research project, but also in my daily living problems. I am fortunate and proud of having him as my tutor and friend.

The results achieved in this Ph.D. thesis would not be possible without the collaboration of several groups. Firstly, I would like to acknowledge the NePhoS research group at the Universitat Rovira i Virgili where this work has been carried out. Then, I would acknowledge the MNT (Micro- and Nano-Tecnologies) group from Department of Electronics, Polytechnic University of Catalonia (UPC), leaded by Professor Ramon Alcubilla, and the collaborators Dr. Trifon Trifonov and Dr. Angel Rodríguez for the fabrication of the macroporous-silicon photonic crystal (PhC) slab samples. I also acknowledge the group of Dr. Yago Olaizola from CEIT & TECNUN, University of Navarra for providing the PhC slabs fabricated by laser-interference lithography, and the FICMA group of Dr. Francez Días at the University Rovira i Virgili and Dr. Joan J. Carvajal for the KTP and RTP samples.

My special thanks go to Dr. Enric García-Caurel and Dr. Martin Foldyna from the LPICM group at Ecole Polytechnique, Paris. Enric made possible my three months intership in their laboratory and helped me with the experimental procedures, the laboratory equipment (MM16 Mueller po-

larimeter), and also with my daily troubles in Paris. I am very grateful to Martin for the nano-structured PhC slab samples, he lent me, and for his valuable comments and suggestions about the polarimetry measurements. I very appreciate that I could work with such professionals and kind people.

I am thankful to all my colleagues from the NePhoS group, Ph.D. students, and secretaries from the University Rovira i Virgili who have made my stay in Spain enjoyable over all these years. Special thanks for my close friends Alexandre Restrepo, Ronnie Juraske, Stella Vallejos, Kinga Jurasz, Edgar Sotter, Imma Planell and many others who were my "second" family in Tarragona. I also thank to Cris Blasi for her patience with my "thesis writing" stress and for helping me to improve my Spanish.

I would like to express my gratitude to Dr. Jaromír Hubálek from the Brno University of Technology who brought me the idea of going to Spain for the Erasmus student program, and consequently has changed my life for last five years.

Finally, the most kindly thanks go to Lukáš Vojkůvka, a person with which all this "story" has started. Thank you for being such good friend!

UNIVERSITAT ROVIRA I VIRGILI
DEVELOPMENT OF OPTICAL CHARACTERIZATION METHODS FOR MICRO- AND NANO-SCALE PLANAR PHOTONIC BAND GAP STRUCTURES
Zdenek Kral
DL: T-1537-2009/ISBN:978-84-692-4556-9

UNIVERSITAT ROVIRA I VIRGILI
DEVELOPMENT OF OPTICAL CHARACTERIZATION METHODS FOR MICRO- AND NANO-SCALE PLANAR PHOTONIC BAND GAP STRUCTURES
Zdenek Kral
DL: T-1537-2009/ISBN:978-84-692-4556-9

UNIVERSITAT ROVIRA I VIRGILI
DEVELOPMENT OF OPTICAL CHARACTERIZATION METHODS FOR MICRO- AND NANO-SCALE PLANAR PHOTONIC BAND GAP STRUCTURES
Zdenek Kral
DL: T-1537-2009/ISBN:978-84-692-4556-9

Chapter 1

Introduction and objectives

Photonic crystals are periodically structured electromagnetic media which prohibit the propagation of light inside the structure for frequencies within a band gap (a frequency range in which the existence of any electromagnetic modes is forbidden). Due to this ability, they have enabled existing new ways of light control and have become an attractive structure for constructing integrated optical devices.

As was first shown by E. Yablonovitch [Yablonovitch 87], the geometry and the dielectric constant of the photonic crystal structure are the main factors which dramatically change the propagation properties of the photons inside it. This fact permits a precise control over the electromagnetic field dispersion (photonic bands structure) inside the photonic crystal by appropriate tuning of its structure (e.g. by changing the design of the photonic crystal lattice or by introducing defects into the otherwise perfect periodic structure). However, previous theoretical analysis is of high importance.

The photonic band structure calculations are used to determine and predict the dispersion relations of perfect, infinitely extended photonic crystals, and photonic crystals with simple defects such as isolated cavities and waveguides. More complex simulations such as transmission and reflection from finite slabs of photonic crystal material or through waveguide bends are usually analyzed through direct simulations of Maxwell's equations, based on Finite-Difference Time Domain (FDTD) or Finite Element (FE) methods. An alternative is combining band structure calculations with elements from diffractive optics, which enables to determine the re-

flection and transmission properties of finite photonic crystal (PhC) slabs [Whittaker 99, Whittaker 02].

In recent years, most investigations have been concentrated on the modeling and fabrication of photonic crystal materials. Many research groups have also been focused on the experimental measurement of the photonic crystal band structure. Initial studies of the photonic crystal bands have been carried out in the microwave regime by phase-sensitive transmission measurements [Yablonovitch 89] that yield the wave vector inside the crystal at a given frequency. Another technique, based on the in-plane transmission in two-dimensional (2D) waveguide photonic crystals has been used to map the photonic bands from Fabry-Pérot fringes within the sample [Labilloy 97]. Several authors have also measured the photonic bands dispersion in 2D photonic crystals by means of the Angular-Dependent Reflectance Spectroscopy, first proposed by Astratov et al. [Astratov 98, Astratov 99a].

The present work is focused on the development of optical characterization methods based on several techniques to study the optical and geometrical properties of micro- and nano-structured PhC slabs. We propose here a procedure to improve the recognition of the photonic bands with these methods and we validate it by its application to various photonic crystal samples.

1.1 Objectives

The aim of this Doctoral Thesis is comprised within the framework of the development of characterization methods and their implementation to planar photonic structures that are useful within the NePhoS research group at the University Rovira i Virgili and that are valuable for the rest of scientific community. To this end, the following objectives have been established:

- Development of an experimental technique based on the Bragg diffraction in the near and middle infra red (IR) spectral range to determine the lattice properties of photonic crystal structures.

- Application of the Angular-Dependent Reflectance Spectroscopy technique to characterize the band structure of PhC slabs in the near and middle IR spectral range.

- Application of Angle-Resolved Spectroscopic Polarimetry to characterize the band structure of planar photonic crystal structures in the visible spectral range.

- Implementation of a numerical simulation tool i) to predict the optical behavior of the studied samples using the different measurement techniques, and ii) to interpret the results obtained from the measurements.

1.2 Document structure

The outline of this Doctoral Thesis is as follows. In chapters 2 and 3 the framework of the present work is established. Chapter 2 is an introduction to the concept of the Photonic Crystals and its modeling. In this chapter, special attention is paid to the numerical formalisms implemented for the calculation of the photonic band structure of the studied samples and for the calculation of the reflectance properties of the PhC slabs, related to the characterization techniques studied in this work. In chapter 3 a brief introduction to the fabrication techniques used to obtain the samples studied later in the work is given. These two chapters are not aimed at giving an exhaustive treatment of these subjects, just to establish the state-of-the-art and to give the necessary background for the following chapters.

In the fourth chapter the optical Bragg Diffraction technique for the characterization of the lattice structure of the Photonic Crystals is introduced. The next two chapters correspond to the techniques applied in this work for the experimental measurement of the photonic bands and photonic guided modes in PhC slabs. Chapter 5 is devoted to the presentation of the application of the Angular-Dependent Reflectance Spectroscopy to the characterization of PhC slabs in the middle IR, while chapter 6 presents the results obtained on the application of the Angle-Resolved Spectroscopic Polarimetry.

1.3 Framework

This Doctoral Thesis was made in the framework of the NePhoS research group at the University Rovira i Virgili and funded by the Spanish Ministry

of Science under project number TEC2005-02038, and HOPE CSD2007-00007 (Consolider-Ingenio 2010). The three months intership provided by the LPICM group at Ecole Polytechnique, Paris was also partially funded by the Generalitat de Catalunya with the grant 2007-BE2-00163.

UNIVERSITAT ROVIRA I VIRGILI
DEVELOPMENT OF OPTICAL CHARACTERIZATION METHODS FOR MICRO- AND NANO-SCALE PLANAR PHOTONIC BAND GAP STRUCTURES
Zdenek Kral
DL: T-1537-2009/ISBN:978-84-692-4556-9

UNIVERSITAT ROVIRA I VIRGILI
DEVELOPMENT OF OPTICAL CHARACTERIZATION METHODS FOR MICRO- AND NANO-SCALE PLANAR PHOTONIC BAND GAP STRUCTURES
Zdenek Kral
DL: T-1537-2009/ISBN:978-84-692-4556-9

UNIVERSITAT ROVIRA I VIRGILI
DEVELOPMENT OF OPTICAL CHARACTERIZATION METHODS FOR MICRO- AND NANO-SCALE PLANAR PHOTONIC BAND GAP STRUCTURES
Zdenek Kral
DL: T-1537-2009/ISBN:978-84-692-4556-9

Chapter 2

Introduction to the modeling of photonic crystals

This chapter provides a basic introduction to the methods used in this work for the modeling of photonic crystals. However, it is out of the scope of this chapter to give a complete review of all of the work that has been done so far in this field, because of its vast extension. The chapter is thought to give the reader the theoretical background for the understanding of the results presented in the thesis.

2.1 Fundamentals of photonic crystals

Photonic crystals[1] are artificially created materials with a periodic variation of its refractive index on a wavelength scale [John 87]. The particular behavior of photons inside these materials is analogous to that of electrons in ordinary semiconductors. From the theory of quantum mechanics, a conduction electron propagating in the periodic potential caused by atoms in the crystal lattice, behaves like a wave that suffers reflections from different lattice planes, so called Bragg reflections [Ashcroft 76]. The existence

[1]It must be noted that the denomination 'Photonic Crystals' is not correct as they are not crystalline structures. The correct denomination for these materials is Photonic Band Gap materials. However, the term Photonic Crystals is widely used and accepted, as they are a photonic analogy of the actual molecular crystals. For this reason this last denomination will be used throughout this work.

UNIVERSITAT ROVIRA I VIRGILI
DEVELOPMENT OF OPTICAL CHARACTERIZATION METHODS FOR MICRO- AND NANO-SCALE PLANAR PHOTONIC BAND GAP STRUCTURES
Zdenek Kral
DL: T-1537-2009/ISBN:978-84-692-4556-9

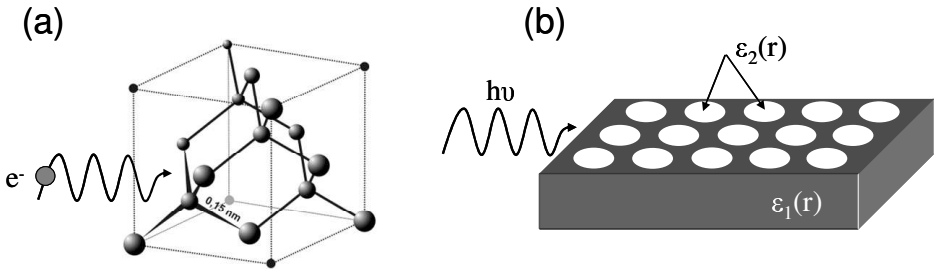

Figure 2.1: (a) Schematic illustration of an electron wave propagating in a silicon crystalline structure; (b) Schematic illustration of the propagation of a photon in a two-dimensional photonic crystal structure with periodic variation of the dielectric constant.

of a periodic potential, causing Bragg reflections, results in the build up of constructive and destructive interferences between all the reflected waves giving rise to the formation of energy bands (allowed energy states) and energy gaps (forbidden energy states). If the electron has an energy inside the gap, it can not propagate in certain directions in the crystal. Depending on the strength of the periodic potential and on the lattice structure, the gap can extend to cover all possible propagation directions, resulting in a complete band gap. A fundamental example of band gap in semiconductors is a gap between the valence and the conduction band, where in normal situation (perfect silicon crystal without impurities) no electron with energy within the gap will be found.

An optical analogous to a crystal lattice of a semiconductor is the photonic crystal, in which the atoms or molecules are replaced by optical scatterers with a size and a period of the order of magnitude of the wavelength (Figure 2.1), and the periodic potential is replaced by a periodic dielectric function (or, equivalently, a periodic refractive index). Let's consider photons moving through a block of transparent dielectric material that contains a number of tiny air holes arranged in a lattice pattern. The photons will pass through regions of high refractive index (the dielectric) and regions of low refractive index (the air holes). This contrast in refractive index looks just like the periodic potential that an electron experiences travelling through a silicon crystal. The holes in the structure act as strong scatterers. For certain wavelengths and directions, the interference of the scattered electromagnetic waves by different lattice planes is destructive. Waves with these wavelengths are Bragg reflected and can

UNIVERSITAT ROVIRA I VIRGILI
DEVELOPMENT OF OPTICAL CHARACTERIZATION METHODS FOR MICRO- AND NANO-SCALE PLANAR PHOTONIC BAND GAP STRUCTURES
Zdenek Kral
DL: T-1537-2009/ISBN:978-84-692-4556-9

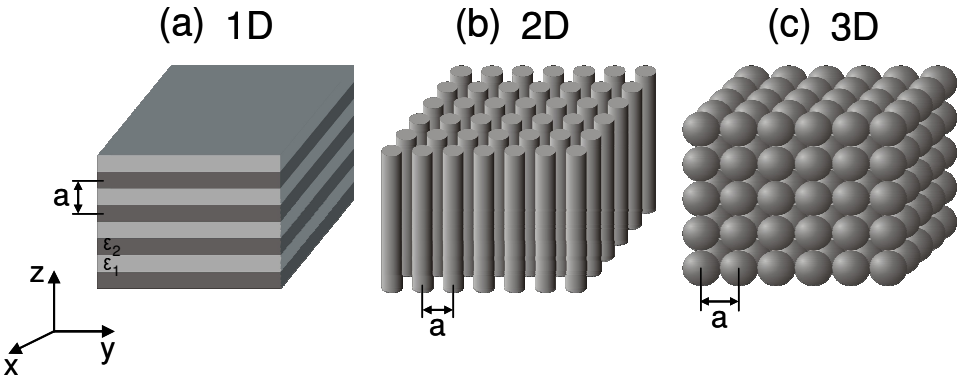

Figure 2.2: Schematic illustration of one-dimensional (a), two-dimensional (b) and three-dimensional (c) photonic crystals.

not propagate inside the structure in the direction of the Bragg reflection. This results in a formation of allowed frequency regions separated by forbidden regions, known as photonic band gaps. The patterned dielectric material thus will block light with wavelengths in the photonic band gap, while allowing other wavelengths to pass freely. The photonic band gap is therefore an optical analogue of the band gap of a semiconductor [Yablonovitch 87, Yablonovitch 89, Yablonovitch 91b, Yablonovitch 91a, Yablonovitch 93b, Yablonovitch 93a, Joannopoulos 97].

Photonic crystals can be classified depending on the dimension of their periodicity into three categories [Joannopoulos 08]: that are, one-dimensional (1D), two-dimensional (2D) and three-dimensional (3D) crystals depending on whether the periodic variation of the dielectric constant is created in one, two or three dimensions (Figure 2.2).

The one-dimensional (1D) photonic crystal (Figure 2.2a) is a periodic dielectric multilayer structure, which consists of alternating layers of material with different dielectric constants. This type of photonic crystal can act as a mirror (a Distributed Bragg Reflector) or localize light modes for light with a frequency within a specified range. The electromagnetic wave propagation in a periodic multilayer was first studied by Lord Rayleigh in 1887, who showed that such structure has a band gap, however, with some limitations. The 1D photonic crystals are generally angle-dependent on the incidence and exhibit the photonic band gap for light traveling at normal incidence. As we move away from the normal incidence (on-axis propagation), the band gap disappears, because the off-axis direction contains no

periodic dielectric regions to coherently scatter the light and split open a gap. Special example of 1D photonic crystal is an omnidirectional mirror, which reflects light for any angle of incidence and any polarization over a specified range of wavelengths. Such 1D crystal was proposed by Winn et. al. [Winn 98], and first experimentally realized by Fink et. al. [Fink 98]. Omnidirectional reflection is not a general property of 1D crystals. There are two necessary conditions. First, the dielectric contrast between the two mirror materials must be sufficiently large, and second, the smaller of the two dielectric constants of the materials must be larger than the dielectric constant of the ambient medium by a critical amount. Combining these two criteria, the omnidirectional mirrors may even exhibit an omnidirectional band gap [Xifré-Peréz 05, Bria 02, Chigrin 99]. The applications of the dielectric multilayer structures are widespread e.g. high-reflection mirrors, stop-band filters, anti-reflection coatings, etc.

A two-dimensional (2D) photonic crystal (Figure 2.2b) is a structure periodic along two of its axes and homogeneous along the third axis. This structure can block certain wavelengths of light at any angle in the plane of periodicity, thus it can exhibit a complete in-plane photonic band gap. For light propagating in this plane, the harmonic modes can be divided into two independent polarizations, each with its own band structure.

We adopt the convention that for the TM (the transverse magnetic) mode the electric field vector E is parallel to the scatterers, while for the TE (the transverse electric) mode it is the magnetic field vector H which is parallel to the scatterers. We use this electromagnetic mode convention since it is also used in the book of Busch [Busch 04], and in the vast majority of the literature concerning photonic crystals.

The earliest theoretical analysis of the 2D photonic crystal was made by Plihal et al. [Plihal 91b]. The studied structure consisted of a periodic array of circular dielectric rods in a square arrangement, embedded in a background medium of different dielectric constant. The band structure analysis showed the existence of photonic band gaps for different polarizations of the electromagnetic waves, i.e. H- and E-polarization depending on whether the magnetic H or the electric field E was polarized along the rods. Many different configurations have since been studied in an attempt to find 2D structures that have a large in-plane complete photonic band gap. Examples include square [Villeneuve 92], triangular [Plihal 91a], honeycomb

[Cassagne 96], and interstitial [Anderson 96, Wang 99] lattices coupled with square [Villeneuve 92, Padjen 94], diamond [Wang 99, Padjen 94, Agio 00], hexagonal [Padjen 94, Baba 95], elliptic [Qiu 99], and triangular [Padjen 94, Baba 95] shaped rods.

A specific example of 2D photonic structure, which can confine light also in the third dimension is a photonic crystal slab (PhC slab). It is also a periodic structure with the periodicity along two of its axes, but of a finite thickness in the third axis. Such alternative 2D structure system has a band gap for propagation in the plane of periodicity and uses the index guiding to confine light in the third dimension. An example is the structure that consists of a high-refractive-index film (a semiconductor, for example) perforated with a 2D photonic lattice and sandwiched between low-refractive-index media. In this structure, light is controlled vertically by total internal reflection (due to the refractive index contrast of the high-index core and the low-index cladding), and laterally by distributed Bragg reflection due to the presence of the 2D photonic pattern. The PhC slab has been extensively studied because it generates a pseudo-photonic band gap that covers almost all of the 3D angles and can be realized using standard lithographic techniques based on 2D patterns [Johnson 99, Chutinan 02, Chutinan 00, Painter 99, Baba 99, Krauss 96]. Another example is the PhC slab fabricated on a SOI (silicon-on-insulator) substrate [Shinya 02, Loncar 00b, Loncar 00a, Notomi 02]. The SOI substrate itself is intrinsically a slab waveguide structure that is very effective at confining light. The PhC slabs made from SOI wafers are extremely promising because they make use of commercially available high-quality wafers and mature Si nanofabrication technology. Also, the SOI slab fabrication process is relatively easy and compatible with the current device fabrication process, which makes these structures suitable for the realization of photonic integrated circuits. Several applications have been found for 2D photonic crystals and PhC slabs: semiconductor lasers [Imada 99] and light-emitting diodes [Fan 97], optical fibers [Knight 98], low-loss waveguides and bends [Johnson 99, Chutinan 02, Chutinan 00, Baba 99, Kuchinsky 00, Loncar 00b], polarizers [Ohtera 99], or channel drop filters [Fan 99, Chutinan 01, Fan 98b, Fan 98a].

The most promising photonic material from the application point of view is a three-dimensional (3D) photonic crystal with the possibility of complete 3D photonic band gap. The 3D photonic crystal was first pro-

posed by Yablonovitch [Yablonovitch 87] and John [John 87] in 1987, exactly one hundred years after Lord Rayleigh (1887) discovered a band gap in the one-dimensional multilayer structure. The suggestion of a material with a complete photonic band gap was shortly followed by other authors Yablonovitch and Gmitter [Yablonovitch 89], Satpathy [Satpathy 90], Leung and Liu [Leung 90], and Ho [Ho 90]. However, it took three more years, in 1991, before the first artificial 3D photonic crystal was produced by mechanically drilling an array of holes along the three lattice vectors of the fcc (face-centered) lattice into a block of dielectric medium with a refractive index of 3.6. This photonic crystal has been named "Yablonovite", after its discoverer and showed a stop-band for the transmission of microwave radiation between 13 and 15 GHz [Yablonovitch 91a]. Other 3D structures that have band gaps at microwave and radio frequencies have been developed by Ozbay [Ozbay 94] and Noda [Noda 99].

The first 3D photonic crystal with a complete band gap at infrared wavelengths was proposed by Ho et al. [Ho 94]. The so-called "woodpile" or "picket fence" structure was formed by a stack of dielectric rectangular "logs". This 3D photonic band gap structure has been also extensively studied by other authors (Sözüer and Dowling [Sozuer 94]). Lin et al. [Lin 98] obtained a complete band gap with a woodpile structure fabricated by stacking micro-machined silicon wafers at a wavelength of 12 μm. Subsequently, the same authors achieved a band gap around a wavelength of 1.6 μm by reducing the size of the structure [Lin 99]. The key factor to fabricate the woodpile structure was the accurate alignment of successive layers, however it has become extremely difficult to achieve the required accuracy as the dimensions of the structure were reduced, and as the number of the layers was increased.

Another 3D photonic band gap structure was realized by self-arrangement of sub-micron-sized silica spheres in a colloidal suspension. By subsequent infiltration of the space between the spheres with a high-refractive dielectric material and dissolving away the spheres, a structure called inverse opal was created. This method has been published by several authors (Wijnhoven et al. [Wijnhoven 98], Blanco et al. [Blanco 00], Vlasov et al. [Vlasov 97, Vlasov 01])

In spite of a constantly growing development, the fabrication of useful 3D photonic crystals that work in the near-IR (780-3000 nm) and visible

(450-750 nm) regions of the spectrum (the regions of their most promising applications) is still a difficult task [Noda 00]. The problem consists in the fundamentals of the band gap theory itself. Almost all of the applications for photonic crystals rely on the existence of the photonic band gap. The frequency at which the band gap occurs is directly related to the size and period of the scattering elements that make up the photonic lattice. Specifically, the size and period of the features must be of the order $\lambda/2$, where λ is the wavelength of light at which the gap occurs. Therefore, to achieve a band gap in the visible region one should be able to fabricate structures with lattice constants in the order of one quarter of micron. Moreover, the technology should be able to fabricate precisely small elements with roughly ten lattice periods in each direction. To fulfill all these conditions is technically very difficult, especially when any deviations in the size or in the period may affect the properties of the photonic crystal.

2.2 Photonic bands calculation

The mathematical formulation of bands in a photonic crystal has been adapted from quantum mechanics and solid state physics. To study the propagation of light in photonic crystals, we shall start with the Maxwell equations and formulate the eigenvalue problem of the wave equation.

2.2.1 Maxwell equations and eigenvalue problem

Maxwell equations in the most general form are given in MKS units as follows:

$$\nabla\cdot \mathbf{D}(\mathbf{r},t) = 0, \tag{2.1}$$

$$\nabla\cdot \mathbf{B}(\mathbf{r},t) = 0, \tag{2.2}$$

$$\nabla \times \mathbf{E}(\mathbf{r},t) = -\frac{\partial}{\partial t}\mathbf{B}(\mathbf{r},t), \tag{2.3}$$

$$\nabla \times \mathbf{H}(\mathbf{r},t) = \frac{\partial}{\partial t}\mathbf{D}(\mathbf{r},t), \tag{2.4}$$

where $\mathbf{E}$ and $\mathbf{H}$ are the macroscopic electric and magnetic field vectors, $\mathbf{D}$ and $\mathbf{B}$ are the electric displacement and magnetic induction vectors. We restrict our study to the eigen-modes of the radiation field, therefore we

assume here no free charges or electric currents. In order to solve the wave equations derived from Maxwells equations, we need so-called constitutive equations that relate $\mathbf{D}$ to $\mathbf{E}$ and $\mathbf{B}$ to $\mathbf{H}$. Since we do not deal here with magnetic materials, we take the magnetic permeability of the photonic crystal equal to that in free space, μ_0:

$$\mathbf{B}(\mathbf{r},t) = \mu_0 \mathbf{H}(\mathbf{r},t). \tag{2.5}$$

As for the dielectric constant[2], we assume that it is real, isotropic, perfectly periodic with respect to the spatial coordinate $\mathbf{r}$, and does not depend on frequency (and therefore independent of time as well). The periodicity of the dielectric constant is defined by a function

$$\epsilon(\mathbf{r} + \mathbf{a}_i) = \epsilon(\mathbf{r}) \quad (i = 1, 2, 3), \tag{2.6}$$

where $\{\mathbf{a}_i\}$ are the elementary lattice vectors (Appendix A) of the photonic crystal. We denote the dielectric constant of free space by ϵ_0 and the relative dielectric constant of the photonic crystal by $\epsilon(\mathbf{r})$[3]. The electric displacement is thus given by

$$\mathbf{D}(\mathbf{r},t) = \epsilon_0 \epsilon(\mathbf{r}) \mathbf{E}(\mathbf{r},t). \tag{2.7}$$

All of these quantities are potentially functions of both position $\mathbf{r}$ and time t. In the particular case of the light propagation in a periodic dielectric media (e.g. a photonic crystal), the general Maxwell's equations can be simplified by replacing equations (2.5) and (2.7) in the master Maxwell's equations (2.1-2.4), we obtain following form:

$$\nabla \cdot \{\epsilon(\mathbf{r}) \cdot \mathbf{E}(\mathbf{r},t)\} = 0, \tag{2.8}$$

$$\nabla \cdot \mathbf{H}(\mathbf{r},t) = 0, \tag{2.9}$$

$$\nabla \times \mathbf{E}(\mathbf{r},t) = -\mu_0 \frac{\partial}{\partial t} \mathbf{H}(\mathbf{r},t), \tag{2.10}$$

[2]Some authors also call it the relative permittivity.

[3]Some authors use ϵ_r for the relative dielectric constant (or relative permittivity) and ϵ for the permittivity $\epsilon_0 \epsilon_r$. In this work, we adopt the convention of dropping the r subscript, since we work only with the dimensionless ϵ_r.

UNIVERSITAT ROVIRA I VIRGILI
DEVELOPMENT OF OPTICAL CHARACTERIZATION METHODS FOR MICRO- AND NANO-SCALE PLANAR PHOTONIC BAND GAP STRUCTURES
Zdenek Kral
DL: T-1537-2009/ISBN:978-84-692-4556-9

$$\nabla \times \mathbf{H}(\mathbf{r},t) = \epsilon_0 \epsilon(\mathbf{r}) \frac{\partial}{\partial t} \mathbf{E}(\mathbf{r},t), \tag{2.11}$$

When we eliminate $\mathbf{E}(\mathbf{r},t)$ or $\mathbf{H}(\mathbf{r},t)$ in equations 2.10 and 2.11, we obtain the following wave equations:

$$\frac{1}{\epsilon(\mathbf{r})} \nabla \times \{\nabla \times \mathbf{E}(\mathbf{r},t)\} = -\frac{1}{c^2} \frac{\partial^2}{\partial t^2} \mathbf{E}(\mathbf{r},t), \tag{2.12}$$

$$\nabla \times \left\{ \frac{1}{\epsilon(\mathbf{r})} \nabla \times \mathbf{H}(\mathbf{r},t) \right\} = -\frac{1}{c^2} \frac{\partial^2}{\partial t^2} \mathbf{H}(\mathbf{r},t), \tag{2.13}$$

where c stands for the light velocity in free space:

$$c = \frac{1}{\sqrt{\epsilon_0 \mu_0}}. \tag{2.14}$$

The field functions $\mathbf{E}$ and $\mathbf{H}$, thanks to the linearity of Maxwell's equations, can be expressed in a form of harmonic fields:

$$\mathbf{E}(\mathbf{r},t) = \mathbf{E}(\mathbf{r}) e^{-i\omega t}, \tag{2.15}$$

$$\mathbf{H}(\mathbf{r},t) = \mathbf{H}(\mathbf{r}) e^{-i\omega t}, \tag{2.16}$$

where ω is the eigen-angular frequency, and $\mathbf{E}(\mathbf{r})$ and $\mathbf{H}(\mathbf{r})$ are the eigenfunctions of the wave equations. By inserting equations (2.15) and (2.16) into (2.12) and (2.13), in a few steps it is possible to recast the Maxwell's equations in a closed form either for the electric or magnetic fields:

$$\frac{1}{\epsilon(\mathbf{r})} \nabla \times \{\nabla \times \mathbf{E}(\mathbf{r})\} = \left(\frac{\omega}{c}\right)^2 \mathbf{E}(\mathbf{r}), \tag{2.17}$$

$$\nabla \times \left\{ \frac{1}{\epsilon(\mathbf{r})} \nabla \times \mathbf{H}(\mathbf{r}) \right\} = \left(\frac{\omega}{c}\right)^2 \mathbf{H}(\mathbf{r}). \tag{2.18}$$

We have transformed Maxwell's equations in an eigenvalue problem, where $\left(\frac{\omega}{c}\right)^2$ are the eigenvalues, and the fields $\mathbf{E}(\mathbf{r})$ and $\mathbf{H}(\mathbf{r})$ are the eigenfunctions of our problem. There are two important properties of the equations (2.17) and (2.18). One property is that they are scale-independent and the other is the time reversal symmetry of the wave equation. This means that we can solve the equations once and then apply the same results

to problems at all length scales and frequencies. In other words, the scaling law tells us that two photonic crystals which are similar to each other essentially have the same photonic band structure, that is, the difference between the two band structures is simply the scales of frequency and the wave vector. Because of this scale invariance, it is convenient to use dimensionless units for distance and time. Distances are usually represented as multiples of a (a=lattice constant), and all angular frequencies in units of $2\pi c/a$, which is equivalent to a/λ (λ= vacuum wavelength) [Sakoda 05].

2.2.2 Periodicity and Bloch-Floquet theorem

By definition, a photonic crystal is a periodic arrangement of different dielectric media which implies that the dielectric constant $\epsilon(\mathbf{r})$ is a periodic function of the position ($\mathbf{r}$) defined by the equation 2.6. The analogy between the electronic wave equation in ordinary crystals with a periodic potential and the periodic dielectric function in photonic crystals allows to impose the Bloch-Floquet theorem into equations (2.17) and (2.18). The Bloch-Floquet theorem states that the general solution of equations (2.17) and (2.18) is invariant under a translational symmetry[4]. $\mathbf{E}(\mathbf{r})$ and $\mathbf{H}(\mathbf{r})$ from (2.17) and (2.18) are thus characterized by a wave vector $\mathbf{k}$ in the first Brillouin zone[5] and by a band index n as

$$\mathbf{E}(\mathbf{r}) = \mathbf{E}_{kn}(\mathbf{r}) = u_{kn}(\mathbf{r})e^{ik\cdot r}, \tag{2.19}$$

$$\mathbf{H}(\mathbf{r}) = \mathbf{H}_{kn}(\mathbf{r}) = v_{kn}(\mathbf{r})e^{ik\cdot r}, \tag{2.20}$$

where $u_{kn}(\mathbf{r})$ and $v_{kn}(\mathbf{r})$ are periodic vectorial functions that satisfy the following relations

$$u_{kn}(\mathbf{r} + a_i) = u_{kn}(\mathbf{r}), \tag{2.21}$$

$$v_{kn}(\mathbf{r} + a_i) = v_{kn}(\mathbf{r}), \quad (i = 1, 2, 3). \tag{2.22}$$

[4] $\mathbf{E}_k(\mathbf{r}) = \mathbf{E}_k(\mathbf{r} + \mathbf{R}) = e^{ik\cdot\mathbf{R}}\mathbf{E}_k(\mathbf{r})$, $\mathbf{H}_k(\mathbf{r}) = \mathbf{H}_k(\mathbf{r} + \mathbf{R}) = e^{ik\cdot\mathbf{R}}\mathbf{H}_k(\mathbf{r})$, where $\mathbf{R} = \sum_i n_i a_i$ is a linear combination of elementary lattice vectors.

[5] Detailed description of the first Brillouin zone and irreducible Brillouin zone is given in Appendix A.

2.2.3 Plane-wave expansion method

The plane wave expansion method is one of the techniques used to calculate the photonic band structure. This method has been taken from solid state physics and adapted to the photonic crystals. The method is based on the Fourier expansion of the electromagnetic field and the dielectric function $\epsilon(\mathbf{r})$. The photonic band structure can be obtained straightforwardly by considering the wave equation (2.17) or (2.18) in the reciprocal space[6]. To this end, the inverse of the periodic dielectric function $\epsilon(\mathbf{r})$ should be expanded in a Fourier series on the reciprocal lattice $\mathbf{G}$:

$$\frac{1}{\epsilon(\mathbf{r})} = \sum_{G} \kappa(\mathbf{G}) e^{i\mathbf{G}\cdot\mathbf{r}}, \tag{2.23}$$

where the Fourier coefficients $\kappa(\mathbf{G})$ are obtained through an integration over the primitive unit cell, whose volume is defined by Ω, as follows:

$$\kappa(\mathbf{G}) = \frac{1}{\Omega} \int_{\Omega} d^3r \frac{1}{\epsilon(\mathbf{r})} e^{-i\mathbf{G}\cdot\mathbf{r}}. \tag{2.24}$$

Considering the spatial periodicity of the functions (2.19) and (2.20), the eigenfunctions of the electromagnetic field will be expanded in Fourier series like the inverse of the dielectric function $\epsilon^{-1}(\mathbf{r})$ in (2.23). The Fourier expansion leads to the following form of the eigenfunctions:

$$\mathbf{E}_{\mathbf{k}n}(\mathbf{r}) = \sum_{\mathbf{G}} \mathbf{E}_{\mathbf{k}n}(\mathbf{G}) e^{i(\mathbf{k}+\mathbf{G})\cdot\mathbf{r}}, \tag{2.25}$$

$$\mathbf{H}_{\mathbf{k}n}(\mathbf{r}) = \sum_{\mathbf{G}} \mathbf{H}_{\mathbf{k}n}(\mathbf{G}) e^{i(\mathbf{k}+\mathbf{G})\cdot\mathbf{r}}. \tag{2.26}$$

For the sake of simplicity, the coefficients of reciprocal lattice space $\mathbf{E}_{\mathbf{k}n}(\mathbf{G})$ and $\mathbf{H}_{\mathbf{k}n}(\mathbf{G})$ are denoted by the same symbols as the original ones in real space. Substituting (2.23), (2.25) and (2.26) into (2.17) and (2.18), we obtain the following eigenvalue equations for the expansion coefficients $\{\mathbf{E}_{\mathbf{k}n}(\mathbf{G})\}$

[6] see Appendix A

and $\{\mathbf{H}_{\mathbf{k}n}(\mathbf{G})\}$:

$$-\sum_{\mathbf{G}'}\kappa(\mathbf{G}-\mathbf{G}')(\mathbf{k}+\mathbf{G}')\times\{(\mathbf{k}+\mathbf{G}')\times\mathbf{E}_{\mathbf{k}n}(\mathbf{G}')\}=\left(\frac{\omega_{\mathbf{k}n}}{c}\right)^2\mathbf{E}_{\mathbf{k}n}(\mathbf{G}),\quad(2.27)$$

$$-\sum_{\mathbf{G}'}\kappa(\mathbf{G}-\mathbf{G}')(\mathbf{k}+\mathbf{G})\times\{(\mathbf{k}+\mathbf{G}')\times\mathbf{H}_{\mathbf{k}n}(\mathbf{G}')\}=\left(\frac{\omega_{\mathbf{k}n}}{c}\right)^2\mathbf{H}_{\mathbf{k}n}(\mathbf{G}),\quad(2.28)$$

where $\omega_{\mathbf{k}n}$ denotes the eigen-angular frequency of the eigenmodes $\mathbf{E}_{\mathbf{k}n}(\mathbf{r})$ and $\mathbf{H}_{\mathbf{k}n}(\mathbf{r})$. By solving these two sets of equations numerically, we can obtain the dispersion relation of the eigenmodes, or equivalently, the photonic band structure.

In order to solve equations 2.27 and 2.28, the most used approach is the truncation of the expansions 2.23, 2.25 and 2.26 up to a finite number N_G of vectors[7] of the reciprocal lattice $\mathbf{G}'$. With this truncation, equations 2.27 and 2.28 are matrix eigenvalue equations that can be solved with standard numerical procedures. The result is a set of eigenvalues $\{\omega_i\}$ and, for each eigenvalue, a set of the expansion coefficients $\{\mathbf{H}_{\mathbf{k}n}(\mathbf{G}_i)\}$ or $\{\mathbf{E}_{\mathbf{k}n}(\mathbf{G}_i)\}$.

2.3 Numerical calculation of the interaction of light with photonic crystal planar structures

The analysis methods developed in this Doctoral Thesis provide calculation of the interaction between light and photonic crystal planar structures. These methods use a scattering matrix (S-matrix) treatment introduced by Whittaker and Culshaw [Whittaker 99]. This treatment is based on the modeling of the propagation of light in a patterned multilayer structure using the S-matrix formalism [Ko 88] and incorporates the extended boundary conditions necessary to describe the coupling with the external radiation, which is the basis for the characterization methods developed in this work.

The S-matrix formalism is originated in the development of the propagating waves at each layer of the structure as a sum of plane waves which can propagate at directions not necessarily perpendicular to the scatterers. The plane waves are eigen functions for a given layer and constitute a complete basis set of functions for the propagating waves. Then, the S-matrix method

[7] Number of the plane waves used in the expansion.

UNIVERSITAT ROVIRA I VIRGILI
DEVELOPMENT OF OPTICAL CHARACTERIZATION METHODS FOR MICRO- AND NANO-SCALE PLANAR PHOTONIC BAND GAP STRUCTURES
Zdenek Kral
DL: T-1537-2009/ISBN:978-84-692-4556-9

is used to relate the waves at each layer of the structure with those at the other layers, and also with the waves at the incident medium and at the substrate. The S-matrix formalism is specially adequate for this modeling since it deals better with numerical overflow than other methods such as the transfer-matrix method. A brief outline of the method is given in this section. Results of the simulations are shown in chapters 5 and 6.

The formalism begins with the determination of the eigenstates in each layer of the strucutre. For this reason, the Maxwell equations are solved for a structure indefinite in the z direction, and where the waves can propagate in any direction. To this end, first the electric and magnetic fields are expanded as a sum of plane waves with different amplitudes. The magnetic field[8] thanks to the Bloch-Floquet theorem can be expressed as

$$\mathbf{H}(\mathbf{r},z)=\sum_{\mathbf{G}}\mathbf{H}_{\mathbf{k}}(\mathbf{G},z)e^{i(\mathbf{k}+\mathbf{G})\cdot\mathbf{r}}, \tag{2.29}$$

where $\mathbf{k}=(k_x,k_y)$ is the Bloch wave vector, $\mathbf{G}$ is the reciprocal lattice vector, and $\mathbf{r}=(x,y)$. An harmonic time dependence with ω angular frequency is assumed.

It is also necessary to introduce the Fourier expansion of the dielectric function:

$$\epsilon(\mathbf{G})=\frac{1}{S}\int_{unitcell}d\mathbf{r}\;\epsilon(\mathbf{r})e^{i\mathbf{G}\cdot\mathbf{r}}, \tag{2.30}$$

where S is the area of the in-plane unit cell. By substituting the expansions in the Maxwell curl equations, the momentum representation in component form is obtained:

$$\begin{aligned} i\hat{k}_y h_z(z)-h_y'(z)&=-i\hat{\epsilon}e_x(z)\\ h_x'(z)-i\hat{k}_x h_z(z)&=-i\hat{\epsilon}e_y(z)\\ i\hat{k}_x h_y(z)-i\hat{k}_y h_x(z)&=-i\hat{\epsilon}e_z(z)\end{aligned} \tag{2.31}$$

and

$$\begin{aligned} i\hat{k}_y e_z(z)-e_y'(z)&=i\omega^2 h_x(z)\\ e_x'(z)-i\hat{k}_x e_z(z)&=i\omega^2 h_y(z)\\ i\hat{k}_x e_y(z)-i\hat{k}_y e_x(z)&=i\omega^2 h_z(z),\end{aligned} \tag{2.32}$$

where the h_x, h_y and h_z are the coefficients of the expansion 2.29 expressed

[8] analogous for the electric field

as the three components. This is, h_x, h_y and h_z are Fourier space vectors whose index is the **G** in the expansion 2.29. The $\hat{k}_x, \hat{k}_y$ are diagonal matrices with $(\hat{k}_x)_{GG} = (k_x + G_x)$ and $(\hat{k}_y)_{GG} = (k_y + G_y)$, and the primes denote differentiation with respect to z. The notation adopted in this section to distinguish various types of vector and matrix is described in the following: bold faces denote three vectors (**E**,**H**), while lower case italics are used for Fourier space vectors (***e***,***h***). For a finite system with N_G reciprocal lattice vectors, the matrices that occur are mostly of dimension $N_G \times N_G$, indicated by hatted lower case ($\hat{\epsilon}, \hat{\eta}$), or $2N_G \times 2N_G$, for which various upper case symbols will be used ($\mathcal{E}$, $\mathcal{H}$, Φ).

The next step is to find the eigen states of each layer of the structure for waves that can propagate not only perpendicular to the scatterers but in any angle. To this end, the waves are expanded as a sum:

$$\begin{aligned}\mathbf{H}(\mathbf{r}, z) = \sum_{\mathbf{G}} \phi_x(\mathbf{G}) \left\{ \hat{\mathbf{x}} - \frac{1}{q}(k_x + G_x)\hat{\mathbf{z}} \right\} e^{i(\mathbf{k}+\mathbf{G})\cdot\mathbf{r}+iqz} \\ +\phi_y(\mathbf{G}) \left\{ \hat{\mathbf{y}} - \frac{1}{q}(k_y + G_y)\hat{\mathbf{z}} \right\} e^{i(\mathbf{k}+\mathbf{G})\cdot\mathbf{r}+iqz},\end{aligned} \tag{2.33}$$

where $\hat{\mathbf{x}}$, $\hat{\mathbf{y}}$ and $\hat{\mathbf{z}}$ are the conventional unit vectors defining the coordinate axes and $\phi_x(\mathbf{G})$, $\phi_y(\mathbf{G})$ are expansion coefficients. Substituting this expansion into the Maxwell equations 2.31 and 2.32, an eigenvalue equation for ω and for the expansion coefficients ϕ_x and ϕ_y is obtained,

$$[\mathcal{H}(q^2 + K) + \mathcal{K}]\phi = \omega^2\phi, \tag{2.34}$$

where $\phi = (\phi_x, \phi_y)^T$. With the proper transformations this equation can be transformed to an eigenvalue equation for q:

$$[(\omega^2 - \mathcal{K})\mathcal{E}(\omega^2 - \mathcal{K}) - \omega^2 K]\phi = q^2(\omega^2 - \mathcal{K})\phi, \tag{2.35}$$

where:

$$\mathcal{H} = \begin{pmatrix} \hat{\eta} & 0 \\ 0 & \hat{\eta} \end{pmatrix}, \tag{2.36}$$

$$K = \begin{pmatrix} \hat{k}_x\hat{k}_x & \hat{k}_x\hat{k}_y \\ \hat{k}_y\hat{k}_x & \hat{k}_y\hat{k}_y \end{pmatrix}, \tag{2.37}$$

$$\mathcal{K} = \begin{pmatrix} \hat{k}_y\hat{\eta}\hat{k}_y & -\hat{k}_y\hat{\eta}\hat{k}_x \\ -\hat{k}_x\hat{\eta}\hat{k}_y & \hat{k}_x\hat{\eta}\hat{k}_x \end{pmatrix}, \tag{2.38}$$

$$\mathcal{E} = \begin{pmatrix} \hat{k}_y\hat{\eta}\hat{k}_y & -\hat{k}_y\hat{\eta}\hat{k}_x \\ -\hat{k}_x\hat{\eta}\hat{k}_y & \hat{k}_x\hat{\eta}\hat{k}_x \end{pmatrix}. \tag{2.39}$$

The solution to this equation is a set of eigenvectors ϕ_n with their corresponding eigenvalues q_n for a given $\mathbf{k}$ and ω, and for each of the layers of the structure. This equation can be solved by truncating the expansions at a finite number of reciprocal lattice vectors $\mathbf{G}$ and using standard matrix algorithms. The calculations in this work have been all carried out with 121 plane waves. Although this is a small number of plane waves, it has been tested that the convergence is enough for the simulations carried out in the work. This is mainly due to the fact that the characterization methods developed in this work are applied to the lower bands of the photonic crystals.

Any electromagnetic wave propagating inside one of the layers of the structure can be expanded as a sum of these eigenmodes:

$$\begin{pmatrix} h_x(z) \\ h_y(z) \end{pmatrix} = \sum_n \begin{pmatrix} \phi_{x_n} \\ \phi_{y_n} \end{pmatrix} (e^{iq_n z}a_n + e^{iq_n(d-z)}b_n), \tag{2.40}$$

and

$$\begin{pmatrix} -e_y(z) \\ e_x(z) \end{pmatrix} = \sum_n \begin{pmatrix} \hat{\eta} & 0 \\ 0 & \hat{\eta} \end{pmatrix} \left\{ q_n^2 + \begin{pmatrix} \hat{k}_x\hat{k}_x & \hat{k}_x\hat{k}_y \\ \hat{k}_y\hat{k}_x & \hat{k}_y\hat{k}_y \end{pmatrix} \right\} \times \begin{pmatrix} \phi_{x_n} \\ \phi_{y_n} \end{pmatrix} \frac{1}{q_n}(e^{iq_n z}a_n + e^{iq_n(d-z)}b_n). \tag{2.41}$$

Here, the a_n and b_n correspond to the coefficients of the expansion. The a_n correspond to the coefficients for eigenmodes propagating in the forward direction (towards positive z) and the b_n correspond to eigenmodes propagating in the backward direction (see Figure 2.3). Thus, any propagating wave in one of the layers of the structure is parameterized in the form of a vector of the amplitudes $(a, b)^T$. The S-matrix relates the amplitudes

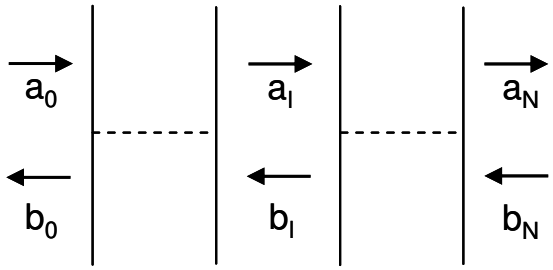

Figure 2.3: Labeling scheme for forward and backward going waves in different layers of the structure. l=0 is the surface, l=N the substrate. After reference [Whittaker 99].

(expansion coefficients) in two different layers of the structure:

$$\begin{pmatrix} a_l \\ b_{l'} \end{pmatrix} = S(l', l) \begin{pmatrix} a_{l'} \\ b_l \end{pmatrix} = \begin{pmatrix} S_{11} & S_{12} \\ S_{21} & S_{22} \end{pmatrix} \begin{pmatrix} a_{l'} \\ b_l \end{pmatrix}. \tag{2.42}$$

It is important to note that the S-matrix relates the amplitudes of the waves propagating inward (a_l and $b_{l'}$) with respect the two layers, l and l', with the amplitudes propagating outwards ($a_{l'}$ and b_l). It is this detail that confers numerical stability to the S-matrix formalism. The actual values of the S_{11}, S_{12}, S_{21} and S_{22} are obtained by requiring that the fields on either side of the interface satisfy the electromagnetic boundary conditions, this is continuity of the in-plane components H_x, H_y, E_x and E_y. Once the S-matrix for the whole structure is calculated, reflection and transmission coefficients can be determined. The relevant S-matrix for this calculation is the one relating the amplitudes in the incident medium ($l = 0$) with the amplitudes in the substrate ($l = N$): $S(0, N)$. For an experiment in which light is incident on the sample surface, the amplitudes a_0 are determined by the incident wave and $b_N = 0$ (as no wave is incident from the substrate). Thus, the reflected amplitudes are $b_0 = S(0, N)a_0$. Then, it is only necessary to translate the amplitudes a_0, b_0, a_N and b_N into experimental angle and polarization-dependent external plane waves. An external plane wave is specified by its polarization and direction of propagation, defined by polar coordinates (θ, ϕ) relative to the surface normal (see Figure 2.4). Writing $k_0 = \sqrt{\epsilon\omega/c}$, where ϵ is the dielectric constant of the external medium, the in-plane wave vector is

$$\mathbf{k} = k_0 \, sin\,\theta(cos\,\phi\hat{\mathbf{x}} + sin\,\phi\hat{\mathbf{y}}). \tag{2.43}$$

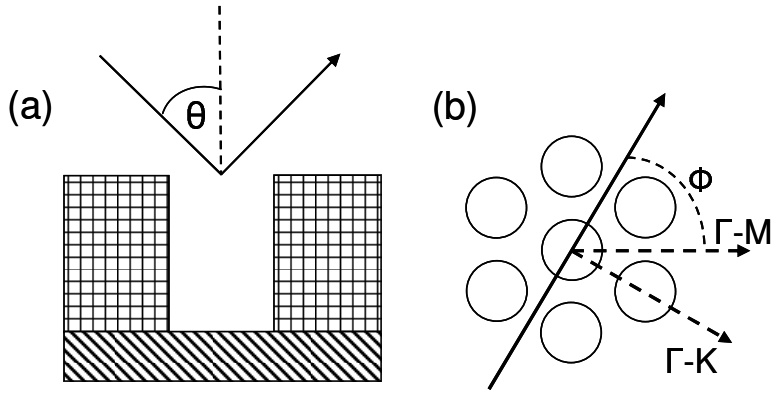

Figure 2.4: Schematic illustration of the direction of light propagation defined by polar coordinates (θ, ϕ) relative to the surface normal. (a) Cross section and (b) planar view, showing a triangular lattice of holes and examples of the high-symmetry direction. A [Whittaker 99].

Then, the TE- and TM-polarized incident plane waves are given by the field components

$$\begin{aligned}
\mathbf{E}_{TE} &= \epsilon_0 \omega c Z^{1/2} (sin\,\phi \hat{\mathbf{x}} - cos\,\phi \hat{\mathbf{y}}) e^{i(\mathbf{k}\cdot\mathbf{r}+qz)} \\
\mathbf{H}_{TE} &= Z^{-1/2} (cos\,\theta\, cos\,\phi \hat{\mathbf{x}} + cos\,\theta\, sin\,\phi \hat{\mathbf{y}} - sin\,\theta \hat{\mathbf{z}}) e^{i(\mathbf{k}\cdot\mathbf{r}+qz)} \\
\mathbf{E}_{TM} &= \epsilon_0 \omega c Z^{1/2} (cos\,\theta\, cos\,\phi \hat{\mathbf{x}} + cos\,\theta\, sin\,\phi \hat{\mathbf{y}} - sin\,\theta \hat{\mathbf{z}}) e^{i(\mathbf{k}\cdot\mathbf{r}+qz)} \\
\mathbf{H}_{TM} &= Z^{-1/2} (-sin\,\phi \hat{\mathbf{x}} + cos\,\phi \hat{\mathbf{y}}) e^{i(\mathbf{k}\cdot\mathbf{r}+qz)},
\end{aligned} \tag{2.44}$$

where $Z = \sqrt{\mu_0/(\epsilon_0 \epsilon)}$ is the intrinsic impedance of the external medium. These fields can be easily expressed in terms of the a_0 amplitudes. Thus, the b_0 can be obtained from the S-matrix and translated back into the amplitudes of the reflected plane waves and reflection coefficients, for the different polarizations.

UNIVERSITAT ROVIRA I VIRGILI
DEVELOPMENT OF OPTICAL CHARACTERIZATION METHODS FOR MICRO- AND NANO-SCALE PLANAR PHOTONIC BAND GAP STRUCTURES
Zdenek Kral
DL: T-1537-2009/ISBN:978-84-692-4556-9

Chapter 3

Fabrication of 2D photonic crystal slabs

This chapter refers to some technologies related with the fabrication of the planar photonic crystal structures that are investigated in the present work. Each section describes the fabrication process of a particular type of planar photonic crystal.

3.1 Lithography

Lithography is generally a process used to transfer a pattern from a mask to a surface. The modern lithography techniques adapted in the micro-fabrication industry mostly refer to photolithography (optical lithography), which is basically a photographic process by which a light-sensitive polymer, called a photoresist, is exposed and developed to form three-dimensional relief images on the substrate. However, there are several other lithography techniques available nowadays, which mainly differ in their physical principle and size of the pattern to be able to print with adequate control. There is:

- Optical lithography (photolithography)
  - Deep Ultra-Violet (DUV)
  - Extreme Ultra-Violet (EUV)
  - X-ray

  - Immersion

- Electron Beam lithography (EBL)
- Nanoimprint lithography
- Laser Interference lithography (LIL)

A typical *photolithography* procedure consists of depositing a layer of photoresist (by spin coating) several nanometers thick on a substrate. After coating, the resulting photoresist film is prebaked, which removes the solvent included in the photoresist. The main reason for removing the solvent content is to stabilize the resist film. The subsequent step is placing a transparent plate (UV transparent glass or deep UV transparent quartz) covered by a thin patterned Cr layer with opaque areas, called a photo-mask between a source of illumination and the substrate. Then, the layer of photoresist is exposed to light. There are three methods of exposing a photoresist through a master pattern: (i) contact printing which offers high resolution, but practical problems such as mask damage, (ii) proximity printing, where the mask is kept a set distance above the substrate (lower resolution), and (iii) projection printing of the image of the mask onto the substrate throught a reduction lens. During the exposure, light passes through the photo-mask onto a photoresist-covered substrate, whereas the mask acts as a stencil. The light induces a photochemical reaction in the exposed photoresist zones. After exposure and subsequent post-exposure bake, the substrate is immersed in a developer solution where either the exposed zones (positive tone resist) or the un-exposed zones (negative tone) of photoresist are removed.

The ability to project a clear image of a very small feature onto the photoresist-covered substrate is limited by the wavelength of the light that is used and the ability of the reduction lens system to capture enough diffraction orders from the illuminated mask. In optical projection lithography, resolution is given by the equation

$$W = \frac{k_1 \cdot \lambda}{NA}, \tag{3.1}$$

where λ and NA are the exposure wavelength and numerical aperture of the optical lithography tool, and k_1 is a constant for a specific lithographic process (k_1 depends on resist and substrate reflectivity).

UNIVERSITAT ROVIRA I VIRGILI
DEVELOPMENT OF OPTICAL CHARACTERIZATION METHODS FOR MICRO- AND NANO-SCALE PLANAR PHOTONIC BAND GAP STRUCTURES
Zdenek Kral
DL: T-1537-2009/ISBN:978-84-692-4556-9

Lithography systems have progressed from blue wavelengths (436 nm mercury lamp filtered for G- and H-lines) to UV (365 nm I-line) to deep-UV (248 nm line-narrowed KrF laser) to todays mainstream high resolution wavelength of 193 nm (ArF excimer laser). In the meantime, projection tool numerical apertures have risen from 0.16 for the first scanners to amazingly high 0.93 NA systems today producing features well under 100 nm in size. The strategy to meet the continued demands for higher resolution and larger depth of focus is to develop new lasers or migrate to an expensive synchrotron to generate enough EUV (extreme ultraviolet) and X-ray photons. An alternative is the use of *immersion photolithography*, which is a resolution enhancement technique that replaces the usual air gap between the final lens and the substrate surface with a liquid medium that has a refractive index greater than one. The resolution is increased by a factor equal to the refractive index of the liquid. Current immersion lithography tools use highly purified water for this liquid, achieving feature sizes of 37 nm [Wagner 07], with plans to bring 32 nm parts to market in late 2009.

An alternative to photolithography is *electron beam lithography* (EBL), in which the photons for resist exposure are replaced by electrons. The EBL is a technique for creating structures in electron-beam sensitive resists by a focused electron beam. Because of its intrinsic high resolution (down to 10 nm) and flexibility, EBL is at present the primary lithographic technique used in sub-quarter-micron device research (for prototyping of special circuits, optical waveguides, nanodevices, quantum wires, finFETs, single photon detectors, etc.). However, for the massive production of chips it is not suitable due to the high cost and slow rate of production.

Nanoimprint lithography, first suggested by Chou et al. [Chou 96] is a novel method of fabricating nanometer scale patterns. It is a simple process with low cost, high throughput and high resolution ($\approx$ 20 nm). It creates patterns by mechanical deformation of imprint resist and subsequent processes. The imprint resist is typically a monomer or polymer formulation that is cured by heat (thermoplastic nanoimprint) or UV light (photo nanoimprint) during the imprinting. Adhesion between the resist and the template is controlled to allow proper release. A key benefit of nanoimprint lithography is its simplicity. There is no need for complex optics, high-energy radiation sources or finely tailored photoresists designed for high resolution and sensitivity. Moreover, a broader range of materials with varying prop-

erties are available for use with nanoimprint lithography. The increased material variability gives the freedom to design new functional materials rather than sacrificial etch resistant polymers. A functional material may be imprinted directly to form a layer in a chip with no need for pattern transfer into underlying materials. Potential applications of nanoimprint lithography are in the fabrication of electronic devices (MOSFET, O-TFT, single electron memories), in optics (subwavelength resonant grating filter, polarizers, waveplate, anti-reflective structures), photonic and biological applications.

3.1.1 Laser-interference lithography

In this subsection we introduce the *Laser-Interference Lithograhpy* (LIL) in detail since this technique was used for the fabrication of photonic crystal (PhC) slabs that are investigated in chapter 6. The LIL is a technique based on the recording of a laser interference pattern on a material [Zhang 07]. This method, also called holographic lithography was first proposed and implemented for the fabrication of photonic crystals by Berger et al. [Berger 97]. They fabricated a 2D hexagonal pattern in a photosensitive polymer, which subsequently served as an etch mask for transfer to a high-index silicon substrate.

The laser interference pattern consists of a periodic series of fringes representing the high- and low-intensity regions (intensity minima and maxima) produced by the interference of two or more coherent beams. The configuration and the number of interfering beams determine the geometry of the pattern. The spatial period of the features to be recorded can be as small as half the wavelength of the interfering light. The interference lithography method, however, can create only defect-free photonic structures.

Figure 3.1 shows the four-beam interference lithography system. There is a laser beam that is divided into four beams by using three beam splitters. These four beams are afterwards guided towards the sample in which they interfere, using four mirrors. To describe the interference we introduce the

UNIVERSITAT ROVIRA I VIRGILI
DEVELOPMENT OF OPTICAL CHARACTERIZATION METHODS FOR MICRO- AND NANO-SCALE PLANAR PHOTONIC BAND GAP STRUCTURES
Zdenek Kral
DL: T-1537-2009/ISBN:978-84-692-4556-9

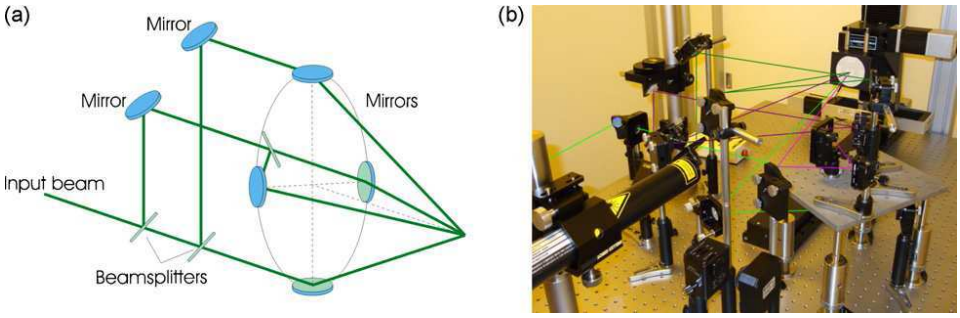

Figure 3.1: Four-beam laser interference lithography system (a) shematic illustration and (b) experimental setup [Ellman 08].

electric field of each laser beam as:

$$\begin{aligned}
\mathbf{E_1} &= A_1\mathbf{p_1}\, cos(k\mathbf{n_1}\cdot\mathbf{r} \pm 2\pi ft + \phi_1),\\
\mathbf{E_2} &= A_2\mathbf{p_2}\, cos(k\mathbf{n_2}\cdot\mathbf{r} \pm 2\pi ft + \phi_2),\\
\mathbf{E_3} &= A_3\mathbf{p_3}\, cos(k\mathbf{n_3}\cdot\mathbf{r} \pm 2\pi ft + \phi_3),\\
\mathbf{E_4} &= A_4\mathbf{p_4}\, cos(k\mathbf{n_4}\cdot\mathbf{r} \pm 2\pi ft + \phi_4),
\end{aligned} \tag{3.2}$$

were A_1, A_2, A_3 and A_4 are the amplitudes; $\mathbf{p_1}$, $\mathbf{p_2}$, $\mathbf{p_3}$ and $\mathbf{p_4}$ are the unit polarization vectors; $k = \frac{2\pi}{\lambda}$ is the wave number; $\mathbf{n_1}$, $\mathbf{n_2}$, $\mathbf{n_3}$ and $\mathbf{n_4}$ are the unit vectors in the direction of propagation; $\mathbf{r}$ is the position vector; f is the frequency and ϕ_1, ϕ_2, ϕ_3 and ϕ_4, are the phase constants of the beams. The superposition of these four beams can be expressed as:

$$\sum_{m=1}^{4} \mathbf{E_m} = \sum_{m=1}^{4} A_m\mathbf{p_m}\, cos(k\mathbf{n_m}\cdot\mathbf{r} \pm 2\pi ft + \phi_m). \tag{3.3}$$

The interference intensity distribution can be then determined by averaging the square of the resulting electric field (Equation 3.3) over time. It is important to notice that this intensity, which is implicit in the propagation and position vectors, depends on the angles of incidence θ between the beams and the sample. Other process parameters that have to be adjusted are the polarization of the beams and the energy.

Figure 3.2 shows an example of the PhC slab fabricated with the LIL technique. The sample is a silicon wafer with the native silicon oxide layer (SiO_2) over it and with an i-line positive low-viscosity photoresist (AZ1505)

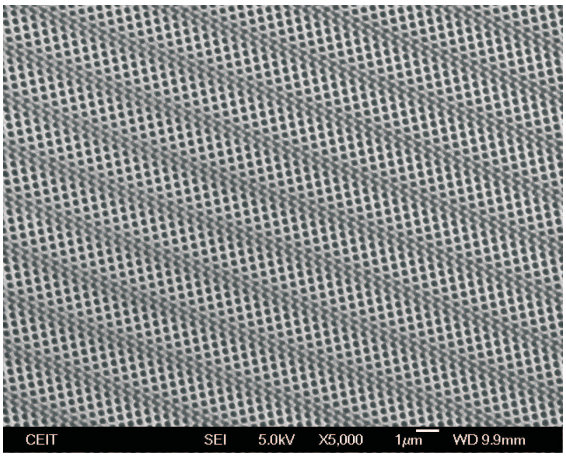

Figure 3.2: SEM image of the photoresist PhC slab produced by laser-interference lithography (LIL) [Ellman 08].

deposited by spin coating on the top. The thickness of the deposited photoresist film is 400 nm. An annealing process (pre-bake at 100 °C for 30 seconds) is applied just after the spinning of the photoresist. The photoresist is patterned by the four-beam laser interference with an 8 ns laser pulse of 18 mJ/cm^2 fluence. The angle of incidence θ between the beams and the sample is set to 20°. The main TM polarized laser beam comes from a frequency-tripled Quantel Nd:YAG laser (355 nm) with a coherent length of 3 m. After the patterning, the photoresist is subjected to a post-exposure bake (at 110 °C for 2 minutes), which reduces the standing waves effect on the photoresist. The development of the photoresist is carried out by soaking the wafers in a solution of (AZ-315B) developer and ultra pure water (1:5) at room temperature during 30 seconds. Finally, second post-bake process (at 115 °C for 30 seconds) is applied to improve the definition of the geometries in the photoresist [Ellman 08, Perez-Hernandez 08].

3.2 Electrochemical etching and oxidation

Etching is the most used subtractive technique in microfabrication. It can be described as pattern transfer by chemical/physical removal of a material from a substrate. Etching can be wet or dry depending on whether the etch reactants come from a liquid source or from a gas/vapor phase source. The parameters which determine the suitability of wet or dry etching technique

are the etch rate, selectivity, and anisotropy. The etch rate is usually specified in angstrom per minute (Å/min) units. In general, dry etching has lower etch rate than wet etching. Selectivity refers to the ability of the reactive species to etch away only the material intended for removal, while leaving all other materials intact (dry etching has less selectivity than wet etching). Anisotropy is a property which determine whether the etching proceeds in one or different directions at different rates (dry etching has higher degree of anisotropy than wet etching).

Dry etching is technique assumed from micro-semiconductor devices industry to fabricate 2D photonic structures. There are different types of dry-etching methods depending on which physical process is involved. Generally, dry etching is a process by which a solid surface is etched in the gas or vapor phase, physically by ion bombardment (highly anisotropic and low selective), chemically by a chemical reaction through a reactive species at the surface (isotropic and high selective), or by combined physical and chemical mechanisms (anisotropic with reasonably good selectivity). Most dry etching techniques are plasma-assisted. They are commonly divided into three groups: chemical plasma etching, synergetic reactive ion etching, and physical ion-beam etching. There exist combinations like a chemically assisted ion beam etching, which is probably the most used dry etching technique for 2D planar photonic crystals, photonic crystal waveguides and microcavities. In this technique, reactive species are introduced into the process independently of the etching ion beam, and in this way make it possible to control the physical and chemical parameters separately.

Wet etching is a method based on removing a material from a solid surface by immersing "a wafer" (e.g. silicon crystal) in a liquid bath of a chemical reactants. There are two kinds of wet etching reactants, isotropic and anisotropic. Isotropic reactants attack the material being etched at the same rate in all directions, whilst anisotropic reactants attack at different rates in different directions. Anisotropic etching does not cause undercutting, and is preferred in applications where straight side walls are essential. Anisotropic etching requires a substrate with a well defined crystalline structure such as silicon. The etching is directional and proceeds along the exposed plane in the crystal lattice. As atoms are removed from the crystal lattice, different planes are exposed to the reactant. Since the density of atoms on the planes varies, the etch rate varies significantly.

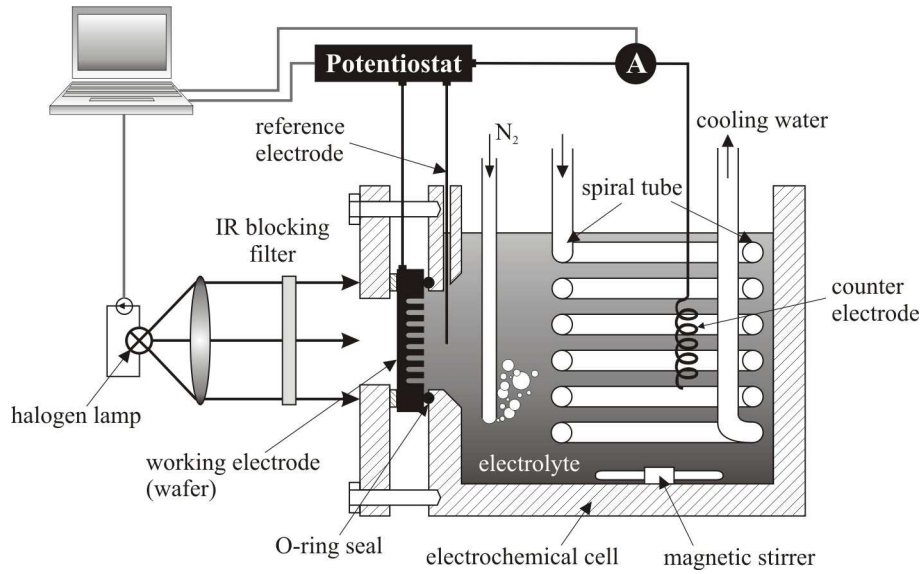

Figure 3.3: Schematic illustration of the electrochemical etching set-up. The wafer is mounted onto an electrochemical etching cell with the pre-structured front side in contact with the electrolyte [Trifonov 04].

3.2.1 Light-assisted electrochemical etching of silicon

In this subsection we focus on a wet etching technique that uses selective etching phenomena, the ability of the reactive species to etch away only the material in desired direction of the crystal. The technique is applied to crystalline silicon in order to fabricate the PhC slabs that will be the subject of the optical characterization in chapter 5.

The PhC slabs based on macroporous silicon[1] consist of ordered array of pores (holes) formed by electrochemical etching of n-type silicon ⟨100⟩ (Si) in acid solution (HF solution). The Si wafer is prestructured by oxidation, photolithography and subsequent tetramethyl ammonium hydroxide (TMAH) etching to form the initial pits, which serve as nucleation centers for the ordered pore growth. In the backside of the prestructured wafer, an indium tin oxide layer is sputtered to provide a low-resistance transparent ohmic contact. The wafer is then mounted together with a counter and reference electrodes in an electrochemical cell with the front side in contact with the electrolyte (see Figure 3.3). The silicon dissolution occurs only under anodic polarization. A positive voltage is applied to the n-type sili-

[1]Macroporous silicon is named because of the generally 'macroscopic' feature size of the etched pores (1-50 μm).

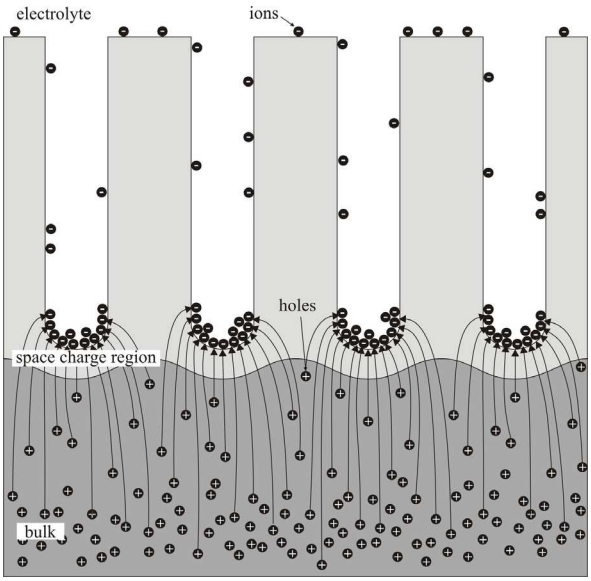

Figure 3.4: Schematic illustration of the macropore formation in low doped n-type Si. A [Trifonov 04].

con against the platinum counter electrode. The pore formation mechanism illustrated in figure 3.4 is ruled by the reverse-biased space-charge region (SCR) [Trifonov 04] at the silicon-electrolyte interface. The silicon wafer is backside illuminated in order to generate positive carriers (holes) in the bulk of the semiconductor, which are in n-type silicon a minority. The positive carriers (holes), required for anodic dissolution of silicon, diffuse through the silicon wafer and reach the silicon/electrolyte interface where they are consumed in the dissolution reaction [Trifonov 04]. The holes do not penetrate the area between the pores, they are focused by the space-charge region (SCR) mainly at the pore tips and promote dissolution there. Thus, the macropore walls become passivated against dissolution and pores grow in direction perpendicular to the wafer surface. Stable pore growth and well-ordered macropore arrays are only achievable if etching parameters, such as HF concentration, doping level, applied voltage and photogenerated current, are properly adjusted [Lehmann 90, Lehmann 93, Lehmann 99]. It must be noted that this can also be done in p-type silicon, where no illumination is necessary. The drawback is that the illumination provides a way of controlling the current (essential for stable macropore formation), which is not possible for p-type silicon. Figure 3.5 shows an example of a n-type macrporous silicon structure with the indicated dimensions of the

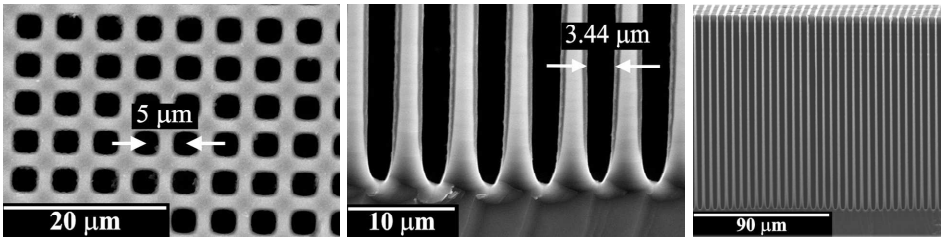

Figure 3.5: SEM images of the macroporous silicon PhC slab illustrating the main geometric features. A [Trifonov 04].

lattice constant and pore diameter in the depth. As it can be seen in the figure, the pores exhibit strong conical shape with decreasing of pore diameter in depth. The diameter (or size) of the pores is mainly dependent on the applied current. By adjusting the applied potential and the backside illumination intensity, uniform or even modulated pores in the depth can be obtained [Lehmann 93, Lehmann 99, Trifonov 04].

3.2.2 Anodization of aluminum

Another approach for producing planar photonic crystal structures (studied in chapter 6) is the anodic growth of porous alumina. The process consists of an anodic oxidation of aluminum foil in an acid solution (mostly sulphuric H_2SO_4, oxalic $(COOH)_2$ or phosphoric acid H_3PO_4), where a porous oxide film is formed on the surface. This covering film, the porous anodic alumina (PAA) is the result of the formation of a regular structure, in which the porous cells grow perpendicularly to the aluminum substrate with self-organized hexagonal ordering over the surface. The driving force for the self-assembly is attributed to mechanical stress caused by the repulsive forces between neighboring pores during anodization [Thompson 97, Sui 02, Foll 03, Choi 04].

The geometrical properties of PAA such as cell size, pore diameter, interpore distance or pore depth are dependent on the anodizing conditions. For example, the interpore distance is determined by the applied voltage during the anodization process. The pore diameter strongly depends on the electrolyte (the acid solution and its concentration), temperature, anodizing time and voltage. The ordering degree of the pores, which is essential for the derived applications is related with the fabrication technique used to produce PAA structure. In general, there are two widely used meth-

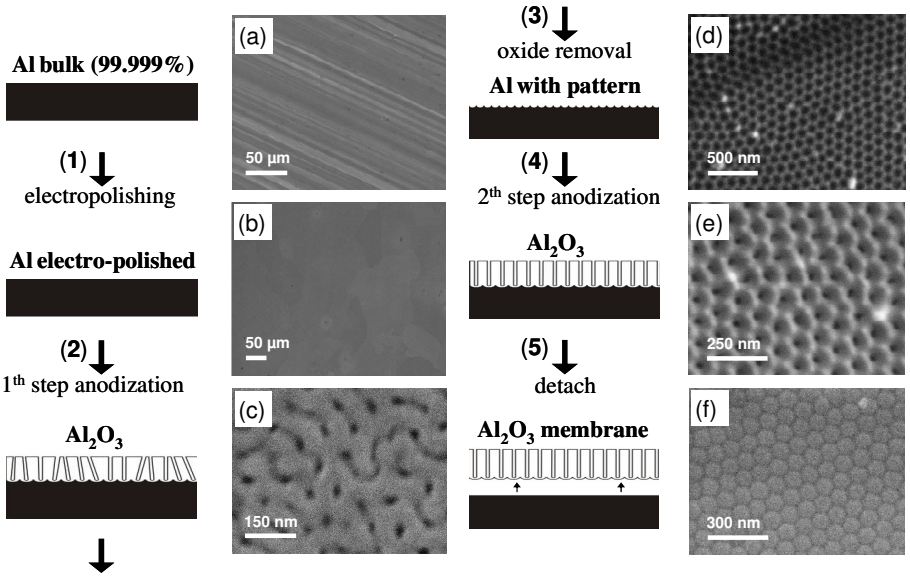

Figure 3.6: A scheme of step-by-step fabrication process of porous alumina based on two step anodization. Each step is represented by a drawing together with an SEM image of the surface corresponding to particular state. (a) Surface image of high purity (99.99 %) aluminum foil before the treatment (b) Surface image of the aluminum foil after electropolishing (c) Top view on the surface of the self-ordered alumina oxide layer after first anodization cycle (d) Top view on the surface of the patterned aluminum foil after alumina oxide removal (e) Top view on the surface of the ordered alumina oxide layer after second anodization cycle (f) Bottom surface image of the detached alumina oxide membrane. [Vojkůvka 07, Marsal 07, Marsal 08]

ods: (i) a self-organized two-step anodization leading to a 2D polydomain (quasi-monodomain) structure, and (ii) a pre-patterned guided anodization resulting in a 2D perfectly ordered pore lattice with a narrow size distribution and high aspect ratio [Masuda 05, Eftekhari 08].

The two-step anodization method was discovered in 1995 by Masuda and Fukuda [Masuda 95]. This fabrication approach relies on a natural pre-patterning of the aluminum substrate by the first anodization cycle and subsequent selective dissolution of the resulting anodic alumina film, leaving a pattern that is a replica of the hexagonal pore arrangement preserved on the aluminum surface. This pattern serves as nucleation centers for the formation of regular pores, which grow during the second anodization perpendicularly to the aluminum substrate and gives rise a 2D polydomain porous alumina structure. The two-step fabrication process represented by a schematic drawing step-by-step is shown in figure 3.6.

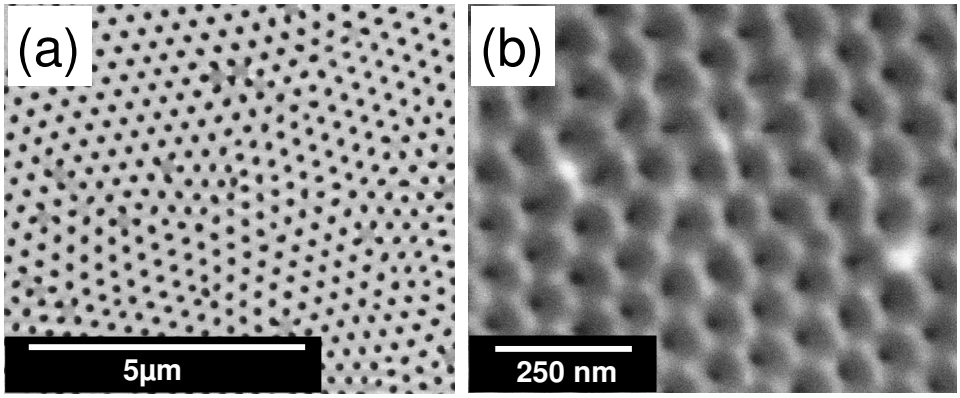

Figure 3.7: An example of 2D polydomain porous anodic alumina structure fabricated by two-step anodization. [Vojkůvka 07, Marsal 07, Marsal 08]

The procedure starts with a cleaning of high purity aluminum foil (99.99%) with acetone in an ultrasonic bath. Then, it is immersed in a mixture containing $HF/HNO_3/HCl/H_2O$ at a proper ratio in order to remove impurities from the surface. Subsequent annealing in N_2 atmosphere and electropolishing is applied to obtain large single cystalline grains and to reduce the surface roughness [Rauf 09] (1). In the next phase, the polished aluminum sample is mounted in the electrochemical cell that is filled with the electrolyte and the first anodization step (2) is performed under an appropriate voltage in the potenciostatic mode. The exact value of applied voltage is highly electrolyte-dependent [Li 98, Choi 04]. Since pores are randomly created on the surface, the initial pore arrangement is very irregular (Figure 3.6c). However, due to the repulsive forces between neighboring pores during the long-anodization, self-organization occurs. As a result, hexagonally close-packed arrays are obtained at the interface between the porous alumina layer and the aluminum substrate. After the first anodization step, the porous alumina oxide layer grown on the aluminum surface is removed by a selective wet chemical etching (3) in a solution containing of 0.4 M phosphoric acid and 0.2 M chromic acid (1:1 volume ratio) [Montero-Moreno 07, Schwartz 76]. The dissolution of the alumina oxide layer is carried out at the temperature between 60°and 80°C. The second anodization step (4) is repeated under the same experimental conditions as they were used in the first step. Finally, if it is necessary the PAA film can be detached (5) from the aluminum substrate. An example of resulting PAA structure is shown in figure 3.7. The structural characteristics such as the interpore distance can vary between 10 to

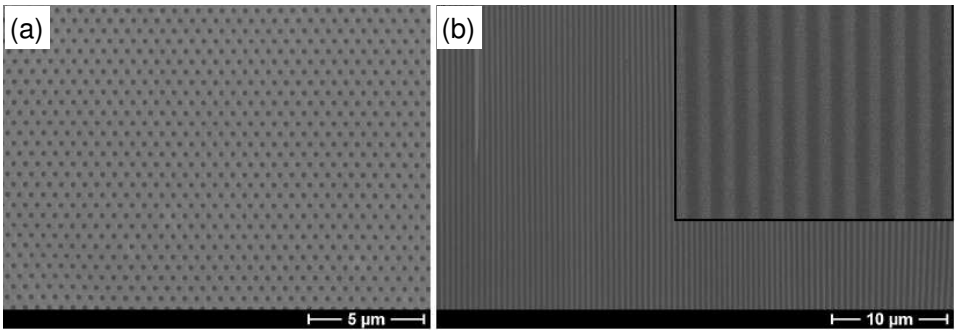

Figure 3.8: An example of 2D monodomain porous anodic alumina structure fabricated by anodization of pre-patterned aluminum. (a) Surface SEM image of perfectly ordered hexagonal structure; (b) Cross-section which demonstrates the high aspect ratio of the structure. [Choi 03, Choi 04]

500 nm with the pore diameter in the range of 5 to 400 nm depending on the anodizing parameters. The pore depth can reach several hundreds of microns after the second anodization period [Vojkůvka 07].

The pre-patterned guided anodization method is based on the texturing of electropolished aluminum foil before anodizing to obtain ideally ordered pores. Several techniques have been successfully used to form the pattern on the aluminum surface: focused ion beam lithography, holographic lithography, resist-assisted focus ion beam lithography or with a tip of the scanning probe microscope [Eftekhari 08]. However, the drawback of these techniques is the low throughput and the high cost, since each sample has to be treated individually. An alternative is the nanoimprint lithography suggested by Chou et al. [Chou 96]. The idea for the fabrication of a monodomain porous alumina structure with the nanoimprint lithography was proposed initially by Masuda et al. in 1997 [Masuda 97]. They prepared a master stamp consisting of hexagonal dot arrays with 150 nm lattice constant based on a SiC single-crystal wafer by e-beam lithography. The master stamp was placed on the aluminum and mechanically pressed using an oil press to form a regular arrangement of shallow concave depressions onto the aluminum surface. The predetermined pattern acts as initiation points and guide the growth of channels during the anodic oxidation. Later, Masuda et. al. [Masuda 01] showed that not only hexagonal but also square and honeycomb configurations can be fabricated by using a master stamp having appropriate configurations before anodization. Figure 3.8 shows an example of 2D monodomain PAA structure fabricated by anodization of pre-patterned aluminum. As can be

seen, the structure exhibits an ideally ordered hexagonal structure (a) with a very high aspect ratio (b).

An alternative technique that can be applied to the fabrication of ordered PAA structures is hard anodization (HA). The HA has been widely used in industry for high-speed fabrication of mechanically robust, very thick (>100 μm) and low-porosity alumina films since the 1960s. The typical HA process is characterized by the use of sulphuric acid at relatively low temperatures and high current densities. Lee at al. [Lee 06], in 2006, reported a new self-ordering regime of nano-PAA that is based on the HA of aluminium substrates using oxalic acid and applying potentials of 100-150 V, which are more than three times higher than the voltage (40 V) used in conventional oxalic acid anodization. On the basis of this newly found self-ordering regime, they fabricated novel PAA membranes with periodically modulated diameters of nanopores, with an interpore distance of 200-300 nm, and with extremely high aspect ratio (>1.000). They demonstrated that the HA process offers a big advantage over conventional anodization processes in terms of considerably shortened fabrication times due to the high-speed film growth rate. The growth rate of the porous oxide film is 25-35 times larger (>50 μmh^{-1}) than for conventional anodization processes. In academic research, however, the HA process is not favoured and has not been frequently applied to the development of nanostructured materials because of difficulties in controlling important structural parameters, such as pore size, interpore distance and the aspect ratio of the nanopores of the resulting alumina membranes.

UNIVERSITAT ROVIRA I VIRGILI
DEVELOPMENT OF OPTICAL CHARACTERIZATION METHODS FOR MICRO- AND NANO-SCALE PLANAR PHOTONIC BAND GAP STRUCTURES
Zdenek Kral
DL: T-1537-2009/ISBN:978-84-692-4556-9

UNIVERSITAT ROVIRA I VIRGILI
DEVELOPMENT OF OPTICAL CHARACTERIZATION METHODS FOR MICRO- AND NANO-SCALE PLANAR PHOTONIC BAND GAP STRUCTURES
Zdenek Kral
DL: T-1537-2009/ISBN:978-84-692-4556-9

Chapter 4

Characterization of photonic structures using Bragg diffraction

4.1 Introduction

In this chapter we develop an experimental technique based on the Bragg diffraction in the near and middle infra red (IR) spectral range to determine the lattice properties of photonic structures. Bragg diffraction is a particular type of X-ray diffraction [Warren 90, Guinier 94], which was first proposed by William Lawrence Bragg and William Henry Bragg in 1913 in response to their discovery that crystalline solids produce patterns of reflected X-rays. They found that for certain specific wavelengths and angles of incidence, intense peaks of reflected radiation (known as Bragg peaks) were produced. This occurs in crystalline solids when electromagnetic radiation or subatomic particle waves[1] with wavelength comparable to the atomic spacing are scattered from lattice planes periodically separated by the interplanar distance d. The scattered waves interfere constructively when the path length different between the waves is equal to an integer multiple of the wavelength (see Figure 4.1). The path difference between two waves undergoing constructive

[1] such as electrons or low-energy neutrons

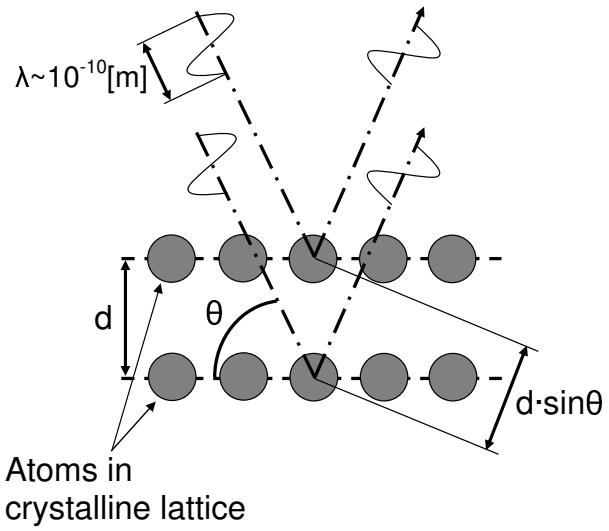

Figure 4.1: Schematic drawing of X-Ray Bragg diffraction from the lattice planes of a crystalline solid.

interference is given by Bragg law:

$$2d\cdot \sin\theta = n\cdot \lambda, \tag{4.1}$$

where λ is the wavelength, d is the spacing between the planes in the atomic lattice, θ is the angle between the incident ray and the scattering planes, and n is an integer known as the order of the diffracted beam. The diffraction pattern is obtained by measuring the intensity of the scattered waves as a function of the scattering angle. In practice, Bragg diffraction is mostly employed in X-ray crystallography [Sands 94] where the produced pattern gives information of the separations of crystallographic planes allowing one to deduce the crystal structure.

4.2 Bragg diffraction in near-and mid-IR

Analogous to crystalline solids, Bragg diffraction at optical wavelengths may be also used to characterize photonic crystal lattices [Sakoda 97, Sakoda 99]. Following the theory of diffraction [Saleh 91, Goodman 96, Born 80], in the far field the Fraunhofer approximation applies: the complex amplitude[2] of

[2]with the implicit assumption that the scalar approximation for the electromagnetic field can be applied at optical frequencies

UNIVERSITAT ROVIRA I VIRGILI
DEVELOPMENT OF OPTICAL CHARACTERIZATION METHODS FOR MICRO- AND NANO-SCALE PLANAR PHOTONIC BAND GAP STRUCTURES
Zdenek Kral
DL: T-1537-2009/ISBN:978-84-692-4556-9

the diffracted monochromatic wave $U(x,y)$ at a distance z of a diffracting element can be written as:

$$U(x,y) \propto \int\int_{-\infty}^{\infty} U(\xi,\eta) exp\left[-j\frac{2\pi}{\lambda z}(x\xi + y\eta)\right] d\xi d\eta, \tag{4.2}$$

where $U(\xi,\eta)$ is the complex amplitude of the wave at the plane of the diffacting element, with coordiantes ξ and η and λ is the wavelength of the incident wave. Following the scalar approximation the measured intensity at the (x,y) plane is proportional to the square modulus of the complex amplitude:

$$I(x,y) \propto \|U(x,y)\|^2. \tag{4.3}$$

Equation (4.2) states that: the complex amplitude of the diffracted wave at a distance z of the diffracting element (with z big enough to be considered in the far field) is proportional to the Fourier transform of the wave amplitude at the plane of the diffractive element with a scale factor. The scale factor is such that the spatial frequencies of the Fourier transform (ν_x and ν_y) are related to the coordinates at the observation plane (x,y) through the expression $\nu_x = x/(\lambda z)$ and $\nu_y = y/(\lambda z)$. Otherwise, the resulting wave amplitude in (4.2) can be expressed as a function of the viewing angle instead of the observation plane coordinates, taking into account that $x << z$ and $y << z$:

$$sin(\theta_x) = \frac{x}{z}\ , \text{and } sin(\theta_y) = \frac{y}{z}, \tag{4.4}$$

where θ_x and θ_y are the angles of the viewing direction with respect to the planes $y - z$ and $x - z$, respectively (see Figure 4.1-1 from reference [Saleh 91]).

The $U(\xi,\eta)$ in equation (4.2) is the complex amplitude of the wave after transmission or reflection on the diffracting element. In particular, we intend to study photonic lattices in reflection, and thus the wave reflects on the surface of a 2D photonic crystal slab (PhC slab) with scatterers distributed periodically in a dielectric matrix, and where the scatterers and the dielectric matrix have different reflectivities. This can be expressed as a reflectivity function such as the following:

$$r(\xi,\eta) = \left[r_{Unit\,Cell} * lattice_{\vec{a}_1,\vec{a}_2}\right](\xi,\eta), \tag{4.5}$$

where $r_{Unit\,Cell}$ is the reflectivity function of a unit cell containing one of the scatterers, $*$ is the convolution operation and $lattice_{\vec{a}_1,\vec{a}_2}$ is the Bravais lattice corresponding to the photonic crystal, with lattice vectors $\vec{a}_1$ and $\vec{a}_2$. In this expression, the convolution operation indicates that the unit cell is repeated indefinitely at all the lattice positions. If a monochromatic plane wave normally incident to the surface is assumed, with amplitude U_0, the reflected wave amplitude can be written as:

$$U(\xi,\eta) = U_0 r(\xi,\eta). \tag{4.6}$$

Following the interpretation of the diffraction formula in equation (4.2), the complex amplitude of the diffracted field at a distance z is proportional to the Fourier transform of the field amplitude at the plane of the diffraction element with a λz scale. Hence:

$$U(x,y) \propto \mathcal{F}(r_{Unit\,Cell})(\frac{x}{\lambda z},\frac{y}{\lambda z}) \cdot lattice_{\vec{b}_1,\vec{b}_2}(\frac{x}{\lambda z},\frac{y}{\lambda z}), \tag{4.7}$$

where $\mathcal{F}(r_{Unit\,Cell})$ is the Fourier transform of the function representing the unit cell reflectivity and $\vec{b}_1$ and $\vec{b}_2$ are primitive vectors of the reciprocal lattice, that meet the condition:

$$exp\left[j2\pi\,(\vec{a}_i \cdot \vec{b}_j)\right] = \delta_{ij}, \tag{4.8}$$

with δ_{ij} the Kronecker delta symbol.

The light intensity that results from the field amplitude in equation (4.7) corresponds to a group of diffraction maxima at positions (or viewing angles) defined by the reciprocal lattice with the scale factor λz. The factor corresponding to the Fourier transform of the unit cell modulates the relative intensity of these diffraction maxima.

In this work we are restricted to one-and two-dimensional photonic crystal structures with lattice sizes within a range of few microns. This permits us to measure the intensity of the diffracted light with a standard FTIR spectrometer. We use infra-red light from a halogen-tungsten lamp pointed perpendicular to the sample surface and we collect the diffraction spectra at a set of viewing angles along a given direction of the photonic crystal lattice. A maximum of the detected intensity for a given wavelength and at a given

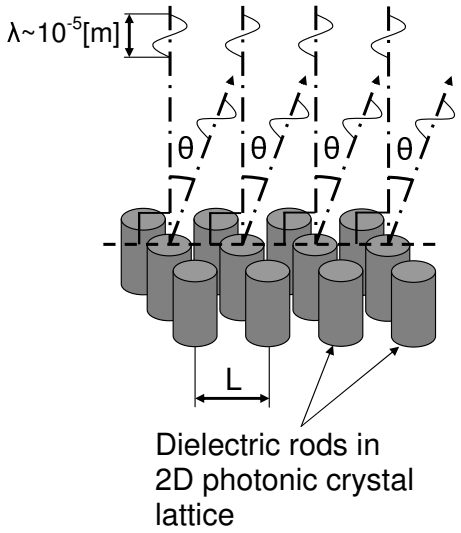

Figure 4.2: Schematic drawing of Bragg diffraction at optical wavelengths from a 2D photonic crystal lattice.

viewing angle will be obtained when the following condition is fulfilled:

$$(\frac{x}{\lambda z}, \frac{y}{\lambda z}) = (\frac{sin(\theta_x)}{\lambda}, \frac{sin(\theta_y)}{\lambda}) = K_1\vec{b}_1 + K_2\vec{b}_2, \tag{4.9}$$

with K_1 and K_2 integer numbers, which correspond to the diffraction orders. For a given measurement direction on the photonic lattice, the previous equation can be rewritten as a function of a single viewing angle and a single integer order K:

$$\frac{sin(\theta)}{\lambda} = K(\frac{1}{L}), \tag{4.10}$$

where L is the characteristic distance between the rows of scatterers at that particular measurement direction (see Figure 4.2). By measuring the intensity changes in a diffracted spectra as a function of the angle we are able with proper data post-processing to evaluate the lattice period of the photonic crystal structure.

4.3 Sample optical recognition

In this section we present the photonic structures which are subjects of the optical characterization by the previously proposed Bragg diffraction technique. The optical recognition of the samples is a step previous to the

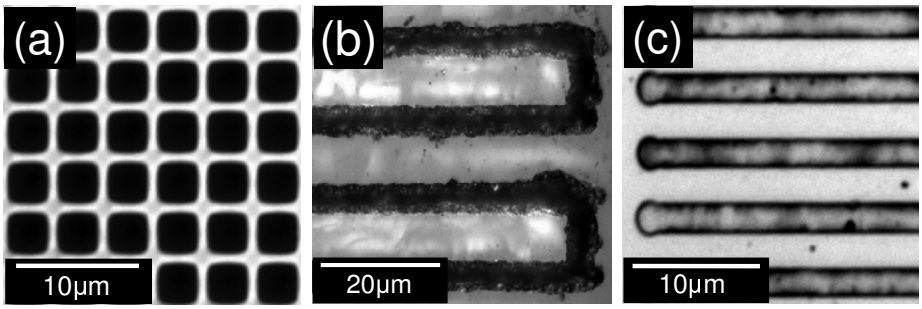

Figure 4.3: Optical microscope images of: (a) Two-dimensional photonic crystal structure (2D PhC slab) formed in a crystalline silicon background; (b) diffraction grating generated on the surface of a RTP crystal by ultrafast laser ablation; (c) diffraction grating generated on the surface of a periodically poled LN crystal by selective chemical etching of one of the ferroelectric domains.

measurement of the Bragg diffraction, since it is necessary to identify the lattice directions on the sample in order to place the sample correctly in the measurement setup. We study three different lattice structures shown in figure 4.3(a-c). Images of these samples are taken with an optical microscope Carl Zeiss Axio Imager A1 with a 50× objective connected to a CCD camera ProgRes C10 from JenOptic (Figure 4.4). The image processing is done using i-Solution (iMTechnology) software. Figure 4.3a shows an example of a 2D PhC slab consisting of a periodic array of square air holes formed in a crystalline silicon background. The sample is fabricated by electrochemical etching of a pre-structured N-type silicon wafer at room temperature in aqueous HF electrolyte [Trifonov 05, Trifonov 04]. The lattice constant

Figure 4.4: Optical microscope Carl Zeiss Axio Imager A1 with CCD camera ProgRes C10 from JenOptik.

UNIVERSITAT ROVIRA I VIRGILI
DEVELOPMENT OF OPTICAL CHARACTERIZATION METHODS FOR MICRO- AND NANO-SCALE PLANAR PHOTONIC BAND GAP STRUCTURES
Zdenek Kral
DL: T-1537-2009/ISBN:978-84-692-4556-9

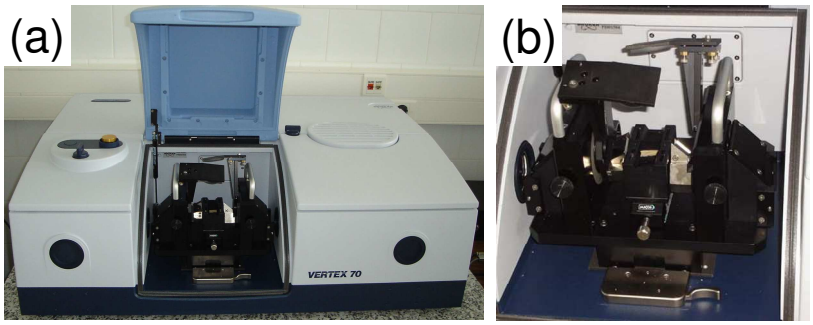

Figure 4.5: (a) FTIR spectrometer Bruker-Vertex 70; (b) Detail of the reflectivity attachment consisting of a removable sample holder and two movable arms with the reflective mirrors. Each arm can be moved independently in a range of angles between 12°and 90°.

estimated from the microscope image is approximately 4 μm. Figure 4.3b shows an example of a one-dimensional photonic crystal (diffraction grating) based on the non-linear optical material $RbTiOPO_4$ (RTP), fabricated by a microstructuration of the sample surface using ultrafast laser ablation. The distance between the grooves estimated by the optical microscope is approximately 15 μm. The third sample is also a diffraction grating, but made of a different non-linear optical material $LiNbO_3$ (LN), and fabricated by selective etching of ferroelectric domains. Figure 4.3c shows the sample topology with the indicated scale. The distance between the grooves estimated by the optical microscope is approximately 5.1 μm. Details about the fabrication process of both non-linear one-dimensional photonic crystals can be found elsewhere [Carvajal 08].

4.4 Experimental measurement of Bragg diffraction

The Bragg diffraction spectra of the photonic structures presented in figure 4.3(a-c) were measured using a FTIR spectrometer Bruker-Vertex 70 equipped with a special reflectivity attachment (see Figure 4.5). As a light source, the infra-red light from an halogen-tungsten lamp incorporated in the FTIR spectrometer was used. The incident light was pointed perpendicular to the sample surface and the diffraction spectra were measured at a set of angles. The diffracted light was collected by the reflective mirror fixed on

K	Wavenumber (cm^{-1})						
	sin(20°)	sin(30°)	sin(40°)	sin(50°)	sin(60°)	sin(70°)	sin(80°)
2D PhC							
1	7310	5000	3889	3264	2887	2660	2539
2	14619	10000	7779	6527	5774	5321	5077
3	21929	15000	11668	9791	8660	7981	7616
1D RTP							
1	1949	1333	1037	870	770	709	677
2	3898	2667	2074	1741	1540	1419	1354
3	5848	4000	3111	2611	2309	2128	2031
1D LN							
1	5733	3922	3050	2560	2264	2087	1991
2	11466	7843	6101	5119	4528	4173	3982
3	17199	11765	9151	7679	6792	6260	5973

Table 4.1: Rough estimation of the wavenumbers at which the Bragg peaks appear for some selected angles and three diffraction orders. The frequencies are represented in wavenumber units according to the FTIR spectrometer set-up. The lattice constant values obtained from the optical microscope have been used for this estimation.

the movable arm and detected with a liquid nitrogen-cooled detector. The measurements were performed along the principal lattice directions defined by the structure (see Appendix A). The specular reflection spectrum at an incidence angle of 12°was taken as a reference.

The lattice sizes of the photonic crystals indicate that the frequencies at which the Bragg diffraction peaks may appear lie in the mid-and near-IR. Using the equation 4.10, and the lattice constants obtained from the optical recognition, we made a previous rough estimation. Table 4.1 shows the calculated frequencies at which the Bragg peaks appear for the given diffraction order K and the sinus of the angle of incidence θ. This estimation helps us to correctly choose the spectral range of the measurements.

An example of measured Bragg diffraction spectra for the 2D silicon-based PhC slab (Figure 4.3a) is given in figure 4.6. The graph presents the intensity of Bragg-diffracted IR light as a function of the frequency for some selected angles (30°, 40°, 50°, 60°, 70°and 80°) measured for light incident in the ΓX direction. Based on the previous estimation shown in table 4.1, the spectral range was set from 10000 $cm^{-1}$to 3000 cm^{-1}. As it can be observed, there are several diffraction peaks (the intensity maxima) at frequencies that increase with increasing angle of incidence. One of the peaks is labeled with

UNIVERSITAT ROVIRA I VIRGILI
DEVELOPMENT OF OPTICAL CHARACTERIZATION METHODS FOR MICRO- AND NANO-SCALE PLANAR PHOTONIC BAND GAP STRUCTURES
Zdenek Kral
DL: T-1537-2009/ISBN:978-84-692-4556-9

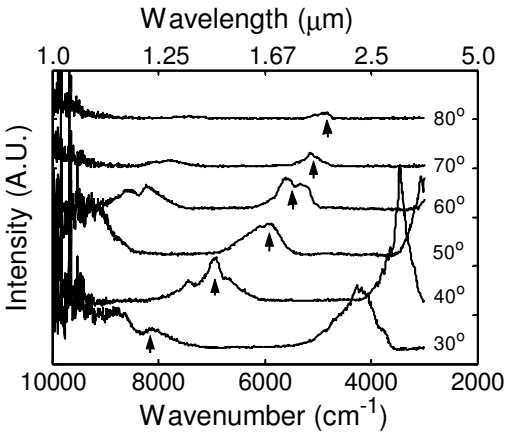

Figure 4.6: Experimental Bragg diffraction spectra of a 2D silicon-based PhC slab (see Figure 4.3a) measured with the FTIR spectrometer. The measurement was performed for light incident in the ΓX direction at a set of angles. The intensity curves for the selected angles shown in the graph are slightly offset for clarity. One of the Bragg diffraction peaks is indicated by arrows.

arrows. A better visualization of the Bragg peaks is achieved with a 3D plot, shown in figure 4.7. The intensity spectra is plotted versus the sinus of the Bragg diffraction angle θ and the wavelength λ. The intensity maxima in the 3D plot correspond to the peaks of different diffraction orders. With this representation, it is easy to identify the diffraction peaks and their order.

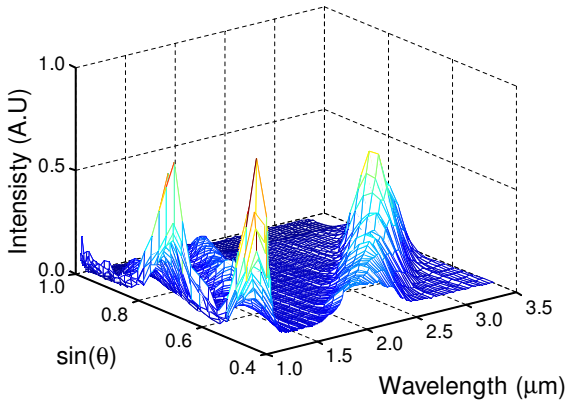

Figure 4.7: 3D plot of the Bragg diffraction spectra of a 2D silicon-based PhC slab. The intensity maxima correspond to the Bragg peaks of three diffraction orders.

4.5 Data analysis

To evaluate the lattice constant from the Bragg diffraction spectra, the collected data need to be post-processed. To this end, a method including several steps was developed. As can be seen in the example of the Bragg diffraction spectra shown in figure 4.6, there are some resonances particularly in the range between 10000 $cm^{-1}$and 8500 cm^{-1}. These unwanted intensity maxima correspond to saturation of the DLaTGs detector used in the experiment. To reduce this noise, the first step of the post-processing procedure consists of performing a windowed average of the spectrum: the reflectivity value at a given wavenumber f is replaced by the average reflectivities for an interval of wavenumbers around f.

It is also important to consider the dependence of the diffracted intensity on the Bragg diffraction angle. It can be seen in figure 4.6 that the magnitude of the intensity (the intensity maxima labeled by arrows) decreases as the collection angle of the Bragg-diffracted light increases. For all the wavelengths, this dependence of the intensity with the angle θ shows the same tendency. The following step is to remove this general tendency by a flattening procedure, demonstrated in figure 4.8. The flattening procedure consists of fitting the intensity for a given wavelength as a function of the θ angle to a straight line and subtracting the resulting straight line from the data. Figure 4.8a depicts the intensity versus the diffraction angle for a given wavelength, indicated on the graph. The dashed line represents the linear fitting of the tendency. Figure 4.8b shows the flattened intensity in a normalized scale. The intensity maxima (diffraction peaks) are indicated by arrows. To show how the flattening procedure improves the recognition of the Bragg peaks, the flattened spectra are represented in a 3D plot as a function the sinus of the Bragg diffraction angle θ and the wavelength (Figure 4.9). The three diffraction orders can be now clearly recognized.

The final step to evaluate the lattice constant is to fit the flattened data with a function where at least one adjustable parameter is related to the lattice constant. Concerning the shape of the diffraction maxima (see Figure 4.9), the function that can represent better their behavior is a Gaussian with two variables, the wavelength λ and the sinus of the diffraction angle θ.

UNIVERSITAT ROVIRA I VIRGILI
DEVELOPMENT OF OPTICAL CHARACTERIZATION METHODS FOR MICRO- AND NANO-SCALE PLANAR PHOTONIC BAND GAP STRUCTURES
Zdenek Kral
DL: T-1537-2009/ISBN:978-84-692-4556-9

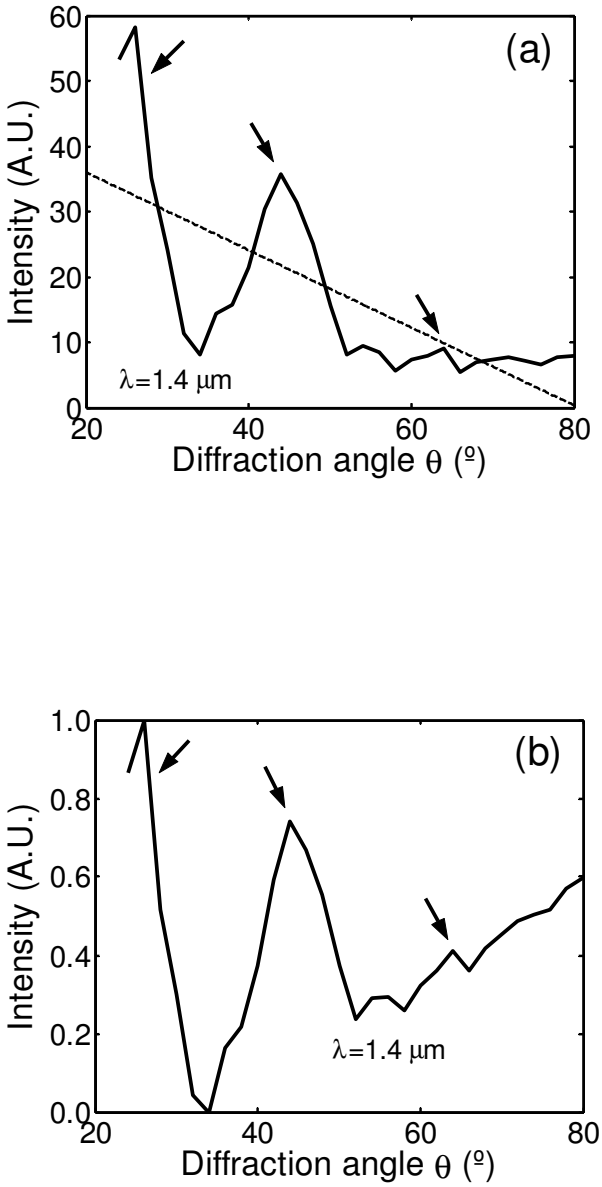

Figure 4.8: Example of the flattening procedure on the spectra shown in figure 4.6 for one selected wavelength: (a) Fitting the intensity trend with increasing angle of incidence to a straight line (dashed line) and subtracting the resulting straight line from the data; (b) Flattened intensity at a normalized scale. The arrows point to the maxima corresponding to the three diffraction orders observed in this measurement.

UNIVERSITAT ROVIRA I VIRGILI
DEVELOPMENT OF OPTICAL CHARACTERIZATION METHODS FOR MICRO- AND NANO-SCALE PLANAR PHOTONIC BAND GAP STRUCTURES
Zdenek Kral
DL: T-1537-2009/ISBN:978-84-692-4556-9

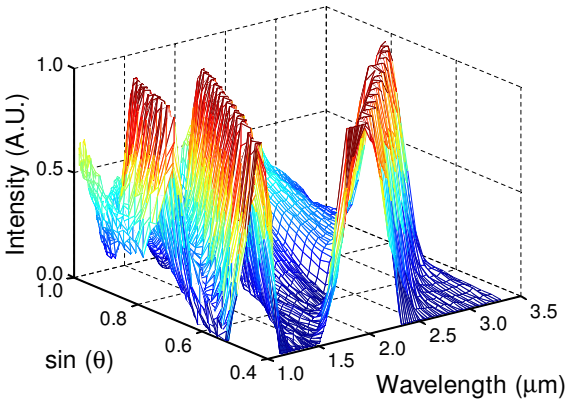

Figure 4.9: 3D plot of the flattened Bragg diffraction spectra from figure 4.6. The intensity maxima correspond to the three diffraction orders.

The proposed function is:

$$I(\lambda, sin\theta; a, w_n) = \sum_{n=1}^{3} exp[(\frac{sin\theta - \frac{n\lambda}{a}}{w_n})^2], \tag{4.11}$$

where the w_n takes into account the width of the diffraction maxima, a is the lattice constant and n is an integer (the number of the diffraction order). Each of the terms with index n in equation 4.11 corresponds to one of the diffraction orders. It must be noted that the lattice constant a is the same for all the diffraction orders. The parameters to be determined are the lattice constant a and the widths of the diffraction peaks $\{w_n\}$. By fitting this function to the experimental data (minimizing the difference between the function 4.11 and the flattened data), the lattice constant can be extracted.

The procedure for the fitting consists of defining a function of merit that evaluates the difference between the fitting function 4.11 and the flattened data. This is a function of the fitting parameters a and the $\{w_n\}$. If the flattened data I_i are measured at a set of pairs wavelength-diffraction angle $\{(\lambda_i, sin(\theta_i))\}$, with $i = 1...N$, then this function of merit is defined as:

$$\chi^2(a, w_1, w_2, ...) = \frac{1}{N} \sum_{i=1}^{N} (I_i - I(\lambda, sin(\theta_i); a, w_1, w_2, ...))^2 \tag{4.12}$$

By finding the minimum of this function using standard numerical algorithms it is possible to estimate the fitting parameters. This technique

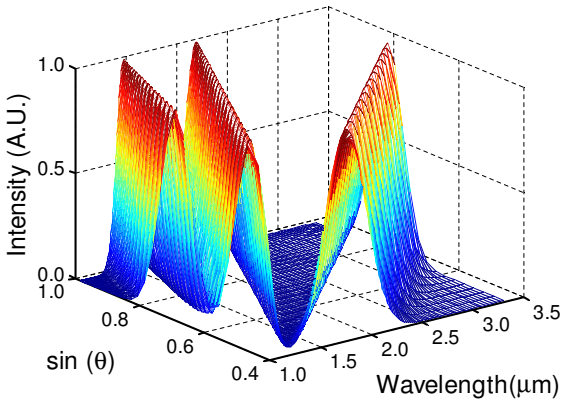

Figure 4.10: 3D plot of the function 4.11 fitted to the experimental data (Figure 4.9) of the 2D silicon-based PhC slab (Figure 4.3a). The initial fitting parameters of the function 4.11 are a=4 μm and w_n=0.01, n=1,2,3.

gives a robust estimation of the lattice constant from the data, since all the measured spectra for a given sample are taken into account simultaneously. Figure 4.10 shows a 3D plot of the function 4.11 fitted to the flattened experimental data of the 2D silicon-based PhC slab (Figure 4.3a). The lattice parameters of the diffraction gratings from figure 4.3b and figure 4.3c were characterized by following the same approach. An extensive summary of all measurements is given in the next section.

4.6 Results and conclusions

In this chapter we have developed a technique based on the Bragg diffraction at optical wavelengths to characterize photonic crystal structures. We have demonstrated the feasibility of the technique and we have analyzed the lattice properties of different photonic crystals. The Bragg diffraction spectra were measured using a commercial FTIR spectrometer with a special reflectivity attachment. The measured data were fitted to the theoretical model to determine the lattice constants.

The analysis of the experimental data consisted of several steps illustrated with an example in section 4.5. The results are graphically interpreted in figure 4.11 for the 2D silicon-based PhC slab, in figure 4.12 for the diffraction grating generated on the surface of a RTP crystal, and in figure 4.13 for the diffraction grating generated on the surface of a periodically poled LN crystal. For example, figure 4.11a shows a 2D gray map of the

Sample	Opt. microscope	Measured by Bragg diffraction	
	$\frac{1}{n}\sum_{i=1}^{n} a_i, n = 10$	$\Gamma - X$	$\Gamma - M$
2D PhCs	4 μm	4.3 μm	4.1 μm
		1^{st} meas.	2^{nd} meas.
RTP-crystal	15 μm	14.9 μm	15.1 μm
LN-crystal	5.1 μm	5.2 μm	5.3 μm

Table 4.2: Lattice constant evaluation.

measured Bragg diffraction spectra of the 2D silicon-based PhC slab after the flattening procedure represented as a function of the wavelength and the sinus of the diffraction angle. The white zones in the graph are the diffraction peaks. Figure 4.11b is a 2D plot of the fitting function generated by equation 4.11 and fitted to the flattened Bragg diffraction spectra. In this case, three diffraction orders could be observed in the measurements and were considered for the fitting function.

The overall summary of the obtained results is given in table 4.2, where the second column shows the average value of the lattice constants estimated from the optical microscope images (Figure 4.3) and the third and fourth columns present the values obtained by the analysis of the Bragg diffraction spectra. Two measurements on each sample were performed. The Bragg diffraction spectra of the 2D silicon-based PhC slab were measured for the light incident along the main lattice directions ΓX and ΓM. For the diffraction gratings, the spectra were collected for light incident perpendicular to the grooves in two different measurements (1^{st} and 2^{nd}). A good agreement between the optical microscope estimation and the measured diffraction spectra has been obtained.

UNIVERSITAT ROVIRA I VIRGILI
DEVELOPMENT OF OPTICAL CHARACTERIZATION METHODS FOR MICRO- AND NANO-SCALE PLANAR PHOTONIC BAND GAP STRUCTURES
Zdenek Kral
DL: T-1537-2009/ISBN:978-84-692-4556-9

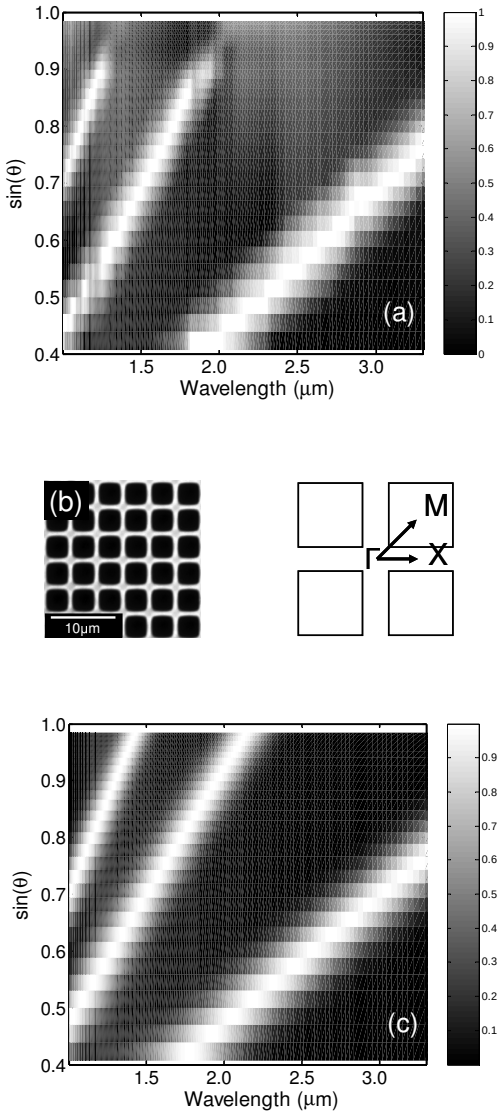

Figure 4.11: 2D silicon-based PhC slab: (a) 2D gray map of the flattened Bragg diffraction spectra, (b) Detail image of the lattice structure with indicated main lattice directions (sketch on the right), (c) 2D plot of the fitting function generated by equation 4.11 and fitted to the flattened Bragg diffraction spectra. Three diffraction orders were considered for fitting the experimental data by the fitting function.

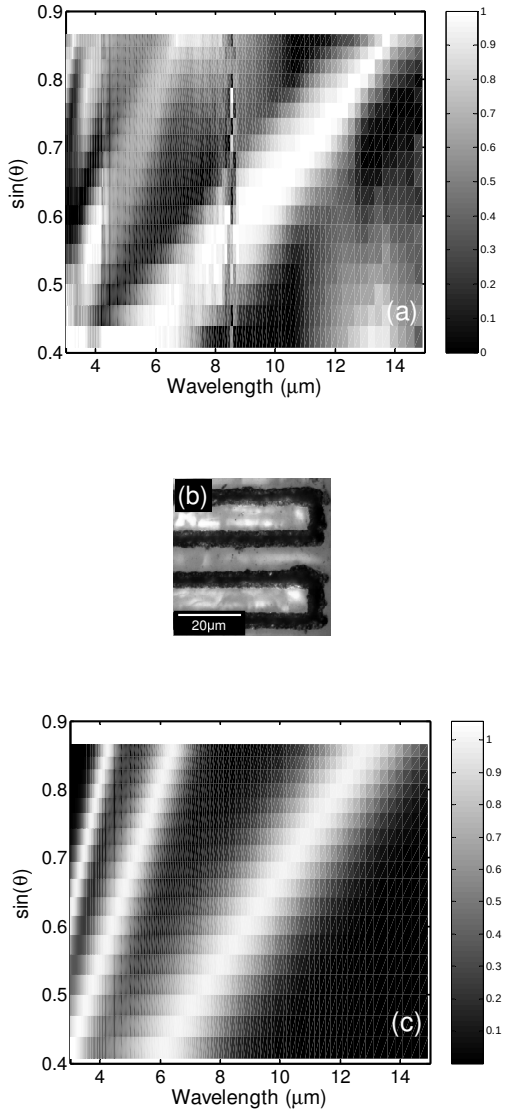

Figure 4.12: Diffraction grating generated on the surface of a RTP crystal: (a) 2D gray map of the flattened Bragg diffraction spectra, (b) Detail image of the lattice structure, (c) 2D plot of the fitting function generated by equation 4.11 and fitted to the flattened Bragg diffraction spectra. Three diffraction orders were considered for fitting the experimental data by the fitting function.

UNIVERSITAT ROVIRA I VIRGILI
DEVELOPMENT OF OPTICAL CHARACTERIZATION METHODS FOR MICRO- AND NANO-SCALE PLANAR PHOTONIC BAND GAP STRUCTURES
Zdenek Kral
DL: T-1537-2009/ISBN:978-84-692-4556-9

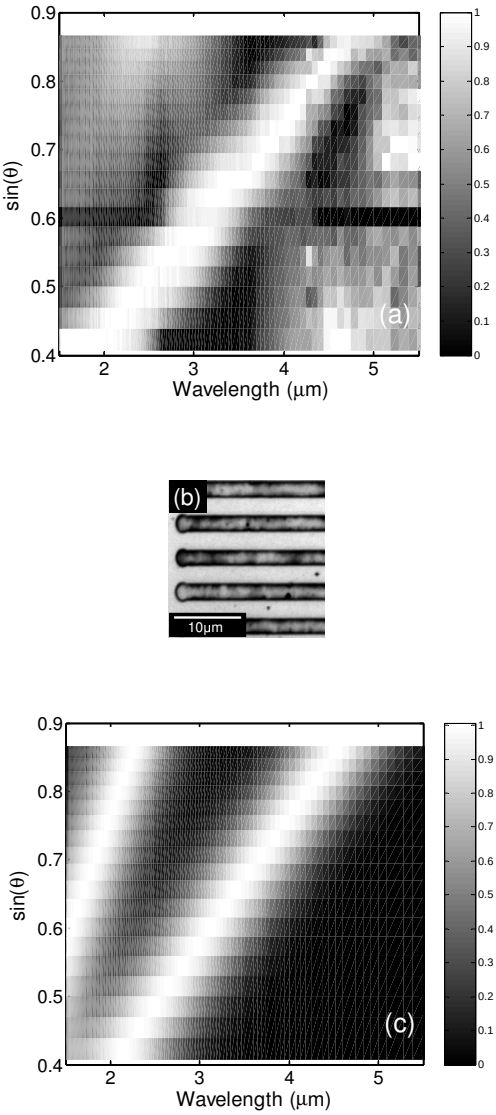

Figure 4.13: Diffraction grating generated on the surface of a periodically pooled LN crystal: (a) 2D gray map of the flattened Bragg diffraction spectra, (b) Detail image of the lattice structure, (c) 2D plot of the fitting function generated by equation 4.11 and fitted to the flattened Bragg diffraction spectra. Two diffraction orders were considered for fitting the experimental data by the fitting function.

UNIVERSITAT ROVIRA I VIRGILI
DEVELOPMENT OF OPTICAL CHARACTERIZATION METHODS FOR MICRO- AND NANO-SCALE PLANAR PHOTONIC BAND GAP STRUCTURES
Zdenek Kral
DL: T-1537-2009/ISBN:978-84-692-4556-9

UNIVERSITAT ROVIRA I VIRGILI
DEVELOPMENT OF OPTICAL CHARACTERIZATION METHODS FOR MICRO- AND NANO-SCALE PLANAR PHOTONIC BAND GAP STRUCTURES
Zdenek Kral
DL: T-1537-2009/ISBN:978-84-692-4556-9

Chapter 5

Angular-Dependent Reflectance Spectroscopy (ADRS)

5.1 Introduction

This chapter deals with an optical technique developed in this work to characterize the band structure of photonic crystal (PhC) slabs[1]. PhC slabs of different configurations (lattice types, scatterer shapes, sizes, and materials) are experimentally studied by means of Angular-Dependent Reflectance Spectroscopy (ADRS). This technique, first proposed by Astratov at al. [Astratov 98] is based on the observation of the resonant coupling of external radiation incident at oblique angles to the photonic modes that propagate inside the slab structure. An overview of this and other related techniques, together with the State-of-the-art is presented in section 5.2. In section 5.3 we perform numerical simulations of the interaction of the incident beam with the samples, using the S-matrix formalism introduced in chapter 2. Such calculations help us to predict and correctly interpret the experimental

[1]Photonic crystal slab is a 2D structure with periodicity along two of its axes, but of a finite thickness. On the contrary, 2D photonic crystal means a structure indefinite in the third dimension, and thus of infinite thickness. Such a definition is used throughout all this work.

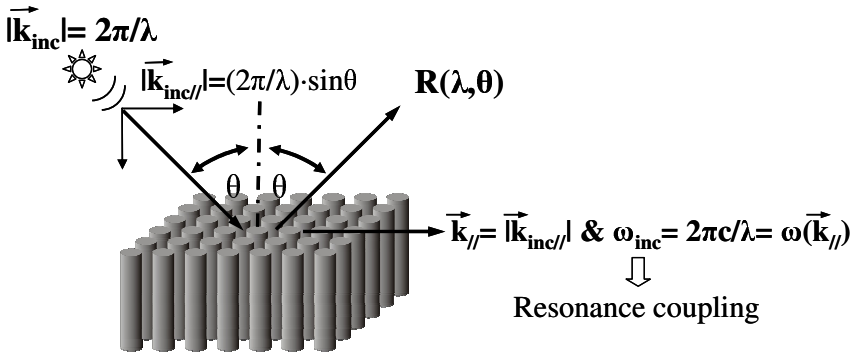

Figure 5.1: Schematic drawing of the ADRS experimental geometry, where $|\mathbf{k}_{inc_{//}}|$ is the modulus of the incident light wavevector component parallel to the sample surface, and $|\mathbf{k}_{//}|$ is the modulus of the parallel wavevector of a propagating mode inside the PhC slab.

measurements of the ADR spectra, given in section 5.4. In the last section, we compare results of the simulations with the experimental measurements of ADRS and we state the conclusions.

5.2 State-of-the-art of ADRS technique

The ADRS is a technique based on the identification of resonant features in the reflectivity spectra at different angles of incidence. Such resonant features are related to the coupling of the external radiation to the modes of the PhC slab. They appear when the incident light wavevector component parallel to the sample surface ($\mathbf{k}_{inc_{//}}$) matches the parallel wavevector of a propagating mode inside the PhC slab (Figure 5.1). The $\mathbf{k}_{//}$ is related to the angle of incidence θ of the light onto the photonic crystal surface and to the incident light wavelength as $\mathbf{k}_{//} = (2\pi/\lambda)\,\sin\theta$. When the angle of incidence is varied, the parallel wavevector changes and the matching condition occurs at different energies. Therefore, the dispersion of the photonic modes in a given direction can be extracted from the energy position of the resonant features in the reflectivity spectra, and then plotted versus the wavevector.

In the last two decades, there have been several scientific groups using the ADRS for identification of the photonic bands. V. N. Astratov at al. first demonstrated this technique on a 2D photonic crystal waveguide consisting of a honeycomb lattice of air holes in an AlGaAs/GaAs

dielectric medium [Astratov 98, Astratov 99a, Astratov 99b, Astratov 00a, Culshaw 00]. The same approach was also used to study heavy photon dispersion in 1D patterned AlGaAs waveguides [Astratov 00b, Bristow 02]. A few years later, the group led by M. Galli used the same technique, although they called it Variable-Angle Reflectance (VAR)[2] to investigate the photonic band structure of GaAs/AlGaAs-based 2D PhC slabs [Galli 02a, Andreani 03, Patrini 03]. Several other authors demonstrated the capability of this technique to study photonic structures of different characteristics e.g.: 1D photonic crystals made of (Si/SiO_2) multilayers [Patrini 02a]; 2D photonic crystals based on macroporous silicon [Galli 02b, Bettotti 02] or GaAs/AlGaAs [Pacradouni 00, Businaro 03]; silicon-on-insulator waveguides [Patrini 02b, Peyrade 02, Belotti 06a, Belotti 06b]; and 3D structures based on synthetic opals [Pavarini 05, Pallavidino 06] or noble metals [Romanato 03].

One drawback of the ADRS (VAR) technique is the so-called light-line problem in PhC slabs. This problem is based on the fact that the dispersion of light in the cladding material[3] is separated into two regions of: truly guided (evanescent) modes which lie below the light line in the first Brillouin zone (see Appendix A) and have zero radiation losses, and quasi-guided (radiative) modes which lie above the light line and have a finite radiative width due to out-of-plane diffraction. The ADRS (VAR) technique is capable to probe only quasi-guided modes, since these are the modes that can be excited by the radiation incident from the medium. However, this limitation can be overcome by a complementary technique called Attenuated-Total Reflectance (ATR), which allows to expand the frequency-wave vector range, thereby allowing one to study also the truly guided photonic modes [Galli 04, Galli 05b, Galli 05a, Galli 06a]. This is done by placing a high refractive index prism at a small distance from the sample surface, hence an efficient coupling between the evanescent fields at the air-prism-sample interfaces is achieved, thereby excitation of truly guided modes that lie below the light line is possible. The thickness of the air layer between the prism and the sample surface is a crucial parameter, because it determines the coupling strength of the incident light to the guided modes of the photonic crystal.

[2] In some articles it can also be find as Angle-Resolved Reflectance.
[3] A material with different refractive index surrounding the slab, but it can be also air.

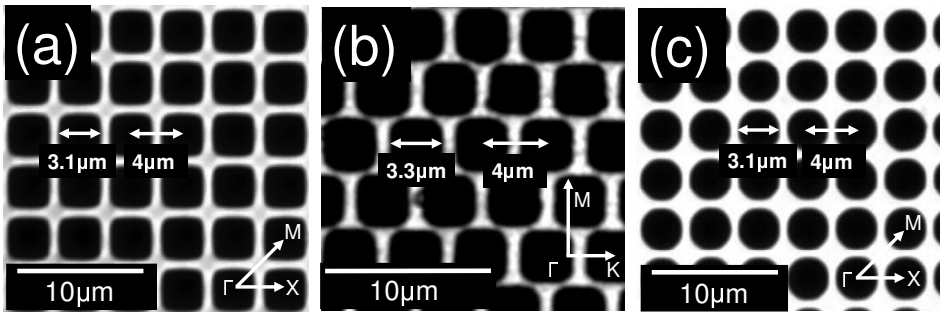

Figure 5.2: Optical microscope images of two-dimensional photonic crystal structures (2D PhC slab) with (a) square air holes in square lattice arrangement, (b) square air holes in triangular lattice arrangement, and (c) circular air holes in square lattice arrangement etched into crystalline silicon. The lattice parameters are included in the images.

Another technique which can be related with ADRS (VAR) is the Angle-Resolved Photoluminescence (ARP). This technique uses the photoluminescence emission excited from an active medium (e.g. InAsP/InP quantum wells) inside the photonic structure by a laser beam. The emission is then collected outside of the structure at different angles by an optical fiber coupled to a Fourier-transform spectrometer. The collected spectra are used to determine the photonic band dispersion through conservation of the wavevector parallel to the sample surface [Butte 02, David 05, Galli 06b, Alija 07, Postigo 07, Martinez 08].

5.3 Sample characteristics

This section is devoted to the introduction of the PhC slab samples that are subjects of the optical characterization by ADRS technique. Figure 5.2 presents optical microscope images of PhC slabs based on macroporous silicon with different lattice configurations, fabricated by light-assisted electrochemical etching (introduced in chapter 3). The lattice parameters as lattice constant, hole diameter (width for square hole), and the main lattice orientations are included in the images. Figure 5.3 shows a scanning electron microscope (SEM) image of PhC slab that consists of a crystalline silicon wafer covered with an PMMA fotoresist layer. The resist layer has thickness of 400 nm and the refractive index of the PMMA material is n=1.55 [Kaplan 04]. The 2D structure, created in the electron resist layer by

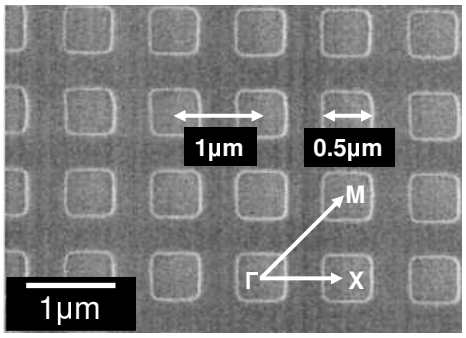

Figure 5.3: SEM surface-image of PhC slab fabricated on PMMA fotoresist layer by combination of electron beam lithography and wet etching. The slab consists of square air holes arranged in a square lattice, etched in PMMA, with thickness (or holes depth) of 400 nm. The characteristic parameters of the lattice are indicated.

electron-beam lithography combined with wet etching, consists of an ordered array of square air holes arranged in a square lattice. The characteristic dimensions of the photonic structure (estimated by SEM) are indicated in the figure.

5.4 Numerical simulation of ADRS using the Scattering matrix method

The objective of this section is the simulation of the ADRS technique by a numerical method based on the S-matrix treatment[4] proposed by Whittaker et al. [Whittaker 99]. This method follows the same approach as the plane-wave expansion (PWE) computational technique but including additional features to calculate the photonic modes propagating inside the sample and the coupling efficiency of the incident wave to these modes. The PWE method introduced in chapter 2 considers a 2D photonic crystal as indefinite in the third dimension, however this is not the case of the samples that are actually studied in this work, where the photonic structure is delimited by the sample surface and by the substrate. Thus, in order to simulate the interaction of the incident light with the samples, it is necessary to find an expression for the photonic modes inside the PhC slab. Such expression must be able to represent modes with oblique propagation directions. This is accomplished by a modification of the standard PWE method to allow

[4] A general theory of the S-matrix is discussed in chapter 2.

propagation in directions with a component in the third dimension. Then, in combination with the S-matrix treatment, the coupling of the incident light to these modes can be computed and translated to the reflectance spectra.

To explain the numerical method for simulation of ADRS, we should start with a classical model of calculating the photonic bands of an ideal 2D photonic crystal (indefinite in the third dimension) by the PWE method. The PWE method assumes that an electromagnetic wave propagating inside a photonic crystal must fulfil Bloch's theorem (Chapter 2), and consequently, it can be expanded as a sum of plane waves propagating along all directions defined by the reciprocal lattice (Equation 2.25 for the electric field in chapter 2 or equivalently equation 2.26 for the magnetic field). By restricting the expansion to a limited number of plane waves and applying Maxwell's equations to equations 2.25 and 2.26, a set of eigenvalue problems is derived. This set can be separated in independent eigenvalue equations 2.27 and 2.28 by recalling that for 2D photonic crystals two independent polarizations (TE and TM, with the magnetic and electric fields along the holes, respectively) can be defined. The result of these eigenvalue problems is that for a given in-plane Bloch wavevector $\mathbf{k}$ only some frequencies can propagate inside the 2D photonic crystal, giving rise to the photonic bands and the photonic band gaps.

An example of calculated photonic band structure using the PWE method is given in figure 5.4. The diagram illustrates the photonic bands of an ideal 2D photonic crystal (infinite in the third dimension) consisting of an ordered array of air holes with square section arranged in a square lattice. The lattice constant (the distance between two holes in the lattice) is a=4 μm, the holes width w=0.78a and the refractive index of the dielectric medium n=3.4. The sizes of the lattice constant and the air holes are obtained from an optical microscope image of an actual fabricated sample such as the one shown in figure 5.2a. The bands for both the TE (dashed lines) and TM (full lines) polarizations correspond to Bloch wavevectors along the ΓX lattice direction. The dash-and-dot straight line indicates the light line, this is: the ω-k points corresponding to waves propagating in free space perpendicular to the holes. In relation with the ADRS, this is equivalent to light incident at 90°. The wavelength scale at the right y-axis indicates that some of the photonic bands lie in the middle infra red (IR) region of the electromagnetic spectrum.

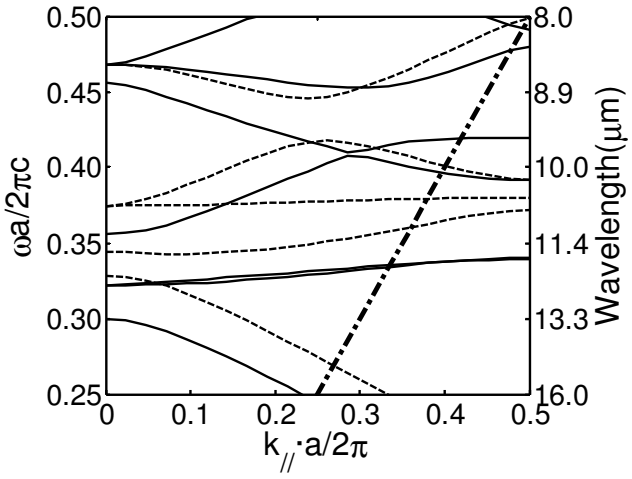

Figure 5.4: Photonic band structure represented in ω-k space of a 2D photonic crystal consisting of an array of square air holes in a dielectric, arranged in a square lattice. The lattice constant is a=4 μm, the holes width w=0.78a and the refractive index of the dielectric material n=3.4. The bands are calculated for both TE (dashed lines) and TM (solid lines) polarizations and for light incident along the ΓX lattice direction (see Appendix A). The dash-and-dot straight line corresponds to the light line.

Figure 5.4 shows a conventional representation of the photonic band diagram, however this interpretation is not convenient for our purposes. The aim of our study is the identification of resonant features in the reflectivity spectra measured at different angles of incidence. Therefore, we plot the measured ADR spectra as a function of the angle of incidence and the wavenumber. Consequently, it is necessary to represent the photonic bands and the simulations of the ADR spectra as a function of the measurement variables. For instance, in figure 5.5 the bands are plotted as a function of the angle of incidence and the wavenumber, and they are equivalent to the photonic bands shown in figure 5.4.

As it was previously mentioned the fabricated 2D photonic crystals studied in this work are not indefinite in the third dimension, hence the mathematical model we use here to calculate the ADR spectra introduces the third dimension to the equations 2.25 and 2.26 by allowing the wave to propagate also along the z direction (the idea is demonstrated in figure 5.6). For instance, for the magnetic field the wave expansion can be expressed as:

$$H(r,z) = \sum_{\mathbf{G}} h_{\mathbf{k}}(\mathbf{G}) e^{i(\mathbf{k}+\mathbf{G})r + i\mathbf{q}z}. \tag{5.1}$$

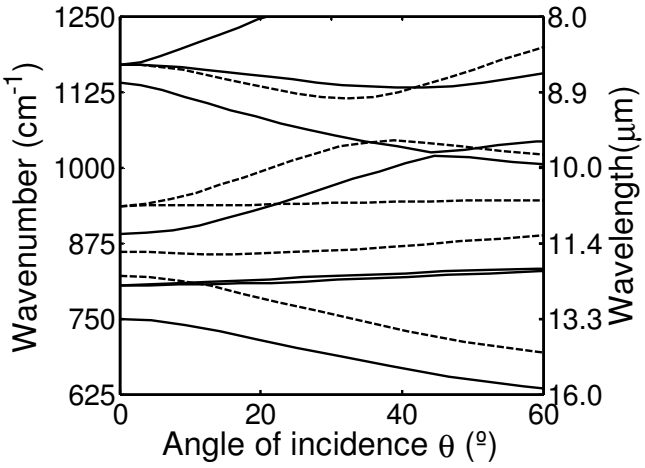

Figure 5.5: Photonic band structure represented in the wavenumber-angle of incidence space of 2D photonic crystal structure as in figure 5.4. Dashed lines correspond to TE bands, while solid lines correspond to TM bands. The bands are calculated for light incident along the ΓX lattice direction.

This expansion spans over all the vectors **G** of the reciprocal lattice, **k** is the Bloch parallel wavevector (since the waves propagating inside the ordered structure must comply with the Bloch theorem, introduced in chapter 2), r is the position in the $x-y$ plane, z is the position along the holes and **q** is the wavevector along the z direction. The introduction of the z component of the wavevector **q** is necessary in order to allow the modeling of waves that propagate inside the photonic crystal in an oblique direction and that can couple to light from the incident medium. By limiting the expansion of equation 5.1 to a finite number of reciprocal wavevectors **G** and applying Maxwell's equations (introduced in chapter 2) to equation 5.1 an eigenvalue problem is obtained for **q**, at a given **k** and wave frequency ω. The solutions of this eigenvalue problem are the modes allowed to propagate inside the sample. Once these modes are determined, a S-matrix procedure is used to impose the boundary conditions at the sample interfaces, this is: continuity of the in-plane components of the electric and magnetic fields and of the parallel wavevector component **k**. With this, it is possible to calculate the coupling efficiency of the incident light to the modes of the photonic crystal and to obtain the reflection coefficients for the two incident polarizations. It must be noted that, from the mathematical derivation of the S-matrix treatment it can be concluded that there may not be only one mode propagating within the photonic crystal sample with a given **k** and ω, but several

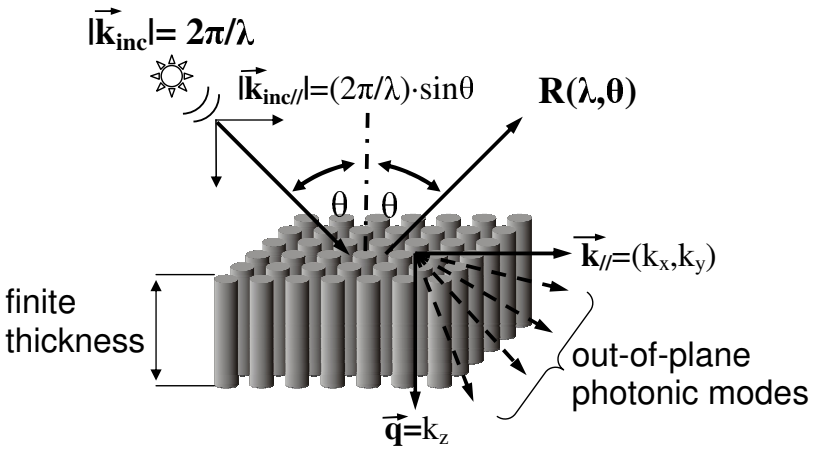

Figure 5.6: Schematic drawing illustrating the light propagation inside a PhC slab (2D photonic crystal of a finite thickness). The drawing shows the z component of the wavevector $\mathbf{q}$ introduced in equation 5.1.

modes for different values of $\mathbf{q}$ (Figure 5.6), and that these modes do not propagate parallel to the sample surface.

It is known [Whittaker 99] that when the incident light couples to a mode propagating inside the photonic crystal, a distinctive feature appears in the spectrum. Such feature can be a maximum, a minimum or an inflection. If the light is incident at an angle θ and the wave frequency at which the feature appears is ω, the magnitude of the parallel wavevector is:

$$|k_{//}| = \frac{\omega}{c} sin\theta, \tag{5.2}$$

with c the speed of light in vacuum. Since this magnitude is conserved as light enters the photonic crystal, it can be used to identify the photonic modes in the spectra. Figure 5.7 shows a representative example of calculated ADR spectra for a sample consisting of an ordered array of square air holes arranged in a square lattice with lattice constant a=4 μm. The width of the holes is w=0.78a and their depth is 7.5 μm. The refractive index of the dielectric medium is n=3.4. These dimensions are estimated from an optical microscope image of the sample shown in figure 5.2a. The incident light is TE-polarized and directed along the rows of the photonic crystal (the ΓX lattice direction). The corresponding angles of incidence are indicated in the graph. One of the resonant features is labeled by arrows, as it can be seen, its wavenumber changes with the angle of incidence.

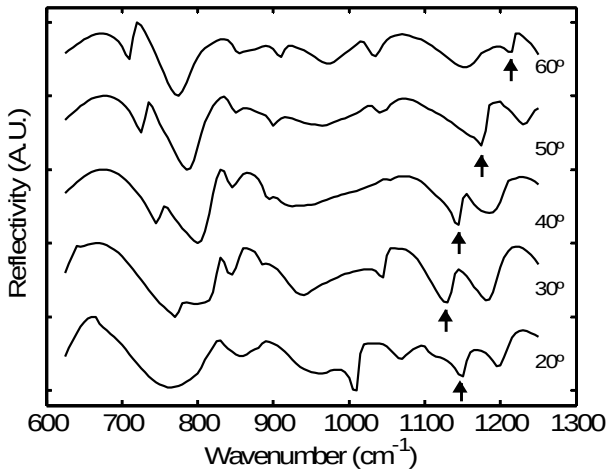

Figure 5.7: Calculated angular-dependent reflectance (ADR) spectra for several angles of light incidence (indicated at the right). The spectra are computed for TE-polarized light along the ΓX lattice direction. The arrows point to a photonic-band related resonant feature.

Nevertheless, with this representation it is difficult to recognize the photonic band-related resonant features. To improve their visibility we use a two dimensional representation showing the ADR spectra in a gray map plotted as a function of the angle of incidence and the wavenumber. An example is given in figure 5.8 which demonstrates separately for each polarization the same ADR spectra as in figure 5.7. The photonic bands for both TE (white-dashed lines) and TM (white-black-solid lines) polarizations are included in the graphics. With such representation some resonant features related to coupling of TE-polarized light to the photonic modes can be clearly identified (Figure 5.8a). As it can be observed from figure 5.8b, there is no coupling to TM modes for this photonic structure in the mid-IR spectral range. Looking at figure 5.8a, it is worth noting that, the resonant features (photonic modes) do not match exactly with the corresponding photonic bands (with the same $\mathbf{k}_{||}$ and $\mathbf{q}$=0), but they appear at higher frequencies. The reason for this blue shift is that the frequency is proportional to the modulus of the wavenumber (considering all in-plane and out-of-plane components) inside the photonic crystal layer. The photonic bands correspond to modes with zero $\mathbf{q}$, while the modes represented by the resonant features have nonzero $\mathbf{q}$ and consequently higher frequency or wavenumber.

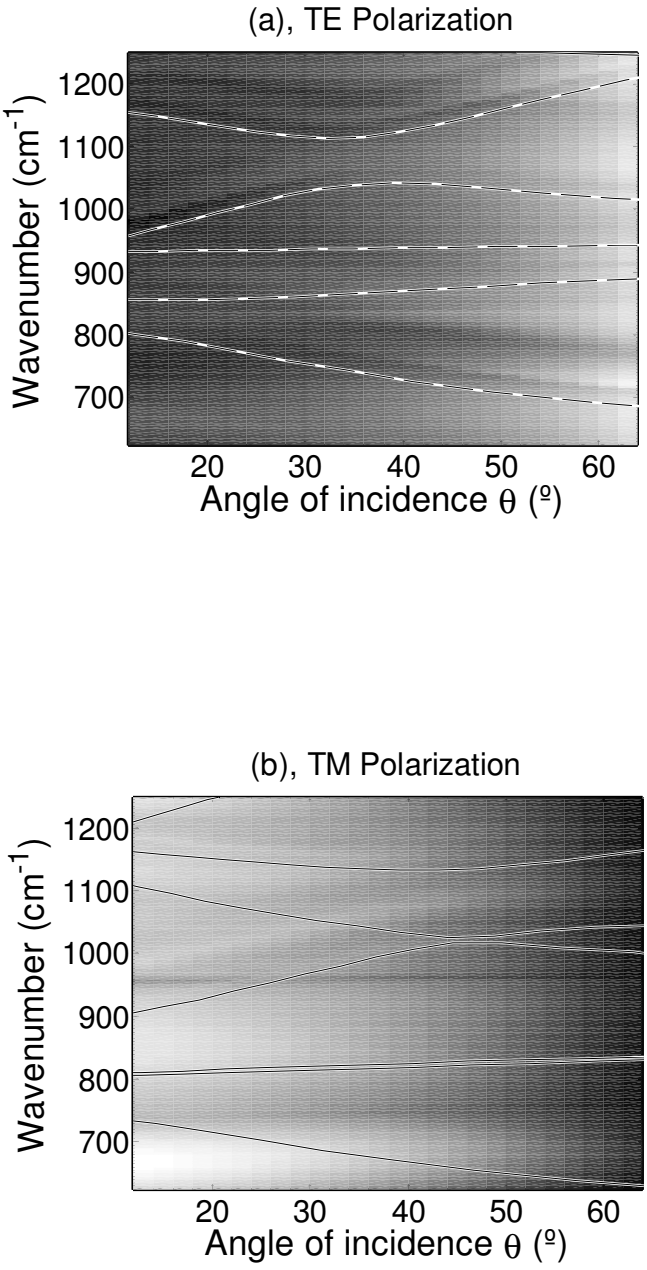

Figure 5.8: 2D plots of the calculated ADR spectra as a function of the angle of incidence and the wavenumber. The two graphs show calculations corresponding to TE and TM polarization of the incoming light along the ΓX principal lattice direction. The characteristics of the sample are the same as in the previous figure 5.7, this is: a square lattice of square air holes etched on silicon with lattice constant a=4 μm, the holes width is w=0.78a and depth is 7.5 μm. The white-black lines correspond to the PWE method calculated photonic bands for this structure.

5.4.1 Effects of slab thickness

The slab thickness plays an important role in determining whether a PhC slab has a band gap in its guided modes [Johnson 99]. We do not study here the photonic band gap, but we investigate how the quasi-guided modes represented by the resonant features change with the thickness[5] of the PhC slab. We perform the numerical simulation of ADR spectra considering the photonic lattice structure shown in figure 5.2a, with three different thicknesses: (a) 7.5 μm, (b) 12.5 μm, and (c) 17.5 μm. The results are presented in figure 5.9(a-c) as a gray map of the calculated reflectivity as a function of the angle of incidence and the wavenumber. We show here only graphs with the ADR spectra of TE-polarized incident light, since a very weak coupling with TM-polarized incident light to the photonic modes was observed in the previous study (Figure 5.8b). Figure 5.9 demonstrates that, for a given band, there are several corresponding modes (resonant features) in the spectra. This indicates that the incident light couples to more that one mode with the same $\mathbf{k}$ but with different $\mathbf{q}$. By comparing the graphs in figure 5.9, it can be concluded that with increasing thickness the number of modes for a given band also increases. Furthermore, the shift between the wavenumber of the photonic band and the lowest mode associated with that band becomes smaller with increasing thickness. This denotes that in the photonic structure with bigger thickness, a wave can propagate in a direction with a smaller angle with respect to the interface. Finally, another characteristic of the spectra in figure 5.9 must be noted: the reflectance spectra show oscillations, particularly in the range of the lower angles (the dark and light stripes in the 2D plot) and their number also increases with the thickness. These oscillations correspond to Fabry-Pérot interferences between the light beams reflected at the interfaces of the photonic crystal layer with the air and with the substrate. The period of such interferences becomes smaller as the thickness of the PhC slab becomes bigger [Král 08b].

[5]Taking into account that the PhC slabs studied in this work consist of arrays of holes etched in different materials, the thickness of the slab is equivalent to the depth of the holes.

UNIVERSITAT ROVIRA I VIRGILI
DEVELOPMENT OF OPTICAL CHARACTERIZATION METHODS FOR MICRO- AND NANO-SCALE PLANAR PHOTONIC BAND GAP STRUCTURES
Zdenek Kral
DL: T-1537-2009/ISBN:978-84-692-4556-9

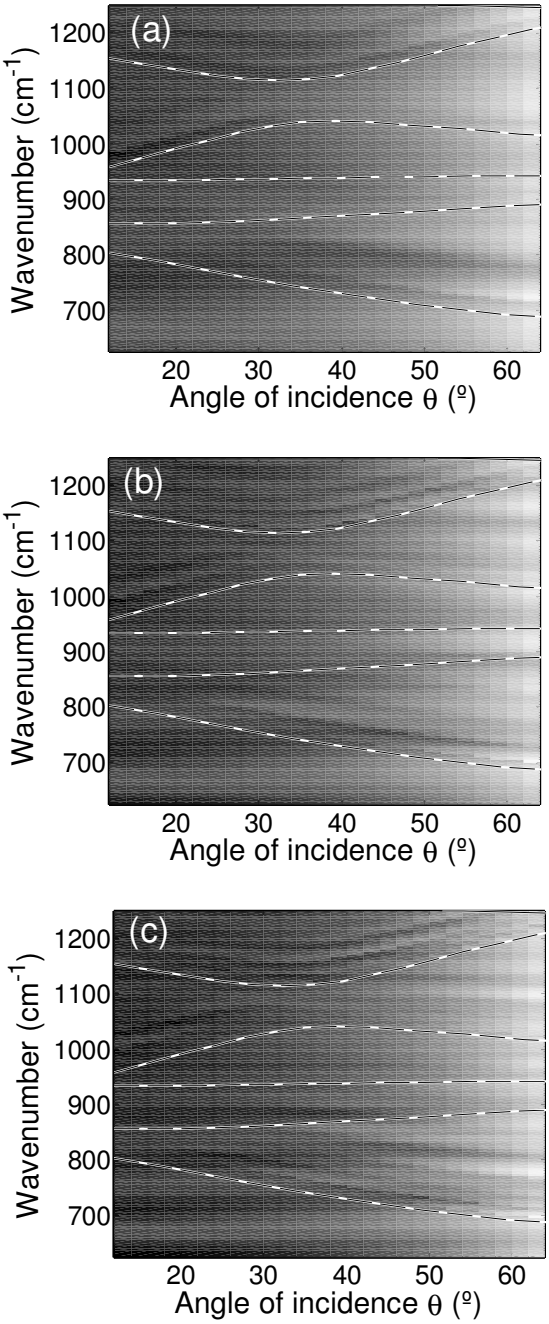

Figure 5.9: Calculated ADR spectra of a PhC slab with the lattice characteristics as the sample in figure 5.2a, but of different thicknesses: (a) 7.5 μm, (b) 12.5 μm, and (c) 17.5 μm. The spectra are represented as a gray map of the reflectivity with respect to the angle of incidence and the wavenumber. The spectra correspond to incident TE light. The bands for the TE polarization and the ΓX lattice direction are overlapped to the graphs.

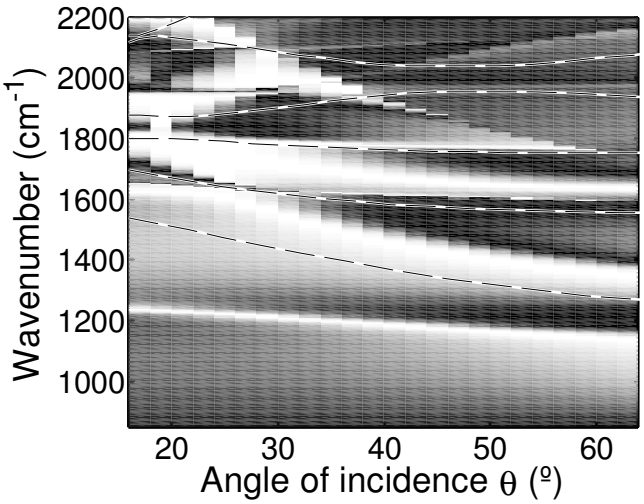

Figure 5.10: Calculated ADR spectra of a PhC slab with the lattice characteristics as the sample in figure 5.2b, consisting of square air holes in a dielectric material with a refractive index n=3.4 (Silicon) arranged in a triangular lattice. The lattice constant is a=4 μm, w=0.83a. The spectra correspond to TE-polarized incident light. The bands for the TE polarization and the ΓM lattice direction are overlapped to the graph.

5.4.2 Study of different lattice structures

Using the same numerical simulation technique we investigate here PhC slabs with different lattice configurations. We present calculations of ADR spectra that correspond to PhC slab with lattice characteristics shown in figures 5.2b and 5.2c. The ADR spectra of the PhC slab consisting of an ordered array of square air holes in a dielectric material with a refractive index n=3.4 (Silicon) arranged in a triangular lattice are shown in figure 5.10. The lattice constant is a=4 μm, while the holes width is w=0.83a and their depth is 4 μm. The simulations for TE-polarized incident light coming along the ΓM lattice direction show some modes related with the three lowest photonic bands (beginning at 1500 cm^{-1}, 1700 cm^{-1}and 1800 cm^{-1}at 20°), although it is not easy to recognize them.

Figure 5.11 shows calculated ADR spectra of the PhC slab consisting of an ordered array of circular air holes arranged in a square lattice of a dielectric medium (Silicon) with a refractive index n=3.4 (Figure 5.2c). The lattice constant is a=4 μm, the holes diameter is d=0.78a and their depth is 4 μm. The ADR spectra are computed for TE-polarized incident light coming along the ΓM lattice direction of the square lattice. The simulation

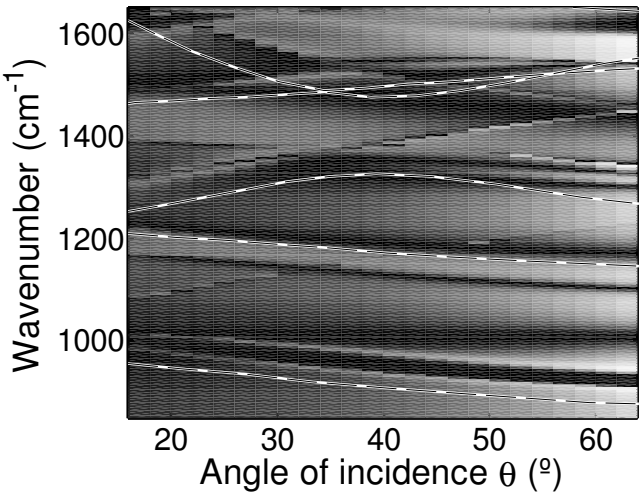

Figure 5.11: Calculated ADR spectra of a PhC slab consisting of circular air holes arranged in a square lattice of a dielectric material (Silicon) with a refractive index n=3.4. The lattice constant is a=4 μm and the holes diameter is d=0.78a. The bands for the TE polarization and the ΓM lattice direction are overlapped to the graph.

results show clear multiple photonic modes (resonant features) related to the first (beginning at 950 cm^{-1}at 20°), second (beginning at 1200 cm^{-1}at 20°) and third (beginning at 1250 cm^{-1}at 20°) photonic bands. As in the case of the previous results presented in figures 5.8 and 5.9, a blue shift of the photonic modes (resonant features) with respect to the bands can be observed.

5.4.3 Effects of different dielectric material

Besides studying the ADR spectra of several lattice configurations we also present simulations on the PhC slab made of a dielectric material with low refractive index. The PhC slab structure, corresponding to the sample in figure 5.3, consists of an ordered array of square air holes in a dielectric material with refractive index n=1.55 (PMMA photoresist) arranged in a square lattice. The lattice constant is a=1 μm, the holes width is w=0.5a and their depth is 400 nm. The computed ADR spectra for the incident light directed along the ΓM direction of the square lattice are plotted in figures 5.12. Figure 5.12a corresponds to TE polarized incident light, while figure 5.12b corresponds to TM polarized incident light. The photonic bands for TE polarization are overlapped to the gray map of figure 5.12a while

the bands for TM polarization are overlapped to the map in figure 5.12b. The simulation results show resonant coupling of the incident light to the TE photonic modes (represented with three white stripes in figure 5.12a) related with three photonic bands (beginning at 5900 cm^{-1}, 6100 $cm^{-1}$and 8000 cm^{-1}at 20°), and to the TM photonic modes (two white stripes in figure 5.12b) related with two photonic bands (beginning at 5700 $cm^{-1}$and 6000 cm^{-1}at 20°). The significant shift in frequency (blue shift), between the bands and the photonic modes, is probably caused by the small thickness (holes depth) of the PhC slab. This is in agreement with our previous results (see Figure 5.9) where we have found that the blue shift between the photonic bands and the resonant features associated with that bands becomes smaller with increasing thickness and vice versa.

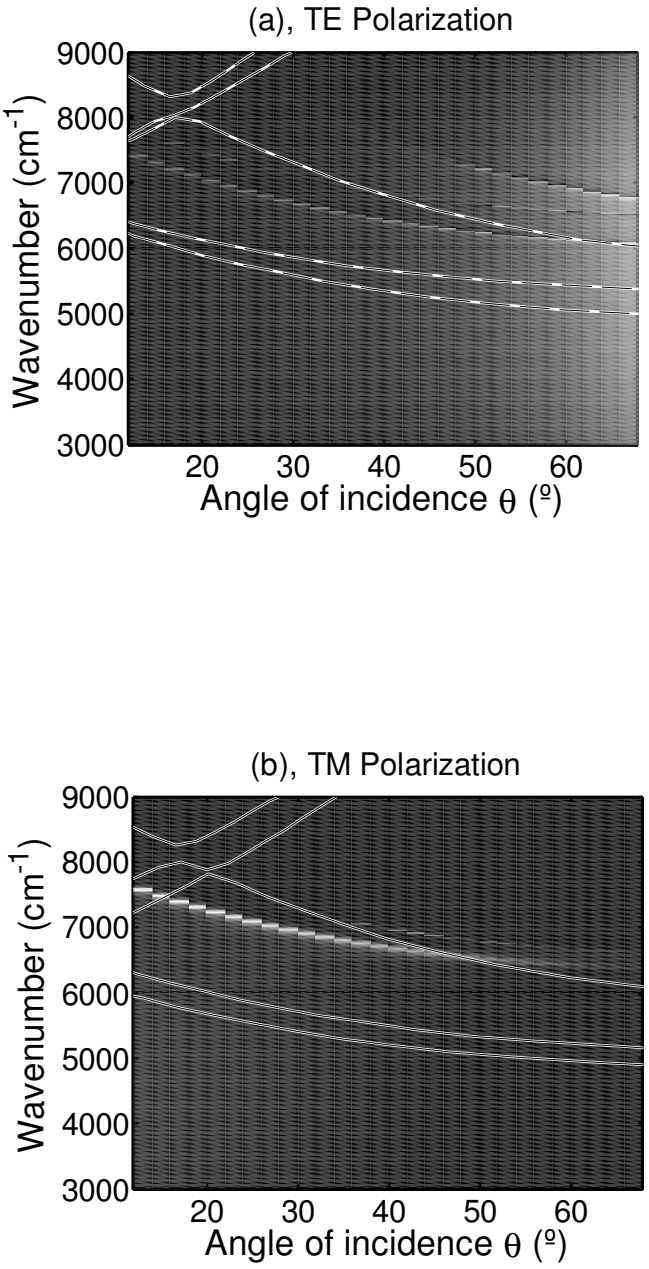

Figure 5.12: Calculated ADR spectra of a PhC slab consisting of square air holes in PMMA arranged in a square lattice. The thickness of the slab is 400 nm, the lattice constant a=1 μm, and the holes width w=0.5a. The two graphs show calculations corresponding to TE (a) and TM (b) polarization of the incoming light along the ΓM lattice direction.

5.5 Experimental measurements using ADRS

In this section we present the experimental characterization of PhC slabs using Angular-Dependent Reflectance Spectroscopy (ADRS). We describe the measurement conditions and we show with one example that an adequate post-processing of the measured data is crucial in order to recognize the resonant features (photonic modes) in the spectra and to achieve a good agreement with the numerical simulations from the previous section.

Many experimental investigations on photonic crystals were linked with the ADRS method. Some of them are cited in section 5.2, but in contrast to previous studies e.g. [Astratov 98, Astratov 99a, Galli 02a, Andreani 03, Astratov 97] the lattice dimensions of the PhC slabs studied here require that the measurements are carried out in the spectral range of the middle infra red (mid-IR) light. This has been demonstrated in the previous section 5.4 where the numerical calculations show that for the investigated samples (except the one with the square air holes arranged in a square lattice with the lattice constant of 1 μm, shown in figure 5.3), the first photonic bands appear in the range between 600 cm^{-1}up to 3000 cm^{-1}. Only few experimental measurements on this range have been reported so far [Galli 02b, Bettotti 02] and none, up to our knowledge, reached up to 600 cm^{-1}, which is the lowest wavenumber that can be reached with our measurement setup. The drawback of measuring in such spectral range is the recognition of the resonant features (photonic modes) in the ADR spectra. Although in previous works [Astratov 98, Astratov 99a, Astratov 99b, Astratov 00a, Astratov 00b] a direct recognition of the resonant features is reported, in the mid-IR spectral range there are several sources of clutter that make this direct recognition a difficult task. Therefore, we propose here a procedure to improve the recognition and we present the application of this procedure to our samples.

The ADR spectra are measured using a Fourier-transform infra red (FTIR) spectrometer (Bruker, model Vertex 70) equipped with a special reflectivity attachment[6]. The reflectivity equipment consists of a removable sample holder and two movable arms with mirrors that enable to point and collect the light in a range of angles between 12°and 90°. The IR light is brought from a broadband halogen-tungsten lamp incorporated in the FTIR spectrometer. The reflected light is collected by the mirror on the movable

[6]The equipment has been already introduced in figure 4.5 of chapter 4.

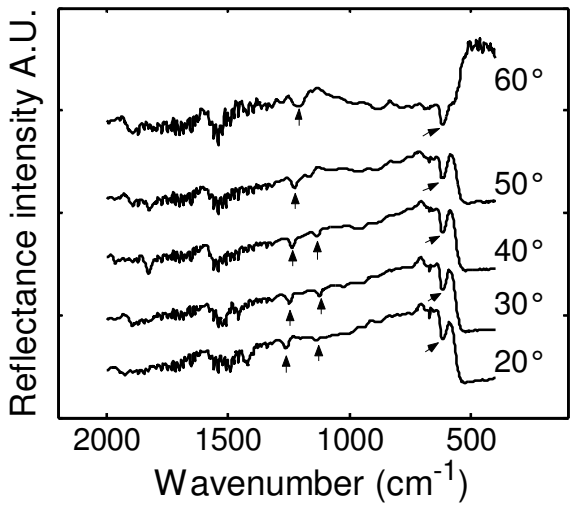

Figure 5.13: A representative example of measured angular-dependent reflectance (ADR) spectra for some selected angles of incidence (indicated at the right). The measured sample (Figure 5.2a) consists of an ordered array of square air holes electro-chemically etched in a crystalline silicon wafer (n=3.4) to form a square lattice with lattice constant of a=4 μm, holes width w=0.78a and thickness (holes depth) 7.5 μm. The measurement is carried out for incidence light along the ΓX lattice direction and for unpolarized light. Three photonic band-related resonant features are indicated by arrows in the graph. The intensity spectra are plotted with offset for clarity.

arm and detected with a liquid-nitrogen cooled MCT[7] detector. The angle of incidence and reflected light is varied from 12°to 66°in steps of 2°. The spectral resolution is set to 4 cm^{-1}. A polished N-type silicon wafer is used as an absolute reflectance reference. The measurements are performed for light incident along the principal lattice directions of the PhC slab structure, according to the explanation in appendix A. It is important to remark that all experimental measurements are carried out with unpolarized light, in contrast with the numerical simulations in the previous section which were presented for TE or TM incident light polarization.

One representative example of measured ADR spectra (reflectance intensity) is given in figure 5.13. The ADRS measurement is performed on the PhC slab previously shown in figure 5.2a of this chapter. The incident light in the measurement is directed along the rows of the PhC slab (the ΓX lattice direction). The intensity spectra are shown for some selected angles of incidence, indicated in the graph. The photonic band-related resonant

[7]Mercury-Cadmium Telluride

features can be either maxima, minima or inflection points of the spectra. Three of them are indicated by arrows. As it can be seen, their wavenumber changes with the angle of incidence. In this example, it is clearly shown that in the mid-IR spectral range the resonant coupling is weak (concerning the shape of the resonant features). Moreover, there exist other features not related to the photonic bands (such as those related to the silicon optical properties [Astratov 98, Galli 02b, Bettotti 02]), which make specially difficult the recognition of the band-related resonant features. For this reason it has been necessary to develop a procedure to post-process the measured data.

A better visualization of the resonant features is obtained with a flattening of the reflectance intensity as a function of the angle of incidence for a fixed wavelength. The flattening (fully described in section 4.5 of chapter 4) removes from the spectra the general decreasing tendency of the reflected intensity with increasing angle of incidence. Subsequently, the ADR spectra are represented as a function of the angle of incidence and the wavenumber in a 2D gray-map graph. Figure 5.14 shows the ADR spectra from figure 5.13 after the flattening procedure, for a range of measured angles (from 12°to 66°in steps of 2°). The photonic bands, calculated with the PWE method are overlapped to the graph.

A further improvement in the resonant features recognition is achieved by filtering out the resonances in the IR spectra that are related to material characteristics. We take into account that the wavenumber of the photonic bands usually changes with $\mathbf{k}_{//}$, while the material-related features correspond to a fixed wavenumber. This leads to the idea that the partial derivative of the reflectance with respect to the angle of incidence may filter out the material-related features. For our measurements, this partial derivative is approximated using finite differences between two reflectivity spectra corresponding to two neighboring angles. Thus, if the reflectance R is measured at a set of wavenumbers ω_i and of angles of incidence θ_j, the partial derivative at a wavenumber ω_i and angle of incidence θ_j is expressed as:

$$\frac{\partial R}{\partial \theta}(\omega_i, \theta_j) \approx \frac{R(\omega_i, \theta_{j+1}) - R(\omega_i, \theta_j)}{\theta_{j+1} - \theta_j}. \tag{5.3}$$

Figure 5.15 shows the $\partial R/\partial\theta$ of the ADR spectra from figure 5.14 overlapped with the calculated photonic bands of an ideal 2D photonic crystal structure

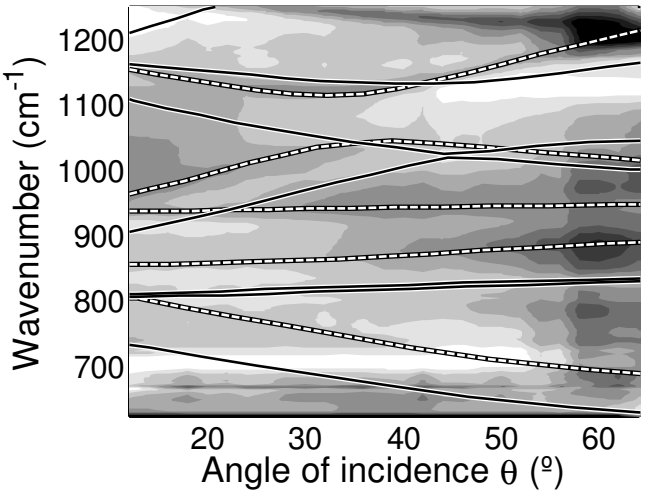

Figure 5.14: 2D plot of the measured ADR spectra (see Figure 5.13) represented as a function of the angle of incidence light and wavenumber after the flattening procedure. The PWE calculated photonic bands are overlapped to the gray map, the white-dashed and white-black-solid lines correspond to the TE and TM polarization, respectively. The measurement is performed for unpolarized incident light along the ΓX lattice direction.

(with infinite thickness). As it is demonstrated, this magnitude permits a better recognition of the photonic band-related resonant features [Král 08a, Král 08b].

By application of the post-processing procedure demonstrated on the example above we have been able to characterize photonic modes of the different PhC slabs. A summary of all experimental results together with the corresponding numerical simulations is given in the following section.

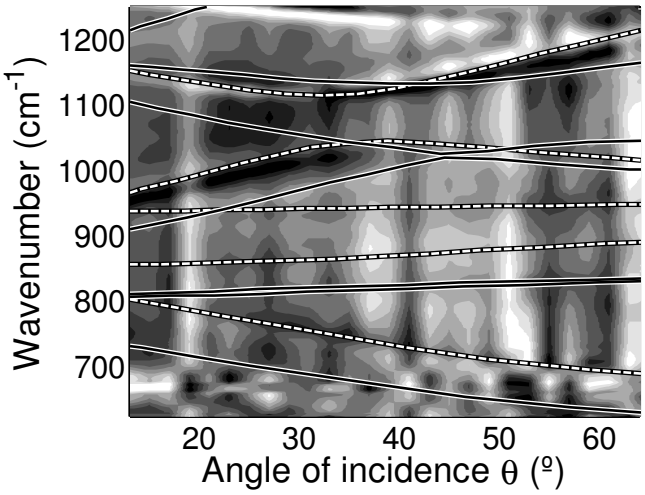

Figure 5.15: 2D plot of the partial derivative $\partial R/\partial\theta$ applied to the ADR spectra shown in figure 5.14, overlapped with the calculated TE (white-dashed lines) and TM (white-black-solid lines) photonic bands.

5.6 Results and conclusions

In this chapter we have applied the Angular-Dependent Reflectance Spectroscopy (ADRS) to the characterization of photonic bands in PhC slabs. The objective was the implementation of the ADRS technique to our samples with lattice parameters that require the measurement to be carried out in the mid-IR spectral range.

First, we have implemented a numerical method to simulate the interaction of the incident light with the PhC slab and thus to compute the ADR spectra. The numerical method relies on the plane-wave expansion (PWE) and the S-matrix formalism including some particularities to achieve the goal of calculating the ADR spectra.

In the second part of this chapter, the experimental measurements of the ADRS were performed with a FTIR spectrometer equipped with a special reflectivity attachment. We have observed that in the mid-IR spectral range the recognition of the characteristic resonant features related to photonic bands is particularly difficult and that the measured spectra need to be post-processed. To this end, we have developed a procedure that significantly improves the recognition of these features and allows the detection of some photonic modes predicted by the numerical simulations. The results of the numerical simulations and measurements of the ADRS on various PhC slabs

are concluded in the following paragraphs:

- Effects of slab thickness

  We have investigated how the photonic modes represented by the resonant features change with the thickness of the PhC slab. We have studied a PhC slab consisting of an ordered array of square air holes (pores) arranged in a square lattice with three different holes depths: (a) 7.5 μm, (b) 12.5 μm, and (c) 17.5 μm. The numerical simulations shown in figure 5.16 have revealed that for a given photonic band (the most visibly for the TE photonic band beginning at 1130 cm^{-1}at 20°) of an ideal 2D photonic crystal (with infinite thickness), the incident light can couple to several photonic modes in the PhC slab. These modes correspond to waves that do propagate at different angles with respect to the sample surface. Furthermore, the number of these modes increases with increasing depth of the etched holes.

  The measurement results of the ADRS shown in figure 5.17 have confirmed the existence of several resonant features for a single photonic band and their increasing number with increasing hole depth. Furthermore, the resonant coupling of the incidence light is observed only to TE photonic modes, which is in good agreement with the calculations.

  It must be also noted that the calculations of the ADR spectra predicted oscillations (black and white stripes in figure 5.16), particularly in the range of the lower angles, however they are not visible in the ADRS measurements. These oscillations correspond to Fabry-Pérot interferences between the waves reflected at the interfaces of the PhC slab.

- Study of different lattice structures

  We have applied the ADRS to different types of lattice configurations with the objective to study the versatility of the technique. The calculated ADR spectra (Figure 5.18a) of the PhC slab with a square lattice structure of circular air holes etched in silicon predicted the existence of multiple photonic modes that are replicas of some TE photonic bands (first beginning at 950 cm^{-1}, second beginning at 1200 cm^{-1}, third beginning at 1250 cm^{-1}, and fourth beginning at 1450 cm^{-1}at 20°). The existence of these photonic modes has been confirmed in the

ADRS measurements. Figure 5.18c) shows clear white/black stripes corresponding to photonic modes that are related to second, third, and fourth TE band.

In the case of a triangular lattice structure with square air holes etched in silicon, the calculated (a) and measured (c) ADR spectra (Figure 5.19) also show some band-related photonic modes, particularly with the first, second, and fourth TE photonic band.

- Effects of different dielectric material

  Finally, we have studied whether the ADRS technique can be also used to characterize the photonic modes in the PhC slab made of low refractive index materials. We have computed the ADR spectra of PhC slabs based on PMMA (Figure 5.20a,b). The spectra have revealed that resonant coupling of the incident light to the photonic modes occurs, but due to the low contrast in the refractive index between the scatterer (air, n=1) and the slab material (PMMA electro resist n=1.55), it is not possible to distinguish whether the light couples to TE or TM modes. This observation has been proved with the measurement of the ADR spectra (Figure 5.20c,d). It is worth noting that the measurements were carried out with unpolarized light.

  It is also interesting to point out that the significant shift in frequency (blue shift) between the photonic bands corresponding to an ideal 2D photonic crystal and the photonic modes of the PhC slab. This blue shift is probably caused by the small thickness (holes depth=400 nm) of the PhC slab compared to the lattice constant (a=1 μm). This is in agreement with our previous results (see Figure 5.9) where we have found that the blue shift of the resonant features with respect to the photonic bands becomes smaller with increasing thickness and vice versa.

UNIVERSITAT ROVIRA I VIRGILI
DEVELOPMENT OF OPTICAL CHARACTERIZATION METHODS FOR MICRO- AND NANO-SCALE PLANAR PHOTONIC BAND GAP STRUCTURES
Zdenek Kral
DL: T-1537-2009/ISBN:978-84-692-4556-9

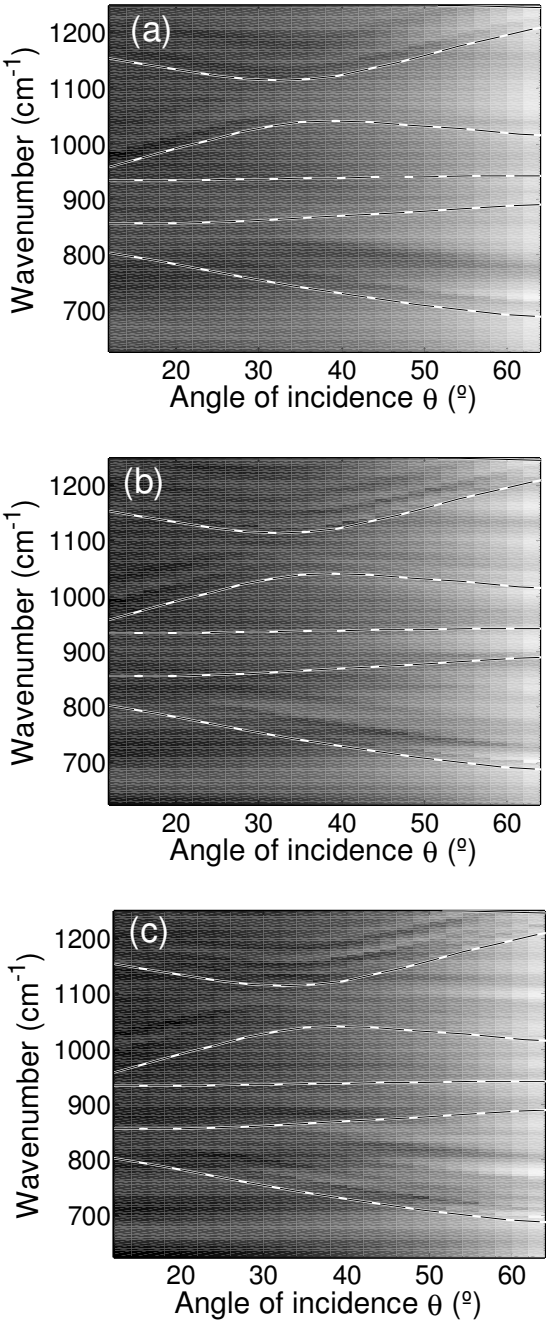

Figure 5.16: Effects of slab thickness: Calculated ADR spectra of a 2D PhC slab structure of different thicknesses (holes depth): (a) 7.5 μm, (b) 12.5 μm, and (c) 17.5 μm. The PhC slab consists of an array of square air holes in a dielectric, arranged in a square lattice. The spectra correspond to TE-polarized incident light. The bands for the TE polarization and the ΓX lattice direction are overlapped to the graphs.

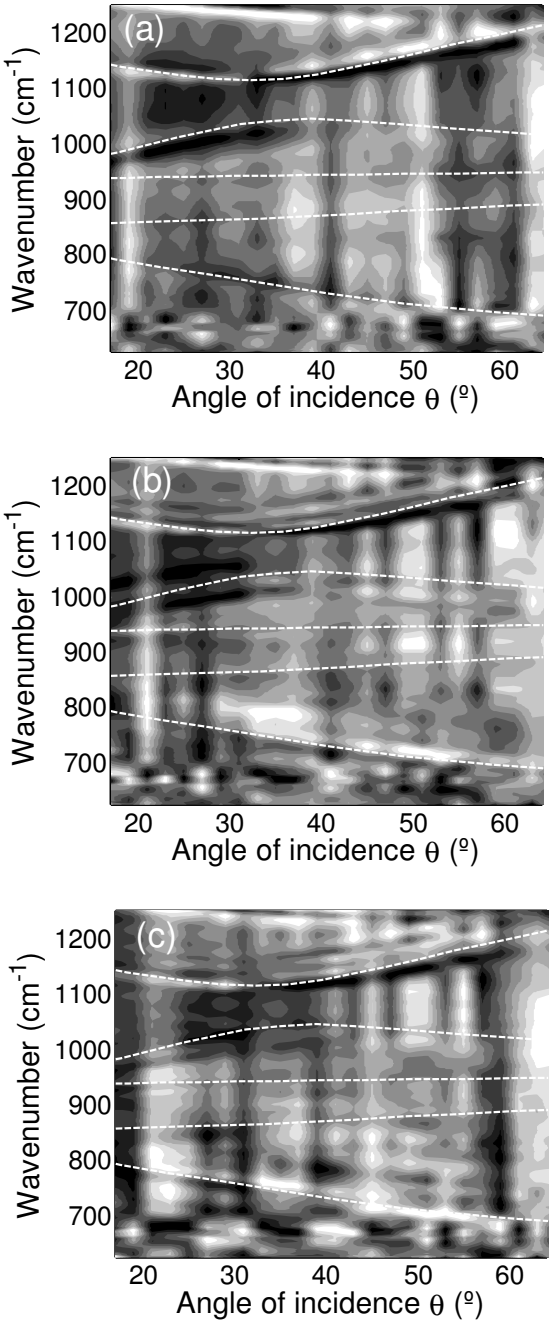

Figure 5.17: Effects of slab thickness: Measured ADR spectra of 2D PhC slabs with different thicknesses (holes depth): (a) 7.5 μm, (b) 12.5 μm, and (c) 17.5 μm. The PhC slabs consist of an array of square air holes in silicon, arranged in a square lattice (Figure 5.2a). The bands for the TE polarization and the ΓX lattice direction are overlapped to the graphs.

UNIVERSITAT ROVIRA I VIRGILI
DEVELOPMENT OF OPTICAL CHARACTERIZATION METHODS FOR MICRO- AND NANO-SCALE PLANAR PHOTONIC BAND GAP STRUCTURES
Zdenek Kral
DL: T-1537-2009/ISBN:978-84-692-4556-9

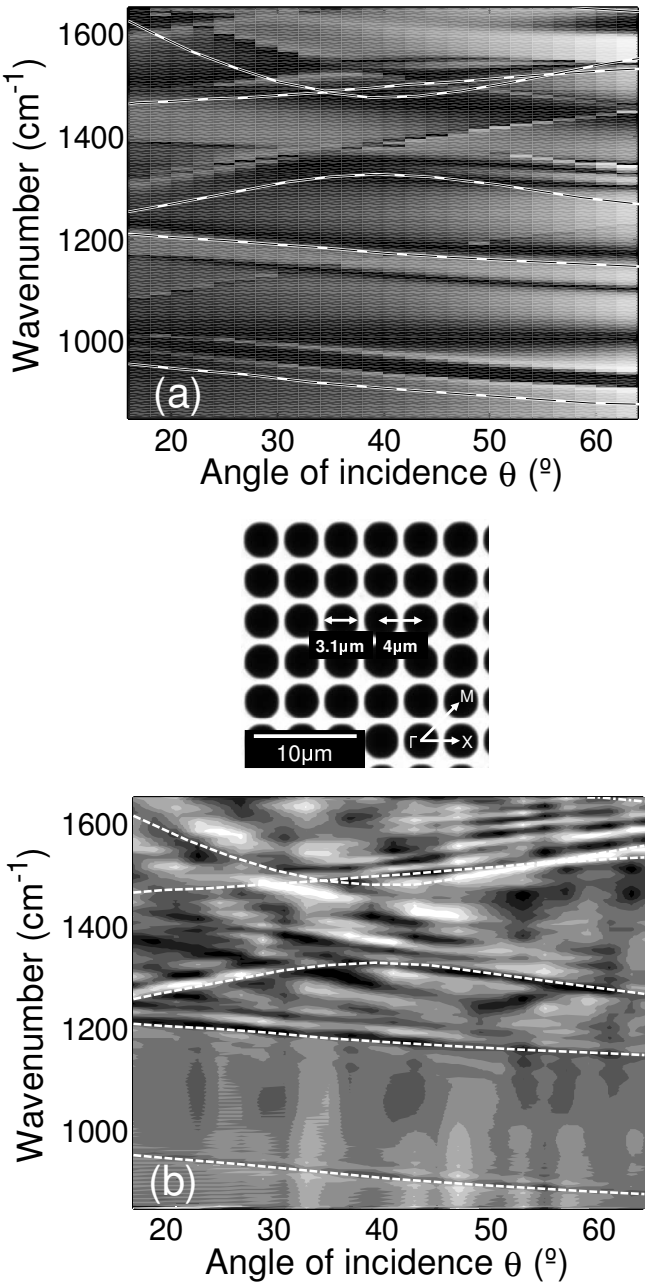

Figure 5.18: Study of different lattice structures: 2D silicon-based PhC slab with a square lattice structure of circular air holes. The microscope image in the middle shows the lattice structure where the lattice constant, holes width and main lattice directions are indicated. The graphs of calculated (a) and measured (b) ADR spectra for light incident along the ΓM lattice direction are represented as a function of the angle of incidence and the wavenumber. The calculated TE (dashed lines) photonic bands of the corresponding photonic crystal are overlapped to the graph.

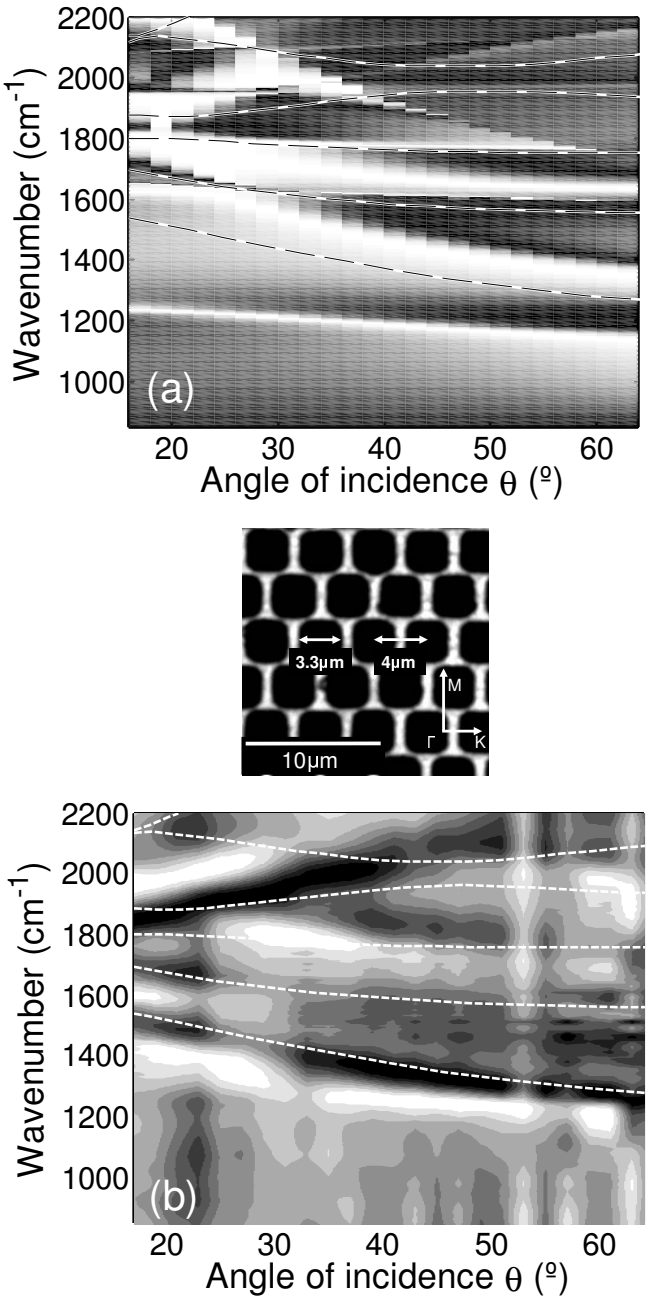

Figure 5.19: Study of different lattice structures: 2D silicon-based PhC slab with a triangular lattice structure of square air holes. The microscope image in the middle shows the lattice structure where the lattice constant, holes width and main lattice directions are indicated. The graphs of calculated (a) and measured (b) ADR spectra for light incident along the ΓM lattice direction are represented as a function of the angle of incidence and the wavenumber. The calculated TE (dashed lines) photonic bands of the corresponding photonic crystal are overlapped to the graph.

UNIVERSITAT ROVIRA I VIRGILI
DEVELOPMENT OF OPTICAL CHARACTERIZATION METHODS FOR MICRO- AND NANO-SCALE PLANAR PHOTONIC BAND GAP STRUCTURES
Zdenek Kral
DL: T-1537-2009/ISBN:978-84-692-4556-9

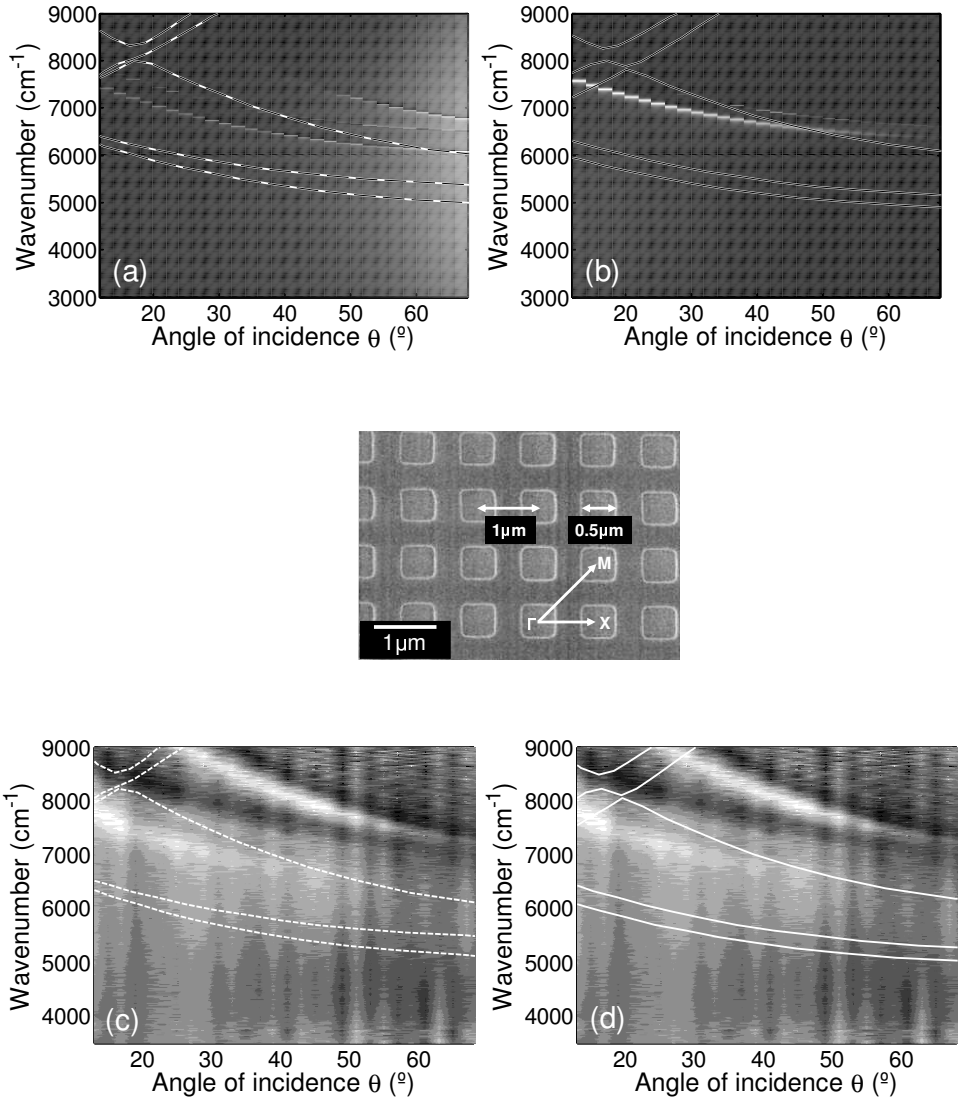

Figure 5.20: Effects of different dielectric material: 2D PhC slab based on nanostructured PMMA electro resist with refractive index n=1.55. The figure shows graphs of calculated (a),(b) and measured (c),(d) ADR spectra for light incident along the ΓM lattice direction. The microscope image in the middle shows the lattice structure where the lattice constant, holes width and main lattice directions are indicated. The calculations correspond to light incident with the TE polarization (a) and TM polarization (b). The measurements correspond to unpolarized incident light. The calculated TE (dashed lines) and TM (solid lines) photonic bands of the corresponding photonic crystal are overlapped to the graph.

UNIVERSITAT ROVIRA I VIRGILI
DEVELOPMENT OF OPTICAL CHARACTERIZATION METHODS FOR MICRO- AND NANO-SCALE PLANAR PHOTONIC BAND GAP STRUCTURES
Zdenek Kral
DL: T-1537-2009/ISBN:978-84-692-4556-9

UNIVERSITAT ROVIRA I VIRGILI
DEVELOPMENT OF OPTICAL CHARACTERIZATION METHODS FOR MICRO- AND NANO-SCALE PLANAR PHOTONIC BAND GAP STRUCTURES
Zdenek Kral
DL: T-1537-2009/ISBN:978-84-692-4556-9

Chapter 6

Angle-Resolved Spectroscopic Polarimetry (ARSP)

6.1 Introduction

In this chapter we examine an alternative spectroscopic technique to the ADRS, the Angle-Resolved Spectroscopic Polarimetry (ARSP). Polarimetry, in general is a powerful technique for the study and accurate determination of the dielectric function, optical properties and geometric characteristics of anisotropic materials [Azzam 76, Azzam 77, Boher 04, Hatit 08].

2D photonic crystals are materials with an inherent optical anisotropy [Netti 01]: the photonic bands and the photonic band gaps depend strongly on the light polarization and the propagation direction. Polarimetry is a technique that measures the change in the polarization state of the light upon reflection or transmission. Therefore, by making polarimetry angle-resolved in the reflection it can provide additional information about the photonic band structure.

The objective of this chapter is the development and application of the ARSP technique to characterize the band structure of photonic crystal (PhC) slabs. To do so, we first theoretically study the viability of the technique for the characterization of such materials with numerical simulations.

The method is based on the Mueller matrix polarimetry, which involves the complete polarimetric description of the light by real four-dimensional Stokes vectors and the polarization changes with 4×4 Mueller matrices. The experimental measurements are then performed on real samples with a spectroscopic Mueller-matrix polarimeter [Garcia-Caurel 04]. The main concern of this work is studying the polarization changes upon reflection on the structure in order to identify the photonic modes related to the TE-TM photonic bands and modes of the slabs.

6.2 Spectroscopic polarimetry

Spectroscopic polarimetry is a technique widely used in the optical characterization of a great variety of samples [Aspnes 04, Arwin 08, Novikova 06, Tkachenko 06]. It is based on the change of light intensity and polarization state caused by interaction with the sample. These changes depend on the material optical properties, on the sample surface geometry, on the angle of incidence, and on the initial polarization state of the beam. The correlation between the polarization states of the incident and the reflected light beams can be described either in terms of a 2×2 complex Jones matrix, when depolarization can be neglected, or more generally by a 4×4 real Muelller matrix [Azzam 77].

Considering a fully polarized light (a monochromatic plane wave) incident on a non-depolarizing optical system consisting of either one or successive series of optical elements, the resulting polarization of the emerging light can be described by taking the product of a Jones matrix of the optical system and a Jones vector of the incident light. The Jones vector is defined by a complex 2x1 column vector whose elements $(E_x(t)e^{j\delta_x(t)}, E_y(t)e^{j\delta_y(t)})$ are the time-dependent complex amplitudes of the x and y components of the electric field. In the absence of non-linearity, the light polarization on the output of the optical system is related to the light at the input of the optical system by the linear equations

$$\begin{aligned} E_{o,x} &= J_{11}E_{i,x} + J_{12}E_{i,y}, \\ E_{o,y} &= J_{21}E_{i,x} + J_{22}E_{i,y}, \end{aligned} \tag{6.1}$$

where $\mathbf{E}_i$ refers to the incident wave, and $\mathbf{E}_o$ to the outgoing wave. Equations

in 6.1 can be combined in a matrix form

$$\begin{bmatrix} E_{o,x} \\ E_{o,y} \end{bmatrix} = \begin{bmatrix} J_{11} & J_{12} \\ J_{21} & J_{22} \end{bmatrix} \begin{bmatrix} E_{i,x} \\ E_{i,y} \end{bmatrix}, \tag{6.2}$$

or, more concisely,

$$\mathbf{E}_o = J\mathbf{E}_i, \tag{6.3}$$

where

$$J = \begin{bmatrix} J_{11} & J_{12} \\ J_{21} & J_{22} \end{bmatrix} \tag{6.4}$$

is the 2×2 transformation matrix called the Jones matrix. The Jones matrix J describes the overall effect of the optical system on the incident light. Its components are, in general, complex and they are functions of: the optical system under consideration; the frequency of the incident light (the light wave); the orientation of the system with respect to the incident wavevector; the location and azimuthal orientation of the input and output coordinate axes around the incident and the outgoing wavevectors; and the particular outgoing light wave, when more than one wave is generated as a result of the interaction between the incident light wave and the optical system.

The Jones matrix description is only applicable to light that is fully polarized propagating through a non-depolarizing optical system. Light which is unpolarized, partially polarized, or incoherent travelling through a depolarizing optical system that may also decrease the degree of polarization must be treated using Mueller matrix formalism. The Mueller-matrix formulation is based on the representation of the polarization state of the light wave by a Stokes vector and the depolarizing optical system by a 4×4 Mueller matrix. Any fully polarized, partially polarized, or unpolarized state of light wave can be represented by a Stokes vector. The Stokes vector $\mathbf{S}$ is defined by a set of four real quantities

$$\mathbf{S} = \begin{bmatrix} S_0 \\ S_1 \\ S_2 \\ S_3 \end{bmatrix} = \begin{bmatrix} I \\ Q \\ U \\ V \end{bmatrix}, \tag{6.5}$$

called the Stokes parameters, whereas each parameter has the dimensions

of intensity. They are a mathematically convenient alternative to the more common description of incoherent or partially polarized radiation in terms of its total intensity I , (fractional) degree of polarization p, and the shape parameters of the polarization ellipse. In terms of the Cartesian components of the transverse electric field, the four Stokes parameters, denoted by S_0, S_1, S_2 and S_3, are defined as follows

$$\begin{aligned} S_0 &= \langle E_x^2(t)\rangle + \langle E_y^2(t)\rangle, \\ S_1 &= \langle E_x^2(t)\rangle - \langle E_y^2(t)\rangle, \\ S_2 &= 2\langle E_x(t)E_y(t)cos[\delta_y(t) - \delta_x(t)]\rangle, \\ S_3 &= 2\langle E_x(t)E_y(t)sin[\delta_y(t) - \delta_x(t)]\rangle. \end{aligned} \tag{6.6}$$

In equation 6.6 $\langle v\rangle$ stands for the time average of v,

$$\langle v\rangle = \frac{1}{T}\int_0^T v\, dt. \tag{6.7}$$

where T is an interval of time long enough to make the time-average integral independent of T itself. If a beam of light is initially in the state $\mathbf{S}_i$ and then passes through an optical system defined by a 4×4 Mueller matrix and comes out in a state $\mathbf{S}_o$, then it is written:

$$\mathbf{S}_o = M\mathbf{S}_i, \tag{6.8}$$

where M is the 4×4 Mueller matrix and $\mathbf{S}_i, \mathbf{S}_o$ are the Stokes vectors of incident and outgoing beam, respectively. For a non-depolarizing optical system, the Mueller matrix can be derived from the Jones matrix defined in equation 6.2. The 4×4 Mueller matrix M is then called a pure Mueller matrix. The expression of such a relation between the Mueller matrix and the Jones matrix can be written as:

$$M = A(\mathbf{J} \times \mathbf{J}^*)A^{-1}, \tag{6.9}$$

where $\mathbf{J}$ in this equation is not the Jones matrix itself, but a coherency vector with the 4 components of the Jones matrix in the appropriate order $\{J_{11}, J_{12}, J_{21}, J_{22}\}$, A is the 4×4 coherency matrix (from equation (1.138a)

in [Azzam 77]):

$$A = \begin{bmatrix} 1 & 0 & 0 & 1 \\ 1 & 0 & 0 & -1 \\ 0 & 1 & 1 & 0 \\ 0 & i & -i & 0 \end{bmatrix}, \tag{6.10}$$

and the A^{-1} stands for its inverse matrix. If we carry out the mathematic operation in equation 6.9, we obtain:

$$M = \begin{bmatrix} \frac{1}{2}(E_1 + E_2 + E_3 + E_4) & \frac{1}{2}(E_1 - E_2 - E_3 - E_4) & F_{13} + F_{42} & -G_{13} - G_{42} \\ \frac{1}{2}(E_1 - E_2 + E_3 - E_4) & \frac{1}{2}(E_1 + E_2 - E_3 - E_4) & F_{13} - F_{42} & -G_{13} + G_{42} \\ F_{14} + F_{32} & F_{14} - F_{32} & F_{12} + F_{34} & -G_{12} + G_{34} \\ G_{14} + G_{32} & G_{14} - G_{32} & G_{12} + G_{34} & F_{12} - F_{34} \end{bmatrix}, \tag{6.11}$$

where

$$\begin{aligned} &E_i = J_i J_i^* = |J_i|^2, i = 1, 2, 3, 4, \\ &F_{ij} = F_{ji} = Re(J_i J_j^*) = Re(J_j J_i^*), i, j = 1, 2, 3, 4, \text{ and} \\ &G_{ij} = -G_{ji} = Im(J_i^* J_j) = -Im(J_j^* J_i), i, j = 1, 2, 3, 4, \end{aligned} \tag{6.12}$$

are auxiliary quantities to simplify the notation. Note that J_1, J_2, J_3, and J_4 are used in equation 6.12 to represent J_{11}, J_{22}, J_{12}, and J_{21} from equation 6.4, respectively. Employing the above formulas (equation 6.11 and equation 6.12), the Mueller matrix of an optical system whose Jones matrix is known can be constructed. In this case, from the sixteen elements of the 4×4 Mueller matrix, only seven would be independent [Azzam 77, Gil 00, Hovenier 94].

The optical instrument that measures the intensity and polarization changes between the incident and reflected beam is called polarimeter. There are different classes of polarimeters. A classical ellipsometer which is devoted to the study of samples described by a diagonal Jones matrix. In other words, it is dedicated to the characterization of non-depolarizing isotropic thin films. Other type is a generalized ellipsometer that can measure any Jones matrix[1] (diagonal or not), thus it can be used for any isotropic or anisotropic non-depolarizing sample. The last type is a Mueller-matrix polarimeter/ellipsometer, which provides a complete polarimetric characteri-

[1] also the Mueller matrix

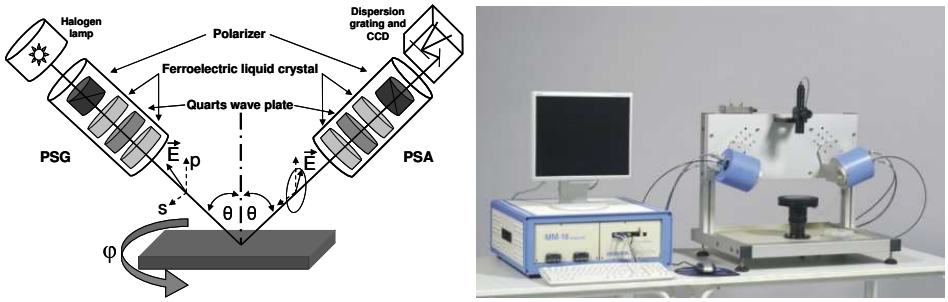

Figure 6.1: Schematic drawing of the Mueller-matrix polarimeter in the reflection configuration (left) with a picture of the actual instrument MM16 (right).

zation of any type of samples, including partially depolarizing ones, which can not be described by a Jones matrix [Kaplan 04].

In this work the Mueller-matrix type of polarimeter is used. Figure 6.1 shows the geometry and the picture of an actual polarimeter MM16 from Horiba Jobin-Yvon [Garcia-Caurel 04]. The instrument is based on modulation and analysis of light polarization by ferroelectric liquid crystal cells. It consists of a Polarization State Generator (PSG) and a Polarization State Analyzer (PSA) that can be adapted to work in reflection or transmission mode. Both the PSG and the PSA consist of a linear polarizer, a quartz retardation plate and two ferroelectric liquid crystal devices, each of which can be switched between two different states. As a result, the PSG can generate four different polarization states for the illumination beam and the PSA with its elements in reverse order is used to analyze the polarization of the emerging beam over another set of four different polarization states. Finally, the polarimeter subsequently measures a set of sixteen raw spectra at high resolution and calculates the complete 16-element Mueller matrix. The incident PSG and reflection PSA arms are attached to an automatic goniometry unit that permits variable-angle spectroscopy measurements in a range of angles of incidence between 45°and 90°in steps of 0.1°. This instrument also includes an automatically adjustable 360°rotating stage allowing measurements at different azimuth angles in the horizontal plane ($x - y$ plane). The source of illumination of the polarimeter is a 30W halogen lamp, and the detector is a CCD array with 2 nm resolution coupled to a commercial Jobin-Yvon diffraction grating optimized for operating in the visible range between 430 nm and 850 nm. The calibration of the MM16 polarimeter is achieved by the Eigenvalue Calibration Method [Compain 99], which is a

general and self-consistent method for the calibration of polarization modulators, polarimeters and Mueller-matrix ellipsometers [Foldyna 08].

6.3 Sample characteristics

In this section we present the 2D photonic structures that will be studied with the spectroscopic polarimetry. One of the goals of this Doctoral Thesis is the development of optical characterisation methods for photonic crystals based on nanoporous alumina slabs, which are fabricated within the framework of the NePhoS (Nano-electronic and Photonic Systems) research group. These nanoporous alumina slabs consist of a quasi-ordered array in triangular arrangement of holes etched in the alumina matrix. Their optical properties (lattice constant corresponding to visible wavelengths, refractive index, luminescence) make them a good candidate for future photonic applications. However, since the fabricated samples are not completely ordered and only triangular lattices can be obtained, this chapter will also focus on another kind of PhC slabs. They consist of an ordered array of holes etched in photoresist onto silicon substrates produced by Laser-Interference Lithography (LIL) [Ellman 08]. These structures can be fabricated in both square and triangular geometries with lattice constants and refractive indices similar to those of the nanoporous alumina. With this, the scope of applicability of the characterization technique is enlarged. Furthermore, there exist other pre-patterning techniques [Chou 96, Masuda 97, Pang 98, Masuda 01, Choi 03] to obtain ordered nanostructures with a periodic variation of the refractive index that provide with other kinds of samples that can also be studied with the methods shown in this chapter.

Figure 6.2 shows an example of a nanoporous Anodic Aluminium Oxide (np-AAO) slab. The np-AAO slab is produced by electrochemical anodization under appropriate fabrication conditions which are described in detail in chapter 3. Figure 6.2a is a SEM image of the sample surface, where the clustered natural self-ordering of the pores can be observed. The pores are naturally ordered and grown in a triangular lattice unless pre-patterning techniques are used [Chou 96, Masuda 97, Pang 98, Masuda 01, Choi 03]. Figure 6.2b shows a closer view of one of the clusters where the triangular lattice ordering is demonstrated. Finally, figure 6.2c shows a cross-section view of the sample to illustrate the high aspect ratio and radius uniformity

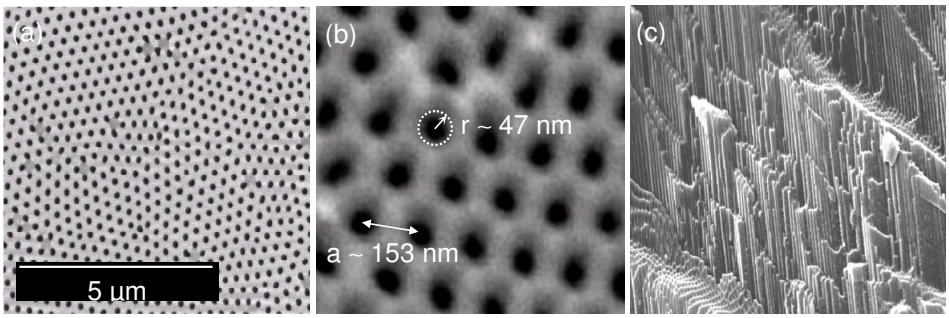

Figure 6.2: SEM images of a np-AAO slab obtained by electrochemical anodization. a) Surface picture showing the self-ordering of the pores, b) surface view at a higher magnification that illustrates the typical characteristic sizes considered later in the calculations, and c) cross-section view that illustrates the in-depth pore uniformity.

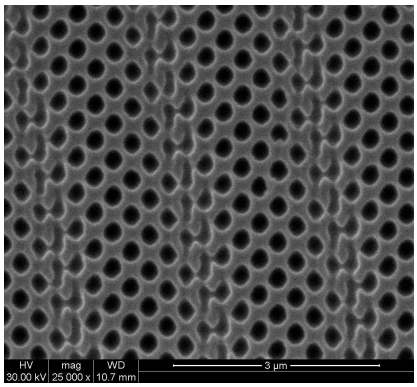

Figure 6.3: SEM image of the photoresist PhC slab produced by laser-interference lithography (LIL). The picture shows the square lattice with lattice constant a∼450 nm and the periodic modulation with a period of ∼2 μm, along the ΓM lattice direction. [Ellman 08]

of the pores. Taking into account that one of the goals of this chapter is the numerical simulation of the interaction of the incident light with these samples, it is necessary to define an ideal sample that is a model of this np-AAO slab. Therefore, in the numerical simulations we will assume a model of np-AAO PhC slab based on average values of the fabricated samples. The characteristics of the model are the following: np-AAO slab (n=1.67) surrounded by air with a perfect triangular arrangement of cylindrical air pores with complete radius uniformity (lattice constant a=153 nm, pore radius r= 47 nm).

Figure 6.3 shows a sample fabricated by the LIL technique introduced in Chapter 3. The sample is a silicon wafer with the native silicon oxide layer

UNIVERSITAT ROVIRA I VIRGILI
DEVELOPMENT OF OPTICAL CHARACTERIZATION METHODS FOR MICRO- AND NANO-SCALE PLANAR PHOTONIC BAND GAP STRUCTURES
Zdenek Kral
DL: T-1537-2009/ISBN:978-84-692-4556-9

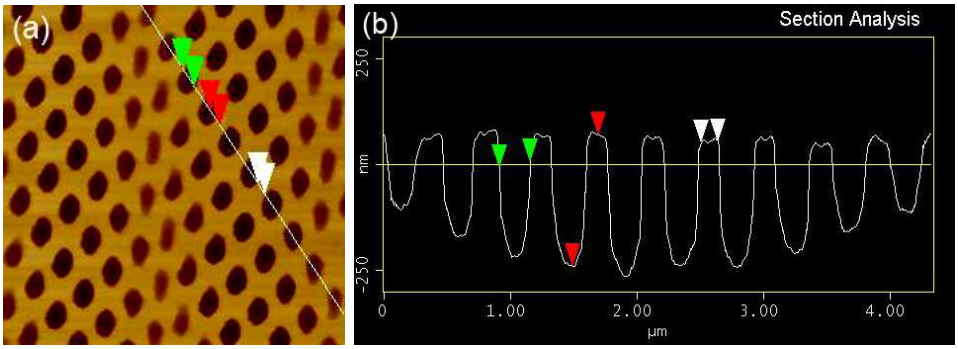

Figure 6.4: (a) AFM topographic image of the photoresist PhC slab surface, (b) section profile in the direction marked with the white line (a). [Ellman 08]

(SiO_2) over it and with an i-line positive low-viscosity photoresist (AZ1505) deposited by spin coating on the top. The thickness of the deposited photoresist film is 400 nm. The parameters of the sample are estimated by atomic force microscopy (AFM). Figure 6.4 shows an AFM topographic image of the surface together with a section profile. From a set of AFM measurements, average values for the characteristic parameters of these photonic crystals have been estimated in order to define an ideal sample, suitable for numerical calculations. These average values are: lattice constant a=450 nm, the depth of the holes is d=370 nm and their radius is r=140 nm. It can be observed from figure 6.3 that the photoresist pattern presents a periodic modulation of the lattice constant with a period of $\sim$2 μm, in the ΓM direction of the lattice. This modulation is due to very small deviations from the adequate value in the angles of incidence of the four interfering beams.

6.4 Numerical calculation of angle-resolved polarimetry spectra

In this section we apply the numerical calculation method based on the S-matrix formalism, introduced in section 2.3 of chapter 2, with a view to study the suitability of the angle-resolved spectroscopic polarimetry for the characterization of PhC slabs. The S-matrix formalism permits to calculate the reflection coefficients for a selected polarization of the incident and reflected beams. These reflection coefficients take into account modulus and

phase and thus are indeed the four components of the 2×2 complex Jones matrix, which for a non-depolarizing optical system can be converted into an equivalent 4×4 real Mueller matrix, used in spectroscopic Mueller polarimetry.

It has been mentioned that 2D photonic crystals exhibit an inherent optical anisotropy: the photonic bands depend strongly on the light polarization and propagation direction. In this section we will study polarimetry (a measurement technique strongly related to the polarization characteristics of the samples) with respect to the characterization of photonic crystals.

Taking into account that in the subsequent sections of this chapter the analysis of measurements carried out with a MM16 polarimeter (figure 6.1) will be presented, the calculations shown in this section will consider spectra of two kinds: i) angle-resolved spectra for a fixed azimuth angle ϕ and variable angle of incidence θ and ii) angle-resolved spectra for a fixed angle of incidence θ and variable azimuth angle ϕ.[2]

6.4.1 Calculation of ARSP at fixed azimuth angle

This subsection shows calculations of angle-resolved polarimetry spectra for two different photonic structures: i) np-AAO PhC slab with a triangular lattice and ii) photoresist PhC slab with a square lattice. These numerical simulations demonstrate the polarization changes of light upon the reflection at various angles of incidence θ and for a fixed azimuth angle ϕ.

Figure 6.5 presents an example of calculated polarimetry spectra in the form of the modulus of the Jones matrix components for the np-AAO PhC slab. The calculation is carried out at a range of angles of incidence θ and for a fixed azimuth angle ϕ that corresponds to the ΓM direction of the triangular lattice (Appendix A). The numerical simulation assumes 121 plane waves to ensure the convergence and a model of np-AAO PhC slab with the following parameters: ordered triangular lattice of cylindrical air pores with lattice constant of a=153 nm, pore radius r=47 nm, refractive index of the slab material (Aluminium Oxide) n=1.67, and thickness of the slab (or equivalently pore depth) d=300 nm. The modulus of the Jones matrix components is presented in a gray map graph as a function of the normalized

[2]Note in figure 6.1 the definition of the azimuth angle ϕ and the angle of incidence θ. The azimuth angle ϕ is defined with respect to the lattice orientation, thus 0 degrees corresponds to the ΓX direction, both for the triangular and for the square lattices.

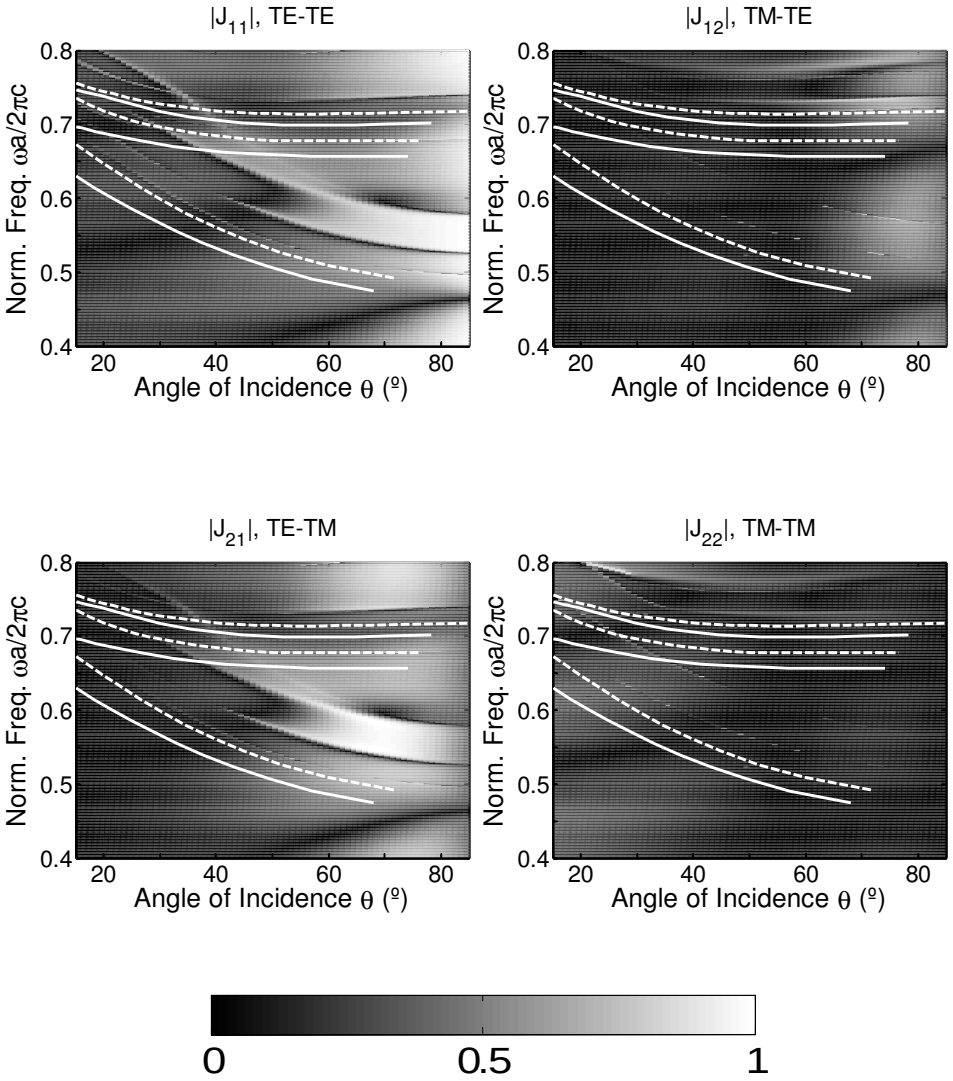

Figure 6.5: Angle-resolved polarimetry spectra of a np-AAO PhC slab. The four gray maps show the modulus of the Jones matrix components that characterize the change of polarization upon reflection on the slab. The light is incident on the sample along the Γ-M direction of the photonic crystal triangular lattice. The four gray maps correspond to the components $|J_{11}|$ (TE-polarized incident beam and TE-polarized detected light), $|J_{12}|$ (TE-polarized incident beam and TM-polarized detected light), $|J_{21}|$ and $|J_{22}|$. The photonic bands calculated for the ΓM lattice direction of the corresponding photonic crystal are overlapped to the gray map graphs: TE polarization (dashed lines) and TM polarization (solid lines).

incident light frequency, $\omega a/2\pi c$, and of the angle of incidence, θ. The four components of the Jones matrix are labeled in figure 6.5, together with the corresponding polarizations of the incident and outgoing light beams. Thus, component $|J_{11}|$ corresponds to the TE-polarized incident beam and the TE-polarized emerging beam. In order to evidence the relative strength of the Jones matrix components, the four graphs are represented with the same gray scale. The TE and TM photonic bands[3] are overlapped to the graphs. As it can be observed, several features related to photonic bands can be recognized in the spectra. More concisely, in the $|J_{11}|$ and $|J_{21}|$ components, the features correspond to TE bands, while for the $|J_{12}|$ and $|J_{22}|$ the features correspond to TM bands. It should be pointed out that there is a significant amount of cross-polarization: an incident TE-polarized beam is reflected with TE polarization, but also in a certain amount with TM polarization. It is also interesting to note that the oscillations of the reflection coefficient due to Fabry-Pérot interferences are visible (the dark and bright stripes).

The calculation of polarimetry spectra for the photoresist sample with a square lattice produced with LIL is shown in figure 6.6. The figure shows the modulus of the Jones matrix components presented in the same form as in the previous figure: four gray map graphs as a function of the normalized incident light frequency, $\omega a/2\pi c$, and of the angle of incidence, θ. The calculation is carried out at a range of angles of incidence θ and for a fixed azimuth angle ϕ that corresponds to the ΓX direction of the square lattice. The parameters used for the model of the photoresist PhC slab are the following: ordered square lattice with lattice constant of a=450 nm, pore radius r=140 nm, refractive index of the slab material (photoresist AZ1505) $n = 1.67$, and thickness of the slab (or equivalently holes depth) d=370 nm. The spectra presented in figures 6.5 and 6.6 reveal that for both photonic crystal structures the incident light of given polarization can couple to the modes propagating inside the slab. However, there is a remarkable difference between PhC slabs with triangular lattice and with square lattice. While for the former cross-polarization is noticeable in the $|J_{12}|$ and $|J_{21}|$ components, for the latter it is nonexistent since the $|J_{12}|$ and $|J_{21}|$ components vanish.

To validate the theoretical results demonstrated by the calculations of

[3]calculated with the lattice characteristics of the np-AAO PhC slab, but considering an ideal 2D photonic structure infinite in the third dimension

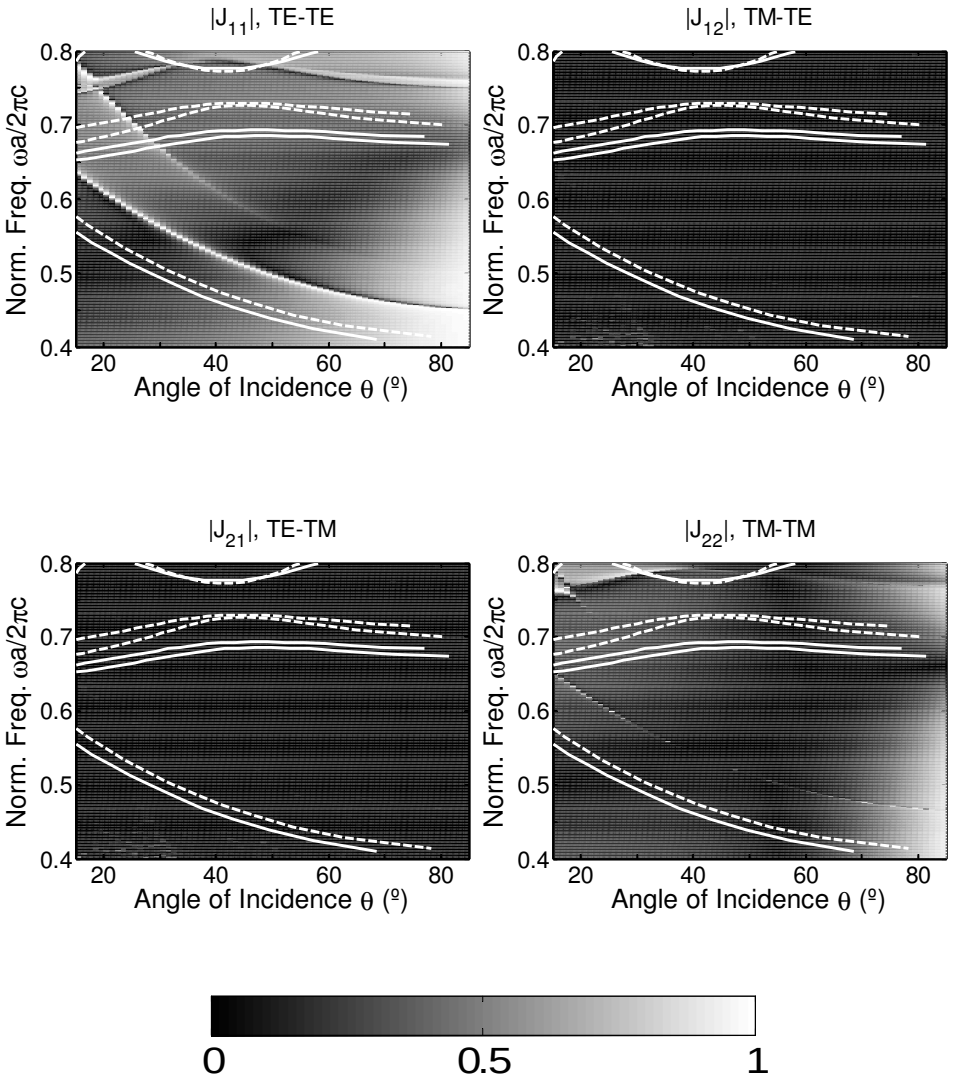

Figure 6.6: Angle-resolved polarimetry spectra of a photoresist PhC slab. The light is incident along the ΓX direction of the photonic crystal square lattice. The photonic bands calculated for ΓX lattice direction of the corresponding photonic crystal are overlapped to the graphs: TE polarization (dashed lines) and TM polarization (solid lines).

angle-resolved polarimetry spectra presented in this section, we will use spectroscopic Mueller polarimetry to measure real samples. The Mueller polarimetry provides a complete polarimetric characterization of any type of samples including partially depolarizing ones. Furthermore, it should be pointed out that the studied np-AAO samples cause a partial degree of depolarization of the reflected light in the experimental measurements, because of its quasi-ordered nature and the roughness of the sample surface caused by the etching process. Therefore, the experimental angle-resolved polarimetry spectra can not be described by the mathematical model proposed in chapter 2, which assumes perfectly ordered and smooth samples. For this reason, the following results will focus on the photoresist PhC slab fabricated with LIL, which can be an alternative material to np-AAO, with similar optical properties and a regularly ordered structure.

To compare the calculated polarimetry spectra with prospective experimental measurements on real samples constituted by photoresist PhC slabs (figure 6.3), the spectra need to be converted[4] from the Jones matrix components shown in figure 6.6 into its equivalent Mueller matrix representation used in spectroscopic Mueller polarimetry. Figure 6.7 shows the Mueller matrix components presented in a gray map graph as a function of the normalized incident light frequency and of the angle of incidence. As it can be seen in some of the Mueller matrix components, the spectra exhibit the same band related features that have been observed in Jones matrix representation. This is demonstrated in figure 6.8, which shows a detailed view of the M_{34} component. The photonic bands of the corresponding photonic crystal for the TE polarization (dashed lines) and for the TM polarization (solid lines) are overlapped to the graph.

[4] assuming a non-depolarizing optical system

UNIVERSITAT ROVIRA I VIRGILI
DEVELOPMENT OF OPTICAL CHARACTERIZATION METHODS FOR MICRO- AND NANO-SCALE PLANAR PHOTONIC BAND GAP STRUCTURES
Zdenek Kral
DL: T-1537-2009/ISBN:978-84-692-4556-9

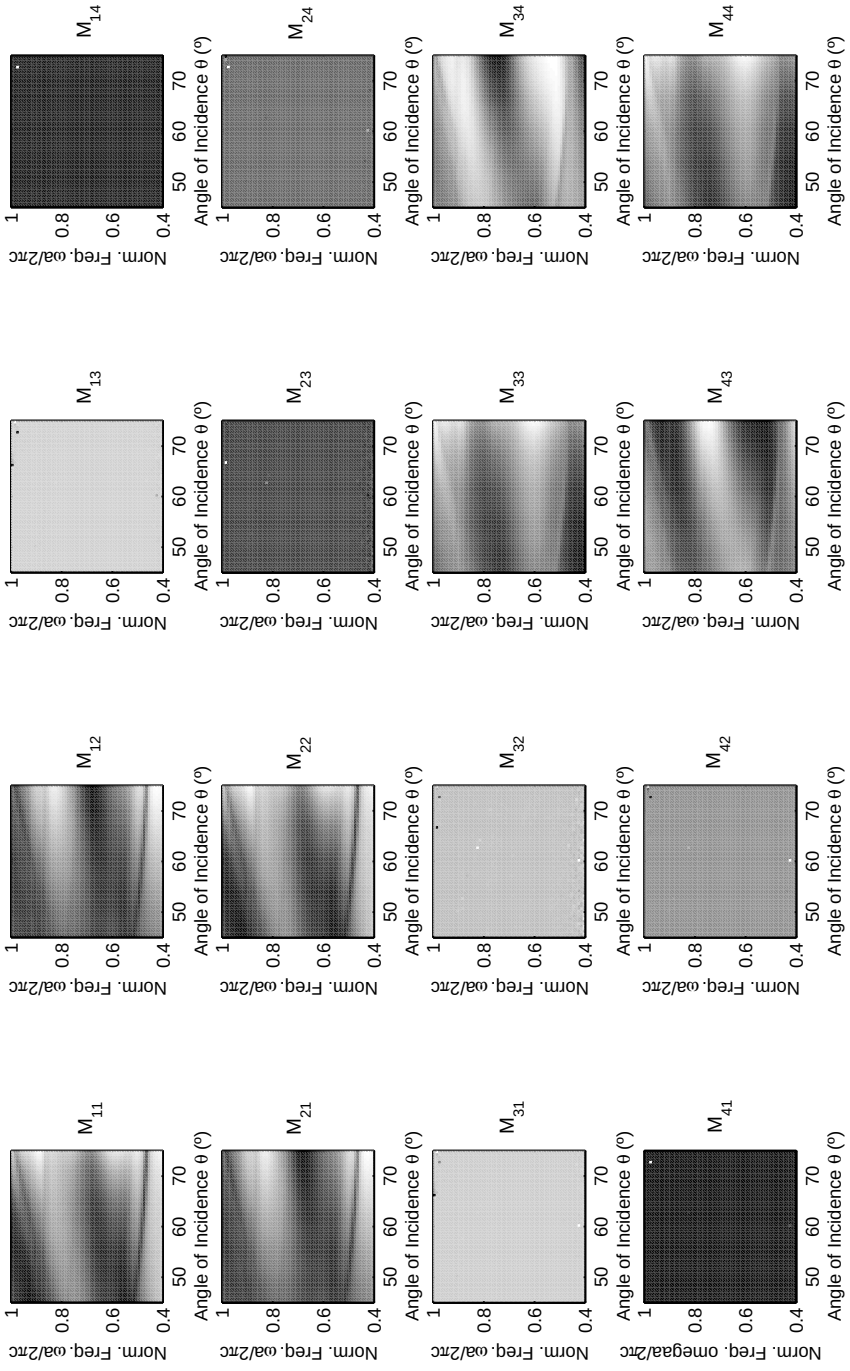

Figure 6.7: Angle-resolved polarimetry spectra of a photoresist PhC slab represented in terms of the Mueller matrix components, and plotted as a function of the normalized incident light frequency, $\omega a/2\pi c$, and of the angle of incidence, θ. The Mueller matrix components are represented with the same gray scale.

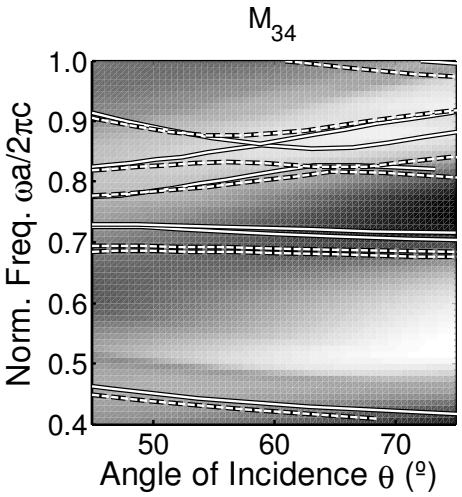

Figure 6.8: Detailed view of the M_{34} component of the Mueller matrix shown in figure 6.7. The photonic bands calculated for the ΓX lattice direction of the corresponding photonic crystal are overlapped to the gray map graphs: TE polarization (dashed lines) and TM polarization (solid lines).

6.4.2 Calculation of ARSP at fixed angle of incidence

In the previous subsection we have implemented a numerical method based on the S-matrix formalism to calculate the angle-resolved polarimetry spectra at a fixed azimuthal angle as a function of the angle of incidence. The resulting polarimetry spectra exhibit some resonant features corresponding to coupling of the incident light to photonic modes in the PhC slabs, related to the photonic bands.

In this subsection we apply an alternative approach to studying these photonic bands by calculating the polarimetry spectra of the photoresist PhC slab at a fixed angle of incidence and varying the azimuth angle. In this way the photonic band distribution can be studied along all lattice symmetries. With this strategy, the recognition of the band-related resonant features in the spectra is easier since these features must obey the symmetry properties of the lattice.

The representation of these spectra requires the use of polar coordinates, in which the frequency of the incident light ω is represented by the distance to the center of the plot and the azimuth angle ϕ is represented by the polar angle. In order to understand this representation in polar coordinates, the relation with the standard photonic band representation (ω vs. k) is demonstrated in the following figures 6.9 and 6.10. Figure 6.9 shows the

photonic bands, calculated with the PWE method, of an ideal 2D photonic crystal structure (infinite in the z direction) consisting of a square lattice of circular holes, with lattice dimensions a=450 nm and r=140 nm. These dimensions are average values obtained from the actual samples such as the one shown in figure 6.3, fabricated by LIL. The calculated photonic bands are plotted in a standard representation as a function of the normalized incident light frequency, $\omega a/2\pi c$, and the wavevector k. Figure 6.9 shows four separate graphs each corresponding to one of the lattice directions (ΓX or ΓM) and one of the light polarizations (TE or TM), indicated in the graphs. Only the four lowest photonic bands are presented for clarity. The dashed-and-dot straight line represents the light line, this is: the $\omega - k$ points corresponding to waves incident from air onto a slab of the photonic crystal at an angle of incidence of 90°. It is important to note that the first photonic band (solid line with circles) lies below this light line. The straight solid line labeled 60°corresponds to waves incident onto a PhC slab from air at an angle of incidence of 60°. Each angle of incidence corresponds to such a line in the $\omega - k$ representation.

The representation of the photonic bands as a function of the azimuth angle for a fixed angle of incidence corresponds to the intersection of the bands in figure 6.9 with the corresponding straight line, for all azimuth angles. This is illustrated in figure 6.10, where the calculated photonic bands as a function of the azimuth angle for an angle of incidence (AOI) of 60°are shown. The two graphs for TE and TM polarizations are plotted. In these graphs, the distance to the center corresponds to the normalized frequency of the incident light , $\omega a/2\pi c$ while the polar angle corresponds to the azimuthal angle, ϕ. Since in these graphs, the normalized frequency $\omega a/2\pi c$ is represented as the distance to the center, the $x-$ and $y-$ scales are in normalized frequency units. The dotted, the dashed, and the solid lines correspond to the second (dotted line), third (dashed line), and fourth (solid line) photonic bands from figure 6.9, respectively. The main directions of the square lattice structure (ΓX and ΓM) are indicated in the graphs. The first photonic band presented in figure 6.9 (the solid line with circles) intersects the light line for any angle of incidence at the zero frequency. Thus, this first band is only represented in the polar plot by the central point.

According to the photonic band representation of figure 6.10, the calculated angle-resolved polarimetry spectra of the photoresist PhC slab is

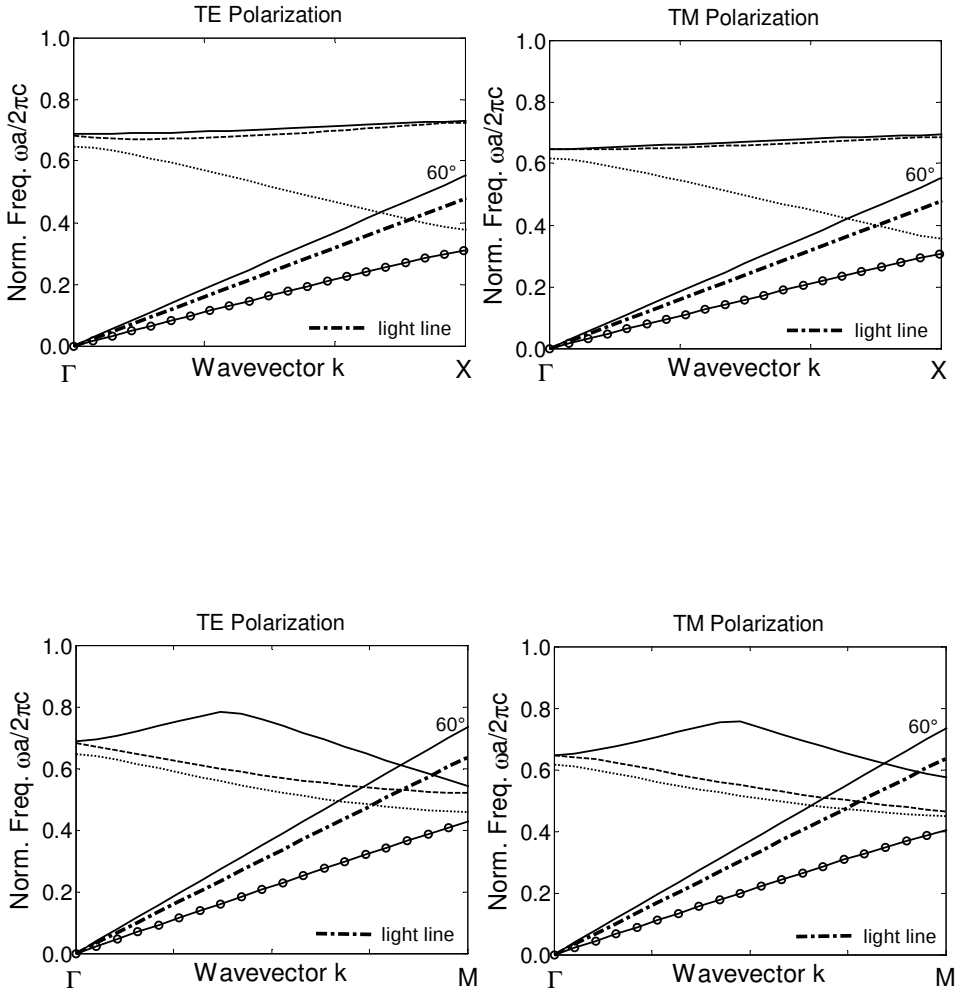

Figure 6.9: Band structure for an ideal (infinite in the z direction) 2D photonic crystal with square lattice of cylindrical holes on a host material with n=1.67. Lattice constant a=450 nm, pore radius r=140 nm. The bands are calculated along the main lattice directions ΓX and ΓM for both polarizations, TE and TM. The dashed-and-dot straight line represents the light line (ω-k values for light incident onto a slab of the photonic crystal at an angle of incidence of 90°). The solid straight line represents the ω-k values of light incident onto a slab of the photonic crystal at an angle of incidence of 60°.

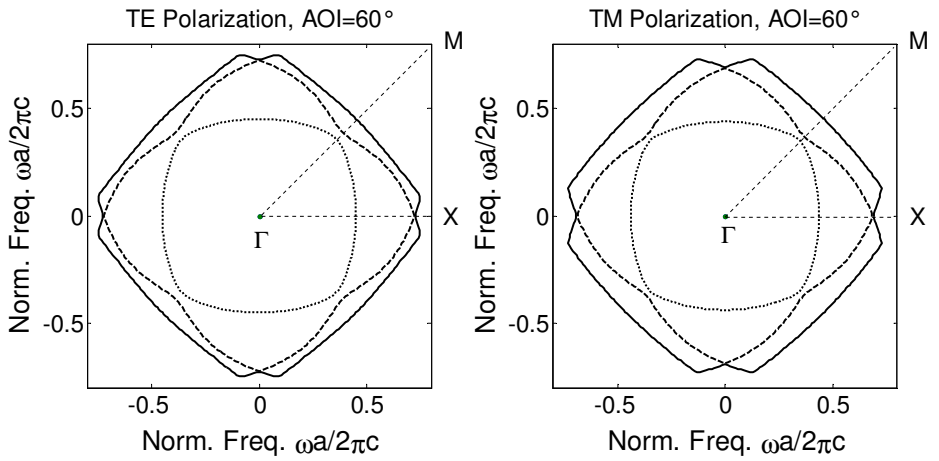

Figure 6.10: Band structure of the 2D photonic crystal considered in the previous figure 6.9. The bands are here plotted in polar coordinates, where the radial coordinate is the normalized frequency $\omega a/2\pi c$ and the angular coordinate corresponds to the azimuthal angle ϕ. The bands are calculated at the fixed angle of incidence (AOI) θ=60°for both polarizations, TE and TM. The main lattice directions of the square lattice structure (ΓX and ΓM) are indicated.

plotted in figure 6.11 as a function of the normalized frequency, $\omega a/2\pi c$, and the azimuth angle, ϕ. In the calculation of the spectra we considered 121 plane waves and the light incident at 60°. We used the model of the photoresist PhC slab with following parameters: ordered square lattice with lattice constant a=450 nm, pore radius r=140 nm, refractive index of the slab material (photoresist AZ1505) $n = 1.67$, and thickness of the slab (or equivalently the hole depth) d=370 nm. The calculated spectra show resonant features that indicate that the incident light is coupling to photonic modes (the electromagnetic states propagating inside the PhC slab). To relate these resonant features with corresponding photonic bands, let us focus on one of the Mueller matrix components (M_{13}). Figure 6.12 shows this component with the previously calculated photonic bands. Each band is plotted separately in different graphs in order to improve the recognition. Figure 6.12 shows the resulting graphs of the M_{13} with the second (a), third (b), and fourth (c) photonic band. As it can be seen, the resonant features have the same shape as the photonic bands, but they appear at higher frequencies than the corresponding bands. This shift in frequency (blue shift) is in agreement with our previous results reported in chapter 5, where it has been shown that the frequency of the resonant features is proportional to the modulus of the wavenumber (considering all in-plane and out-of-plane

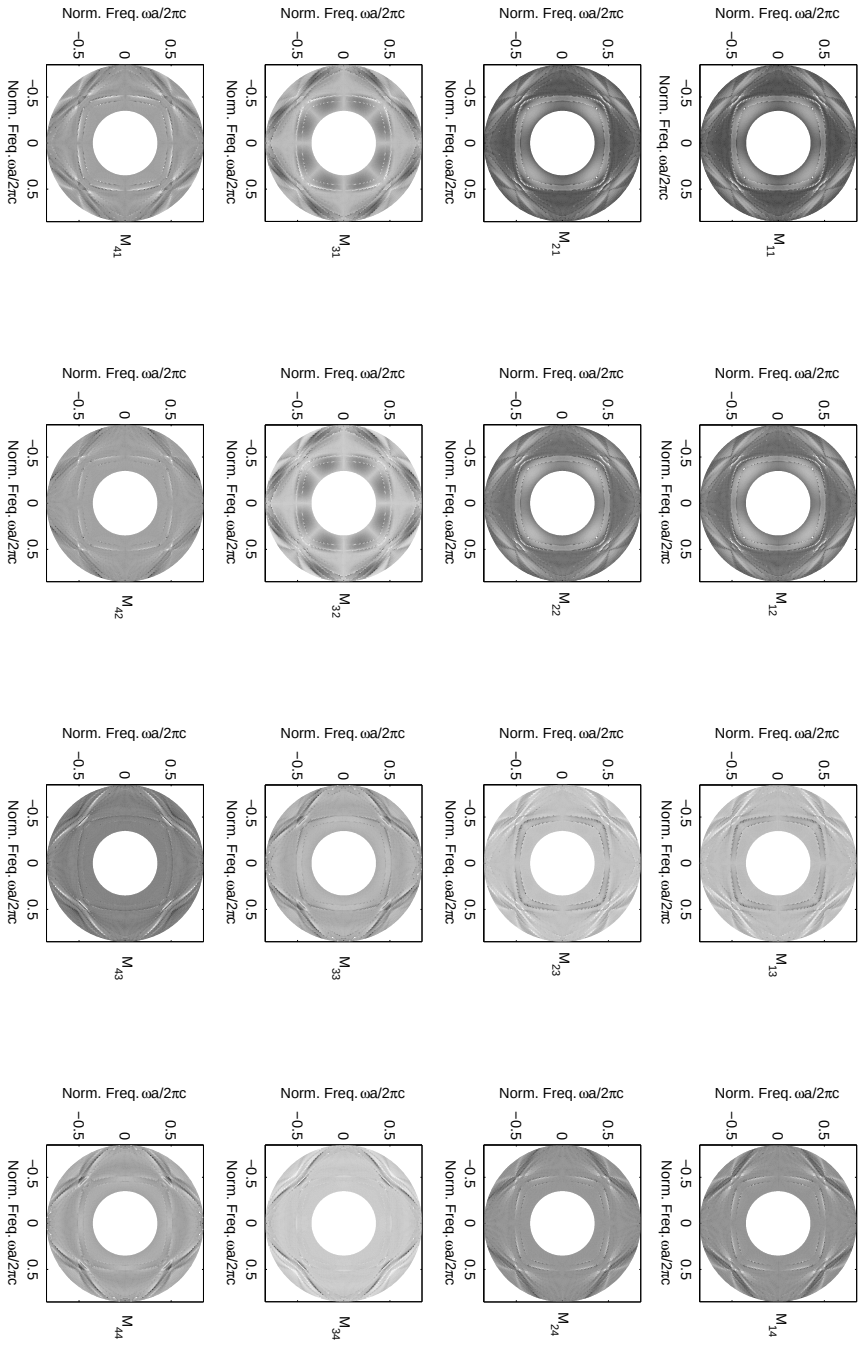

Figure 6.11: Angle-resolved polarimetry spectra of a photoresist PhC slab in terms of the Mueller matrix components. The components are plotted in polar coordinates where the distance to the center corresponds to the normalized frequency ($\omega a/2\pi c$) and the polar angle corresponds to the azimuth angle.

UNIVERSITAT ROVIRA I VIRGILI
DEVELOPMENT OF OPTICAL CHARACTERIZATION METHODS FOR MICRO- AND NANO-SCALE PLANAR PHOTONIC BAND GAP STRUCTURES
Zdenek Kral
DL: T-1537-2009/ISBN:978-84-692-4556-9

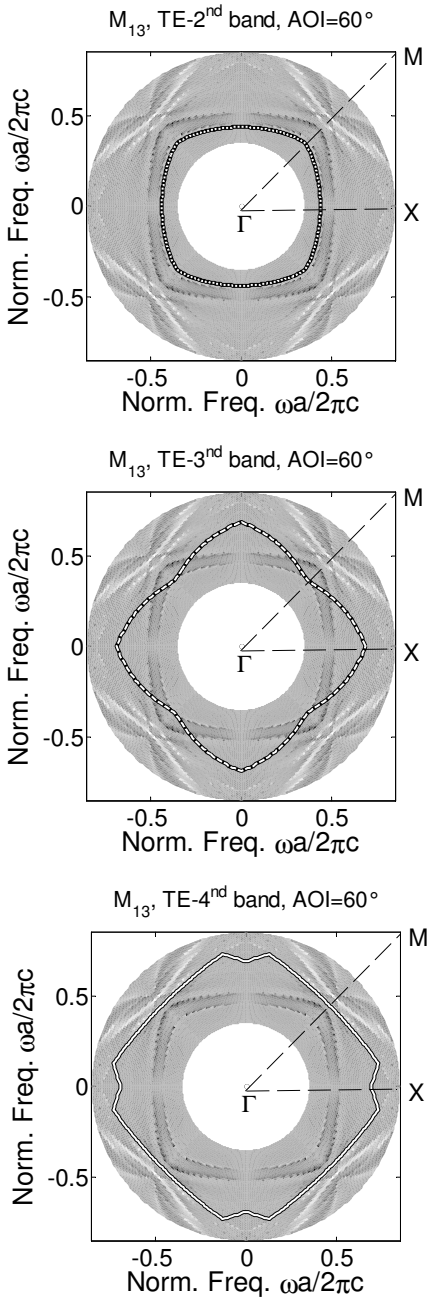

Figure 6.12: Detailed view of the selected Mueller matrix component M_{13} from figure 6.11. The three first photonic bands calculated for the ideal photonic crystal (Figure 6.10) are overlapped to the graphs. Each band is plotted in a separate graph: (a) M_{13} with the second photonic band (white dotted line), (b) M_{13} with the third photonic band (white dashed line), and (c) M_{13} with the fourth photonic band (white solid line). The main lattice directions of the square lattice structure (ΓX and ΓM) are indicated in the graphs.

components). The resonant features have nonzero q, and consequently their frequency is higher than the frequency of the corresponding photonic bands (with the same $k_{//}$ and q=0). Another characteristic of the spectra should be noted: for a given photonic band, there are several corresponding resonant features. This indicates that the incident beam couples to several modes in the PhC slab with different nonzero q values [Král 09].

6.5 Experimental measurements with ARSP

In this section we show the experimental measurements carried out with the Mueller matrix polarimeter MM16 [Garcia-Caurel 04] on the photoresist PhC slabs. We measure the polarimetry spectra with two different configurations of the MM16 polarimeter: i) with a fixed azimuth angle ϕ and variable angle of incidence θ and ii) with a fixed angle of incidence θ and variable azimuth angle ϕ. According to the theoretical study we represent the measured spectra in two separated subsections.

6.5.1 Measurement of ARSP at fixed azimuth angle

The polarimetry spectra were measured in the reflection mode at a fixed azimuth angle ϕ and for a range of angles of incidence θ starting from 45°to 71°, with a step of 2°. The photoresist PhC slab sample was placed in horizontal position on the sample holder, which is an electromechanically driven rotation plate with 1°azimuth resolution. The measurements were carried out in the visible spectral range (430-850 nm) at two fixed azimuth angles ϕ that correspond to the main lattice directions (ΓX and ΓM) of the photoresist PhC slab. Figure 6.13 shows an example of the obtained polarimetry spectra in the form of the Mueller matrix components. All the spectra are represented in the same gray scale to permit comparison between the different components. In order to study in more detail these measurements, we will focus the attention on one of the components of the Mueller matrix. Figure 6.14 shows the M_{34} component for measurements in two lattice directions: ΓX (figure 6.14a) and ΓM (figure 6.14b). The calculated TE and TM photonic bands of the corresponding 2D photonic crystal with a lattice constant a=450 nm are overlapped to the graphs.

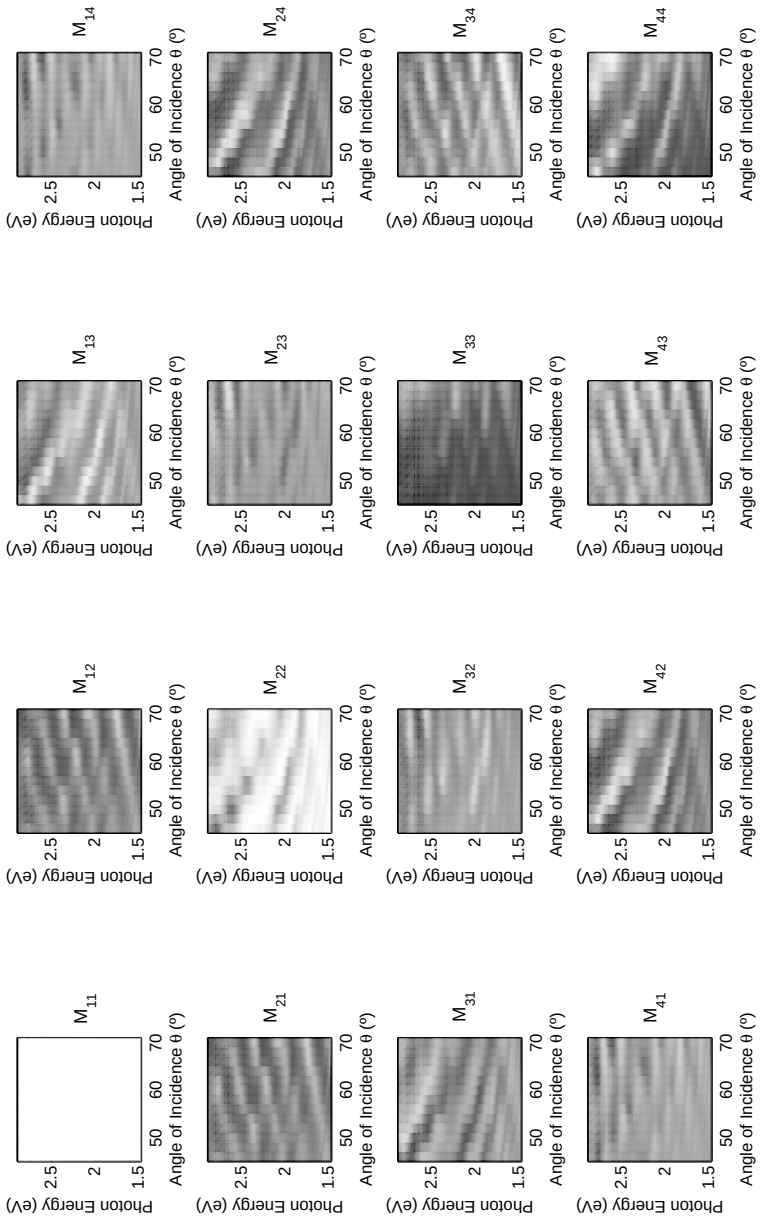

Figure 6.13: Angle-resolved polarimetry spectra of the photoresist PhC slab measured with the MM16 Mueller matrix polarimeter. The measurement was performed at the fixed azimuth angle ϕ that corresponds to the ΓX lattice direction of the sample and with variable angle of incidence θ, in the range from 45°to 71°. The polarimetry spectra are plotted as a function of the photon energy, and of the angle of incidence, θ.

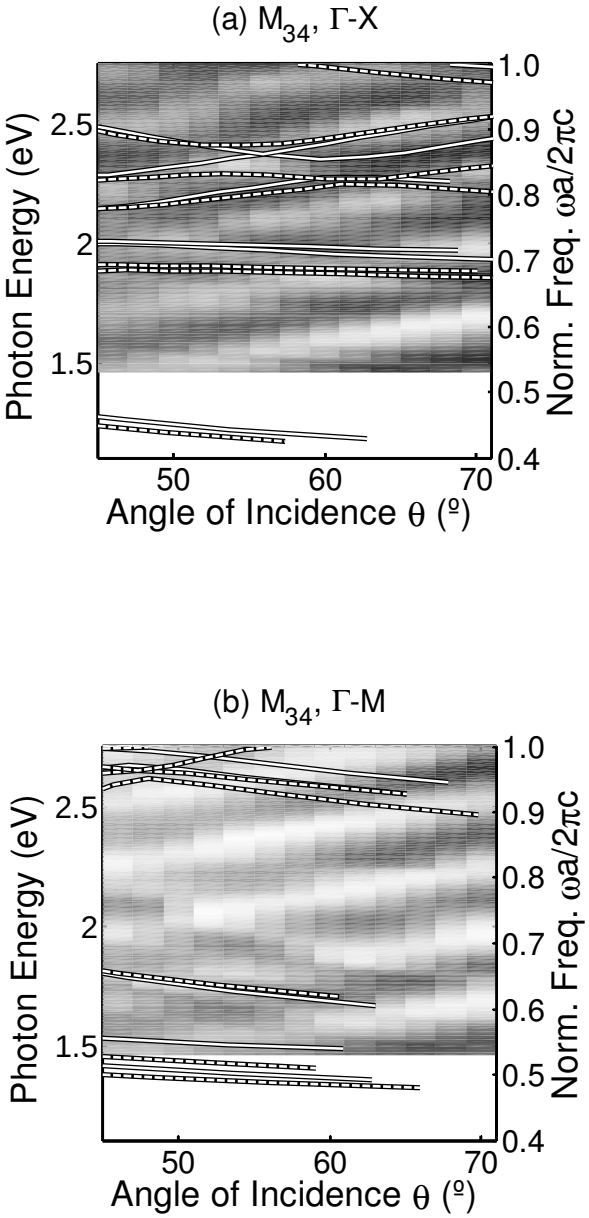

Figure 6.14: Detailed view of the selected Mueller matrix component M_{34} from figure 6.13. The calculated photonic bands for an ideal photonic crystal with the same characteristics as the sample (lattice constant a=450 nm) are overlapped to the graphs. The two graphs represent the measurements: (a) along ΓX and (b) ΓM lattice direction of the sample.

UNIVERSITAT ROVIRA I VIRGILI
DEVELOPMENT OF OPTICAL CHARACTERIZATION METHODS FOR MICRO- AND NANO-SCALE PLANAR PHOTONIC BAND GAP STRUCTURES
Zdenek Kral
DL: T-1537-2009/ISBN:978-84-692-4556-9

6.5.2 Measurement of ARSP at fixed angle of incidence

The second series of measurements was carried out in the reflectivity configuration with a fixed angle of incidence, θ. The angle-resolved polarimetry spectra on the photoresist PhC slab samples were measured as a function of the azimuth angle and at three different fixed angles of incidence, θ=50°, 60°, and 70°. The measurements were carried out in the visible spectral range (430-850 nm) and for azimuth angles ϕ between 0°to 180°with a step of 5°. It should be noted that the azimuth angle ϕ is defined with respect to the lattice orientation, thus 0°corresponds to the ΓX direction of the photoresist PhC slab square lattice. Figure 6.15 shows an example of the polarimetry spectra in the form of the Mueller matrix components at the angle of incidence θ=60°. As in section 6.4.2, the measurements are represented in polar coordinates, where the distance to the center correponds to the photon energy (or equivalently the light frequency) and the polar angle corresponds to the azimuth angle. With this, the lower limit of the photon energy for the data is 1.46 eV, while the upper limit is 2.76 eV.

In the figure 6.16 the M_{13} Mueller matrix component from figure 6.15 is shown with the aim to relate the resonant features with the corresponding photonic bands. The M_{13} is overlapped with the previously calculated TE photonic bands[5] (figure 6.10) of the corresponding 2D photonic crystal. On each graph with the M_{13} component, only one band is included in order to improve the recognition of the band-related features. Thus, figure 6.16a) corresponds to the second photonic band, 6.16b) to the third photonic band and 6.16c) to the fourth (the first photonic band is not represented as it lies below the light line).

[5]Only TE photonic bands are included in these graphs because, due to the small index contrast, TE and TM photonic bands are very similar. This similarity is even more evident in polar representation.

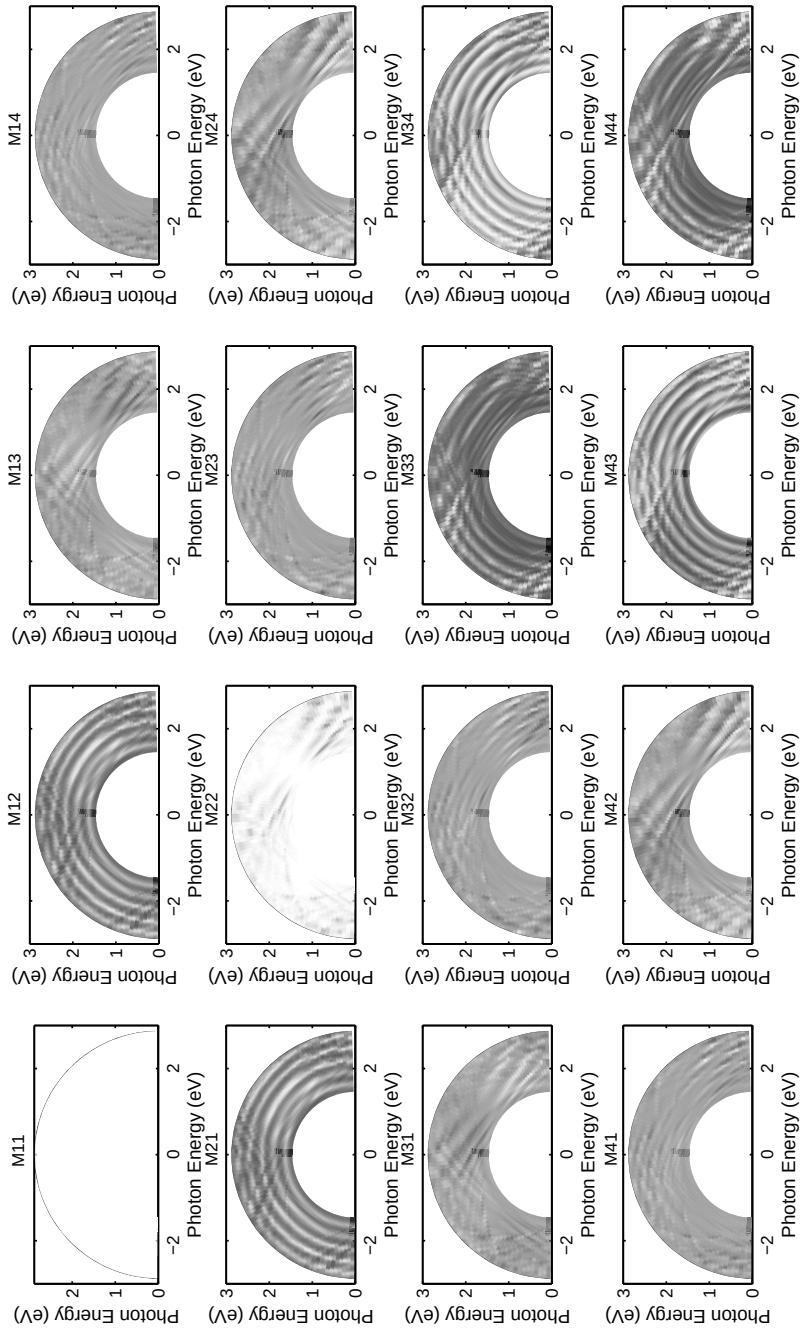

Figure 6.15: Angle-resolved polarimetry spectra of the photoresist PhC slab measured with the MM16 Mueller matrix polarimeter. The measurement for the angle of incidence (AOI) θ=60°, in the range of azimuth angles from 0°to 180°was performed by rotating the optic axis with respect to the plane of incidence. The polarimetry spectra are plotted in polar coordinates, where the distance to the center corresponds to the photon energy and the polar angle corresponds to the azimuth angle, ϕ.

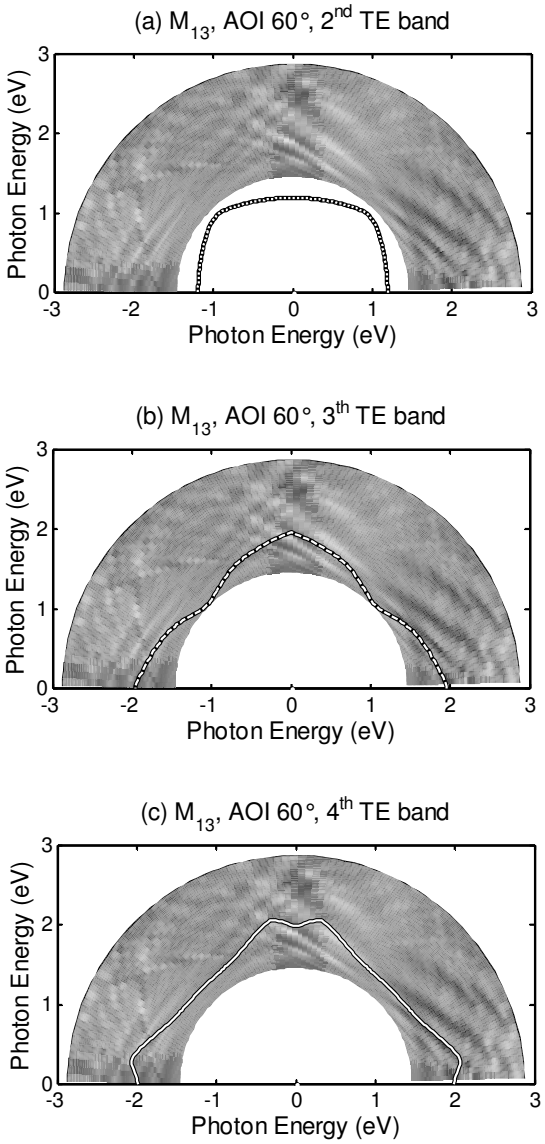

Figure 6.16: Detailed view of the selected Mueller matrix component M_{13} from figure 6.15. The calculated TE photonic bands corresponding to the ideal 2D photonic crystal are overlapped to the graphs. Each band is plotted in a separate graph: (a) M_{13} with the second TE photonic band (white dotted line), (b) M_{13} with the third TE photonic band (white dashed line), and (c) M_{13} with the fourth TE photonic band (white solid line).

6.6 Discussion and conclusions

In this chapter we have presented an alternative approach to study the photonic bands and photonic modes in photonic crystal slabs by Angle-Resolved Spectroscopic Polarimetry (ARSP). We have first studied the viability of the polarimetry technique for the characterization of such materials with numerical simulations. To this end, we have implemented a numerical algorithm based on the S-matrix formalism introduced in chapter 2 to calculate the polarization changes upon reflection on the photonic structure. With this we are able to identify the coupling of the incident light into photonic modes related to the TE-TM photonic bands. The calculations are used then to predict the results of measurements with Mueller matrix polarimetry, which involves the complete polarimetric description of the light by real four-dimensional Stokes vectors and the polarization changes with 4×4 Mueller matrices. Following these methodology we have studied photoresist PhC slab samples with a series of experimental measurements carried out with the MM16 Mueller matrix polarimeter. The following figures compare the calculation results with the experimental measurements on the photoresist PhC slab sample.

Figure 6.17 compares the calculated (a) and the measured (b) polarimetry spectra for the fixed azimuth angle ϕ[6] and variable angle of incidence θ. Looking at the spectra (b), two stripes (resonant features) that may correspond to a replica of the first band (which is out of the measurement range) can be recognized. These features are predicted by the S-matrix calculation shown in spectra (a). However, it is difficult to recognize them since the features are overlapped with clearly visible Fabry-Pérot oscillations (periodic black and white stripes). These oscillation are due to light interferences on the interfaces of the photoresist layer. In order to improve the recognition of resonant features in these spectra, a post-processing of the data obtained from the polarimetry measurements could be useful. In contrast with the post-processing procedure introduced on chapter 5, where a post-processing was necessary to filter out features in the spectra related to material resonances in the IR, in this case the Fabry-Pérot oscillations could be filtered out. To achieve this filtering, the Fabry-Pérot oscillations can be fitted

[6]the azimuth angle ϕ is defined with respect to the ΓX lattice orientation of the square lattice.

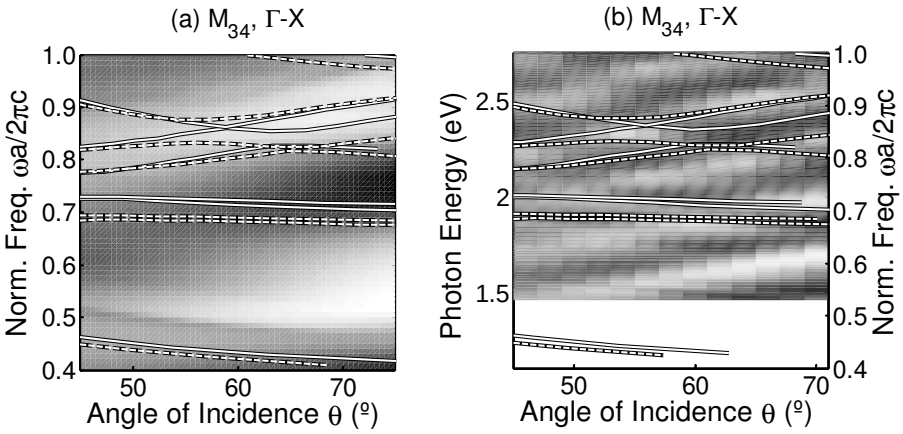

Figure 6.17: Comparison of calculated (a) and measured (b) angle-resolved polarimetry spectra. The two graphs show polarimetry spectra for fixed azimuth angle ϕ and variable angle of incidence θ. The spectra correspond to the Mueller matrix component M_{34}. Graph (a) shows the M_{34} from the Mueller matrix in figure 6.7, while graph (b) shows the M_{34} from figure 6.13. The calculated TE and TM photonic bands that correspond to an ideal 2D photonic crystal (infinite in z direction) are overlapped to the graphs. The graphs are represented with the same gray scale.

using a model of a uniform layer on the substrate with an effective index, and then they can be subtracted from the measured spectrum.

Figure 6.18 illustrates the results corresponding to calculations and measurements with a fixed angle of incidence θ and variable azimuth angle ϕ. The calculated spectra (a, and b) of the selected M_{13} component (from figure 6.11) exhibit clear resonances related to the 2^{nd}, 3^{th}, and 4^{th} (TE or TM) photonic band. The measured spectra (c, and d) represented also with the M_{13} component (from figure 6.15) show some resonances, mainly related to the 4^{th} band (Solid line). It is difficult, however, to distinguish between TM and TE bands. The reason of such similarity is due to the very small refractive index contrast of the slab material. Probably, photonic crystals with a higher refractive index contrast would show a better separation between resonances for TE and TM bands.

It is also interesting to note that the resonance feature related to the 4^{th} band shifts to smaller frequencies as the angle of incidence increases. This can be seen in figure 6.19, where the polarimetry spectra for variable azimuth angle ϕ measured at three different angles of incidence θ= 50°, 60°, and 70°are shown. The resonant feature appears at frequencies higher than that of the 4^{th} photonic band, and with increasing angle of incidence, the

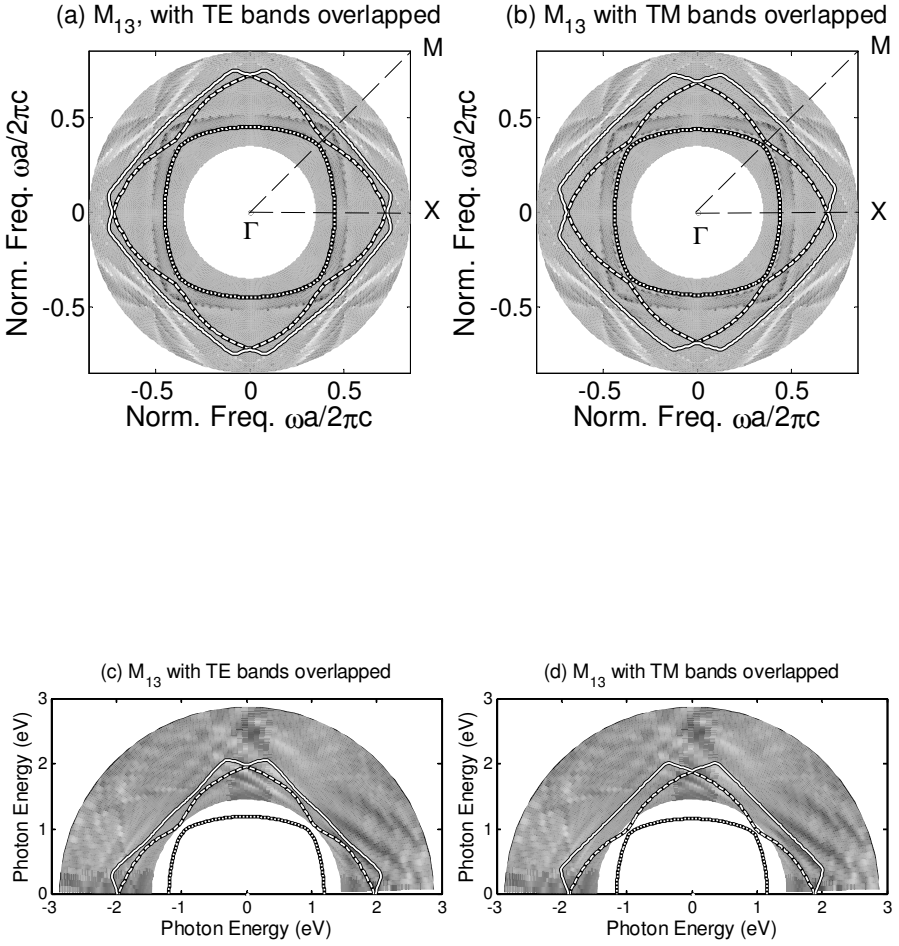

Figure 6.18: Comparison of calculated (a, and b), and measured (c, and d) angle-resolved polarimetry spectra, for fixed angle of incidence (AOI) θ=60°and variable azimuth angle ϕ. The spectra are plotted in polar coordinates, where the distance to the center corresponds to the normalized frequency (graphs a and b) or to the photon energy (c and d). The polar angle corresponds to the azimuth angle. The component M_{13} of the Mueller matrix is shown. The photonic bands for the corresponding ideal photonic crystal with lattice constant a=450 nm are overlapped to the graphs. The dotted line corresponds to the 2^{nd} photonic band, the dashed line to the 3^{th} and the solid line to the 4^{th}.

photonic band and the related feature shift to lower values. Furthermore, there are other resonant features in each spectrum with the same shape than the one corresponding to the 4^{th} photonic band, but appear at lower frequencies. These are replicas of the resonant feature corresponding to the 4^{th} photonic band, but in contrast with the replicas of resonant features observed in silicon PhC slab, these appear at smaller frequencies. This fact indicates that these replicas are not due to the coupling to modes related to this 4^{th} photonic band that propagate at different angles with respect to the PhC slab surface. Moreover, the replicas appear along the ΓM direction of the photonic lattice, which is the direction of the modulation in pore size and lattice constant of the photoresist PhC slab. For these reasons, these replicas can be explained as higher diffraction orders caused by the modulation.

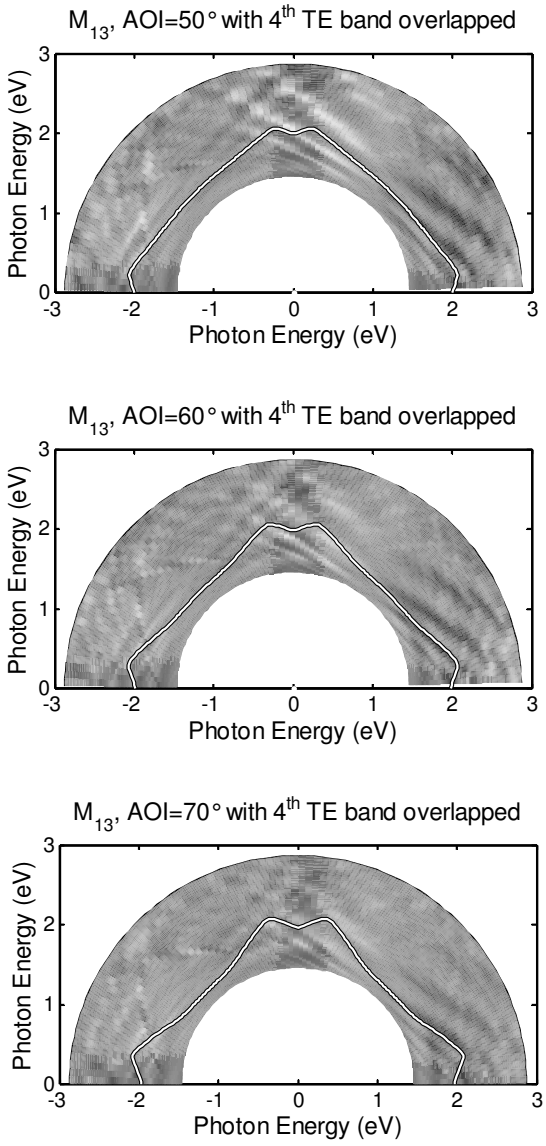

Figure 6.19: Angle-resolved polarimetry spectra measured for three different angles of incidence (AOI) θ and variable azimuth angle ϕ. The M_{13} component of the Mueller matrix is shown in polar coordinates. The 4^{th} TE band of the corresponding ideal 2D photonic crystal (infinite in z direction) is overlapped to each graph in order to relate the resonance features with this band.

UNIVERSITAT ROVIRA I VIRGILI
DEVELOPMENT OF OPTICAL CHARACTERIZATION METHODS FOR MICRO- AND NANO-SCALE PLANAR PHOTONIC BAND GAP STRUCTURES
Zdenek Kral
DL: T-1537-2009/ISBN:978-84-692-4556-9

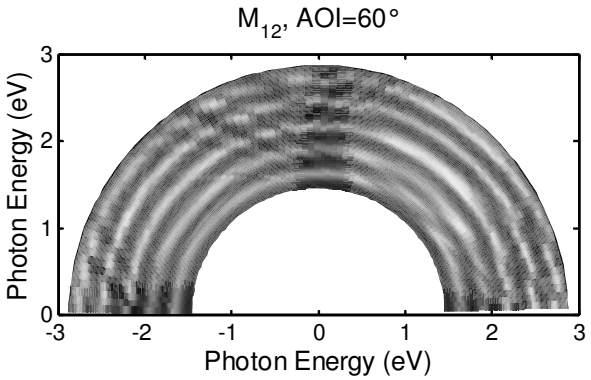

Figure 6.20: Angle-resolved polarimetry spectra measured for fixed angle of incidence (AOI) θ=60°and variable azimuth angle ϕ. The M_{12} component of the Mueller matrix is shown in polar coordinates. The black and white semicircular stripes in the spectra are the characteristic Fabry-Pérot resonances.

Finally, figure 6.20 shows an example of the M_{12} component with measured spectrum, which is very sensitive to the thickness of the photoresist layer, and shows clear Fabry-Pérot oscillations that overlap any other feature that could be related with coupling to the photonic modes.

UNIVERSITAT ROVIRA I VIRGILI
DEVELOPMENT OF OPTICAL CHARACTERIZATION METHODS FOR MICRO- AND NANO-SCALE PLANAR PHOTONIC BAND GAP STRUCTURES
Zdenek Kral
DL: T-1537-2009/ISBN:978-84-692-4556-9

UNIVERSITAT ROVIRA I VIRGILI
DEVELOPMENT OF OPTICAL CHARACTERIZATION METHODS FOR MICRO- AND NANO-SCALE PLANAR PHOTONIC BAND GAP STRUCTURES
Zdenek Kral
DL: T-1537-2009/ISBN:978-84-692-4556-9

Chapter 7

Summary and conclusions

The characterization of photonic band gap materials (Photonic Crystals) is a fundamental issue in the development of the technologies for their fabrication and future application. This Doctoral Thesis has dealt with the development of optical characterization methods and their implementation to planar photonic structures. According to the objectives established in the present work we have obtained several results that are concluded in the following paragraphs:

In Chapter 3, we have developed an experimental technique based on the Bragg diffraction in the near and middle infra red (IR) spectral range to determine the lattice properties of planar photonic structures.

- We have adapted a commercial FTIR spectrometer equipped with a special reflectivity attachment to measure the Bragg diffraction spectra.

- We have investigated the lattice characteristics of several photonic planar structures based on different materials and obtained fabrication methods. More concisely, we measured Bragg diffraction spectra of: (a) 2D PhC slabs consisting of a periodic array of square air holes in a crystalline silicon background, (b) 1D photonic crystal (diffraction grating) based on the non-linear optical material $RbTiOPO_4$ (RTP), fabricated by a microstructuration of the sample surface using ultrafast laser ablation, and (c) 1D photonic crystal (diffraction grating)

based on non-linear optical material called $LiNbO_3$ (LN), and fabricated using selective etching of ferroelectric domains.

- The resulting Bragg diffraction spectra, obtained from the FTIR spectrometer showed several diffraction peaks (the intensity maxima) at frequencies increasing with the diffraction angle θ. In order to extract the information about the lattice constant of the particular sample, we have developed a post-processing procedure consisting of several steps: (i) apply a smoothing of each spectrum to reduce noise (the smoothing is calculated by averaging, for each measured wavelength, the diffracted intensity for a range of neighboring wavelengths) (ii) flattening the intensity as a function of the angle of incidence θ for a fixed wavelength. The flattening consists of fitting the intensity as a function of the angle of incidence (for each measured wavelength λ) to a straight line and subtracting the resulting straight line from the data, and (iii) fitting the flattened data with a Gaussian function of two variables, the wavelength λ and the sinus of the diffraction angle θ. The fitting functions depend on several adjustable parameters that are related to the lattice constant and to the spread of the diffraction peaks. With this method, we determined the lattice constants of the samples mentioned above and we compared the values with the estimation by an optical microscope. A good agreement with the theoretical model and the measured data has been obtained.

In Chapter 4, we have applied the Angular-Dependent Reflectance Spectroscopy technique (ADRS) to the characterization of photonic bands in PhC slabs. The objective was the implementation of the technique to our samples with lattice parameters that require the measurement to be carried out in the mid-IR spectral range.

- To this end, we have adapted the FTIR equipment to the angular-dependent reflectivity measurements.

- We measured the ADR spectra of different types of samples with different lattice configurations (e.g. PhC slabs based on macroporous silicon or photoresist, with square or triangular lattices, different values of the lattice constant and different sizes of the holes/scatterers).

- To explain correctly the measurement results, we have implemented

a numerical method to simulate the interaction of the incident light with the PhC slab and thus to compute the ADR spectra. From the calculations we have observed that for a given photonic band of the ideal 2D photonic crystal structure (infinite in the third dimension), the incident light can couple to several modes in the PhC slab (with a finite thickness). This coupling is recognized in the spectra as resonant features consisting of maxima, minima or inflections on the reflectance. The modes in the PhC slab correspond to states with the same wavevector component parallel to the slab surface as the corresponding photonic band, but with different values of the out-of-plane wavevector component. Thus, this can be interpreted as modes that propagate at different angles with respect to the slab surface. Furthermore, the number of these modes increases with increasing thickness of the slab. The calculations also predicted oscillations in the ADR spectra corresponding to Fabry-Pérot interferences between the waves reflected at the interfaces of the PhC slab.

- Finally, we compared the calculation results with the ADRS measurements. It has been observed that in the mid-IR spectral range the recognition of the photonic band-related resonant features in the measured spectra is particularly difficult. For this reason it has been necessary to develop a procedure to post-process the measured data. The procedure consisted in three steps: first, filtering out the resonances in the IR spectra due to material characteristics. These resonances do no depend on the angle of incidence, but only on the light frequency (wavenumber). On the contrary, photonic band-related features depend both on the wavenumber and on the angle of incidence. Consequently, the filtering is carried out by computing the partial derivative of the reflectance spectra with respect to the angle of incidence. With this, only photonic band-related features remain on the spectra. The second step is to represent the spectra in a 2D plot as a function of the wavenumber and of the angle of incidence, together with the photonic bands calculated for the corresponding photonic crystal. Finally, the photonic band-related features recognition is improved by limiting the range of wavenumbers in the 2D representation. With this method it has been shown that the angular-dependent measurement of spectra and the adequate post-processing of the measured data, when neces-

sary, are fundamental tools in the optical characterization of photonic crystals.

In Chapter 5, we focused on another optical technique to characterize the planar photonic structures, the Angle-Resolved Spectroscopic Polarimetry (ARSP).

- First, the viability of the polarimetry technique for the optical characterization of photonic planar structures has been studied. The study focused on two kinds of structures: i) quasi-ordered nanoporous alumina PhC slabs, fabricated by anodization of aluminum and ii) nanostructured photoresist PhC slabs produced with the laser interference lithography (LIL). To this end, a numerical method based on the S-matrix formalism to calculate the polarization changes upon reflection on the photonic structure has been implemented. This method has permitted to identify the photonic modes related to the TE and TM photonic bands. These samples were chosen because their lattice constants and optical properties produce photonic bands in the visible range, which corresponds to the spectral range of the instrument used in this investigation: the MM16 Mueller polarimeter.

- Two approaches for the optical characterization of planar photonic structures with the ARSP have been considered: (i) with a fixed azimuth angle ϕ and variable angle of incidence θ and (ii) with a fixed angle of incidence θ and variable azimuth angle ϕ.

- The calculations revealed that for a given photonic band of the infinite photonic crystal, the incident light can couple to several modes in the PhC slab related to such photonic band. These modes correspond to waves that propagate at different angles with respect to the sample surface. Furthermore, the number of these modes increases with increasing thickness of the slab. The spectra also show periodic oscillations with the wavelength related to Fabry-Pérot interferences of waves reflected at the interfaces of the PhC slabs. It has also been demonstrated that for PhC slabs based on nanoporous alumina, with a triangular lattice, the off-diagonal components of the Jones Matrix show a certain amount of cross-polarization, but with the same characteristics as the diagonal components. Instead, for PhC slabs with

a square lattice based on nanostructured photoresist samples, there is no cross-polarization.

- We measured the spectra of the nanostructured photoresist slabs using the MM16 Mueller polarimeter: (i) with a fixed azimuth angle ϕ and variable angle of incidence θ and (ii) with a fixed angle of incidence θ and variable azimuth angle ϕ.

- The polarimetry spectra measured with a fixed azimuth angle ϕ and variable angle of incidence θ show resonant features in some of the Mueller matrix components that may correspond to photonic-band-related resonant coupling, in agreement with the S-matrix calculation. However, recognition of these features is difficult due to the presence of the Fabry-Pérot oscillations. An adequate post-processing would be required to compensate these oscillations and thus improve the recognition of the photonic band-related resonant features.

- The polarimetry spectra measured with a fixed angle of incidence θ and variable azimuth angle ϕ permits to identify the main lattice directions on the sample. The measurements demonstrated that all the Mueller matrix components are sensitive to the photonic modes related with the photonic bands. The spectra show resonant features related to photonic bands, however, its recognition is difficult because of two factors: i) the presence of Fabry-Pérot oscillations and ii) the replication of the features due to diffraction caused by modulation of the interpore distance in the sample.

UNIVERSITAT ROVIRA I VIRGILI
DEVELOPMENT OF OPTICAL CHARACTERIZATION METHODS FOR MICRO- AND NANO-SCALE PLANAR PHOTONIC BAND GAP STRUCTURES
Zdenek Kral
DL: T-1537-2009/ISBN:978-84-692-4556-9

Resumen y conclusiones

La caracterización de materiales de gap fotónico (cristales fotónicos) es un aspecto fundamental en el desarrollo de las tecnologías para su fabricación y su futura utilización. Esta tesis doctoral se ha ocupado del desarrollo de métodos ópticos de caracterización, así como de su implementación en estructuras fotónicas planares, también conocidas como láminas de cristal fotónico (photonic cristal slabs). De acuerdo con los objetivos fijados para el presente trabajo, hemos obtenido varios resultados, los cuales se resumen en los párrafos siguientes:

Se ha desarrollado una técnica experimental basada en la difracción de Bragg en el rango espectral de la radiación infrarroja (IR) cercana y media, para determinar las propiedades de varias estructuras fotónicas planas.

- Hemos adaptado un espectrómetro comercial FTIR equipado con un accesorio de medida de reflectividad para diferentes ángulos de incidencia para medir el espectro de difracción de Bragg.

- Hemos investigado las características de varias estructuras fotónicas planares, obtenidas a partir de diferentes materiales y métodos de fabricación. Concretamente, hemos medido y interpretado los espectros de difracción de Bragg de: a) láminas de cristal fotónico 2D con una disposición periódica de agujeros de aire cuadrados formados en una base de silicio cristalino, b) cristal fotónico 1D (red de difracción) basado en el material óptico no lineal RbTiOPO (RTP), fabricado mediante micro-estructuración de la muestra utilizando ablación láser ultra-rápida, y c) cristal fotónico 1D (red de difracción) basado en un material óptico no lineal llamado $LiNbO_3$ (LN), y fabricado mediante ataque químico selectivo de los dominios ferroeléctricos.

- Los espectros de difracción de Bragg obtenidos del espectroscopio FTIR, muestran máximos de difracción cuya longitud de onda se desplaza al ángulo de difracción (θ). Con el fin de obtener la información sobre el parámetro de red de una muestra en concreto, se ha desarrollado un postprocesado de los datos experimentales. El procesado implica diversos pasos: el primero es un suavizado del espectro para reducir el ruido. Esto se consigue mediante un promedio de los valores alrededor de cada longitud de onda medida. El segundo es la elimi-

nación de la tendencia decreciente de la intensidad de la difracción con el ángulo de difracción (θ). Para ello, para cada longitud de onda del espectro (λ), se ajusta la intensidad en función del seno del ángulo a una recta y se substrae esta la recta obtenida de los datos. Finalmente, el tercer paso es el ajuste de los datos obtenidos a una función Gaussiana con dos variables, (λ) y $\sin(\theta)$, que modeliza el comportamiento ideal de la difracción de la muestra. La función depende de un conjunto de parámetros que describen la geometría de la muestra y que se determinan mediante el ajuste. Este método ha permitido investigar los parámetros de red de las muestras mencionadas anteriormente y comparar los valores con la estimación efectuada por un microscopio óptico. Con todo ello se puede apreciar una buena concordancia entre el modelo teórico y las medidas efectuadas.

Se ha aplicado la técnica de la espectroscopia de reflectometría en ángulo variable (Angular-Dependent Reflectance Spectroscopy, ADRS) a la caracterización de bandas fotónicas en láminas de cristal fotónico. El objetivo ha sido la implementación de la técnica a las muestras fabricadas en el marco del grupo NePhoS de la Universitat Rovira i Virgili. Estas muestras tienen parámetros de red que requieren llevar a cabo una medición en un rango espectral del infrarojo (IR) medio.

- Con esta finalidad hemos adaptado el equipo FTIR a las medidas de ADRS usando el accesorio de reflectancia de ángulo de incidencia y de colección variables. Con esta técnica se pueden reconocer en los espectros características resonantes relacionadas con las bandas del cristal fotónico.

- Hemos medido los espectros ADRS de varios tipos de muestras con distintos parámetros de red (por ejemplo, láminas de cristal fotónico basados en silicio macroporoso o en resina fotosensible nanoestrucutrada, con redes de estructura cuadrada o triangular y de distintos tamaños).

- Para poder explicar correctamente los resultados de medición, hemos desarrollado un método que simula la interacción de la luz incidente con las láminas de cristal fotónico y, de ese modo, permite calcular los espectros de ADRS. Los cálculos demuestran que la luz en las láminas

de cristal fotónico se propaga en modos que tienen el mismo vector de onda paralelo que las bandas del cristal fotónico 2D infinito, pero tienen además componentes de vector de onda no nulos en la tercera dimensión. Además, también muestran cómo para un determinado ángulo de incidencia de la luz, ésta se acopla a varios de estos modos, y que el número de modos al que se acopla varia con el grosor de la lámina. Los cálculos de los espectros ADRS también predicen oscilaciones en los espectros ADRS que corresponden a interferencias Fabry-Pérot entre las interfases de la lámina de cristal fotnico.

- Finalmente, hemos comparado los resultados de cálculo con las medidas de ADRS. De esta comparación se puede concluir que en el rango espectral del IR-medio el reconocimiento de características resonantes en el espectro relacionadas con los modos de la lámina fotónica y con las bandas fotónicas es particularmente difícil y es necesario desarrollar un procedimiento de postprocesado de los datos obtenidos de las medidas. El procedimiento ha consistido en el análisis de espectros de ADRS mediante el cálculo de la derivada parcial respecto del ángulo de incidencia. Así, se aumenta la visibilidad de las características resonantes relacionadas con bandas fotónicas mientras que se filtran otras características relacionadas con el material y con ruido de la medida, ya que estas últimas son constantes con el ángulo de incidencia. Además, se representa esta derivada parcial en una gráfica 2D en función del vector de onda paralelo a la superficie de muestras y la frecuencia, junto con las bandas fotónicas calculadas. Al superponer las bandas fotónicas se pueden reconocer con más facilidad las características resonantes. Finalmente, también se comprueba que reduciendo el rango de frecuencias representadas en la gráfica 2D, la visibilidad de las propiedades resonantes aumenta notablemente.

Finalmente, se ha desarrollado otra técnica óptica para caracterizar estructuras fotónicas planas: la polarimetría espectroscópica de ángulo variable.

- Primero, se ha estudiado la viabilidad de la técnica de la polarimetría para la caracterización de i) láminas de cristal fotónico quasi-ordenado basadas en alúmina nanoporosa (fabricadas por anodización electroquímica

de aluminio) y ii) láminas de cristal fotónico basadas en resina fotosensible nanoestructurada sobre silicio (producidas mediante litografía de interferencia láser). Con este propósito, se ha desarrollado un método numérico para calcular los cambios de polarización producidos al reflejarse luz en las estructuras fotónicas. Tal método permite comprobar si en los espectros de polarimetría dependiente del ángulo se pueden identificar características resonantes relacionadas con modos fotónicos y bandas fotónicas.

- Para la técnica de la polarimetría se ha tomado en consideración dos tipos de espectros en función del ángulo: i) con un ángulo de acimut fijo (ϕ) y ángulo de incidencia variable (θ) y ii) con un ángulo de incidencia fijo (θ) y ángulo acimut variable (ϕ).

- Los cálculos resultantes han puesto de manifiesto que los espectros de polarimetría muestran características resonantes relacionadas con el acoplamiento de la luz incidente con modos de la lámina de cristal fotónico. Esto se observa tanto para la polarimetría con azimut fijo (ϕ) como para la polarimetría con ángulo de incidencia fijo (θ). Además, tal y como ocurre con la espectroscopía de reflexión, también se observa el acoplamiento de la luz incidentes a varios modos relacionados con una misma banda fotónica, aunque con diferente componente z del vector de onda. Asimismo, el número de modos aumenta con el incremento de grosor de la lámina. Los espectros también muestran oscilaciones periódicas con la longitud de onda, en relación con las interferencias Fabry-Pérot en la lámina de cristal fotónico. Se ha comprobado que para las muestras de cristal fotónico basado en alúmina nanoporosa con una red triangular, los componentes no-diagonales de la matriz de Jones muestran una cierta cantidad de polarización cruzada. Contrariamente, no se manifiesta polarización cruzada para las muestras de lámina de cristal fotónico basado en resina fotosensible nanoestructurada con red cuadrada.

- Se han medido espectros de láminas de cristal fotónico basado en resina fotosensible nanoestructurada utilizando un polarímetro MM16, que permite medir todas las componentes de la matriz de Mueller: i) con un ángulo de azimut fijo (ϕ) y ángulo variable de incidencia (θ) y ii) con un ángulo fijo de incidencia (θ) y ángulo azimut variable (ϕ).

- Los espectros de polarimetría medidos con un ángulo fijo de incidencia (θ) y ángulo de azimut variable (ϕ) han demostrado que todas las componentes de la matriz de Mueller son sensibles al acoplamiento de la luz incidente con los modos fotónicos (relacionados con las bandas fotónicas). Sin embargo, la distinción entre los modos fotónicos TM y TE no es posible para las muestras estudiadas, debido al pequeño contraste de los índices de refracción entre el material de base del cristal fotónico (alúmina o resina fotosensible) y el material de los centros dispersores (aire).

UNIVERSITAT ROVIRA I VIRGILI
DEVELOPMENT OF OPTICAL CHARACTERIZATION METHODS FOR MICRO- AND NANO-SCALE PLANAR PHOTONIC BAND GAP STRUCTURES
Zdenek Kral
DL: T-1537-2009/ISBN:978-84-692-4556-9

UNIVERSITAT ROVIRA I VIRGILI
DEVELOPMENT OF OPTICAL CHARACTERIZATION METHODS FOR MICRO- AND NANO-SCALE PLANAR PHOTONIC BAND GAP STRUCTURES
Zdenek Kral
DL: T-1537-2009/ISBN:978-84-692-4556-9

Bibliography

[Agio 00] M. Agio & L. C. Andreani. *Complete photonic band gap in a two-dimensional chessboard lattice.* Physical Review B, vol. 61, no. 23, pages 15519–15522, 2000.

[Alija 07] A. R. Alija, L. J. Martinez, P. A. Postigo, J. Sanchez-Dehesa, M. Galli, A. Politi, M. Patrini, L. C. Andreani, C. Seassal & P. Viktorovitch. *Theoretical and experimental study of the Suzuki-phase photonic crystal lattice by angle-resolved photoluminescence spectroscopy.* Optics Express, vol. 15, no. 2, pages 704–713, 2007.

[Anderson 96] C. M. Anderson & K. P. Giapis. *Larger two-dimensional photonic band gaps.* Physical Review Letters, vol. 77, page 2949, 1996.

[Andreani 03] L. C. Andreani, M. Agio, D. Bajoni, M. Belotti, M. Galli, G. Guizzetti, A. M. Malvezzi, F. Marabelli, M. Patrini & G. Vecchi. *Optical properties and photonic mode dispersion in two-dimensional and waveguide-embedded photonic crystals.* Synthetic Metals, vol. 139, no. 3, pages 695–700, 2003.

[Arwin 08] H. Arwin, M. Poksinski & K. Johansen. *Enhancement in ellipsometric thin film sensitivity near surface plasmon resonance conditions.* Physica Status Solidi A, vol. 205, no. 4, pages 817–820, 2008.

[Ashcroft 76] N. W. Ashcroft & N. D. Mermin. Solid state physics. Saunders Collage, Philadelphia, USA, 1976.

[Aspnes 04] D. E. Aspnes. *Expanding horizons: new developments in ellipsometry and polarimetry.* Thin Solid Films, vol. 455-456, pages 3–13, 2004.

[Astratov 97] V. N. Astratov, O. Z. Karimov, Y. A. Vlasov, E. Mao, S. Dickey, B. W. Kim & A. Majerfeld. *Spectroscopy studies of p-type GaAs/AlGaAs MQWs heavily doped with carbon.* Compound Semiconductors 1996, no. 155, pages 1001–1004, 1997.

[Astratov 98] V. N. Astratov, M. S. Skolnick, S. Brand, T. F. Krauss, O. Z. Karimov, R. M. Stevenson, D. M. Whittaker, I. Culshaw & R. M. De la Rue. *Experimental technique to determine the band structure of two-dimensional photonic lattices.* IEE Proceedings-Optoelectronics, vol. 145, no. 6, pages 398–402, 1998.

[Astratov 99a] V. N. Astratov, I. S. Culshaw, R. M. Stevenson, D. M. Whittaker, M. S. Skolnick, T. F. Krauss & R. M. De la Rue. *Resonant coupling of near-infrared radiation to photonic band structure waveguides.* Journal of Lightwave Technology, vol. 17, no. 11, pages 2050–2057, 1999.

[Astratov 99b] V. N. Astratov, D. M. Whittaker, I. S. Culshaw, R. M. Stevenson, M. S. Skolnick, T. F. Krauss & R. M. De La Rue. *Photonic band-structure effects in the reflectivity of periodically patterned waveguides.* Physical Review B, vol. 60, no. 24, pages 16255–16258, 1999.

[Astratov 00a] V. N. Astratov, R. M. Stevenson, I. S. Culshaw, D. M. Whittaker, M. S. Skolnick, T. F. Krauss & R. M. De la Rue. *Reflectivity studies of photonic band structure effects in two-dimensional air/semiconductor lattices.* Physica Status Solidi A-Applied Research, vol. 178, no. 1, pages 565–569, 2000.

[Astratov 00b] V. N. Astratov, R. M. Stevenson, I. S. Culshaw, D. M. Whittaker, M. S. Skolnick, T. F. Krauss & R. M. De La

Rue. *Heavy photon dispersions in photonic crystal waveguides.* Applied Physics Letters, vol. 77, no. 2, pages 178–180, 2000.

[Azzam 76] R. M. A. Azzam. *A perspective on ellipsometry.* Surface science, vol. 56, pages 6–18, 1976.

[Azzam 77] R. M. A. Azzam & N. M. Bashara. Ellipsometry and polarized light. North Holland, Amsterdam, 1977.

[Baba 95] T. Baba & T. Matsuzaki. *Theoretical calculation of photonic gap in semiconductor 2-dimensional photonic crystals with various shapes of optical atoms.* Japanese Journal of Applied Physics, vol. 34, page 4496, 1995.

[Baba 99] T. Baba, N. Fukaya & J. Yonekura. *Observation of light propagation in photonic crystal optical waveguides with bends.* Electronics Letters, vol. 35, page 654, 1999.

[Belotti 06a] M. Belotti, J. Torres, E. Roy, A. Pepin, Y. Chen, D. Gerace, L. C. Andreani & M. Galli. *Replication of photonic crystals by soft ultraviolet-nanoimprint lithography.* Journal of Applied Physics, vol. 99, no. 2, page 024309, 2006.

[Belotti 06b] M. Belotti, J. Torres, E. Roy, A. Pepin, D. Gerace, L. C. Andreani, M. Galli & Y. Chen. *Fabrication of SOI photonic crystal slabs by soft UV-nanoimprint lithography.* Microelectronic Engineering, vol. 83, no. 4-9, pages 1773–1777, 2006.

[Berger 97] V. Berger, O. Gauthier-Lafaye & E. Costard. *Fabrication of a 2D photonic bandgap by a holographic method.* Electronics letters, vol. 33, no. 5, page 425, 1997.

[Bettotti 02] P. Bettotti, L. Dal Negro, Z. Gaburro, L. Pavesi, A. Lui, M. Galli, M. Patrini & F. Marabelli. *P-type macroporous silicon for two-dimensional photonic crystals.* Journal of Applied Physics, vol. 92, no. 12, pages 6966–6972, 2002.

[Blanco 00] A. Blanco, E. Chomski, S. Grabtchak, M. Ibisate, S. John, S. W. Leonard, C. López, F. Meseguer, H. Miguez, J. P.

Mondia, G. A. Ozin, O. Toader & H. M. van Driel. *Large-scale synthesis of a silicon photonic crystal with a complete three-dimensional bandgap near 1.5 micrometres.* Nature, vol. 405, page 437, 2000.

[Boher 04] P. Boher, J. P. Piel & B. Sacépé. *Generalized ellipsometry for the characterization of anisotropic materials: influence of the sample adjustment on the extracted optical indices.* Thin Solid Films, vol. 455-456, pages 581–585, 2004.

[Born 80] Max Born & Emil Wolf. Principles of optics, chapitre 8, page 382. Pergamon Press, Oxford, 6th edition, 1980.

[Bria 02] D. Bria & D. Djafari-Rouhani. *Omnidirectional optical mirror in a cladded-superlattice structure.* Journal of Applied Physics, vol. 91, no. 5, page 2569, 2002.

[Bristow 02] A. D. Bristow, V. N. Astratov, R. Shimada, I. S. Culshaw, M. S. Skolnick, D. M. Whittaker, A. Tahraoui & T. F. Krauss. *Polarization conversion in the reflectivity properties of photonic crystal waveguides.* IEEE Journal of Quantum Electronics, vol. 38, no. 7, pages 880–884, 2002.

[Busch 04] K. Busch, S. Lolkes, R. B. Wehrspohn & H. Foll. Photonic crystals: Advances in design, fabrication, and characterization. 3-527-40432-5. WILEY-VCH, 2004.

[Businaro 03] L. Businaro, F. Romanato, P. Candeloro, E. Di Fabrizio, M. Patrini, M. Galli, C. Andreani, A. Passaseo & M. De Vittorio. *High-resolution complex structures for two-dimensional photonic crystals realized by X-ray diffraction lithography.* Journal of Vacuum Science and Technology B, vol. 21, no. 2, pages 748–753, 2003.

[Butte 02] R. Butte, G. Delalleau, A. I. Tartakovskii, M. S. Skolnick, V. N. Astratov, J. J. Baumberg, G. Malpuech, A. Di Carlo, A. V. Kavokin & J. S. Roberts. *Transition from strong to weak coupling and the onset of lasing in semiconductor microcavities.* Physical Review B, vol. 65, no. 20, page 205310, 2002.

[Carvajal 08] J. J. Carvajal, A. Pena, R. Kumar, M. C. Pujol, X. Mateos, M. Aguiló, F. Díaz, J. R. Vázquez de Aldana, C. Méndez, P. Moreno, L. Roso, T. Trifonov, A. Rodríguez, R. Alcubilla, Z. Král, J. Ferré-Borrull, J. Pallarés, L. F. Marsal, S. Di Finizio, R. Macovez & J. Martorell. *New approaches for the fabrication of photonic structures of non-linear optical materials.* Journal of Luminescence, 2008. in press.

[Cassagne 96] D. Cassagne, C. Jouanin & D. Bertho. *Hexagonal photonic-band-gap structures.* Physical Review B, vol. 53, no. 11, pages 7134–7142, 1996.

[Chigrin 99] D. N. Chigrin, A. V. Lavrinenko, D. A. Yarotsky & S. V. Gaponenko. *All-dielectric one-dimensional periodic structures for total omnidirectional reflection and partial spontaneous emission control.* Journal of Lightwave Technology, vol. 17, no. 11, page 2018, 1999.

[Choi 03] J. Choi, K. Nielsch, M. Reiche, R. B. Wehrspohn & U. Gosele. *Fabrication of monodomain alumina pore arrays with an interpore distance smaller than the lattice constant of the imprint stamp.* Journal of Vacuum Science and Technology B, vol. 21, page 763766, 2003.

[Choi 04] J. Choi. *Fabrication of monodomain porous alumina using nanoimprint lithography and its applications.* PhD thesis, Martin Luther University Halle-Wittenberg, 2004.

[Chou 96] S. Y. Chou, P. R. Krauss & P. J. Renstrom. *Nanoimprint lithography.* Journal of Vacuum Science and Technology B, vol. 14, page 41294133, 1996.

[Chutinan 00] A. Chutinan & S. Noda. *Waveguides and waveguide bends in two-dimensional photonic crystal slabs.* Physical Review B, vol. 62, page 4488, 2000.

[Chutinan 01] A. Chutinan, M. Mochizuki, M. Imada & S. Noda. *Surface-emitting channel drop filters using single defects in two-dimensional photonic crystal slabs.* Applied Physics Letters, vol. 79, page 2690, 2001.

[Chutinan 02] A. Chutinan, M. Okano & S. Noda. *Wider bandwidth with high transmission through waveguide bends in two-dimensional photonic crystal slabs.* Applied Physics Letters, vol. 80, page 1698, 2002.

[Compain 99] E. Compain, Stéphane Poirier & Bernard Drévillon. *General and self-consistent method for the calibration of polarization modulators, polarimeters, and Mueller-matrix ellipsometers.* Applied Optics, vol. 38, no. 16, pages 3490–3502, 1999.

[Culshaw 00] I. S. Culshaw, V. N. Astratov, R. M. Stevenson, D. M. Whittaker, M. S. Skolnick, T. F. Krauss & R. M. De La Rue. *Determination of the band structure of photonic crystal waveguides.* Physica E, vol. 7, no. 3-4, pages 650–655, 2000.

[David 05] A. David, C. Meier, R. Sharma, F. S. Diana, S. P. DenBaars, E. Hu, S. Nakamura, C. Weisbuch & H. Benisty. *Photonic bands in two-dimensionally patterned multimode* GaN *waveguides for light extraction.* Applied Physics Letters, vol. 87, no. 10, page 101107, 2005.

[Eftekhari 08] A. Eftekhari. Nanostructured materials in electrochemistry. 978-3-527-31876-6. Wiley-VCH, 2008.

[Ellman 08] M. Ellman, A. Rodríguez, N. Pérez, M. Echeverria, Y. K. Verevkin, C. S. Peng, T. Berthou, Z. Wang, S. M. Olaizola & I. Ayerdi. *High-power laser interference lithography process on photoresist: effect of laser fluence and polarisation.* Applied Surface Science, 2008. DOI:10.1016/j.apsusc.2008.07.201.

[Fan 97] S. H. Fan, P. R. Villeneuve, J. D. Joannopoulos & E. F. Schubert. *High extraction efficiency of spontaneous emission from slabs of photonic crystals.* Physical Review Letters, vol. 78, no. 17, pages 3294–3297, 1997.

[Fan 98a] S. Fan, P. R. Villeneuve, J. D. Joannopoulos & H. A. Haus. *Channel drop filters in a photonic crystal.* Optics Express, vol. 3, page 4, 1998.

[Fan 98b] S. Fan, P. R. Villeneuve, J. D. Joannopoulos & H. A. Haus. *Channel drop tunneling through localized states.* Physical Review Letters, vol. 80, page 960, 1998.

[Fan 99] S. Fan, P. R. Villeneuve, J. D. Joannopoulos, M. J. Khan, C. Manolatou & H. A. Haus. *Theoretical analysis of channel drop tunneling processes.* Physical Review B, vol. 59, page 15882, 1999.

[Fink 98] Y. Fink, J. N. Winn, S. Fan, Ch. Chen, J. Michel, J. D. Joannopoulos & E. L. Thomas. *A dielectric omnidirectional reflector.* Science, vol. 282, pages 1679–1682, 1998.

[Foldyna 08] M. Foldyna, A. De Martino, E. Garcia-Caurel, R. Ossikovski, C. Licitra, F. Bertin, K. Postava & B. Drévillon. *Critical dimension of biperiodic gratings determined by spectral ellipsometry and* M*ueller matrix polarimetry.* The European Physical Journal - Applied Physics, vol. 42, no. 3, pages 351–359, 2008.

[Foll 03] H. Foll, S. Langa, J. Carstensen, M. Christophersen & I. M. Tiginyanu. *Pores in* III-V *semiconductors.* Advanced Materials, vol. 15, page 183, 2003.

[Galli 02a] M. Galli, M. Agio, L. C. Andreani, L. Atzeni, D. Bajoni, G. Guizzetti, L. Businaro, E. Di Fabrizio, F. Romanato & A. Passaseo. *Optical properties and photonic bands of GaAs photonic crystal waveguides with tilted square lattice.* European Physical Journal B, vol. 27, no. 1, pages 79–87, 2002.

[Galli 02b] M. Galli, M. Agio, L. C. Andreani, M. Belotti, G. Guizzetti, F. Marabelli, M. Patrini, P. Bettotti, L. Dal Negro, Z. Gaburro, L. Pavesi, A. Liu & P. Bellutti. *Spectroscopy of photonic bands in macroporous silicon photonic crystals.* Physical Review B, vol. 65, no. 11, page 113111, 2002.

[Galli 04] M. Galli, M. Belotti, D. Bajoni, M. Patrini, G. Guizzetti, D. Gerace, M. Agio, L. C. Andreani & Y. Chen. *Excitation of radiative and evanescent defect modes in linear photonic crystal waveguides.* Physical Review B, vol. 70, no. 8, page 081307, 2004.

[Galli 05a] M. Galli, D. Bajoni, M. Belotti, F. Paleari, M. Patrini, G. Guizzetti, D. Gerace, A. Agio, L. C. Andreani, D. Peyrade & Y. Chen. *Measurement of photonic mode dispersion and linewidths in silicon-on-insulator photonic crystal slabs.* IEEE Journal on Selected Areas in Communications, vol. 23, no. 7, pages 1402–1410, 2005.

[Galli 05b] M. Galli, D. Bajoni, M. Patrini, G. Guizzetti, D. Gerace, L. C. Andreani, M. Belotti & Y. Chen. *Single-mode versus multimode behavior in silicon photonic crystal waveguides measured by attenuated total reflectance.* Physical Review B, vol. 72, no. 12, page 125322, 2005.

[Galli 06a] M. Galli, D. Gerace, A. Politi, M. Liscidini, M. Patrini, L. C. Andreani, A. Canino, M. Miritello, R. Lo Savio, A. Irrea & F. Priolo. *Direct evidence of light confinement and emission enhancement in active silicon-on-insulator slot waveguides.* Applied Physics Letters, vol. 89, no. 24, page 241114, 2006.

[Galli 06b] M. Galli, A. Politi, M. Belotti, D. Gerace, M. Liscidini, M. Patrini, L. C. Andreani, M. Miritello, A. Irrera, F. Priolo & Y. Chen. *Strong enhancement of Er_{3+} emission at room temperature in silicon-on-insulator photonic crystal waveguides.* Applied Physics Letters, vol. 88, no. 25, page 251114, 2006.

[Garcia-Caurel 04] E. Garcia-Caurel, A. De Martino & B. Drévillon. *Spectroscopic Mueller polarimeter based on liquid crystal devices.* Thin Solid Films, vol. 455-456, pages 120–123, 2004.

[Gil 00] J. J. Gil. *Characteristic properties of Mueller matrices.* Journal of Optical Society of America A, vol. 17, no. 2, pages 328–334, 2000.

[Goodman 96] Joseph W. Goodman. Introduction to fourier optics, chapitre 4, page 73. McGraw-Hill, San Francisco, 2nd edition, 1996.

[Guinier 94] A. Guinier. X-ray diffraction: In crystals, imperfect crystals, and amorphous bodies. 0-486-68011-8. Dover Publications, 1994.

[Hatit 08] S. Ben Hatit, M. Foldyna, A. De Martino & B. Drévillon. *Angle-resolved* M*ueller polarimeter using a microscope objective.* Physica Status Solidi A, vol. 205, no. 4, pages 743–747, 2008.

[Ho 90] K. M. Ho, C. T. Chan & C. M. Soukoulis. *Existence of a photonic gap in periodic dielectric structures.* Physical Review Letters, vol. 65, pages 3152–3155, 1990.

[Ho 94] K. M. Ho, C. T. Chan, C. M. Soukoulis, R. Biswas & M. Sigalas. *Photonic band gaps in three dimensions: New layer-by-layer periodic structures.* Solid State Communications, vol. 89, pages 413–416, 1994.

[Hovenier 94] J. W. Hovenier. *Structure of a general pure Mueller matrix.* Applied Optics, vol. 33, no. 36, pages 8318–8324, 1994.

[Imada 99] M. Imada, S. Noda, A. Chutinan, T. Tokuda, M. Murata & G. Sasaki. *Coherent two-dimensional lasing action in surface-emitting laser with triangular-lattice photonic crystal structure.* Applied Physics Letters, vol. 75, page 316, 1999.

[Joannopoulos 97] J. D. Joannopoulos, P. R. Villeneuve & S. H. Fan. *Photonic crystals.* Solid State Communications, vol. 102, no. 2-3, pages 165–173, 1997.

[Joannopoulos 08] J. D. Joannopoulos, S. G. Johnson, J. N. Winn & R. D. Meade. Photonic crystals-modeling the flow of light.

Princeton University Press, William Street, Princeton, New Jersey 08540, second edition edition, 2008.

[John 87] S. John. *Strong localization of photons in certain disordered dielectric superlattices.* Physical Review Letters, vol. 58, no. 23, pages 2486–2489, 1987.

[Johnson 99] S. G. Johnson, S. H. Fan, P. R. Villeneuve, J. D. Joannopoulos & L. A. Kolodziejski. *Guided modes in photonic crystal slabs.* Physical Review B, vol. 60, no. 8, pages 5751–5758, 1999.

[Kaplan 04] B. Kaplan, T. Novikova, A. De Martino & Bernard Drévillon. *Characterization of bidimensional gratings by spectroscopic ellipsometry and angle-resolved Mueller polarimetry.* Applied Optics, vol. 43, no. 6, pages 1233–1240, 2004.

[Knight 98] J. C. Knight, J. Broeng, T. A. Birks & P. S. J. Russell. *Photonic band gap guidance in optical fibers.* Science, vol. 282, page 1476, 1998.

[Ko 88] D. Y. K. Ko & J. C. Inkson. *Matrix method for tunneling in heterostructures: Resonant tunneling in multilayer systems.* Physical Review B, vol. 38, no. 14, page 9945, 1988.

[Král 08a] Z. Král, J. Ferré-Borrull, J. Pallarés, T. Trifonov, A. Rodriguez, R. Alcubilla & L. F. Marsal. *Characterization of 2D macroporous silicon photonic crystals: Improving the photonic band identification in angular-dependent reflection spectroscopy in the mid-IR.* Materials Science and Engineering B, vol. 147, pages 179–182, 2008.

[Král 08b] Z. Král, J. Ferré-Borrull, T. Trifonov, L. F. Marsal, A. Rodriguez, J. Pallarès & R. Alcubilla. *Mid-IR characterization of photonic bands in 2D photonic crystals on silicon.* Thin Solid Films, vol. 516, pages 8059–8053, 2008.

[Král 09] Z. Král, L. Vojkúvka, E. Garcia-Caurel, J. Ferré-Borrull, L. F. Marsal & J. Pallarès. *Calculation of*

angular-dependent reflectance and polarimetry spectra of nanoporous anodic alumina-based photonic crystal slabs. Photonics and Nanostructures - Fundamentals and Applications, vol. 7, pages 12–18, 2009.

[Krauss 96] T. F. Krauss, R. M. De La Rue & S. Brand. *Two-dimensional photonic-bandgap structures operating at near infrared wavelengths.* Nature, vol. 383, no. 6602, pages 699–702, 1996.

[Kuchinsky 00] S. Kuchinsky, D. C. Allan, N. F. Borrelli & J. C. Cotteverte. *3D localization in a channel waveguide in a photonic crystal with 2*D *periodicity.* Optics Communications, vol. 175, page 147, 2000.

[Labilloy 97] D. Labilloy, H. Benisty, C. Weisbuch, T. F. Krauss, R. M. De La Rue, V. Bardinal, R. Houdre, U. Oesterle, D. Cassagne & C. Jouanin. *Quantitative measurement of transmission, reflection, and diffraction of two-dimensional photonic band gap structures at near-infrared wavelengths.* Physical Review Letters, vol. 79, no. 21, pages 4147–4150, 1997.

[Lee 06] W. Lee, R. Ji, U. Gosele & K. Nielsch. *Fast fabrication of long-range ordered porous alumina membranes by hard anodization.* Nature Materials, vol. 5, pages 741–747, 2006.

[Lehmann 90] V. Lehmann & H. Foll. *Formation mechanism and properties of electrochemically etched trenches in n-type silicon.* Journal of the Electrochemical Society, vol. 137, page 653, 1990.

[Lehmann 93] V. Lehmann. *The physics of macropore formation in low doped n-type silicon.* Journal of the Electrochemical Society, vol. 140, page 2836, 1993.

[Lehmann 99] V. Lehmann & S. Ronnebeck. *The physics of macropore formation in low-doped p-type silicon.* Journal of the Electrochemical Society, vol. 146, page 2968, 1999.

[Leung 90] K. M. Leung & Y. F. Liu. *Full vector wave calculation of photonic band structures in face-centered-cubic dielectric media.* Physical Review Letters, vol. 65, pages 2646–2649, 1990.

[Li 98] A. P. Li, F. Muller, A. Birner, K. Nielsch & U. Gosele. *Hexagonal pore arrays with a 50-420 nm interpore distance formed by self-organization in anodic alumina.* Journal of Applied Physics, vol. 84, no. 11, pages 6023–6026, 1998.

[Lin 98] Shawn-Yu. Lin, J. G. Fleming, D. L. Hetherington, B. K. Smith, R. Biswas, K. M. Ho, M. M. Sigalas, W. Zubrzycki, S. R. Kurtz & J. Bur. *A three-dimensional photonic crystal operating at infrared wavelengths.* Nature, vol. 394, pages 251–253, 1998.

[Lin 99] Shawn-Yu. Lin & J. G. Fleming. *A three-dimensional optical photonic crystal.* Journal of Lightwave Technology, vol. 17, no. 11, pages 1944–1947, 1999.

[Loncar 00a] M. Loncar, T. Doll, J. Vuckovic & A. Scherer. *Design and fabrication of silicon photonic crystal optical waveguides.* IEEE Journal of Lightwave Technology, vol. 18, page 1402, 2000.

[Loncar 00b] M. Loncar, D. Nedeljkovic, T. Doll, J. Vuckovic, A. Scherer & T. P. Pearsall. *Waveguiding in planar photonic crystals.* Applied Physics Letters, vol. 77, page 1937, 2000.

[Marsal 07] L. F. Marsal, L. Vojkůvka, J. Ferré-Borrull, T. Trifonov & J. Pallarés. *Optical characterization of self-ordered porous alumina membranes of various thicknesses.* Physica Status Solidi C - Current Topics in Solid State Physics, vol. 4, no. 6, pages 1918–1922, 2007.

[Marsal 08] L. F. Marsal, L. Vojkůvka, P. Formentin, J. Pallarés & J. Ferré-Borrull. *Fabrication and optical characterization of nanoporous alumina films annealed at different temperatures.* Optical Materials, 2008. in press.

[Martinez 08] L. J. Martinez, A. R. Alija, P. A. Postigo, J. F. Galisteo-Lopez, M. Galli, L. C. Andreani, C. Seassal & P. Viktorovitch. *Effect of implementation of a Bragg reflector in the photonic band structure of the Suzuki-phase photonic crystal lattice.* Optics Express, vol. 16, no. 12, pages 8509–8518, 2008.

[Masuda 95] H. Masuda & K. Fukuda. *Ordered metal nanohole arrays made by a 2-step replication of honeycomb structures of anodic alumina.* Science, vol. 268, pages 1466–1468, 1995.

[Masuda 97] H. Masuda, H. Yamada, M. Satoh, H. Asoh, M. Nakao & T. Tamamura. *Highly ordered nanochannel-array architecture in anodic alumina.* Applied Physics Letters, vol. 71, page 27702772, 1997.

[Masuda 01] H. Masuda, H. Asoh, M.Watanabe, K. Nishio, M. Nakao & T. Tamamura. *Square and triangular nanohole array architectures in anodic alumina.* Advanced Materials, vol. 13, page 189192, 2001.

[Masuda 05] H. Masuda. Highly ordered nanohole arrays in anodic porous alumina. Ordered Porous Nanostructures and Applications. Springer, 2005.

[Montero-Moreno 07] J. M. Montero-Moreno, M. Sarret & C. Muller. *Influence of the aluminum surface on the final results of a two-step anodizing.* Surface and Coatings Technology, vol. 201, no. 14, pages 6352–6357, 2007.

[Netti 01] M. C. Netti, A. Harris, J. J. Baumberg, D. M. Whittaker, M. B. D. Charlton, M. E. Zoorob & G. J. Parker. *Optical trirefringence in photonic crystal waveguides.* Physical Review Letters, vol. 86, no. 8, pages 1526–1529, 2001.

[Noda 99] S. Noda, N. Yamamoto, M. Imada, H. Kobayashi & M. Okano. *Alignment and stacking of semiconductor photonic bandgaps by wafer-fusion.* IEEE Journal of Lightwave Technology, vol. 17, page 1948, 1999.

[Noda 00] S. Noda, K. Tomoda, N. Yamamoto & A. Chutinan. *Full three-dimensional photonic bandgap crystals at near-infrared wevelengths.* Science, vol. 289, page 602, 2000.

[Notomi 02] M. Notomi, A. Shinya, K. Yamada, J. I. Takahashi, C. Takahashi & I. Yokohama. *Structural tuning of guiding modes of line-defect waveguides of silicon-on-insulator photonic crystal slabs.* IEEE Journal of Quantum Electronics, vol. 38, page 736, 2002.

[Novikova 06] T. Novikova, A. De Martino, S. Ben Hatit & B. Drévillon. *Application of Mueller polarimetry in conical diffraction for critical dimension measurements in microelectronics.* Applied Optics, vol. 45, no. 16, pages 3688–3697, 2006.

[Ohtera 99] Y. Ohtera, T. Sato, T. Kawashima, T. Tamamura & S. Kawakami. *Photonic crystal polarization splitters.* Electronics Letters, vol. 35, page 1271, 1999.

[Ozbay 94] E. Ozbay, G. Tuttle, R. Biswas, K.M. Ho, J. Bostak & D. M. Bloom. *New double-etch geometry for millimeter-wave photonic crystals with a semi-tunable photonic band gap.* Applied Physics Letters, vol. 65, page 1617, 1994.

[Pacradouni 00] V. Pacradouni, W. J. Mandeville, A. R. Cowan, P. Paddon, J. F. Young & S. R. Johnson. *Photonic band structure of dielectric membranes periodically textured in two dimensions.* Physical Review B, vol. 62, no. 7, pages 4204–4207, 2000.

[Padjen 94] R. Padjen, J. M. Gererd & J. Y. Marzin. *Analysis of the filling pattern dependence of the photonic bandgap for two-dimensional systems.* Journal of Modern Optics, vol. 41, page 295, 1994.

[Painter 99] O. Painter, T. Vuckovic & A. Scherer. *Defect modes of a two-dimensional photonic crystal in an optically thin dielectric slab.* Journal of the Optical Society of America B, vol. 16, page 275, 1999.

[Pallavidino 06] L. Pallavidino, D. S. Razo, F. Geobaldo, A. Balestreri, D. Bajoni, M. Galli, L. C. Andreani, C. Ricciardi, E. Celasco, M. Quaglio & F. Giorgis. *Synthesis, characterization and modelling of silicon based opals.* Journal of Non-Crystalline Solids, vol. 352, no. 9-20, pages 1425–1429, 2006.

[Pang 98] S. W. Pang, T. Tamamura, M. Nakao, A. Ozawa & H. Masuda. *Direct nano-printing on Al substrate using a SiC mold.* Journal of Vacuum Science and Technology B, vol. 16, page 11451149, 1998.

[Patrini 02a] M. Patrini, M. Galli, M. Belotti, L. C. Andreani, G. Guizzetti, G. Pucker, A. Lui, P. Bellutti & L. Pavesi. *Optical response of one-dimensional (Si/SiO_2)(m) photonic crystals.* Journal of Applied Physics, vol. 92, no. 4, pages 1816–1820, 2002.

[Patrini 02b] M. Patrini, M. Galli, F. Marabelli, M. Agio, L. C. Andreani, D. Peyrade & Y. Chen. *Photonic bands in patterned silicon-on-insulator waveguides.* IEEE Journal of Quantum Electronics, vol. 38, no. 7, pages 885–890, 2002.

[Patrini 03] M. Patrini, M. Galli, A. Agio, L. C. Andreani, D. Bajoni, G. Guizzetti, L. Businaro, E. Di Fabrizio, F. Romanato & A. Passaseo. *Linear optical properties and photonic mode dispersion in GaAs/AlGaAs photonic crystal slabs.* Physica E-Low-Dimensional Systems and Nanostructures, vol. 17, no. 1-4, pages 418–419, 2003.

[Pavarini 05] E. Pavarini, L. C. Andreani, C. Soci, M. Galli, F. Marabelli & D. Comoretto. *Band structure and optical properties of opal photonic crystals.* Physical Review B, vol. 72, no. 4, page 045102, 2005.

[Perez-Hernandez 08] N. Perez-Hernandez. *Fabrication and Characterization of Sub-Micrometric Silver Structures by Self-Assembly and Laser Interference Lithography.* PhD thesis, University of Navara, San Sebastian, October 2008.

[Peyrade 02] D. Peyrade, Y. Chen, A. Talneau, M. Patrini, M. Galli, F. Marabelli, M. Agio, L. C. Andreani, E. Silberstein & P. Lalanne. *Fabrication and optical measurements of silicon on insulator photonic nanostructures.* Microelectronic Engineering, vol. 61-2, pages 529–536, 2002.

[Plihal 91a] A. Plihal & A. A. Maradudin. *Photonic band structure of two-dimensional systems: the triangular lattice.* Physical Review B, vol. 44, page 8565, 1991.

[Plihal 91b] M. Plihal, A. Shambrook, A. A. Maradudin & P. Sheng. *Two-dimensional photonic band structures.* Optics Communications, vol. 80, page 199, 1991.

[Postigo 07] P. A. Postigo, A. R. Alija, L. J. Martinez, M. L. Dotor, D. Golmayo, J. Sanchez-Dehesa, C. Seassal, P. Viktorovitch, M. Galli, A. Politi, M. Patrini & L. C. Andreani. *Laser nanosources based on planar photonic crystals as new platforms for nanophotonic devices.* Photonics and Nanostructures-Fundamentals and Applications, vol. 5, no. 2-3, pages 79–85, 2007.

[Qiu 99] M. Qiu & S. He. *Large complete band gap in two-dimensional photonic crystals with elliptic air holes.* Physical Review B, vol. 60, page 10610, 1999.

[Rauf 09] A. Rauf & et. al. *The effects of electropolishing on the nanochannel ordering of the porous anodic alumina prepared in oxalic acid.* Journal of Solid State Electrochemistry, vol. 13, no. 2, pages 321–332, 2009.

[Romanato 03] F. Romanato, L. Businaro, L. Vaccari, S. Cabrini, P. Candeloro, M. De Vittorio, A. Passaseo, M. T. Todaro, R. Cingolani, E. Cattaruzza, M. Galli, C. Andreani & E. Di Fabrizio. *Fabrication of 3-D metallic photonic crystals by X-ray lithography.* Microelectronic Engineering, vol. 67-8, pages 479–486, 2003.

[Sakoda 97] K. Sakoda. *Numerical analysis of the interference patterns in the optical transmission spectra of a square photonic lat-*

tice. Journal of the Optical Society of America B-Optical Physics, vol. 14, no. 8, pages 1961–1966, 1997.

[Sakoda 99] K. Sakoda, M. Sasada, T. Fukushima, A. Yamanaka, N. Kawai & K. Inoue. *Detailed analysis of transmission spectra and Bragg-reflection spectra of a two-dimensional photonic crystal with a lattice constant of 1.15 μm.* Journal of the Optical Society of America B-Optical Physics, vol. 16, no. 3, pages 361–365, 1999.

[Sakoda 05] Kazuaki Sakoda. Optical Properties of Photonic Crystals. 3-540-20682-5. Springer, Second edition, 2005.

[Saleh 91] B.E.A. Saleh & M. C. Teich. Principles of Photonics, chapitre 4, page 127. John Wiley and Sons, Inc, New York, 1991.

[Sands 94] Donald E. Sands. Introduction to Crystallography. 0-486-67839-3. Dover Publications, January 1994.

[Satpathy 90] S. Satpathy, Ze Zhang & M. R. Salehpour. *Theory of photon bands in three-dimensional periodic dielectric structures.* Physical Review Letters, vol. 64, pages 1239–1242, 1990.

[Schwartz 76] G. C. Schwartz & V. Platter. *Anodic processing for multilevel LSI.* Journal of the Electrochemical Society, vol. 123, no. 1, pages 34–37, 1976.

[Shinya 02] A. Shinya, M. Notomi, I. Yokohama, C. Takahashi, J. I. Takahashi & T. Tamamura. *Two-dimensional Si photonic crystals on oxide using SOI substrate.* Optical and Quantum Electronics, vol. 34, page 113, 2002.

[Sozuer 94] H. S. Sozuer & J. P. Dowling. *Photonic band calculations for woodpile structures.* Journal of Modern Optics, vol. 41, no. 2, pages 231–239, 1994.

[Sui 02] Y. C. Sui. *Pore structure, barrier layer topography and matrix alumina structure of porous anodic alumina film.* Thin Solid Films, vol. 406, no. 1-2, pages 64–69, 2002.

[Thompson 97] G. E. Thompson. *Porous anodic alumina: fabrication, characterization and applications.* Thin Solid Films, vol. 297, pages 192–201, 1997.

[Tkachenko 06] V. Tkachenko, G. Abbate, A. Marino, F. Vita, M. Giocondo, A. Mazzulla & L. De Stefano. *High accuracy optical characterization of anisotropic liquids by merging standard techniques.* Applied Physical Letters, vol. 89, no. 22, page 221110, 2006.

[Trifonov 04] T. Trifonov. *Photonic bandgap analysis and fabrication of macroporous silicon by electrochemical etching.* PhD thesis, Universitat Rovira I Virgili, Avda. Paisos Catalans 26, Campus Sescelades, 43007 Tarragona, Spain, 2004.

[Trifonov 05] T. Trifonov, L. F. Marsal, A. Rodríguez, J. Pallarés & R. Alcubilla. *Fabrication of two-and three-dimensional photonic crystals by electrochemical etching of silicon.* Physica Status Solidi C, vol. 2, no. 8, pages 3104–3107, 2005.

[Villeneuve 92] P. R. Villeneuve & M. Piche. *Photonic band gaps in two-dimensional square lattices: Square and circular rods.* Physical Review B, vol. 46, page 4973, 1992.

[Vlasov 97] Y. A. Vlasov, V. N. Astratov, O. Z. Karimov, A. A. Kaplyanskii, V. N. Bogomolov & A. V. Prokofiev. *Existence of a photonic pseudogap for visible light in synthetic opals.* Physical Review B, vol. 55, no. 20, pages 13357–13360, 1997.

[Vlasov 01] Y. A. Vlasov, X. Z. Bo, J. C. Strum & D. J. Norris. *On-chip natural assembly of silicon photonic bandgap crystals.* Nature, vol. 414, pages 289–293, 2001.

[Vojkůvka 07] L. Vojkůvka, L. F. Marsal & J. Pallarés. *Study of porous alumina porosity after pore widening process.* 2007 Spanish Conference on Electron Devices, Proceedings, pages 41–43, 2007.

[Wagner 07] Ch. Wagner, R. Droste & Jos de Klerk. *TWINSCAN XT:1900i paving the way to sub 40nm imaging and double patterning.* ASML Images Customer Magazine, 2007.

[Wang 99] X. H. Wang, B. Y. Gu, Z. Y. Li & G. Z. Yang. *Large absolute photonic band gaps created by rotating noncircular rods in two-dimensional lattices.* Physical Review B, vol. 60, page 11417, 1999.

[Warren 90] B. E. Warren. X-Ray Diffraction. 0-486-66317-5. Dover Publications, June 1990.

[Whittaker 99] D. M. Whittaker & I. S. Culshaw. *Scattering-matrix treatment of patterned multilayer photonic structures.* Physical Review B, vol. 60, no. 4, pages 2610–2618, 1999.

[Whittaker 02] D. M. Whittaker, I. S. Culshaw, V. N. Astratov & M. S. Skolnick. *Photonic band structure of patterned waveguides with dielectric and metallic cladding.* Physical Review B, vol. 65, no. 7, page 073102, 2002.

[Wijnhoven 98] J. E. G. J. Wijnhoven & W. L. Vos. *Preparation of photonic crystals made of air spheres in titania.* Science, vol. 281, page 802, 1998.

[Winn 98] J. N. Winn, Y. Fink, S. Fan & J. D. Joannopoulos. *Omnidirectional reflection from a one-dimensional photonic crystal.* Optics Letters, vol. 23, no. 20, pages 1573–1575, 1998.

[Xifré-Peréz 05] E. Xifré-Peréz, L. F. Marsal, J. Pallarés & J. Ferré-Borrull. *Porous silicon mirrors with enlarged omnidirectional band gap.* Journal of Applied Physics, vol. 97, no. 6, page 064503, 2005.

[Yablonovitch 87] E. Yablonovitch. *Inhibited spontaneous emission in solid-state physics and electronics.* Physical Review Letters, vol. 58, no. 20, pages 2059–2062, 1987.

[Yablonovitch 89] E. Yablonovitch & T. J. Gmitter. *Photonic band-structure the face-centered-cubic case.* Physical Review Letters, vol. 63, pages 1950–1953, 1989.

[Yablonovitch 91a] E. Yablonovitch, T. J. Gmiter & K. M. Leung. *Photonic band structure: The face-centered-cubic case employing nonspherical atoms.* Physical Review Letters, vol. 67, no. 17, pages 2295–2298, 1991.

[Yablonovitch 91b] E. Yablonovitch, T. J. Gmitter, R. D. Meade A. M. Rappe, K. D. Brommer & J. D. Joannopoulos. *Donor and acceptor modes in photonic band structure.* Physical Review Letters, vol. 67, no. 24, pages 3380–3383, 1991.

[Yablonovitch 93a] E. Yablonovitch. *Photonic band-gap crystals.* Journal of Physics-Condensed Matter, vol. 5, no. 16, pages 2443–2460, 1993.

[Yablonovitch 93b] E. Yablonovitch. *Photonic band-gap structures.* Journal of the Optical Society of America B-Optical Physics, vol. 10, no. 2, pages 283–295, 1993.

[Zhang 07] J. Zhang, Z. Wang, Y. K. Verevkinb, S. M. Olaizola, C. Peng, C. Tand, A. Rodriguez, E. Y. Daumeb, T. Berthoue & S. Tisserand. *Formation of 4-beam laser interference patterns for nanolithography.* In Proceedings of SPIE, vol. 6593, page 65930I, 2007.

UNIVERSITAT ROVIRA I VIRGILI
DEVELOPMENT OF OPTICAL CHARACTERIZATION METHODS FOR MICRO- AND NANO-SCALE PLANAR PHOTONIC BAND GAP STRUCTURES
Zdenek Kral
DL: T-1537-2009/ISBN:978-84-692-4556-9

UNIVERSITAT ROVIRA I VIRGILI
DEVELOPMENT OF OPTICAL CHARACTERIZATION METHODS FOR MICRO- AND NANO-SCALE PLANAR PHOTONIC BAND GAP STRUCTURES
Zdenek Kral
DL: T-1537-2009/ISBN:978-84-692-4556-9

UNIVERSITAT ROVIRA I VIRGILI
DEVELOPMENT OF OPTICAL CHARACTERIZATION METHODS FOR MICRO- AND NANO-SCALE PLANAR PHOTONIC BAND GAP STRUCTURES
Zdenek Kral
DL: T-1537-2009/ISBN:978-84-692-4556-9

Appendix A

The Reciprocal lattice, the Brillouin zone, and the lattice direction

This appendix describe the concept of the reciprocal lattice, the main lattice orientations, and the first (irreducible) and higher Brillouin zones for the two-dimensional square and triangular lattices. These are the 2D crystal lattices considered throughout this work for photonic crystals. The fundamental concept comes from solid-state physics where a crystalline solid can be described with the formalism of Bravais lattices. A Bravais lattice specifies the periodic array in which the repeated units of the structure (such as the crystalline solid or photonic crystal) are arranged [Ashcroft 76]. A Bravais lattice consists of all points with position vectors $\mathbf{R}$ of the form

$$\mathbf{R} = \sum_i n_i \mathbf{a_i}, \tag{A.1}$$

where $\mathbf{a_i}$ are linear independent lattice vectors, and n_i range through all integers. The vectors $\mathbf{a_i}$ are called primitive vectors and are said to generate or span the lattice. A primitive unit cell is defined as a volume of space that, when translated through all the primitive vectors, just fills all of the space.

In the case of photonic crystals, the primitive cell may contain one or more photonic atoms (dielectric scatterers: rods, holes, spheres, etc.), surrounded by a piece of the background material. The calculations of the photonic band structure are then performed over the computational domain that consists of one unit cell by applying periodic boundary conditions to update the fields at the cell boundaries.

Instead of using the real space lattice to perform the calculations, it is usually useful to use its associated reciprocal lattice. Consider a set of points $\mathbf{R}$ constituting a Bravais lattice, and a plane wave e^{ikr}. Wave vectors $\mathbf{K}$, which satisfy the relation

$$e^{i\mathbf{K}\cdot(r+\mathbf{R})} = e^{i\mathbf{K}\cdot r}, \tag{A.2}$$

for any r and for all $\mathbf{R}$, belong to the reciprocal lattice of a Bravais lattice of points $\mathbf{R}$. Factoring out $e^{i\mathbf{K}r}$, the reciprocal lattice can be characterized as the set of wave vectors $\mathbf{K}$ satisfying

$$e^{i\mathbf{K}\cdot r} = 1, \quad i.e. \quad \mathbf{K}\cdot\mathbf{R} = N\cdot 2\pi, \tag{A.3}$$

where N is an integer. A reciprocal lattice is defined with reference to a particular Bravais lattice, which is called the direct lattice. The reciprocal lattice is itself a Bravais lattice. The reciprocal lattice of a reciprocal lattice is just the original direct lattice. In three-dimensional space, if $\mathbf{a_i}$, $i = 1$, 2, 3 are a set of primitive vectors of the direct lattice, the reciprocal lattice can be generated by the primitive vectors $\mathbf{b_i}$, $i = 1$, 2, 3 through

$$\mathbf{G} = \sum_i h_i \mathbf{b_i}, \tag{A.4}$$

where h_i, i=1,2,3 are arbitrary integers and $\mathbf{b_i}$ is related to the real space primitive vectors $\mathbf{a_i}$ according to:

$$\begin{aligned}
\mathbf{b_1} &= 2\pi \frac{\mathbf{a_2}\times\mathbf{a_3}}{\mathbf{a_1}\cdot(\mathbf{a_2}\times\mathbf{a_3})},\\
\mathbf{b_2} &= 2\pi \frac{\mathbf{a_3}\times\mathbf{a_1}}{\mathbf{a_1}\cdot(\mathbf{a_2}\times\mathbf{a_3})},\\
\mathbf{b_3} &= 2\pi \frac{\mathbf{a_1}\times\mathbf{a_2}}{\mathbf{a_1}\cdot(\mathbf{a_2}\times\mathbf{a_3})}.
\end{aligned} \tag{A.5}$$

where $\mathbf{a_1} \cdot (\mathbf{a_2} \times \mathbf{a_3})$ is the volume of the primitive unit cell. In reciprocal space we can construct a region that surrounds the origin such that all k-points enclosed are closer to the origin than to any other reciprocal lattice point. This set of points in k-space is called the first Brillouin zone. As is geometrically evident, the first Brillouin zone is the region enclosed by the sets of planes that are perpendicular bisectors to the lattice vectors connecting the origin in k-space to its nearest neighbor reciprocal lattice points. In general, planes that are perpendicular bisectors of a line joining the origin of k-space of a reciprocal lattice points are called Bragg planes. Hence, the first Brillouin zone can also be defined as the set of points in k-space that can be reached from the origin without crossing any Bragg plane. Due to symmetry reasons, most of the time we only need to analyze a part of the first Brillouin zone. This part is called the irreducible first Brillouin zone. Higher Brillouin zones are simply other regions bounded by the Bragg planes. The second Brillouin zone is defined as the set of points that can be reached from the first Brillouin zone by crossing only one Bragg plane. Similarly, the nth Brillouin zone is the set of points that can be reached from the $(n-1)$th zone by crossing one and only one Bragg plane. Alternatively, the nth Brillouin zone can be defined as the set of points that can be reached from the origin by crossing $n-1$ Bragg planes, but no fewer.

We now consider the two mostly used two-dimensional lattices, namely the square and the triangular lattice. For a square lattice with spacing a, the simplest lattice vectors are

$$\mathbf{a_1} = a\hat{\mathbf{x}} \quad and \quad \mathbf{a_2} = a\hat{\mathbf{y}}, \tag{A.6}$$

where $\hat{\mathbf{x}}$ and $\hat{\mathbf{y}}$ denote unit vectors along the x and y axis, respectively. In order to use equation A.5, we can use a third basis vector in the z-direction of any length. The results are

$$\mathbf{b_1} = (2\pi/a)\hat{\mathbf{x}} \quad and \quad \mathbf{b_2} = (2\pi/a)\hat{\mathbf{y}}. \tag{A.7}$$

It is easily seen that the reciprocal lattice of the square lattice is also a square lattice, but with spacing $2\pi/a$ instead of a. The original lattice, the reciprocal lattice, the first Brillouin zone and the irreducible first Brillouin zone of the square lattice are depicted in figure A.1.

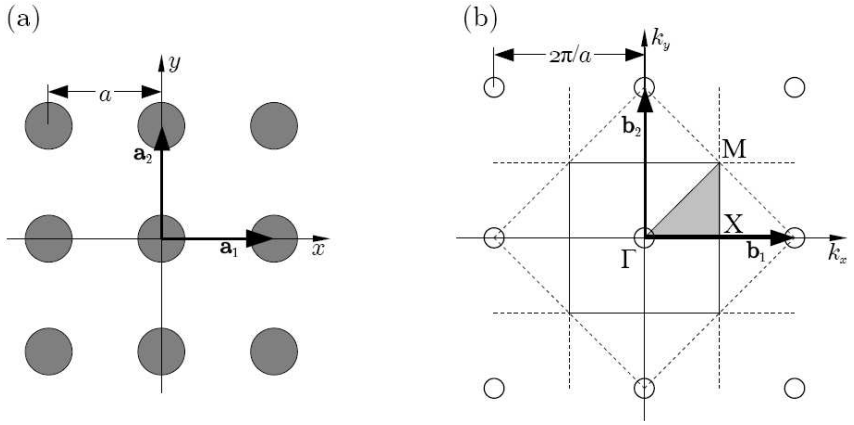

Figure A.1: The two-dimensional square lattice. (a): Square lattice network with spacing a in real space. The lattice vectors are denoted by $\mathbf{a_1}$ and $\mathbf{a_2}$. (b): Corresponding reciprocal lattice, a square lattice with spacing $2\pi/a$. The reciprocal lattice vectors are denoted by $\mathbf{b_1}$ and $\mathbf{b_2}$. The dotted lines are the perpendicular bisectors to the reciprocal lattice vectors connecting the origin (Γpoint) to its nearest neighbor reciprocal lattice points. The region enclosed by these lines and containing the origin is the first Brillouin zone (solid square). The shaded area is the irreducible first Brillouin zone. The symmetry points Γ, M and X are also shown.

The high symmetry k-points, which are the three corners of the irreducible first Brillouin zone, are given by

$$\begin{array}{lll} \Gamma: & k_x = 0, & k_y = 0, \\ X: & k_x = \pi/a, & k_y = 0, \\ M: & k_x = \pi/a, & k_y = \pi/a. \end{array} \tag{A.8}$$

For a triangular lattice with spacing a, the lattice vectors can be chosen as

$$\mathbf{a_1} = a(\sqrt{3}\hat{\mathbf{x}} + \hat{\mathbf{y}})/2 \quad and \quad \mathbf{a_2} = a\hat{\mathbf{y}}, \tag{A.9}$$

shown in figure A.2. Using equation A.5, we obtain the reciprocal lattice vectors

$$\mathbf{b_1} = \frac{4\pi}{\sqrt{3}a}\hat{\mathbf{x}} \quad and \quad \mathbf{b_2} = \frac{4\pi}{\sqrt{3}a}(-\frac{\sqrt{3}}{2}\hat{\mathbf{x}} + \frac{1}{2}\hat{\mathbf{y}}). \tag{A.10}$$

The reciprocal lattice is again a triangular lattice. Figure A.2 shows the original lattice, the reciprocal lattice, the first Brillouin zone and the irreducible first Brillouin zone. The three corners of the irreducible first Brillouin zone,

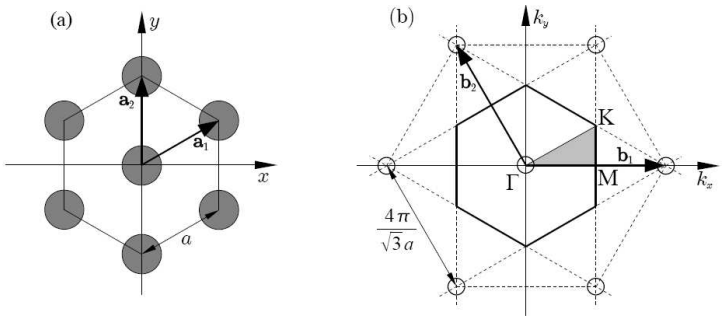

Figure A.2: The two-dimensional triangular lattice. (a) Triangular lattice network with spacing a in real space. The lattice vectors are denoted by $\mathbf{a_1}$ and $\mathbf{a_2}$. (b) Corresponding reciprocal lattice, a triangular lattice with spacing $4\pi/\sqrt{3}a$. The reciprocal lattice vectors are $\mathbf{b_1}$ and $\mathbf{b_2}$. The dotted lines are the perpendicular bisectors to the reciprocal lattice vectors connecting the origin (Γpoint) to its nearest neighbor reciprocal lattice points. The region enclosed by these lines and containing the origin is the first Brillouin zone (solid hexagon). The shaded area is the irreducible first Brillouin zone. The symmetry points Γ, M and K are also shown.

the high symmetry k-points, are defined as follows

$$\begin{array}{lll} \Gamma: & k_x = 0, & k_y = 0, \\ M: & k_x = \frac{2\pi}{\sqrt{3}a}, & k_y = 0, \\ K: & k_x = \frac{2\pi}{\sqrt{3}a}, & k_y = \frac{2\pi}{3a}. \end{array} \tag{A.11}$$

In figure A.3 we show the Bragg planes (dashed lines) and the first four Brillouin zones for the two-dimensional square lattice and triangular lattice space.

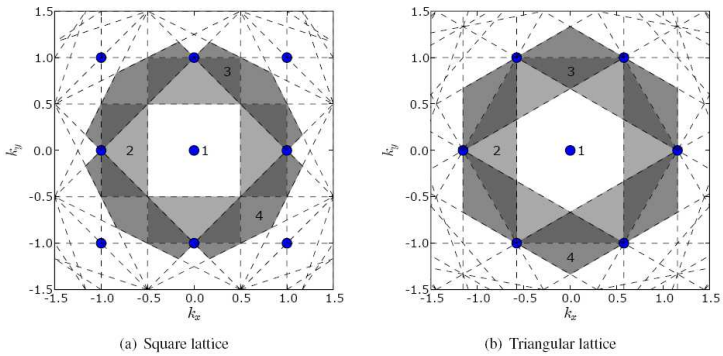

Figure A.3: The Brillouin zones of the square lattice and the triangular lattice. The solid circles are the lattice points and the dashed lines are the Bragg lines. The first four Brillouin zones are marked with different gray scales.

UNIVERSITAT ROVIRA I VIRGILI
DEVELOPMENT OF OPTICAL CHARACTERIZATION METHODS FOR MICRO- AND NANO-SCALE PLANAR PHOTONIC BAND GAP STRUCTURES
Zdenek Kral
DL: T-1537-2009/ISBN:978-84-692-4556-9

UNIVERSITAT ROVIRA I VIRGILI
DEVELOPMENT OF OPTICAL CHARACTERIZATION METHODS FOR MICRO- AND NANO-SCALE PLANAR PHOTONIC BAND GAP STRUCTURES
Zdenek Kral
DL: T-1537-2009/ISBN:978-84-692-4556-9

Appendix B

Published papers and communications

Journal Published Papers

Král, Z., Vojkůvka, L., Garcia-Caurel, E., Ferré-Borrull, J., Marsal, L. F., Pallarés J., *Calculation of angular-dependent reflectance and polarimetry spectra of nanoporous anodic alumina-based photonic crystal slabs*; Photonics and Nanostructures - Fundamentals and Applications, Vol. **7**, Issue **1**, Feb. (2009), p. **12-18**.

Carvajal, J. J, Peña, A., Kumar, R., Pujol, M. C., Mateos, X., Aguiló, M., Díaz, F., Vázquez de Aldana, J. R., Méndez, C., Moreno, P., Roso, L., Trifonov, T., Rodríguez, A., Alcubilla, R., Král, Z., Ferré-Borrull, J., Pallarés, J., Marsal, L. F., Di Finizio, S., Macovez, R., Martorell, J., *New approaches for the fabrication of photonic structures of non-linear optical materials*; Journal of Luminescence, in press, DOI:10.1016/j.jlumin.2009.03.035.

Král, Z., Ferré-Borrull, J., Trifonov, T., Marsal, F. L., Rodríguez, A., Pallarés, J., Alcubilla, R., *Mid-IR Characterization of Photonic Bands in 2D Photonic Crystals on Silicon*; Thin Solid Films, Vol. **516**, Issue: **22**, Sep. (2008), p. **8059-8063**.

DL: T-1537-2009/ISBN:978-84-692-4556-9

Král, Z., Ferré-Borrull, J., Pallarés, J., Trifonov, T., Rodríguez, A., Alcubilla, R., Marsal, F. L., *Characterization of 2D macroporous silicon photonic crystals: improving the photonic band identification in angular-dependent reflection spectroscopy in the mid-IR*; Materials Science and Engineering: B, Vol. **147**, Issues **2-3**, Feb. (2008), p. **179-182**.

Contribution to conferences

Král, Z., Ferré-Borrull, J., Garcia-Caurel, E., Vojkůvka, L., Marsal, F. L., Pallarés, J.,
Oral presentation: Numerical simulation of the photonic band mapping of nanometric porous alumina photonic crystals; E-MRS Spring Meeting, 26-30 May 2008, Strasbourg, France.

Král, Z., Ferré-Borrull, J., Marsal, F. L., Pallarés, J.,
Poster Session: Numerical simulation of angular-dependent reflectance spectroscopy applied to ordered porous alumina; CEN 2008 1st Spanish Conference of Nanophotonics, 2-4 April 2008, Tarragona, Spain.

Král, Z., Ferré-Borrull, J., Trifonov, T., Marsal, F. L., Rodríguez, A., Pallarés, J., Alcubilla, R.,
Oral presentation: Mid-IR Characterization of Photonic Bands in 2D Photonic Crystals on Silicon; E-MRS Fall Meeting, 17-21 September 2007 Warsaw, Poland.

Král, Z., Ferré-Borrull, J., Pallarés, J., Trifonov, T., Rodríguez, A., Alcubilla, R., Marsal, F. L.,
Oral presentation: Reflectivity study of the electromagnetic-wave dispersion relation in two-dimensional macroporous silicon photonic crystals; E-MRS Spring Meeting, 28 May - 1 June 2007, Strasbourg, France.

Král, Z., Ferré-Borrull, J., Marsal, F. L., Pallarés, J., Trifonov, T., Rodríguez, A., Alcubilla, R.,
Poster Session: Reflection analysis of 2D photonic crystal lattice using Bragg-diffraction phenomena; CDE 2007 Spanish Conference on Electron Devices, 31 January - 2 February 2007, El Escorial-Madrid, Spain.

UNIVERSITAT ROVIRA I VIRGILI
DEVELOPMENT OF OPTICAL CHARACTERIZATION METHODS FOR MICRO- AND NANO-SCALE PLANAR PHOTONIC BAND GAP STRUCTURES
Zdenek Kral
DL: T-1537-2009/ISBN:978-84-692-4556-9

Král, Z., Ferré-Borrull, J., Marsal, F. L., Pallarés, J.,
Poster Session: Analysis of 2D photonic crystal lattice using Bragg-diffraction; XXII Trobades Científiques de la Mediterránia , 9-11 October 2006, Mao-Menorca, Spain.

UNIVERSITAT ROVIRA I VIRGILI
DEVELOPMENT OF OPTICAL CHARACTERIZATION METHODS FOR MICRO- AND NANO-SCALE PLANAR PHOTONIC BAND GAP STRUCTURES
Zdenek Kral
DL: T-1537-2009/ISBN:978-84-692-4556-9

Characterization of 2D macroporous silicon photonic crystals: Improving the photonic band identification in angular-dependent reflection spectroscopy in the mid-IR

Zdeněk Král, Josep Ferré-Borrull, Josep Pallarès, Trifon Trifonov, Angel Rodriguez, Ramon Alcubilla, Lluis F. Marsal.

Materials Science and Engineering B, volume 147, pages 179-182, 2008.

UNIVERSITAT ROVIRA I VIRGILI
DEVELOPMENT OF OPTICAL CHARACTERIZATION METHODS FOR MICRO- AND NANO-SCALE PLANAR PHOTONIC BAND GAP STRUCTURES
Zdenek Kral
DL: T-1537-2009/ISBN:978-84-692-4556-9

ELSEVIER

Materials Science and Engineering B 147 (2008) 179–182

MATERIALS SCIENCE & ENGINEERING B

www.elsevier.com/locate/mseb

Characterization of 2D macroporous silicon photonic crystals: Improving the photonic band identification in angular-dependent reflection spectroscopy in the mid-IR

Zdeněk Král [a,*], Josep Ferré-Borrull [a], Josep Pallarès [a], Trifon Trifonov [b], Angel Rodriguez [b], Ramon Alcubilla [b], Lluis F. Marsal [a]

[a] *Nephos, Universitat Rovira i Virgili, Campus Sescelades, Avda. Paisos Catalans 26, 43007 Tarragona, Spain*
[b] *MNT, Universitat Politécnica de Catalunya, Campus Nord, c/ Jordi Girona 1-3, 08034 Barcelona, Spain*

Received 1 July 2007; received in revised form 9 September 2007; accepted 27 September 2007

Abstract

We report the experimental characterization of two-dimensional (2D) macroporous silicon photonic crystals using angular-dependent reflectance spectroscopy in the mid-IR region. We have investigated different sample structures and we have shown that an adequate post-processing of the measured data is crucial in order to recognize the photonic bands and to achieve a good agreement of the measured data with the theoretical predictions for the studied structures.

Keywords: Infrared spectroscopy; Photonic bands; Macroporous silicon; Photonic crystals

1. Introduction

Photonic crystals, first proposed by Yablonovitch [1] and John [2], are artificial materials with a spatial periodicity of their dielectric constant on a wavelength scale. This leads to the existence of photonic bands, which are analogous to the electronic bands in crystalline solids. Furthermore, there exist frequency regions, the photonic band gaps, where light cannot propagate through the material, thus suggesting possibilities for novel light-guiding structures and devices. To enable the fabrication of such devices, it is crucial to have good methods for their characterization.

Photonic crystals have first been characterized in the microwave regime by phase-sensitive transmission measurements [3] that yield the wave vector inside the crystal at a given frequency. Another technique, based on the in-plane transmission in two-dimensional (2D) waveguide photonic crystals has been used to map the photonic bands from Fabry–Pérot fringes within the sample [4]. Several authors have also measured the photonic bands dispersion in 2D photonic crystals by means of the angular-dependent reflectance spectroscopy, first proposed by Astratov et al. [5–9]. This method relies on the observation of resonant features in the reflectance spectra at different incidence angles. The resonant features occur when the incident light wave vector component parallel to the photonic crystal surface ($k_{\parallel}$) matches the wave vector of a propagating mode inside the photonic crystal. The $k_{\parallel}$ is related to the angle of incidence on the photonic crystal surface θ and to the incident light frequency ω as $k_{\parallel} = (\omega/c) \sin\theta$, where c is the speed of light. By recognizing the resonant features in the reflectivity spectra, the photonic bands can be mapped out.

In this paper, we report the characterization of 2D macroporous silicon photonic crystals by angular-dependent reflectance spectroscopy. Many experimental investigations of photonic crystals were linked with this method, but in contrast to previous studies [10–20], the lattice constants of the samples studied here require that the measurements are carried out in the range of the mid-IR. Only few experimental measurements on this range have been reported so far [11,12], and none, up to our knowledge, reached up to 600 cm^{-1}, which is our lower wavenumber limit. The drawback of measuring in such spectral range is the recognition of the resonant features in the spectra. Although in previous

* Corresponding author. Tel.: +34 977 55 86 53.
E-mail address: zdenek.kral@urv.cat (Z. Král).

0921-5107/$ – see front matter © 2007 Elsevier B.V. All rights reserved.
doi:10.1016/j.mseb.2007.09.082

works [5–20] a direct recognition of the resonant features is possible, in the mid-IR range there are several sources of clutter that make this direct recognition a difficult task. Therefore, we propose here a procedure to improve the recognition of the photonic bands and we report the application of this procedure to our samples.

2. Sample preparation

Macroporous silicon photonic crystals of different lattice types were prepared by a photo-electrochemical etching process. An n-type (1 0 0) silicon wafer with a resistivity of 2–6 Ω cm was first pre-structured by oxidation, photolithography and subsequent tetramethyl ammonium hydroxide (TMAH) etching to form the initial pits. Such a patterned structure consists of ordered pyramidal notches that act as nucleation centers for the subsequent ordered pore growth. The pore growth mechanism is ruled by the reverse-biased space charge region at the silicon–electrolyte interface. The positive carriers (holes), required for anodic dissolution of silicon, are focused mainly at the pore tips, which let the pores grow perpendicularly to the surface and at the same time the pore walls become passivated against dissolution. In order to create a good ohmic contact at the silicon–electrolyte interface, a uniform n^+-layer was created on the wafer backside by ion implantation. The electrochemical etching was carried out in aqueous hydrofluoric acid (HF) with a concentration of 5 wt.% at 15 °C. During the anodization, the wafer was backside illuminated by a 100 W halogen lamp, coupled to an IR cut-off filter. More detailed information about the sample fabrication and sample structures used in this paper can be found elsewhere [21].

3. Experimental measurements

All the studied samples have lattice constants that range between 4 μm and 5 μm. Standard plane–wave expansion band calculations show that, for these lattice constants, the first photonic bands lie in the mid-IR range. For this reason, the angular-dependent reflectivity was measured in the mid-IR region (4000–400 cm^{-1}) using a Fourier-transform IR spectrometer (Bruker, model Vertex 70) equipped with a special reflectivity attachment. The light source was a broadband halogen–tungsten lamp. The angle of incidence θ was varied from 12° to 66° in steps of 2° and the plane of incidence was perpendicular to the sample surface. The reflectivity spectra were recorded with a liquid-nitrogen-cooled MCT detector. The spectral resolution was set to 4 cm^{-1}. A polished n-type silicon wafer was used as absolute reflectance reference. The measurements were performed for light incident along the ΓX and ΓM lattice orientations for the square lattice structure, and along the ΓM and ΓZ directions for the triangular lattice.

4. Results and discussion

To recognize the resonant features associated to the coupling of the incident light to the photonic bands we first represent the measured spectra as a 2D plot of the angular-dependent reflectivity versus the wavenumber and the incident light wavevector component parallel to the surface ($k_\parallel$). A representative example of this plot is shown in Fig. 1, where the inset shows the measured structure, the lattice constant a and the measurement direction. The lines correspond to the photonic bands calculated using the known sample geometrical parameters and optical properties. The solid lines correspond to the TE bands while the dashed lines correspond to TM. The black solid line corresponds to the light line (corresponding to an angle of incidence of 90°).

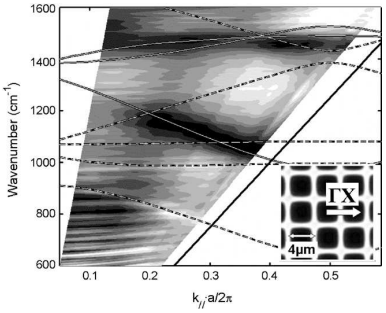

Fig. 1. 2D plot of the angular-dependent reflectivity spectra versus the wavenumber and the angle of incidence. The photonic bands are overlapped to the 2D plot, the -dashed lines and full lines correspond to the TM and TE polarizations, respectively. The inset shows the measured macroporous silicon structure where the lattice constant and the measured lattice direction are indicated.

In this example, it can be seen that in the mid-IR spectral region the coupling is weak and that there exist other features not related to the photonic bands (such as those related to the silicon optical properties [5,11,12]) which make specially difficult the recognition of the resonant features. The calculated photonic bands overlapped to the 2D plot may assist to this recognition, but even in this case the corresponding features are difficult to be seen.

In order to improve the resonant feature recognition, it must be noted that the wavenumber of the photonic bands usually changes with $k_\parallel$, while the material-related features correspond to a fixed wavenumber. This leads to the idea that calculating the partial derivative of the reflectance with respect to the incidence angle may be useful to filter out the material-related features. For our measurements, this partial derivative is approximated using finite differences between two reflectivity spectra corresponding to two neighboring angles. Thus, if the reflectance R is measured at a set of wavenumbers $\{\omega_i\}$ and of incidence angles $\{\theta_j\}$, the partial derivative at a wavenumber ω_i and angle of incidence θ_j is expressed as

$$\frac{\partial R}{\partial \theta}(\omega_i, \theta_j) \approx \frac{R(\omega_i, \theta_{j+1}) - R(\omega_i, \theta_j)}{\theta_{j+1} - \theta_j} \quad (1)$$

Fig. 2 shows the 2D plot of the $\partial R/\partial\theta$ for the same measurement as in Fig. 1 together with the calculated photonic bands.

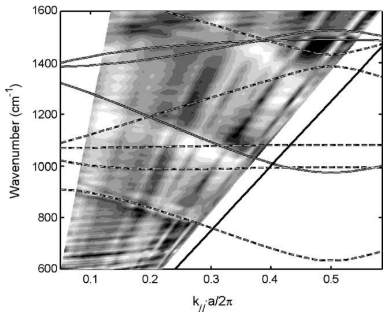

Fig. 2. 2D plot of the $\partial R/\partial\theta$ corresponding to the measurement shown in Fig. 1, overlapped with the calculated photonic bands.

This magnitude permits a better recognition of the photonic band resonant features.

A further improvement in the recognition can be obtained if the 2D plot of the $\partial R/\partial\theta$ is restricted to a wavenumber range where fewer photonic bands are expected. With this, two main outcomes are expected: (i) restricting the range reduces the overall reflectance spectral variations and thus the photonic band-related resonances are in relation enlarged, and (ii) by choosing a range where a small number of photonic bands are expected, it should be easier to distinguish their related features from others. Fig. 3 shows the 2D plot of the reflectance spectra for the same measurement as in Fig. 1, but with a restricted wavenumber range, where the first TM band is clearly identified.

This procedure has been applied to the characterization of macroporous silicon photonic crystals with different lattice structures. Fig. 4 shows a representative set of the obtained results corresponding to samples with square and triangular lattices. The lattice type, the lattice dimension and the lattice orientation of the measurement are specified in the insets.

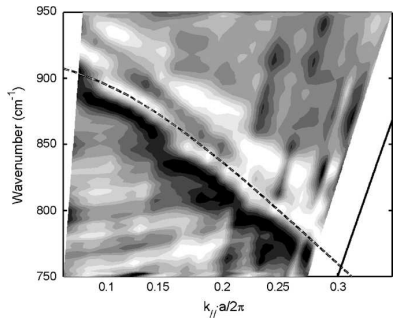

Fig. 3. Range-restricted 2D plot of the $\partial R/\partial\theta$ corresponding to the measurement shown in Fig. 1.

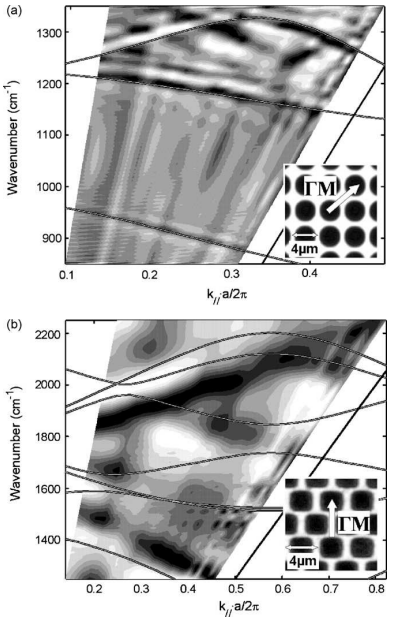

Fig. 4. Measured photonic bands for different samples: (a) round holes in a square lattice and (b) rounded square holes in a triangular lattice. The measured lattice direction and the lattice constant are indicated in the insets.

5. Conclusions

We have applied the angular-dependent reflectivity technique to the characterization of porous silicon photonic crystals. The characteristics of the samples require that the measurement is performed in the mid-IR, which implies the adaptation of the technique. In this spectral range, the recognition of the photonic band-related features is difficult and it is necessary to develop a procedure to post-process the data and improve the band measurement. The procedure is based on the analysis of the 2D plot of the reflectance spectra as a function of the wavevector component parallel to the sample surface and the wavenumber together with the calculated photonic bands. Furthermore, the partial derivative of the reflectance with respect to the incidence angle is used to filter-out the material-related resonances and improve the resonant feature recognition. Finally, by restricting the wavenumber range of the 2D plot, the visibility of the

resonant features is further enhanced. With this method we have been able to distinguish several photonic bands in macroporous silicon structures with different lattice constants and lattice structures.

Acknowledgements

This work was supported by the TEC2006-06531 project from the Spanish Ministerio de Educación y Ciencia. Zdenek Král is grateful to the University Rovira i Virgili for the financial support. Josep Ferré-Borrull acknowledges the Ramon y Cajal fellowship from the Spanish Ministerio de Educación y Ciencia.

References

[1] E. Yablonovitch, Phys. Rev. Lett. 58 (1987) 2059–2062.
[2] S. John, Phys. Rev. Lett. 58 (1987) 2486–2489.
[3] E. Yablonovitch, T.J. Gmitter, Phys. Rev. Lett. 63 (1989) 1950–1953.
[4] D. Labilloy, H. Benisty, C. Weisbuch, T.F. Krauss, R.M. DeLaRue, V. Bardinal, R. Houdre, U. Oesterle, D. Cassagne, C. Jouanin, Phys. Rev. Lett. 79 (1997) 4147–4150.
[5] V.N. Astratov, M.S. Skolnick, S. Brand, T.F. Krauss, O.Z. Karimov, R.M. Stevenson, D.M. Whittaker, I. Culshaw, R.M. De la Rue, IEE P-Optoelectron. 145 (1998) 398–402.
[6] V.N. Astratov, I.S. Culshaw, R.M. Stevenson, D.M. Whittaker, M.S. Skolnick, T.F. Krauss, R.M. De la Rue, J. Lightwave. Technol. 17 (1999) 2050–2057.
[7] V.N. Astratov, D.M. Whittaker, I.S. Culshaw, R.M. Stevenson, M.S. Skolnick, T.F. Krauss, R.M. De la Rue, Phys. Rev. B 60 (1999) R16255–R16258.
[8] V.N. Astratov, R.M. Stevenson, I.S. Culshaw, D.M. Whittaker, M.S. Skolnick, T.F. Krauss, R.M. De la Rue, Appl. Phys. Lett. 77 (2000) 178–180.
[9] V.N. Astratov, R.M. Stevenson, I.S. Culshaw, D.M. Whittaker, M.S. Skolnick, T.F. Krauss, R.M. De la Rue, Phys. Stat. Sol. A 178 (2000) 565–569.
[10] L.C. Andreani, M. Agio, IEEE J. Quantum. Elect. 38 (2002) 891–898.
[11] P. Bettotti, L. Dal Negro, Z. Gaburro, L. Pavesi, A. Lui, M. Galli, M. Patrini, F. Marabelli, J. Appl. Phys. 92 (2002) 6966–6972.
[12] M. Galli, M. Agio, L.C. Andreani, M. Belotti, G. Guizzetti, F. Marabelli, M. Patrini, P. Bettotti, L. Dal Negro, Z. Gaburro, L. Pavesi, A. Liu, P. Bellutti, Phys. Rev. B 65 (2002) 113111.
[13] M. Galli, M. Agio, L.C. Andreani, L. Atzeni, D. Bajoni, G. Guizzetti, L. Businaro, E. Di Fabrizio, F. Romanato, A. Passaseo, Eur. Phys. J. B 27 (2002) 79–87.
[14] M. Patrini, M. Galli, F. Marabelli, M. Agio, L.C. Andreani, D. Peyrade, Y. Chen, IEEE J. Quantum. Elect. 38 (2002) 885–890.
[15] D. Peyrade, Y. Chen, A. Talneau, M. Patrini, M. Galli, F. Marabelli, M. Agio, L.C. Andreani, E. Silberstein, P. Lalanne, Microelectron. Eng. 61 (2) (2002) 529–536.
[16] L.C. Andreani, M. Agio, D. Bajoni, M. Belotti, M. Galli, G. Guizzetti, A.M. Malvezzi, F. Marabelli, M. Patrini, G. Vecchi, Synth. Met. 139 (2003) 695–700.
[17] M. Patrini, M. Galli, A. Agio, L.C. Andreani, D. Bajoni, G. Guizzetti, L. Businaro, E. Di Fabrizio, F. Romanato, A. Passaseo, Physica E 17 (2003) 418–419.
[18] M. Galli, D. Bajoni, F. Marabelli, L.C. Andreani, L. Pavesi, G. Pucker, Phys. Rev. B 69 (2004) 115107.
[19] M. Galli, M. Belotti, D. Bajoni, M. Patrini, G. Guizzetti, D. Gerace, M. Agio, L.C. Andreani, Y. Chen, Phys. Rev. B 70 (2004) 081307.
[20] E. Pavarini, L.C. Andreani, C. Soci, M. Galli, F. Marabelli, D. Comoretto, Phys. Rev. B 72 (2005) 045102.
[21] T. Trifonov, L.F. Marsal, A. Rodriguez, J. Pallares, R. Alcubilla, Phys. Stat. Sol. (c) 2 (2005) 3104–3107.

Mid-IR characterization of photonic bands in 2D photonic crystals on silicon

Zdeněk Král, Josep Ferré-Borrull, Trifon Trifonov, Lluis F. Marsal, Angel Rodriguez, Josep Pallarès, Ramon Alcubilla.

Thin Solid Films, volume 516, pages 8059-8053, 2008.

UNIVERSITAT ROVIRA I VIRGILI
DEVELOPMENT OF OPTICAL CHARACTERIZATION METHODS FOR MICRO- AND NANO-SCALE PLANAR PHOTONIC BAND GAP STRUCTURES
Zdenek Kral
DL: T-1537-2009/ISBN:978-84-692-4556-9

Available online at www.sciencedirect.com
ScienceDirect
Thin Solid Films 516 (2008) 8059–8063
www.elsevier.com/locate/tsf

Mid-IR characterization of photonic bands in 2D photonic crystals on silicon

Zdeněk Král [a], Josep Ferré-Borrull [a,*], Trifon Trifonov [b], Lluis F. Marsal [a], Angel Rodriguez [b], Josep Pallarès [a], Ramon Alcubilla [b]

[a] NePhoS, Universitat Rovira i Virgili, Campus Sescelades, Avda. Paisos Catalans 26, 43007 Tarragona, Spain
[b] MNT, Universitat Politécnica de Catalunya, Campus Nord, c/ Jordi Girona 1–3, 08034 Barcelona, Spain

Available online 10 April 2008

Abstract

We report the characterization of two-dimensional silicon photonic crystals using angular-dependent reflectivity in the mid-IR. The photonic crystals are obtained by electrochemical etching of an ordered array of holes into silicon. The measurements are compared with the theoretical calculations of the corresponding model based on the interaction of the incident light with the photonic crystal sample. A good agreement between the measurements and the calculations is achieved.

Keywords: Infra-red spectroscopy; Photonic bands; Macroporous silicon; Photonic crystals

1. Introduction

Photonic crystals [1, 2] are artificial materials with a spatial periodicity of their dielectric constant on a wavelength scale. This leads to the existence of photonic bands, analogous to the electronic bands in crystalline solids, and to photonic band gaps: frequency ranges where light cannot propagate through the material. Photonic crystals offer great possibilities for novel light-guiding structures and devices and their characterization is a key issue for the fabrication of such devices.

Several methods for the characterization of photonic crystals have been proposed. In the microwave regime phase-sensitive transmission measurements have been used [3] to obtain the wave vector inside the crystal at a given frequency. Another technique, based on the in-plane transmission in two-dimensional (2D) waveguide photonic crystals has been used to map the photonic bands from Fabry–Pérot fringes within the sample [4]. One of the most widespread techniques is the angular-dependent reflectance spectroscopy [5–9], which is based on the identification of resonant features in the reflectivity spectra at different angles of incidence. Such resonant features are related to the coupling of the incident light into the photonic crystal. They appear when the incident light wavevector component parallel to the photonic crystal surface ($k_{//}$) matches the wave vector of a propagating mode inside the photonic crystal. The $k_{//}$ is related to the angle of incidence on the photonic crystal surface θ and to the incident light frequency ω as $k_{//}=(\omega/c)\sin\theta$, where c is the speed of light. By recognizing the resonant features in the reflectivity spectra, the photonic bands can be mapped out.

In this paper we report the characterization of 2D macroporous silicon photonic crystals by angular-dependent reflectance spectroscopy. We first focus on the modeling of the interaction of the incident light with the sample, to be able to simulate and interpret the measurements. Then, we will show the experimental measurements and we will compare them with the results obtained from the modeling.

2. Modeling of the spectrophotometric characterization of 2D photonic crystals

The method we apply to characterize the photonic crystal samples is the angular-dependent reflectance spectroscopy. The experimentally measured reflectance spectra are then compared with model calculations, which simulate the interaction of a plane wave (incident at a given angle and with a given polarization) with the photonic crystal sample. The model allows to evaluate the coupling efficiency of the incident wave to the photonic modes and to obtain the reflection and transmission coefficients.

The samples we study consist of an ordered array of holes etched in a silicon wafer and perpendicular to the sample surface. The distance between holes is constant and ranges

* Corresponding author. Tel.: +34 977 55 86 53.
E-mail address: josep.ferre@urv.cat (J. Ferré-Borrull).

0040-6090/$ - see front matter © 2008 Elsevier B.V. All rights reserved.
doi:10.1016/j.tsf.2008.04.013

between 4 and 6 μm, their shape is approximately square (square with rounded edges), their width is between 1 and 2 μm and their depth can reach up to 200 μm.

The method we use is based on the scattering matrix treatment proposed by Whittaker et al. [10]. This method relies on the plane-wave expansion (PWE) method but it includes some particularities to achieve the goal of calculating the angular-dependent reflectance spectra. The PWE method has its origin in the fact that the refractive index of the photonic crystal is periodic, which implies that any electromagnetic wave propagating inside the material fulfills the Bloch theorem:

$$\mathbf{H}(\mathbf{r}+\mathbf{R}) = e^{j\mathbf{k}\cdot\mathbf{R}}\mathbf{H}(\mathbf{r}), \tag{1}$$

(and equivalently for the electric field). In Eq. (1) $\mathbf{r}=(x,y)$ is the position in the plane of symmetry of the photonic crystal (the holes are oriented along the z direction), $\mathbf{R}$ is a lattice vector and $\mathbf{k}=(k_x,k_y)$ is the in-plane Bloch wavevector. Thus, the plane wave expansion assumes that this wave can be expanded in a sum of plane waves propagating along all the directions defined by the reciprocal lattice:

$$\mathbf{H}(\mathbf{r}) = \sum_{\mathbf{G}} \mathbf{h}_{\mathbf{k}}(\mathbf{G}) e^{j(\mathbf{k}+\mathbf{G})\cdot\mathbf{r}}, \tag{2}$$

where the $\mathbf{G}$ are the reciprocal lattice vectors and the $\mathbf{h_k(G)}$ are the expansion coefficients . It can be shown that Eq. (2) fulfills the Bloch theorem. By restricting the expansion to a limited number of plane waves and applying Maxwell's equations to Eq. (2) (and its equivalent for the electric field) a set of eigenvalue problems is derived. This set can be separated in two independent eigenvalue equations by recalling that for 2D photonic crystals two independent polarizations (TE and TM, with the magnetic and electric fields along the holes, respectively) can be defined. The result of these eigenvalue problems is that for a given Bloch wavevector $\mathbf{k}$ only some frequencies can propagate inside the photonic crystal, giving rise to the photonic bands and the photonic band gaps.

The PWE method considers the 2D photonic crystal as indefinite in the z direction, however this is not the case of our samples, where the photonic crystal is delimited by the sample surface and by the substrate. The model we use to calculate the angular-dependent reflectance introduces the third dimension by allowing the wave to propagate also along the z direction:

$$\mathbf{H}(\mathbf{r},z) = \sum_{\mathbf{G}} \mathbf{h}_{\mathbf{k}}(\mathbf{G}) e^{j(\mathbf{k}+\mathbf{G})\cdot\mathbf{r}+iqz}, \tag{3}$$

where q is the out-of-plane wavevector component. By limiting the expansion and applying Maxwell's equations to Eq. (3) an eigenvalue problem is obtained for q, for given $\mathbf{k}$ and wave frequency. Taking into account that the in-plane wavevector $\mathbf{k}$ is conserved through all the interfaces of the sample (incident medium-photonic crystal and photonic crystal-substrate), the eigenstates with their corresponding eigenvalues $\{q_n\}$ obtained from this problem can be used to calculate the efficiency of the coupling of an incident plane wave with a given $\mathbf{k}$ and frequency to the structure. This is done with the help of a scattering matrix procedure which is obtained by applying the boundary conditions to the fields at each side of an interface. This coupling efficiency can be then translated into reflection and transmission coefficients, and subsequently into angular-dependent transmittance and reflectance spectra.

It must be noted that, from the mathematical derivation of the scattering matrix treatment it can be concluded that there may not be only one mode propagating within the photonic crystal sample with a given $\mathbf{k}$, but several modes for different values of q, and that these modes do not propagate parallel to the sample surface.

Fig. 1 shows the calculation of the reflectance spectra for TE-polarized light for a sample consisting of square holes etched on silicon in a square lattice. The incident light is directed along the rows of the photonic crystal (the ΓX lattice direction). The lattice constant is 4 μm, the width of the holes is 2 μm and the depth is 7.5 μm. The corresponding angles of incidence are indicated in the graph. The photonic band-related resonant features can be either maxima, minima or inflection points of the spectra. One of the resonant features is indicated by arrows, as it can be seen, its wavenumber changes with the incidence angle. Nevertheless, with this representation it is difficult to recognize the photonic band-related resonant features.

A better visualization of the angular-dependent reflectance spectra can be obtained with a 2D representation of the reflectance as a function of the angle of incidence and the frequency. This representation is shown in Fig. 2a), for the same sample as in the previous figure and also for TE-polarization. The photonic bands of the corresponding infinite photonic crystal are also included (black solid lines). In this representation the resonant features can be clearly identified, but a shift between the frequency of the photonic bands and the resonant features can be seen. This shift is due to the fact that the incident light is coupled to modes with a nonzero q, or equivalently to modes that do not travel parallel to the sample surface.

Finally, Fig. 2b) shows the angular-dependent reflectivity spectra for the TE polarization of a sample with the same characteristics as in the previous figures but with a bigger thickness: 12.5 μm. The resonant features can also be recognized, but it is worth noting that, for a given band, there are several corresponding resonant features. This indicates that the incident

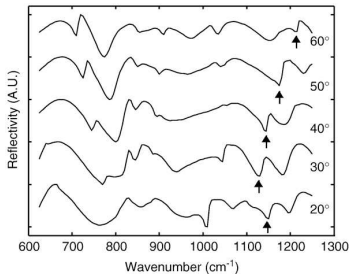

Fig. 1. Calculated angular-dependent reflectivity spectra for different incidence angles (indicated at the right) for TE-polarized light and for the ΓX lattice direction. The arrows point to a photonic-band related resonant feature.

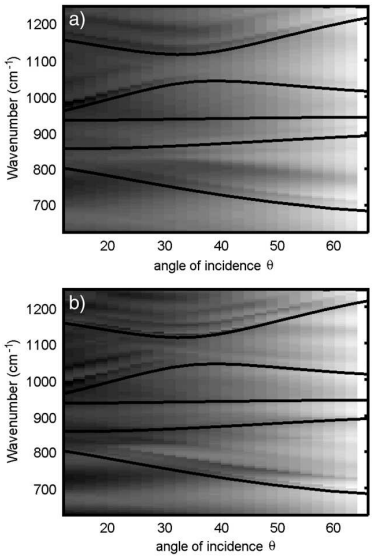

Fig. 2. 2D plots of the calculated angular-dependent reflectivity spectra as a function of the angle of incidence and of the wavenumber, for TE-polarized light and for the ΓX lattice direction. The calculations correspond to two samples with a square lattice of square holes etched on silicon. The distance between holes is 4 μm, their width is 2 μm and their depth is 7.5 μm for a) and 12.5 μm for b). The photonic-band resonant features can be recognized easily. The lines correspond to the actual photonic bands for the structure.

light couples to more that one mode with the same **k** but with different q. From these two figures, we can conclude that when the depth of the holes increases, the number of modes that can propagate inside the photonic crystal with the same **k** and different q increases. Furthermore, the shift between the photonic band and the lowest resonant feature associated with that band becomes smaller for increasing hole depth. This indicates that as the hole depth increases, the wave can propagate inside the photonic crystal in a direction with a smaller angle with the interface. Another characteristic of the spectra in Fig. 2b) must be noted: the reflectance shows oscillations, particularly in the range of the lower angles. These oscillations correspond to Fabry–Pérot interferences between the interfaces of the photonic crystal layer.

3. Experimental

3.1. Sample preparation

The macroporous silicon photonic crystals were prepared by a photo-electrochemical etching process: n-type (100) silicon wafers with 2–6 Ω cm resistivity were first pre-patterned by a standard photolithography process to form the initial pits. Such a patterned structure consists of ordered pyramidal notches that act as nucleation centers for the subsequent ordered pore growth. The pore growth mechanism is ruled by the reverse-biased space charge region at the silicon-electrolyte interface. The positive carriers (holes), required for anodic dissolution of silicon, are focused mainly at the pore tips, which let the pores grow perpendicularly to the surface and at the same time passivates pore walls against dissolution. The electrochemical etching was carried out in aqueous hydrofluoric acid (HF) with a concentration of 5 wt.% at 15 °C. During the anodization, the wafer was backside illuminated by a 100 W halogen lamp, coupled to an IR cut-off filter in order to generate positive carriers for the dissolution. More detailed information about the sample fabrication and sample structures used in this paper can be found elsewhere [11].

3.2. Experimental measurements

The studied samples have a 4 μm lattice constant, which implies that the first photonic bands lie in the mid-IR range. For this reason, the angular-dependent reflectivity was measured in the mid-IR region (4000–400 cm^{-1}) using a Fourier-transform IR spectrometer (Bruker, model Vertex 70) equipped with a special reflectivity attachment. The light source was a broad-band halogen–tungsten lamp. The angle of incidence θ was varied from 12° to 66° in steps of 2°, the plane of incidence was perpendicular to the sample surface and the incident light was unpolarized. The reflectivity spectra were recorded with a liquid nitrogen-cooled MCT detector and the spectral resolution was set to 4 cm^{-1}. A polished n-type silicon wafer was used as reflectance reference.

In the mid-IR spectral region it is especially difficult to identify the photonic band-related resonant features because they appear together with several other features. As it was shown in the previous section, the photonic band-related vary their frequency with the angle of incidence, instead, the other features present in the spectra usually correspond to fixed-frequency resonances. For these reasons, to analyze the angular-dependent reflectivity measurements it is convenient to work with the partial derivative of the reflectivity with respect to the angle [12]. Using this partial derivative, the features with constant frequency with the angle are filtered out, leaving features related to the photonic bands.

Since the measurements are carried out at a discrete number of angles, this partial derivative is approximated by the difference of the spectra for consecutive measured angles:

$$\frac{\partial R}{\partial \theta}\left(\omega_i, \theta_j\right) \approx \frac{R\left(\omega_i, \theta_{j+1}\right) - R\left(\omega_i, \theta_j\right)}{\theta_{j+1} - \theta_j}, \tag{4}$$

where the $\{\omega_i\}$ are the frequencies and the $\{\theta_j\}$ the angles of incidence where the measurements are performed.

Fig. 3 shows the obtained $\partial R/\partial\theta$ for three samples consisting of square holes in a square lattice with a lattice constant 4 μm. The depth of the holes is (from top to bottom) 7.5, 12.5 and

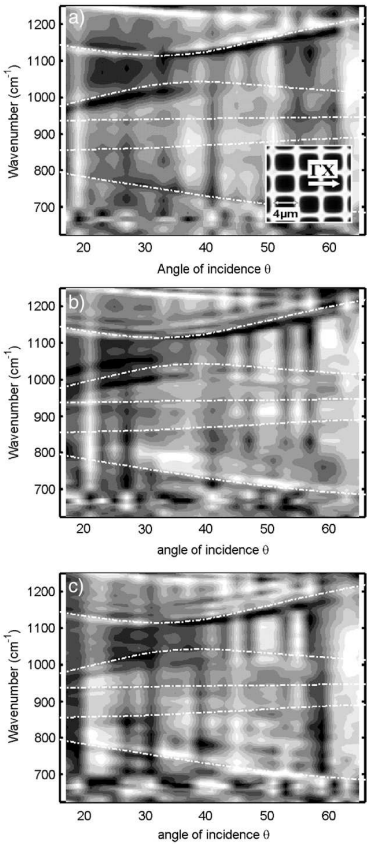

Fig. 3. Measured $\partial R/\partial\theta$ for samples consisting of a square lattice of square holes etched on silicon. The depth of the holes is a) 7.5 μm, b) 12.5 μm and c) 17.5 μm. The inset shows a top view of the sample with the lattice constant and the measurement direction indicated. The corresponding bands for TE-polarized light have been included, while the measurements are carried out using unpolarized light.

17.5 μm. The measurement direction is ΓX. The inset shows a microscope image of the surface of the 7.5 μm hole depth sample, together with the lattice constant and the measurement direction. The corresponding photonic bands for the TE polarization and for the ΓX direction calculated for this sample (taking as the width of the square holes 2 μm) are overlapped to the measurements as dot–dashed white lines.

From the figure it can be deduced that, even after the post-processing with the $\partial R/\partial\theta$, it is difficult to directly recognize the resonant features. The calculated photonic bands overlapped to the measurement help in this recognition and show a clear coupling associated with the lowest band (beginning at 800 cm^{-1} at 20°) and the highest band (beginning at 1150 cm^{-1} at 20°). Furthermore, for the graphs b) and c), the resonant features corresponding to the highest band are repeated at higher frequencies and their number increases with increasing hole depth. This indicates the coupling to the different modes associated to the same band but with different q, and it is in agreement with the calculations.

It is worth noting that although these measurements are carried out with unpolarized light, only TE bands can be recognized. This is also in agreement with the calculations, that do not predict coupling to TM modes in this frequency region for these samples.

4. Conclusions

We applied the angular-dependent reflectivity technique in the mid-IR to the characterization of macroporous silicon photonic crystals. These photonic crystals consist of an ordered array of holes electrochemically etched in a silicon matrix.

The characterization consists in the measurement of the angular-dependent reflectivity with an FTIR equipment and the comparison of the measurement with the mathematical modeling of the interaction of the incident light with the photonic crystal.

From the calculations we have observed that for a given photonic band of the infinite photonic crystal, the incident light can couple to several modes in the finite photonic crystal constituted by our samples. These modes correspond to waves that propagate at different angles with respect to the sample surface. Furthermore, the number of these modes increases with increasing depth of the etched holes.

Finally, we have compared the calculations with the measurement of real samples. We observed that, after the proper post-processing of the data, the spectra show resonant features that can be associated to photonic bands. The existence of several resonant features for a single photonic band, their increasing number with increasing hole depth and the coupling of only TE modes are in good agreement with the calculations.

Acknowledgements

This work was supported by the TEC2006-06531 project from the Spanish Ministerio de Educación y Ciencia. Zdeněk Král is grateful to the University Rovira i Virgili for the financial support. Josep Ferré-Borrull acknowledges the Ramon y Cajal fellowship from the Spanish Ministerio de Educación y Ciencia.

References

[1] E. Yablonovitch, Phys. Rev. Lett. 58 (1987) 2059.
[2] S. John, Phys. Rev. Lett. 58 (1987) 2486.

[3] E. Yablonovitch, T.J. Gmitter, Phys. Rev. Lett. 63 (1989) 1950.
[4] D. Labilloy, H. Benisty, C. Weisbuch, T.F. Krauss, R.M. DeLaRue, V. Bardinal, R. Houdre, U. Oesterle, D. Cassagne, C. Jouanin, Phys. Rev. Lett. 79 (1997) 4147.
[5] V.N. Astratov, M.S. Skolnick, S. Brand, T.F. Krauss, O.Z. Karimov, R.M. Stevenson, D.M. Whittaker, I. Culshaw, R.M. De la Rue, IEE P-Optoelectron. 145 (1998) 398.
[6] V.N. Astratov, I.S. Culshaw, R.M. Stevenson, D.M. Whittaker, M.S. Skolnick, T.F. Krauss, R.M. De la Rue, J. Lightwave. Technol. 17 (1999) 2050.
[7] V.N. Astratov, D.M. Whittaker, I.S. Culshaw, R.M. Stevenson, M.S. Skolnick, T.F. Krauss, R.M. De la Rue, Phys. Rev. B 60 (1999) R16255.
[8] V.N. Astratov, R.M. Stevenson, I.S. Culshaw, D.M. Whittaker, M.S. Skolnick, T.F. Krauss, R.M. De la Rue, Appl. Phys. Lett. 77 (2000) 178.
[9] V.N. Astratov, R.M. Stevenson, I.S. Culshaw, D.M. Whittaker, M.S. Skolnick, T.F. Krauss, R.M. De la Rue, Phys. Status. Solidi. A 178 (2000) 565.
[10] D.M. Wittaker, I.S. Culshaw, Phys. Rev. B, 60 (1999) 2610.
[11] T. Trifonov, L.F. Marsal, A. Rodriguez, J. Pallares, R. Alcubilla, Phys. Stat. Sol. C 2 (2005) 3104.
[12] Z. Kral, J. Ferré-Borrull, J. Pallarès, T. Trifonov, A. Rodriguez, R. Alcubilla, L.F. Marsal, Materials Science and Enginerring B 147 (2008) 179.

UNIVERSITAT ROVIRA I VIRGILI
DEVELOPMENT OF OPTICAL CHARACTERIZATION METHODS FOR MICRO- AND NANO-SCALE PLANAR PHOTONIC BAND GAP STRUCTURES
Zdenek Kral
DL: T-1537-2009/ISBN:978-84-692-4556-9

Calculation of Angular-Dependent Reflectance and Polarimetry Spectra of Nanoporous Anodic Alumina-Based Photonic Crystal Slabs

Zdeněk Král, Lukas Vojkuvka, Enric Garcia-Caurel, Josep Ferré-Borrull, Lluis F. Marsal, Josep Pallarès.

Photonics and Nanostructures - Fundamentals and Applications, volume 7, pages 12-18, 2009.

UNIVERSITAT ROVIRA I VIRGILI
DEVELOPMENT OF OPTICAL CHARACTERIZATION METHODS FOR MICRO- AND NANO-SCALE PLANAR PHOTONIC BAND GAP STRUCTURES
Zdenek Kral
DL: T-1537-2009/ISBN:978-84-692-4556-9

Available online at www.sciencedirect.com
ScienceDirect
ELSEVIER
Photonics and Nanostructures – Fundamentals and Applications 7 (2009) 12–18
PHOTONICS AND NANOSTRUCTURES Fundamentals and Applications
www.elsevier.com/locate/photonics

Invited Paper

Calculation of Angular-Dependent Reflectance and Polarimetry Spectra of Nanoporous Anodic Alumina-Based Photonic Crystal Slabs

Zdeněk Král [a], Lukáš Vojkůvka [a], Enric Garcia-Caurel [b,*], Josep Ferré-Borrull [a], Lluis F. Marsal [a], Josep Pallarès [a]

[a] *NePhoS, Departament d'Enginyeria Electrònica, Elèctrica i Automàtica, Universitat Rovira i Virgili, Av. Paisos Catalans, 26, 43007 Tarragona, Spain*
[b] *Laboratoire de Physique des Interfaces et des Couches Minces, École Polytechnique, Batiment 406, 91128 Palaiseau Cedex, France*

Received 28 July 2008; received in revised form 15 October 2008; accepted 24 November 2008
Available online 30 November 2008

Abstract

Calculations of angular-dependent reflectance and polarimetry spectra of nanoporous anodic alumina-based two-dimensional photonic crystal slabs are presented. The calculations are obtained using a scattering matrix numerical model that gives the polarization change as a function of the incidence angle and of the wavelength. The results reveal that the incident light can couple to several modes propagating in the photonic crystal slab at different angles with respect to the sample surface, and that the number of these modes increases with increasing pore depth. Two different lattice structures are studied: triangular and square. For the triangular lattice the off-diagonal components of the Jones Matrix show a certain amount of cross-polarization, while for the square lattice, there is no cross-polarization.

PACS : 07.60.Fs; 42.70.Qs; 78.20.Bh

Keywords: Spectroscopic polarimetry; Photonic crystals; Porous alumina; Optical characterization; Numerical simulation

1. Introduction

Photonic crystals are materials with a periodic variation of its refractive index on a wavelength scale [1–3]. The particular behaviour of photons inside these materials, with the existence of photonic bands and photonic band gaps, makes them interesting for a great variety of applications: photonic crystal fibres [4], low-threshold lasers [5], photonic circuits [6], etc. Two-dimensional (2D) photonic crystals are a particular class of such materials that can be fabricated with many different techniques, mainly by combination of lithography and etching [7–9]. Nanoporous anodic aluminium oxide (np-AAO) is a material fabricated by anodization of aluminium foils with the pores naturally ordered in a triangular 2D lattice [10–12]. With the conventional methods for growing np-AAO, the pores are naturally ordered but not all over the sample surface [13]. However, in order to obtain perfectly ordered samples, nanoimprint prepatterning techniques can be used [14]. This material may be of special interest in photonic applications for the visible range of the

* Corresponding author at: Laboratoire de Physique des Interfaces et des Couches Minces, École Polytechnique, Batiment 406, 91128 Palaiseau Cedex, France.
E-mail address: josep.ferre@urv.cat (E. Garcia-Caurel).

1569-4410/$ – see front matter
doi:10.1016/j.photonics.2008.11.005

electromagnetic spectrum for several reasons: (i) its dimensions can be tuned for applications in the visible range [15], (ii) it is relatively transparent in this range [16], and (iii) it has luminescent properties [17].

The optical characterization of photonic crystals is an interesting research subject due to the particular optical behaviour of these materials. Much research has been devoted to the development of new characterization techniques that measure different aspects of this optical behaviour: measurement of the photonic band gaps [18], transmission and reflection properties through the photonic crystal samples [19], or measurement of the photonic bands [20]. One of the techniques to measure photonic bands is the Angular-Dependent Reflection Spectroscopy (ADRS) [21–25]. In our previous works we applied this technique to 2D photonic crystals based on macroporous silicon produced by electrochemical etching [26,27].

Spectroscopic polarimetry is a technique widely used in the optical characterization of a great variety of samples [28–31]. Polarimetry measures the change in the polarization state of the light upon reflection or transmission, thus polarimetry is specially suited to materials that show optical anisotropy. 2D photonic crystals, and in particular np-AAO-based photonic crystal slabs, are materials with an inherent optical anisotropy [32]: the photonic bands and the photonic band gaps depend strongly on the light polarization and propagation direction.

In this work we aim at applying an alternative to the ADRS, the angular-dependent reflection polarimetry, to the optical characterization of np-AAO-based photonic crystal slabs. The main objective of this communication is the simulation of such polarimetry measurements. The technique that will be used is the Mueller matrix polarimetry, which involves the complete polarimetric description of the light by real four-dimensional Stokes vectors and the polarization changes with 4×4 Mueller matrices. Our goal is simulating measurements performed with a spectroscopic Mueller polarimeter, designed to work in a broad spectral range (from UV to near IR) [33]. Such instrument is particularly suited to our nanoscale porous alumina photonic crystal slabs, as its expected photonic bands lay in the visible range. This optical instrument is based on modulation and analysis of light polarization by ferroelectric liquid crystals cells. It consists of a polarization state generator (PSG) and polarization state analyzer (PSA) that can be adapted to work in reflection or transmission mode. Both incident (PSG) and reflection (PSA) arms are attached to a goniometry unit that permits variable-angle spectroscopy measurements in the angle of incidence range between 45° and 90°. As a source of illumination, the polarimeter uses a 30 W halogen lamp, and as a detector, a CCD array coupled to a commercial Jobin-Yvon diffraction grating optimized to work between 400 nm and 800 nm.

The rest of this work is organised as follows: in the next section we briefly outline the numerical model we have used to calculate angular-dependent reflectivity and polarimetry spectra. Then, in Section 3 we report the calculation of angle-dependent reflectivity and polarimetry spectra on ideal, perfectly ordered, np-AAO photonic crystal slabs. Finally, in Section 4 we state our conclusions.

2. Numerical model for the interaction of the incident light with the photonic crystal slabs

The main goal of this paper is the study of the polarization state change upon reflection on nanoporous anodic aluminium oxide photonic crystal slabs. To this end we use a numerical method based on the scattering matrix treatment proposed by Whittaker and Culshaw [34]. This method follows the same approach as the plane-wave expansion (PWE) method but including additional features to calculate the photonic modes propagating inside the sample and the coupling efficiency of the incident wave to these modes. The scattering matrix method is based in the fact that the waves propagating inside the structure can be expanded in a sum of plane waves. For instance, for the magnetic field this expansion can be expressed as

$$\mathbf{H}(\mathbf{r}, z) = \sum_{\mathbf{G}} \mathbf{h}_{\mathbf{k}}(\mathbf{G})\, e^{i\omega t + i(\mathbf{k}+\mathbf{G})\mathbf{r} + iqz}. \tag{1}$$

This expansion spans over all the vectors $\mathbf{G}$ of the reciprocal lattice, $\mathbf{k}$ is the Bloch parallel wavevector (since the waves propagating inside the ordered structure must comply with the Bloch theorem), $\mathbf{r}$ is the position in the x–y plane, z is the position along the pores and q is the wavevector along the z direction. The introduction of the z component of the wavevector (q) is necessary in order to allow the modeling of waves that propagate inside the photonic crystal in an oblique direction and that can couple to the photonic crystal slab from the incident medium at a given angle.

By limiting the expansion of Eq. (1) to a finite number of reciprocal wavevectors $\mathbf{G}$ and applying Maxwell's equations an eigenvalue problem is obtained for q, at a given $\mathbf{k}$ and wave frequency ω. The solutions of this eigenvalue problem are the modes allowed to propagate inside the sample. It must be noted that there may not be only one mode propagating within the

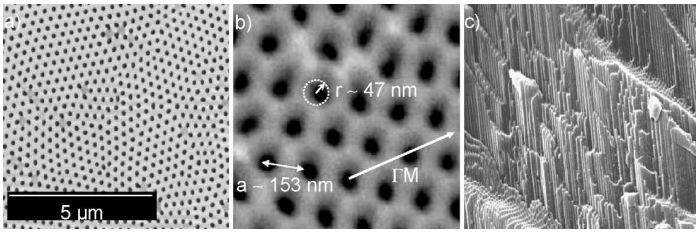

Fig. 1. SEM pictures of a np-AAO slab obtained by electrochemical anodization. (a) Surface picture showing the self-ordering of the pores, (b) surface view at a higher magnification that illustrates the typical characteristic sizes and the lattice direction considered later in the calculations, and (c) cross-section view that illustrates the in-depth pore uniformity.

photonic crystal sample with given **k** and ω, but several modes for the different eigenvalues of q propagating oblique to the sample surface (with $q \neq 0$). Once these modes are determined a scattering matrix procedure is used to impose the boundary conditions at the sample interfaces, this is: continuity of the in-plane components of the electric and magnetic fields and of the parallel wavevector component **k**. With this, it is possible to calculate the coupling efficiency of the incident light to the modes of the photonic crystal slab and to obtain the reflection coefficients for the two incident polarizations. It is known [34] that when the incident light couples to a mode propagating inside the photonic crystal slab, a distinctive feature appears in the spectrum. Such feature can be a maximum, a minimum or an inflection. If the light is incident at an angle θ and the wave frequency at which the feature appears is ω, the magnitude of the parallel wavevector is:

$$|\mathbf{k}| = \frac{\omega}{c}\sin\theta, \tag{2}$$

with c the speed of light in vacuum. Since this magnitude is conserved as light enters the photonic crystal, it can be used to identify the photonic bands in the spectra.

3. Reflectometry and polarimetry of nanoporous anodic aluminum oxide-based 2D photonic crystals

In this section we show the results obtained with the scattering matrix formalism introduced in the previous section. First, in order to illustrate how the features present in the spectra are related to the photonic bands, we show angular-dependent reflectance spectra (ADRS) of photonic crystal slabs based on np-AAO. Nanoporous AAO is a material with air pores in an alumina matrix. Under the appropriate fabrication conditions the pores are naturally ordered in a triangular lattice, although it is not monodomain unless prepatterning techniques are used [14]. Fig. 1 shows an example of a np-AAO slab produced by electrochemical anodization. The specific conditions of the process can be found elsewhere [12]. Fig. 1a is a SEM image of the sample surface, where the clustered natural self-ordering of the pores can be observed. Fig. 1b shows a closer view of one of the clusters where the triangular lattice ordering is demonstrated. Finally, Fig. 1c shows a cross-section view of the sample to illustrate the high aspect ratio and radius uniformity of the pores. The model for the simulations requires that the sample is ideally periodic to apply the Bloch theorem. For this reason, in our simulations we will assume a np-AAO photonic crystal with a perfect triangular arrangement of the pores. More concisely, Fig. 2 shows a schematic diagram of the model for the sample consisting of a slab of alumina ($n = 1.67$), surrounded by air, with a periodic triangular lattice (lattice constant a) of circular holes (radius r). The thickness of the slab (or equivalently the pore

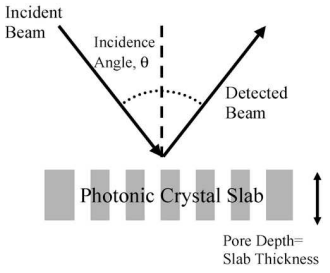

Fig. 2. Schematic diagram illustrating the measurement geometry for angular-dependent spectroscopy and polarimetry.

depth) is d. The diagram also shows the angle of incidence of the light, θ.

Fig. 3 shows the photonic bands, calculated with the PWE method, of an ideal np-AAO 2D photonic crystal (infinite in the z direction), with dimensions $a = 157$ nm and $r = 47$ nm. These dimensions are obtained from an average of the dimensions of actual fabricated samples such as the one shown in Fig. 1. The bands in Fig. 3 correspond to the lattice direction ΓM indicated in Fig. 1b for both the TE (electric field perpendicular to the pores) and TM (magnetic field perpendicular to the pores) polarizations. The dashed straight line corresponds to the light line, this is: the ω–k points corresponding to waves incident at 90°. The wavelength scale at the left y-axis shows that some of the photonic bands and band gaps lie in the UV–vis region of the electromagnetic spectrum.

Fig. 4 shows angular-dependent reflectance spectra for np-AAO photonic crystal slabs with different thicknesses d. The lateral dimensions are the same as for the band calculation in Fig. 3 and illustrated in Fig. 1 The picture shows a 2D representation of the reflection

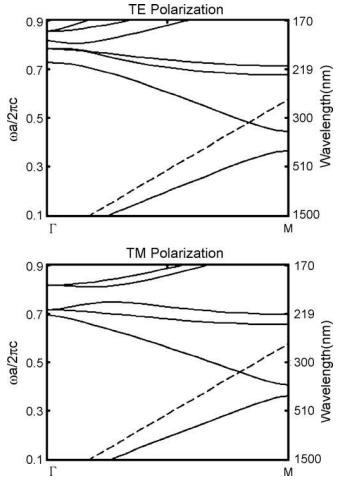

Fig. 3. Photonic band structure (calculated with the PWE method) for the ΓM direction of a 2D photonic crystal with the same characteristics as the np-AAO. The bands for TE (magnetic field along the pores) and TM (electric field along the pores) polarization are shown. The dashed straight line corresponds to the light line, this is: any incident light from the air has ω and k above this line.

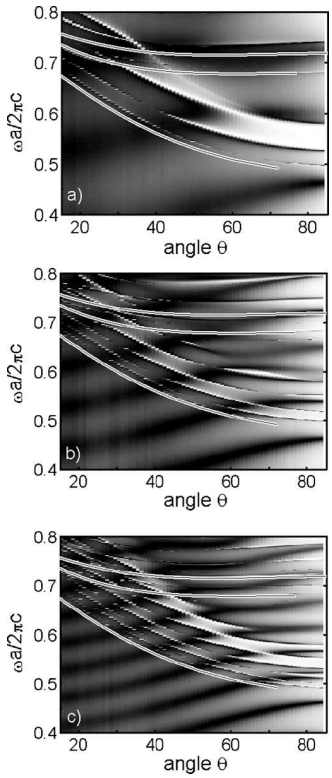

Fig. 4. Angular-dependent reflectance spectra of np-AAO photonic crystal slabs with three different thicknesses: (a) 300 nm, (b) 600 nm and (c) 900 nm. The spectra are represented as a gray map of the reflectivity with respect to the angle of incidence and the normalized frequency. The reflectance spectra are for light incident in the ΓM direction and the bands correspond to the TE polarization and the ΓM direction.

coefficient versus the frequency of the incident light, ω, and its angle of incidence, θ. The corresponding pore depths are $d = 300$ nm, $d = 600$ nm and $d = 900$ nm, from top to bottom. The simulations are performed for light incident along the ΓM direction and for TE polarization of the incident and detected light. The second, third and fourth TE photonic bands for this structure (Fig. 3a) are overlapped to the picture.

The graphs in Fig. 4 show that for the second (with $\omega = 0.66\ 2\pi c/a$ at $\theta = 20^\circ$) and third (with at $\omega = 0.74\ 2\pi c/a$ at $\theta = 20^\circ$) TE bands there exist several resonant features in the ADR spectra. Such features are due to the coupling of the incident light to the photonic modes that propagate inside the structure at different angles with respect to the surface. These photonic modes correspond to the nonzero real eigenvalues q of the wave equation inside the structure. It is important to remark that the resonant features do not match exactly with the corresponding photonic bands (with the same $k_\parallel$ and $q = 0$), but they appear at higher frequencies. The reason for this blue shift is that the frequency is proportional to the modulus of the wavenumber (considering all in-plane and out-of-plane components). The modes indicated by the resonant features have nonzero q, and consequently their frequency is higher than the frequency of the corresponding photonic bands. From the figure it can also be concluded that with increasing pore depth the number of resonant features for a given band also increases. This indicates that the incident beam couples to several modes in the photonic crystal with different nonzero q values.

Finally, another characteristic of the spectra in Fig. 4 must be noted: there are oscillations in the reflectance spectra (the dark and light stripes in the 2D plot) and their number increases with pore depth (or equivalently, with the thickness of the photonic crystal slab). These oscillations correspond to Fabry-Pérot interferences between the light beams reflected at the interfaces of the photonic crystal slab with the surrounding air. The period of such interferences decreases when the thickness of the photonic crystal slab increases.

The main concern of this work is the numerical calculation of the polarization change upon reflection on nanoporous AAO 2D photonic structures with a view to its application to the simulation of Mueller matrix spectroscopic polarimetry measurements. The mathematical model introduced in the previous section permits to calculate the reflection coefficient for a selected polarization of the incident and reflected beams. These four coefficients are the components of the 2×2 complex Jones matrix [35] for the reflection upon the structure, which (for structures with perfectly flat interfaces and perfectly cylindrical pores) can be converted into an equivalent 4×4 real Mueller matrix [36].

Fig. 5 shows angular-dependent polarimetry spectra in the form of the modulus of the four Jones matrix components for the np-AAO 2D photonic crystal slab with thickness 300 nm. The modulus of the Jones matrix components is represented as a function of the

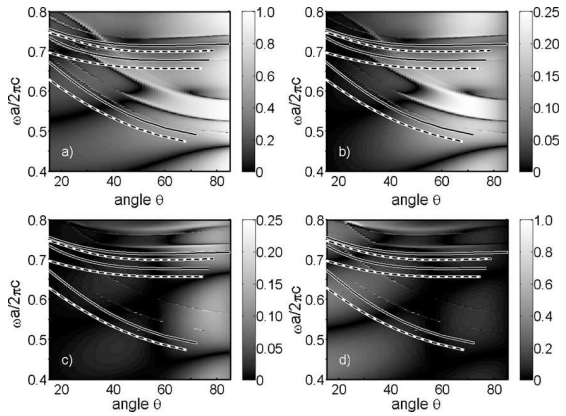

Fig. 5. Angular-dependent polarimetry spectra of a np-AAO photonic crystal slab with thickness 300 nm. The four gray maps show the modulus of the Jones matrix components that characterize the change of polarization upon reflection on the slab. The four gray maps are (a) $J_{\mathrm{TE-TE}}$ component (TE-polarized incident beam and TE-polarized detected light), (b) $J_{\mathrm{TE-TM}}$ (TE-polarized incident beam and TM-polarized detected light), (c) $J_{\mathrm{TM-TE}}$ and (d) $J_{\mathrm{TM-TM}}$. Notice that the cross-polarization components $J_{\mathrm{TE-TM}}$ and $J_{\mathrm{TM-TE}}$ are represented in a smaller gray scale. The spectra are for light incident in the ΓM direction. The bands correspond to both polarizations, TE (solid lines) and TM (dashed lines), and to the ΓM direction.

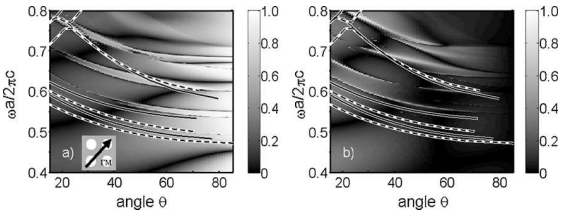

Fig. 6. Angular-dependent polarimetry spectra of a photonic crystal slab with thickness 300 nm and with a square lattice of holes in a material with the same refractive index as np-AAO. The lateral dimensions are $a = 153$ nm and $r = 47$ nm. Only the $J_{TE–TE}$ (a) and $J_{TM–TM}$ (b) components are shown as the cross-polarization components are zero. The spectra are for light incident in the ΓM direction. The bands correspond to both polarizations, TE (solid lines) and TM (dashed lines), and to the ΓM direction.

incident light frequency, ω, and of the angle of incidence, θ. Fig. 5a shows the $J_{TE–TE}$ component (TE-polarized incident beam and TE-polarized detected light), Fig. 5b corresponds to the $J_{TE–TM}$ (TE-polarized incident beam and TM-polarized detected light), Fig. 5c $J_{TM–TE}$ and Fig. 5d $J_{TM–TM}$. Notice that the cross-polarization components $J_{TE–TM}$ and $J_{TM–TE}$ are represented in a smaller gray scale to enable the comparison of the relative strengths of the components. The direction of incidence is along the ΓM direction of the triangular lattice. The TE and TM photonic bands of the corresponding infinite photonic crystal are overlapped to the graph of each Jones matrix element. As it can be observed from the graphs, several features related to photonic bands can be observed in the spectra. More concisely, in the $J_{TE–TE}$ and $J_{TE–TM}$ components, the features correspond to TE bands, while for the $J_{TM–TE}$ and $J_{TM–TM}$ the features correspond to TM bands. It is interesting to note that there is a significant amount of cross-polarization: an incident TE-polarized beam is reflected with TE polarization, but also in a certain amount with TM polarization. As in the case of the ADRS, the oscillations of the reflection coefficient due to Fabry-Pérot interferences are visible.

It is also interesting to study the results that could be obtained for other lattice structures. Although np-AAO grows naturally in a triangular lattice, square lattices of pores in a material with similar refractive index and with similar dimensions can be fabricated. One possibility is the holographic four-beam patterning of photoresist layers [37,38]. Fig. 6 shows the $J_{TE–TE}$ and $J_{TM–TM}$ components for a sample consisting of a square lattice of cylindrical pores in a material with refractive index 1.67. The lattice constant is $a = 153$ nm, the depth of the pores is $d = 300$ nm and their radius is $r = 47$ nm. The incident light is along the ΓM direction of the lattice, as indicated in the graph inset. The $J_{TE–TM}$ and $J_{TM–TE}$ components are not shown since they vanish. It is remarkable the difference between the previous triangular lattice and this square lattice: while for the former cross-polarization is noticeable, for the latter it is nonexistent.

4. Conclusions

We have obtained simulated angular-dependent polarimetric spectra of nanoporous anodic alumina-based two-dimensional photonic crystal slabs. For the simulations, we used a mathematical model based on a scattering matrix treatment to obtain the polarization change upon reflection of incident light onto np-AAO, as a function of the incidence angle and of the wavelength.

The calculations reveal that for a given photonic band of the infinite photonic crystal, the incident light can couple to several modes in the finite photonic crystal constituted by the porous alumina samples. These modes correspond to waves that propagate at different angles with respect to the sample surface. Furthermore, the number of these modes increases with increasing pore depth. The spectra also show periodic oscillations with the wavelength related to Fabry-Pérot interferences in the thickness of the photonic crystal slabs.

We have simulated two different lattice structures: triangular and square lattice. This is interesting because, although np-AAO has a natural triangular structure, other materials with similar optical properties can be fabricated with a square structure. We have found that for the triangular lattice, the off-diagonal components of the Jones Matrix show a certain amount of cross-polarization, but with the same characteristics as the diagonal components. Instead, for the square lattice, there is no cross-polarization.

Acknowledgments

The authors want to thak Dr. Martin Foldyna for the fruitful discussions on Polarimetry. This work was supported by Spanish Ministry of Education and Science (MEC) under grants number TEC2006-06531 and HOPE CSD2007-00007 (Consolider-Ingenio 2010). Josep Ferré-Borrull acknowledges the Ramón y Cajal fellowship from the MEC. Z. Kral acknowledges the Grant 2007-BE2-00163.

References

[1] E. Yablonovitch, Phys. Rev. Lett. 58 (1987) 2059.
[2] S. John, Phys. Rev. Lett. 58 (1987) 2486.
[3] J.D. Joannopoulos, R.D. Meade, J.N. Winn, Photonic Crystals Molding the Flow of Light, Princenton University Press, Princeton, 1995.
[4] P. Russell, Science 299 (2003) 358.
[5] H. Park, S. Kim, S. Kwon, Y. Ju, J. Yang, J. Baek, S. Kim, Y. Lee, Science 305 (2004) 1444.
[6] E. Akmansoy, E. Centeno, K. Vynck, D. Cassagne, J. Lourtioz, Appl. Phys. Lett. 92 (2008) 133501.
[7] G. Mertens, R.B. Wehrspohn, H.-S. Kitzerow, S. Matthias, C. Jamois, U. Gosele, Appl. Phys. Lett. 87 (2005) 241108.
[8] L.J. Martinez, A. Garcia-Martin, P.A. Postigo, Opt. Exp. 12 (2004) 5684.
[9] A. Sugitatsu, T. Asano, S. Noda, Appl. Phys. Lett. 86 (2005) 171106.
[10] H. Masuda, K. Fukuda, Science 268 (1995) 1466.
[11] A. Birner, U. Gruning, S. Ottow, A. Schneider, F. Muller, V. Lehmann, H. Foll, U. Gosele, Phys. Status Solidi A: Appl. Res. 165 (1998) 111.
[12] L.F. Marsal, L. Vojkuvka, J. Ferre-Borrull, T. Trifonov, J. Pallares, Phys. Status Solidi (c) 4 (2007) 1918.
[13] R.B. Wehrspohn, A.P. Li, K. Nielsch, F. Müller, W. Erfurth, U. Gösele, in: K.R. Hebert, R.S. Lillard, B.R. Mac Dougall (Eds.), Oxide Films, PV-2000–4, Electrochemical Society Monographs, Pennington, NJ, 2000, p. 271.
[14] J. Choi, K. Nielsch, M. Reiche, R.B. Wehrspohn, U. Gosele, J. Vac. Sci. Technol. B 21 (2003) 763.
[15] W. Lee, R. Ji, U. Gosele, K. Nielsch, Nat. Mater. 5 (2006) 741.
[16] O. Takayama, M. Cada, Appl. Phys. Lett. 85 (2004) 1311.
[17] W.L. Xu, M.J. Zheng, S. Wu, W.Z. Shen, Appl. Phys. Lett. 85 (2004).
[18] D. Labilloy, H. Benisty, C. Weisbuch, T.F. Krauss, De La Rue, V. Bardinal, R. Houdré, U. Oesterle, D. Cassagne, C. Jouanin, Phys. Rev. Lett. 79 (1997) 4147.
[19] E. Yablonovitch, T.J. Gmitter, Phys. Rev. Lett. 63 (1989) 1950.
[20] V.N. Astratov, M.S. Skolnick, S. Brand, T.F. Krauss, O.Z. Karimov, R.M. Stevenson, D.M. Whittaker, I. Culshaw, R.M. De la Rue, IEE Proc. Optoelectron. 145 (1998) 398.
[21] V.N. Astratov, I.S. Culshaw, R.M. Stevenson, D.M. Whittaker, M.S. Skolnick, T.F. Krauss, R.M. De la Rue, J. Lightwave Technol. 17 (1999) 2050.
[22] V.N. Astratov, D.M. Whittaker, I.S. Culshaw, R.M. Stevenson, M.S. Skolnick, T.F. Krauss, R.M. De La Rue, Phys. Rev. B 60 (1999) R16255.
[23] V.N. Astratov, R.M. Stevenson, I.S. Culshaw, D.M. Whittaker, M.S. Skolnick, T.F. Krauss, R.M. De La Rue, Appl. Phys. Lett. 77 (2000) 178.
[24] V.N. Astratov, R.M. Stevenson, I.S. Culshaw, D.M. Whittaker, M.S. Skolnick, T.F. Krauss, R.M. De la Rue, Phys. Status Solidi A: Appl. Res. 178 (2000) 565.
[25] A.R. Alija, L.J. Martinez, P.A. Postigo, C. Seassal, P. Viktorovitch, Appl. Phys. Lett. 89 (2006) 101102.
[26] Z. Kral, J. Ferre-Borrull, J. Pallares, T. Trifonov, A. Rodriguez, R. Alcubilla, L.F. Marsal, Mater. Sci. Eng. B: Solid State Mater. Adv. Technol. 147 (2008) 179.
[27] Z. Král, J. Ferré-Borrull, T. Trifonov, L.F. Marsal, A. Rodriguez, J. Pallarès, R. Alcubilla, Thin Solid Films 516 (2008) 8059.
[28] D.E. Aspnes, Thin Solid Films 455–56 (2004) 3.
[29] T. Novikova, A. De Martino, S. Ben Hatit, B. Drevillon, Appl. Opt. 45 (2006) 3688.
[30] V. Tkachenko, G. Abbate, A. Marino, F. Vita, M. Giocondo, A. Mazzulla, L. De Stefano, Appl. Phys. Lett. 89 (2006) 221110.
[31] H. Arwin, M. Poksinski, K. Johansen, Phys. Status Solidi A: Appl. Mater. Sci. 205 (2008) 817.
[32] M.C. Netti, A. Harris, J.J. Baumberg, D.M. Whittaker, M.B.D. Charlton, M.E. Zoorob, G.J. Parker, Phys. Rev. Lett. 86 (2001) 1526.
[33] E. Garcia-Caurel, A. De Martino, B. Drevillon, Thin Solid Films 455–456 (2004) 120.
[34] D.M. Whittaker, I.S. Culshaw, Phys. Rev. B 60 (1999) 2610.
[35] R.M.A. Azzam, N.M. Bashara, Ellipsometry and Polarized Light, North Holland, Amsterdam, 1977.
[36] J.W. Hovenier, Appl. Opt. 33 (1994) 8318.
[37] C. Tan, C.S. Peng, V.N. Petryakov, Y.K. Verevkin, J. Zhang, Z. Wang, S.M. Olaizola, T. Berthou, S. Tisserand, M. Pessa, New J. Phys. 10 (2008) 023023.
[38] M. Farhoud, J. Ferrera, A.J. Lochtefeld, T.E. Murphy, M.L. Schattenburg, J. Carter, C.A. Ross, H.I. Smith, J. Vacuum Sci. Technol. B 17 (1999) 3182.

UNIVERSITAT ROVIRA I VIRGILI
DEVELOPMENT OF OPTICAL CHARACTERIZATION METHODS FOR MICRO- AND NANO-SCALE PLANAR PHOTONIC BAND GAP STRUCTURES
Zdenek Kral
DL: T-1537-2009/ISBN:978-84-692-4556-9

New approaches for the fabrication of photonic structures of non-linear optical materials

J. J. Carvajal, A. Peña, R. Kumar, M. C. Pujol, X. Mateos, M. Aguiló, F. Díaz, J. R. Vázquez de Aldana, C. Méndez, P. Moreno, L. Roso, T. Trifonov, A. Rodríguez, R. Alcubilla, Z. Král, J. Ferré-Borrull, J. Pallarés, L. F. Marsal, S. Di Finizio, R. Macovez, J. Martorell.

Journal of Luminescence, in press, DOI:10.1016/j.jlumin.2009.03.035.

UNIVERSITAT ROVIRA I VIRGILI
DEVELOPMENT OF OPTICAL CHARACTERIZATION METHODS FOR MICRO- AND NANO-SCALE PLANAR PHOTONIC BAND GAP STRUCTURES
Zdenek Kral
DL: T-1537-2009/ISBN:978-84-692-4556-9

ARTICLE IN PRESS

Journal of Luminescence ▮ (▮▮▮▮) ▮▮▮–▮▮▮

Contents lists available at ScienceDirect

Journal of Luminescence

journal homepage: www.elsevier.com/locate/jlumin

New approaches for the fabrication of photonic structures of nonlinear optical materials

J.J. Carvajal [a], A. Peña [a], R. Kumar [a], M.C. Pujol [a], X. Mateos [a], M. Aguiló [a], F. Díaz [a,*], J.R. Vázquez de Aldana [b], C. Méndez [b], P. Moreno [b], L. Roso [b], T. Trifonov [c], A. Rodríguez [c], R. Alcubilla [c], Z. Král [d], J. Ferré-Borrull [d], J. Pallarès [d], L.F. Marsal [d], S. Di Finizio [e], R. Macovez [e], J. Martorell [e]

[a] Física i Cristal·lografia de Materials i Nanomaterials (FiCMA–FiCNA), Univ. Rovira i Virgili (URV), Campus Sescelades, Marcel·lí Domingo, s/n, E-43007 Tarragona, Spain
[b] Servicio Láser, Univ. Salamanca, E-37008 Salamanca, Spain
[c] Dept. Enginyeria Electrònica, Univ. Politècnica de Catalunya, E-08034 Barcelona, Spain
[d] Dept. d'Enginyeria Electrònica, Univ. Rovira i Virgili (URV), E-43007 Tarragona, Spain
[e] ICFO—Institut de Ciències Fotòniques, E-08860 Castelldefels, Spain

ARTICLE INFO

PACS:
42.65.–k
42.70.Mp
42.70.Qs
42.79.Dj
42.82.Ds
42.82.Fv

Keywords:
Photonic crystals
Nonlinear optics
$LiNbO_3$
$KTiOPO_4$
Template growth
Liquid phase epitaxy

ABSTRACT

We revisited two different strategies to fabricate 1D photonic crystals of nonlinear optical dielectric materials based on ultrafast laser ablation of the surface of an $RbTiOPO_4$ crystal, and selective etching of ferroelectric domains of the surface of a periodically poled $LiNbO_4$ crystal. We evaluated their behaviour as Bragg diffraction gratings. We also presented the recent advances we developed in a new procedure of fabrication of 2D and 3D photonic crystals of $KTiOPO_4$ (KTP) grown on the surface of a KTP substrate by liquid phase epitaxial means within the pores of a silicon macroporous template. Optical, structural, morphological, and compositional characterization for the photonic crystals produced through this technique are presented.

1. Introduction

Since 1987, when the first work about photonic crystals (PCs) was published [1,2], many interesting properties have been studied in one, two, and three dimensions. Besides their peculiar linear optical properties [3], photonic crystals present many interesting features for controlling the nonlinear optical interactions. They provide the possibility to enhance [4–6] a second-order nonlinear optical interaction and an alternative phase-matching mechanism [7,8]. It has been shown that even in a centrosymmetric material it is possible to hold an efficient second-order interaction employing the photonic crystal properties [9]. Furthermore, the periodic modulation of both refractive index and second-order nonlinear susceptibility might allow backward parametric oscillation [10], a nonlinear effect predicted many years ago but not yet observed experimentally.

To obtain a very efficient and durable nonlinear interaction in a PC it would be adequate to use a material with high second-order nonlinear optical properties, such as $LiNbO_3$ (LN), $KTiOPO_4$ (KTP), and its isostructural $RbTiOPO_4$ (RTP). Lithium niobate, LN, is a ferroelectric material of considerable interest to the optical, laser, and communications industry, due to its large values of nonlinear optical, electro-optic, piezoelectric, and acousto-optical coefficients [11]. Potassium titanyl phosphate, KTP, has been recognized as the material of choice for second-harmonic generation of Nd:YAG light, due to its extremely low onset power threshold, high-power conversion efficiency, and high threshold to laser-induced damage [12]. It has also been the focus of considerable attention for optical parametric oscillation, sum and difference frequency mixing [13], and electro-optic switching [14]. Among the isostructural materials to KTP, RTP presents a high surface damage threshold ($9.0 \times 10^6\,MW\,m^{-2}$) and large temperature matching bandwidth ($50\,K\,cm^{-1}$), double than that of KTP [15].

In this paper, we propose two different strategies to fabricate 1D photonic crystals based on these nonlinear optical materials. These strategies are based on previous methodologies used for the microstructuration of the surface of materials to fabricate

* Corresponding author.
E-mail addresses: joanjosep.carvajal@urv.cat (J.J. Carvajal), f.diaz@urv.cat (F. Díaz).

0022-2313/$ - see front matter © 2009 Elsevier B.V. All rights reserved.
doi:10.1016/j.jlumin.2009.03.035

Please cite this article as: J.J. Carvajal, et al., J. Lumin. (2009), doi:10.1016/j.jlumin.2009.03.035

diffraction gratings, such as the ultrafast laser ablation, and the selective etching of ferroelectric domains. We fabricated diffraction grating on the surface of an RTP and the periodically poled $LiNbO_3$ crystals, and evaluated their behaviour as Bragg diffraction gratings.

One of the challenges for fabricating higher dimensional (2D and 3D) photonic crystals is the production of these structures with sufficient precision to prevent scattering losses blurring the crystal properties. We present here the advances we developed recently in a completely new procedure that combines top-down and bottom-up approaches to fabricate 2D and 3D PCs of nonlinear dielectric materials, and that for the moment has been tested on KTP [16]. These crystals are grown on the surface of a KTP substrate, which gives to the photonic structure the requested crystallographic orientation, within the pores of a silicon macroporous template that gives the final shape to the photonic structure.

2. Strategies to fabricate diffraction gratings: towards the fabrication of 1D photonic crystals

Optical diffraction gratings constitute a fundamental optical component used to periodically modulate the phase or amplitude of incident waves, and are expected to be useful devices for wavelength division multiplexing systems in optical communications and optical sensors. Moreover, in integrated optoelectronics they have applications as optical wave couplers and filters.

2.1. Ultrafast laser ablation

A 1D relief grating was recorded on the surface of an RTP sample by ultrafast laser ablation. This technique uses very short (some tens picoseconds is the limit for the process, depending on the materials) and intense laser pulses to remove thin layers from the surface of a bulk target by means of physical mechanisms different from those taking place in conventional laser ablation. The collateral thermal and mechanical effects around the ablated area are diminished to such an extent that precision and quality of the microstructures higher than those obtained with other techniques can be achieved. Nonlinear absorption and ionization processes are on the basis of this technique. Focusing on dielectrics, within the duration of a pulse and for moderate intensities, a thin layer on the surface of the material is almost fully ionized by multiphoton and collisional mechanisms so that the number of free electrons rapidly amounts to the solid-state density. As a consequence of the poor electric transport properties of the material, surface charging takes place and the ultraintense "quasielectrostatic" field generated overcomes the binding energy of the ions and drag them out of the solid. This mechanism is known as Coulomb explosion and since thermal coupling with the lattice is negligible during this short period of time, the process is a purely non-thermal process.

For larger intensities, total ionization of the surface is achieved for the leading edge of the laser pulse. Therefore, free electrons can absorb energy from the laser pulse in the presence of the lattice atoms and ions by means of inverse bremsstrahlung mechanism. This absorbed energy contributes to raise the temperature of a deeper surface layer by electron heat diffusion to a value close to the thermodynamic critical temperature giving rise to a phase explosion process, resulting in violent expulsion of both vapor and equilibrium liquid droplets [17]. The depth of the ablated layer is determined by the electron heat diffusion length and the laser fluence. Although the process is still very fast, some thermal damage must be expected on the areas surrounding the microstructured region.

We have used a commercial Ti:Sapphire oscillator (Tsunami, Spectra Physics) and a regenerative amplifier system (Spitfire, Spectra Physics) based on chirped pulse amplification (CPA). The system delivers linearly polarized 120-fs pulses with central wavelength 795 nm with a repetition rate of 1 kHz. The maximum available pulse energy is 1 mJ but for the purpose of microstructuring the grating it was reduced to 0.78 μJ using a half-wave plate and a linear polarizer. The transverse mode is gaussian and the beam width is 9 mm ($1/e^2$ criterion). The beam was then focused by a 50 mm achromatic lens resulting in a peak fluence of $\sim 7\,J\,cm^{-2}$ at focus.

The sample was placed on a motorized XYZ translation stage in order to achieve optimal focusing on the target surface. The focused beam moved in straight lines across the sample surface at a constant scanning speed of $130\,\mu m\,s^{-1}$ avoiding iterative passes along the same line. The pitch between successive grooves was set to 15 μm. For this scanning speed, the number of pulses contributing to the ablation of a point within the sample surface was approximately 40. We have estimated the ablation threshold fluence following the procedure described in Ref. [18], giving $1.44 \pm 0.18\,J\,cm^{-2}$ for 40 pulses. For multishot conditions (>100 pulses) the value for the threshold decreases to $1.18 \pm 0.15\,J\,cm^{-2}$ (incubation factor $\xi = 0.783$ [19]).

Fig. 1 shows two pictures, taken with a scanning electron microscope (SEM) FEI QUANTA 600, of the sample after the ultrafast laser ablation process where it can be seen the diffraction grating generated on the surface of the sample. The sample was also observed under a Carl Zeiss Axio Imager A1 optical microscope. The lattice constant estimated from this microscope is approximately 15 μm. However, the roughness achieved on the lateral walls of the channels is still excessive for optical purposes.

We have recorded Bragg-diffraction spectra of this sample by using a FT-IR spectrometer (Bruker-Vertex 70) equipped with a special reflectivity attachment. The light source was a halogen tungsten lamp, and we collected the intensity of the diffracted light with a DLATGS detector in the spectral range from 7500 to $400\,cm^{-1}$. The incoming light was pointed perpendicular to the plane of the sample and the diffraction spectra were measured in a direction perpendicular to the grooves and at collection angles ranging from 24° to 60° in 2° steps. Two repeated measurements were collected for the sample. The measured data are represented in Fig. 2 with an intensity plot as a function of the wavelength and the diffraction angle.

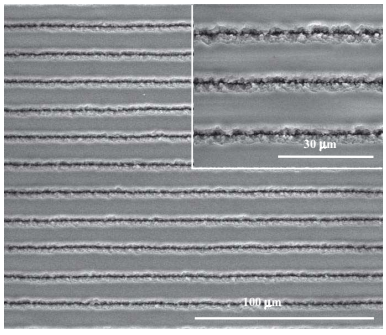

Fig. 1. SEM images of the diffraction grating generated on the surface of an RTP crystal by ultrafast laser ablation.

Please cite this article as: J.J. Carvajal, et al., J. Lumin. (2009), doi:10.1016/j.jlumin.2009.03.035

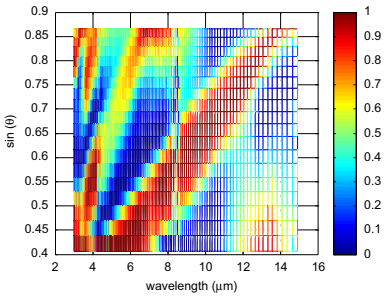

Fig. 2. A 2D intensity plot as a function of the wavelength and the diffraction angle for the diffraction grating generated on the surface of an RTP crystal by ultrafast laser ablation. Dark zones represent the diffraction orders.

To evaluate the lattice constant, the Bragg-diffraction spectra were fitted to the following two-variable function:

$$I(\lambda, \sin\theta) = \sum_{n=1}^{3} \exp\left[\left(\frac{\sin\theta - (n\lambda/a)}{w_n}\right)^2\right] \quad (1)$$

where w_n takes into account the width of the diffraction peaks, a is the lattice constant, and n is an integer (the number of the diffraction order). The fitting of this function to the experimental data gives a robust estimation of the lattice constant from the data, since all the measurements are taken into account simultaneously. The value of the lattice constant measured by this procedure was 14.92 μm, which was in good agreement with the value estimated by optical microscopy.

2.2. *Selective chemical etching of ferroelectric domains in periodically poled crystals*

Ferroelectric domains of opposite spontaneous polarization present different etching speeds when dipped in some acid mixtures. This property has been used to reveal the domain pattern at the surface of periodically poled crystals. However, the selective etching process provides further capabilities for versatile surface engineering of domain-engineered crystals, allowing the production of deep, high aspect ratio structures, with side-walls that can be extremely smooth [20]. These structures can find applications in the fields of optics and optoelectronics for waveguides, Bragg reflectors, and photonic band-gap devices. More recently, the fabrication of periodic 1D and 2D surface structures in congruent LN by periodic electric-field poling at the overpoling regime and selective wet chemical etching under appropriate conditions have also been reported [21–23], with feature sizes and periods down to submicron and nanoscale range.

The most common wet selective etchant reported for the ferroelectric domains of LN has been a mixture of hydrofluoric (HF) and nitric (HNO_3) acids, which attacks the negative z face ($-z$) of LN at a rate that is appreciably higher than the positive z face ($+z$) [20,22,24]. At room temperature, in a 1:2 mixture of HF and HNO_3 acids, the $-z$ face experiences etch rates of $\sim 1\,\mu m\,h^{-1}$, whereas the $+z$ face remains unetched. Even at temperatures up to 368 K, where the $-z$ etch rate increases to $\sim 30\,\mu m\,h^{-1}$, the $+z$ face appears not to etch at all, apart from at isolated sites where defects or dislocations may occur. Furthermore, independent of the mixture composition, the etch depth increased linearly with respect to etch time.

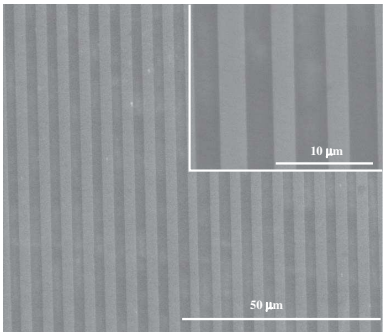

Fig. 3. SEM images of the diffraction grating generated on the surface of a periodically poled LN crystal by selective chemical etching of one of the ferroelectric domains.

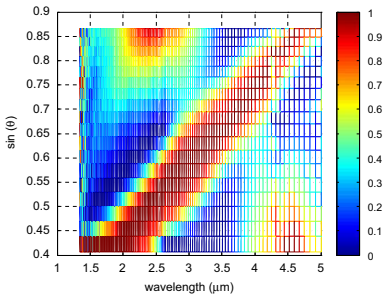

Fig. 4. A 2D intensity plot as a function of the wavelength and the diffraction angle for the diffraction grating generated on the surface of a periodically poled LN crystal by selective chemical etching of one of the ferroelectric domains.

We used a commercially available periodically poled LN crystal sample from INO, 0.5 mm thick, with a period of 5.4 μm. The sample was etched in a HF:HNO_3 = 1:2 acid mixture for 30 min at room temperature. After etching, the surface was monitored by optical and electronic microscopy. The surface of the sample after etching is shown in Fig. 3.

The lattice constant estimated from the optical microscope images is 5.13 μm. The characterization of the Bragg-diffraction spectra (see Fig. 4) resulted in a lattice constant of 5.25 μm.

3. A new strategy to fabricate 2d and 3d photonic crystals

One of the main challenges for the production of photonic structures with higher dimensionality is the fabrication of these structures with sufficient precision to prevent scattering losses

Please cite this article as: J.J. Carvajal, et al., J. Lumin. (2009), doi:10.1016/j.jlumin.2009.03.035

blurring the crystal properties. For this reason, new fabrication techniques can be proposed to avoid or reduce these problems.

The procedure for fabricating 2D and 3D photonic crystals we developed combines two well-known techniques: the fabrication of 2D and 3D macroporous silicon membranes and the epitaxial growth of KTP within the pores of these membranes. This procedure, in addition to its simplicity, results in KTP and silicon integrated in a single structure that would eventually be used to generate or modulate light.

We fabricated these 2D and 3D PCs in four different steps which involved the preparation of high-quality ordered macroporous silicon templates, the growth of the KTP epitaxial layer within the pores of the silicon template, the polishing of the top or bottom surface of the KTP epitaxial layer, and finally, a selective etching of the silicon matrix.

Silicon membranes were prepared by light-assisted electrochemical etching and post-processing. The starting material was n-type $\langle 100 \rangle$ silicon with resistivity of 2–6 Ωcm. The front side of the wafers was patterned with inverted pyramidal shaped pits arranged in a square or triangular periodic lattice with periods ranging from 4.5 to 10 μm by oxidation, photolithography and subsequent etching with tetramethyl ammonium hydroxide (TMAH) that act as nucleation sites for the ordered pore growth along the $\langle 100 \rangle$ direction. A low-resistance transparent ohmic contact was formed by n^+-ion implantation on the back side of the silicon wafer. The wafers were incorporated in an electrochemical etching cell containing a 5 wt% aqueous solution of hydrofluoric acid. The chemical dissolution of silicon requires the generation of positive carriers (holes), which was achieved by using an LED matrix (880 nm peak emission wavelength) for back side illumination and the size and the quality of the pores was controlled by means of a computerized feedback mechanism that regulates the generation of holes by continuously adjusting the back side illumination. Periodicity in the third dimension was introduced by modulating the light intensity during etching which leaded to a modulation of pore diameter in depth. Macroporous arrays with sine-wave modulated pores were produced in this way. In order to fabricate a fully 3D structure, adjacent pores had to be also connected laterally, i.e. in $\langle 110 \rangle$ directions. To do that the samples were subjected to multiple oxidation/oxide-removal cycles after etching. In each cycle, pores became widened because of the dissolution of the silicon consumed during the thermal oxidation. After several cycles, pore walls were dissolved first at the position of diameter maxima of the pores and adjacent pores become then connected sideways. To obtain a free-standing macroporous membrane, the back side of the samples was polished down until the opening of the pores. Fig. 5 shows some SEM images of the silicon templates produced, with thicknesses over 100 μm.

In a second step, the silicon template was closely bound to a KTP single-crystal substrate with typical dimensions 5 mm long, 3 mm wide, and 1 mm thick. The crystal was oriented in such a way that the largest surface was perpendicular to the ***c*** crystallographic direction with the edges parallel to ***a*** and ***b*** crystallographic directions. The template/substrate set was immersed into a solution formed by mixing of K_2O, P_2O, TiO_2, and WO_3 with a molar % composition K_2O–P_2O–TiO_2–WO_3 = 42–14–14–30 for a period of time between 5 and 10 min. WO_3 was used for decreasing the viscosity of the solution and allowing a faster growth process. A special vertical furnace was used for the epitaxial growth experiments of KTP that provided a wide region with practically no axial gradient. The temperature was controlled by a Eurotherm 903 P controller–programmer. We determined accurately the saturation temperature (T_s) and the epitaxial growth of the KTP photonic structure started two degrees below T_s, which provided a supersaturation degree in the solution of about 2%. After the epitaxial growth experiment, the template/substrate/epitaxy composite was removed from the solution, but

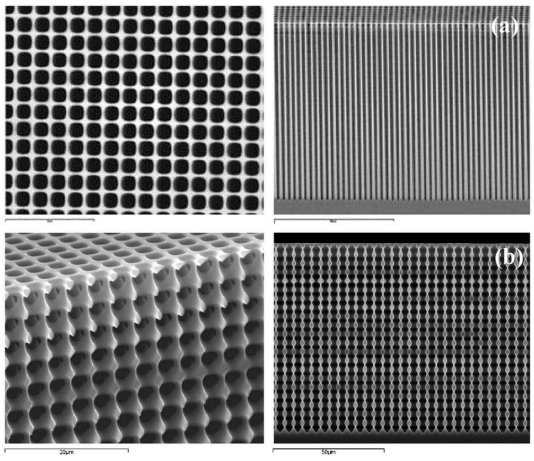

Fig. 5. SEM pictures of a (a) 2D and a (b) 3D macroporous silicon template.

Please cite this article as: J.J. Carvajal, et al., J. Lumin. (2009), doi:10.1016/j.jlumin.2009.03.035

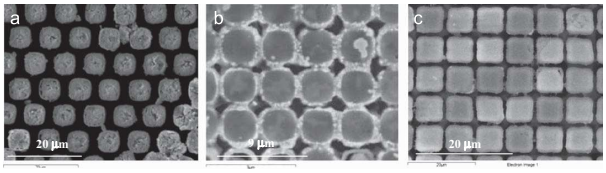

Fig. 6. SEM figures of the top surface of a 2D KTP photonic structure after polishing and partial removing of the silicon template. (a) Sample polished with 0.3 μm-size Al_2O_3 powders. (b) Sample polished using colloidal silicon (Logitech SF1). (c) Sample polished with 0.1 μm-size diamond powders.

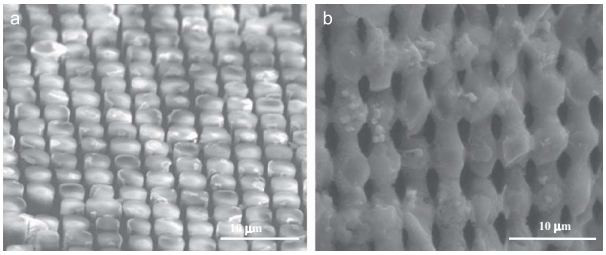

Fig. 7. SEM pictures of a (a) 2D and a (b) 3D KTP photonic crystal after polishing of the top surface and selective etching of the silicon template.

kept inside of the furnace above the surface of the solution while the furnace was cooled down to room temperature at a cooling rate of 15 K/h in order to avoid thermal stresses that could result into cracks in the photonic structures or in the substrate.

After growth, the top part of the KTP photonic structure was polished. The different hardness between silicon and KTP made the polishing process of the two materials simultaneously not easy. We used different procedures for this purpose, including alumina powders, colloidal silicon, and diamond powders. In Fig. 6 several SEM pictures show the top surface of a 2D KTP photonic structure polished following these procedures. The best results were obtained when polishing with diamond powders $\phi = 0.1$ μm.

Once an optical-quality surface for the KTP photonic structure was obtained, the last step in our approach was to remove the silicon template by selective chemical etching with TMAH diluted in distilled water (5 vol%) at 354 K. The effect of the selective etching is clearly visible in Fig. 7, where a side-view image of the KTP photonic structure taken with the SEM is shown.

By using the aforesaid procedure we fabricated different KTP PCs with triangular and square lattices and lattice parameters ranging from 4.5 to 10 μm.

The crystallographic orientation of the substrate is transferred to the KTP photonic structure. To prove this we performed an X-ray texture analysis of the final photonic structure after removing the KTP substrate to ensure that the measured signal comes only from the photonic structure. Part of the silicon membrane was still maintained on the lower part of the photonic structure to give the 2D PCs the necessary mechanical rigidity for further characterization. The texture characterization was performed with a Siemens D5000 diffractometer equipped with an

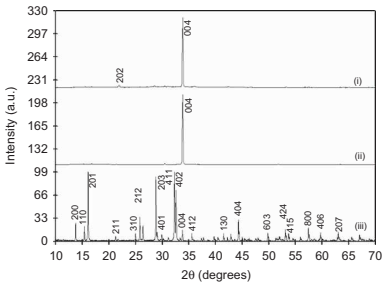

Fig. 8. X-ray powder diffraction patterns of (i) the photonic structure, (ii) KTP substrate, and (iii) KTP crystalline powders.

Euler goniometer and we obtained a 2θ scan from 10° to 70°, with a step size (ss) of 0.05° and a step time (st) of 3 s. This procedure also provided an estimation of the degree of crystallinity of the photonic structure. Fig. 8 shows the 2θ scan for a 2D KTP PC (pattern i), the substrate (pattern ii), and for a KTP crystalline powder sample, milled from a single crystal (pattern iii). The reflections were indexed according to the powder diffraction pattern of KTP, entry 80–0893 of the database maintained by the Joint Committee for Powder Diffraction Studies (JCPDS). As can be seen, the peak with the highest intensity in patterns (i) and (ii) is

Please cite this article as: J.J. Carvajal, et al., J. Lumin. (2009), doi:10.1016/j.jlumin.2009.03.035

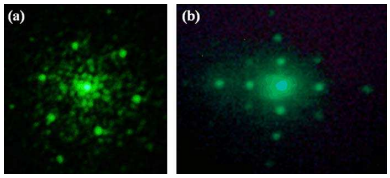

Fig. 9. Pictures of the linear diffraction pattern from a 2D KTP PC with (a) triangular lattice and (b) square lattice.

the (0 0 4) peak. However, this is not the dominant peak in the powder diffraction pattern (iii), which indicates the high degree of texturization and orientation of the KTP columns grown from the KTP substrate. The full-width at half-maximum (FWHM) for the (0 0 4) peak in the photonic structure was found to be 0.4°, very similar to that of the initial substrate, indicating the high degree of crystallinity of the photonic structure. The transference of the crystallographic orientation of the substrate to the KTP PC is advantageous for second-order nonlinear applications since it may allow the use of the most appropriate nonlinear or electro-optic coefficient for a specific application in combination with a phase-matching condition, which would be provided by the photonic structure. This is not possible with bulk KTP where phase-matching relies on the birefringence and the coefficients with the largest nonlinearity cannot be used for efficient SH generation.

A more detailed optical characterization of a 2D KTP PC can be found in Ref. [13]. Here we present the results of some basic light diffraction measurements performed on these structures. The surface of the photonic crystal will act as a diffraction grating and one would expect to see a diffraction pattern in accordance to the KTP photonic structure distribution in a square or triangular lattice. When measuring the linear diffraction in reflection we placed the sample on a XYZ positioning stage mounted on a rotating stage to be able to change the angle of incidence. Once mounted, the sample was illuminated with light at 527 nm. Some pictures of the observed diffraction patterns from samples with triangular and square lattices can be seen in Fig. 9. In those pictures one can see the presence of an intense central spot corresponding to the specular reflection and some other spots that reflect the lattice of the sample.

The PC properties of a 2D KTP structure were demonstrated by performing a measurement of the specular reflection as a function of the wavelength of the incident field. We used a 2D KTP PC of KTP columns in air and periodicity of 4.5 μm. The sample was shined with p-polarized laser pulses, spectrally tuned in the range 940–1220 nm, at an angle of incidence of 25° with respect to the axis of the photonic structure. The specular reflectance spectrum, as shown in Fig. 10, presents a dip at 1100 nm, which corresponds to the spectral position of the third-order Bragg reflection band, which was determined from a numerical calculation using the transfer matrix method.

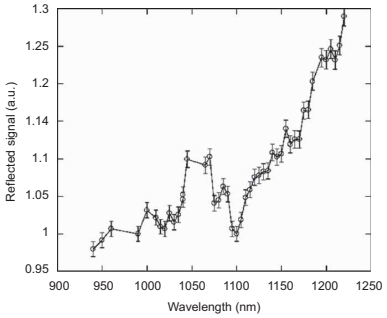

Fig. 10. Measurement of the specular reflection as a function of the wavelength of the incident light.

4. Conclusions

We have used two techniques for the fabrication of 1D photonic crystals: the fabrication of periodically poled ferroelectric materials, such as $LiNbO_3$, and partial removing of one of the ferroelectric domains by selective wet chemical etching; and the microstructuration of the surface of nonlinear optical crystals, such as monoclinic double tungstates and $RbTiOPO_4$, by ultrafast laser ablation.

We have also fabricated 2D and 3D KTP photonic crystals by the templated growth of KTP by liquid phase epitaxy within the pores of a Si template. In this way, the single-crystal substrate provided the desired crystallographic orientation, while the silicon template gave the desired final form to the thin layer.

In the data we collected from the growth procedure we followed there is no indication that KTP PCs with smaller periods could not be grown, as macroporous silicon templates or templates of other kind, with a smaller diameter pore become readily available. Additionally, this approach to fabricate 2D and 3D photonic structures can be extended to other nonlinear and optical materials that can be grown by liquid phase epitaxy.

With these photonic structures, in the future, we pretend to study different effects, such as the generation of light at different frequencies, parametric oscillation, and guiding and bending of light in previously designed line defects.

Acknowledgements

This work was supported by the Spanish government under projects TEC2006-06531, MAT2008-C02-02/NAN, and CONSOLIDER HOPE porject CSD 2007-00007. J.J. Carvajal and M.C. Pujol are supported by the Education and Science Ministry of Spain and European Social Fund under the Ramón y Cajal program, RYC2006-858 and RYC2004-1453, respectively.

References

[1] E. Yablonovitch, Phys. Rev. Lett. 58 (1987) 2059.
[2] S. John, Phys. Rev. Lett. 58 (1987) 2486.
[3] E. Ozbay, I. Bulu, K. Aydin, H. Caglayan, K. Guven, Photon. Nanostruct. 2 (2004) 87.
[4] J. Trull, R. Vilaseca, J. Martorell, R. Corbalan, Opt. Lett. 20 (1995) 1746.
[5] P.P. Markowicz, H. Tiryaki, H. Pudavar, P.N. Prasad, N.N. Lepeshkin, R.W. Boyd, Phys. Rev. Lett. 92 (2004) 083903.
[6] J. Torres, M. Le Vassoi d'Yerville, D. Coquillat, E. Centeno, J.P. Albert, Phys. Rev. B 71 (2005) 195326.
[7] J. Martorell, R. Vilaseca, R. Corbalan, Appl. Phys. Lett. 70 (1997) 702.
[8] M. Centini, C. Sibilia, M. Scalora, G. D'Aguanno, M. Bertolotti, M.J. Bloemer, C.M. Bowden, I. Nefedov, Phys. Rev. E 60 (1999) 4891.
[9] J. Martorell, R. Vilaseca, R. Corbalan, Phys. Rev. A 55 (1997) 4520.
[10] J. Martorell, Appl. Phys. Lett. 86 (2005) 241113.

Please cite this article as: J.J. Carvajal, et al., J. Lumin. (2009), doi:10.1016/j.jlumin.2009.03.035

[11] A.M. Prokhorov, YUS Kuz'miniv, Physics and Chemistry of Crystalline Lithium Niobate, Adam Hilger, Bristol, 1990.
[12] G.D. Stucky, M.L.F. Phillips, T.E. Gier, Chem. Mater. 1 (1989) 492.
[13] H. Vanherzeele, J.D. Bierlein, F.C. Zumsteg, Appl. Opt. 27 (1988) 3314.
[14] J.D. Bierlein, A. Ferretti, L. Brixner, Y. Hsu, Appl. Phys. Lett. 50 (1987) 1216.
[15] Y.S. Oseledchik, S.P. Belokrys, V.V. Osadchuk, A.L. Prosvirnin, A.F. Selevich, V.V. Starshenko, K.V. Kuzemchenko, J. Cryst. Growth 125 (1992) 639.
[16] A. Peña, S. Di Finizio, T. Trifonov, J.J. Carvajal, M. Aguiló, J. Pallarès, A. Rodríguez, R. Alcubilla, L.F. Marsal, F. Díaz, J. Martorell, Adv. Mater. 18 (2006) 2220.
[17] R. Kelly, A. Miotello, Appl. Surf. Sci. 96–98 (1996) 205.
[18] G. Dumitru, V. Romano, H.P. Weber, M. Sentis, W. Marine, Appl. Phys. A 74 (2002) 729.
[19] S. Baudach, J. Bonse, J. Krüger, W. Kautek, Appl. Surf. Sci. 154–155 (2000) 555.
[20] I.E. Barry, G.W. Ross, P.G.R. Smith, R.W. Eason, G. Cook, Mater. Lett. 37 (1998) 246.
[21] S. Grilli, P. Ferraro, P. De Natale, B. Tiribilli, M. Vassalli, Appl. Phys. Lett. 87 (2005) 233106.
[22] K. Terabe, X.Y. Liu, X.J. Li, K. Kitamura, Ferroelectrics 340 (2005) 121.
[23] A. Gruverman, O. Auciello, H. Tokumoto, Appl. Phys. Lett. 69 (1996) 3191.
[24] C.L. Sones, S. Mailis, W.S. Brocklesby, R.W. Eason, J.R. Owen, J. Mater. Chem. 12 (2002) 295.

Please cite this article as: J.J. Carvajal, et al., J. Lumin. (2009), doi:10.1016/j.jlumin.2009.03.035

UNIVERSITAT ROVIRA I VIRGILI
DEVELOPMENT OF OPTICAL CHARACTERIZATION METHODS FOR MICRO- AND NANO-SCALE PLANAR PHOTONIC BAND GAP STRUCTURES
Zdenek Kral
DL: T-1537-2009/ISBN:978-84-692-4556-9